University of California
Santa Barbara

Dynamics of Atmospheric Rivers in High Mountain Asia: Influences on Precipitation, Lightning and Landslides

A dissertation submitted in partial satisfaction
of the requirements for the degree

Doctor of Philosophy
in
Geography

by

Deanna Leigh Nash

Committee in charge:

Professor Leila M.V. Carvalho, Chair
Professor Charles Jones
Professor Qinghua Ding

September 2022

The Dissertation of Deanna Leigh Nash is approved.

_____

Professor Charles Jones

_____

Professor Qinghua Ding

_____

Professor Leila M.V. Carvalho, Committee Chair

June 2022

Dynamics of Atmospheric Rivers in High Mountain Asia: Influences on Precipitation, Lightning and Landslides

by

Deanna Leigh Nash

Acknowledgements

First and foremost, I would like to thank my advisor and committee chair, Professor Leila Carvalho, for her never-ending support and guidance throughout my PhD career. Leila is an amazing listener and she was always supportive of all of my research ideas. She gave me the space to develop my ideas on my own and always offered sharp insight and feedback when I needed it. She truly supported a healthy life-work balance and encouraged me to make my health a priority - something that I am truly grateful for. Thank you so much Leila, for always challenging me, encouraging me to grow, and motivating me to consider a different perspective.

Next, I would like to thank my committee members, Professors Charles Jones and Qinghua Ding for their time, effort, and feedback, which greatly improved this work. Charles spent additional time with me to teach me everything he knows about simulations and to help debug my simulations. Charles, I learned so much about modeling from you, and I am grateful for the experience and skills you helped develop. Qinghua, thank you for always being available for discussion or to help me derive an equation - your support and encouragement were always so energizing.

Thank you to my family and all of my friends who supported me and this dissertation - it meant the world to me to have all of you in my corner. A special thanks to Brandi and Tessa for all the walks, all the scientific conversations, and general mentorship - I'm so glad you were both in the CLIVAC lab.

Last, I would like to thank my husband, Ryan, for his unwavering support throughout this entire graduate journey. He is always my number one supporter - even through multiple relocations, the occasional late nights, and endless code debugging. Ryan, you are my other half and my favorite writing procrastination buddy - I could not have done this without you.

Curriculum Vitae
Deanna Leigh Nash

Education

2022	Ph.D. in Geography, University of California, Santa Barbara.
2017	M.A. in Geography, California State University, Los Angeles.
2013	B.A. in Geography, University of Colorado Colorado Springs.

Research Experience

July 2021	*Advanced Student Program Colloquium* – National Center for Atmospheric Research, Boulder, CO Research on the science of subseasonal to seasonal predictions
2015–2017	*Intern Earth Sciences Division* – Jet Propulsion Laboratory, Pasadena, CA Research on the regional climate model evaluation systems
2015–2016	*Graduate Assistant Geosciences Lab* – California State University Los Angeles, Los Angeles, CA Geographic Information Systems Lab Research Assistant
2014–2015	*Research Assistant Department of Geography* – University of Colorado, Colorado Springs, CO Remote sensing on post-fire vegetation regrowth
2013–2014	*Intern for the Division of the Fire Marshal* – Colorado Springs Fire Department, Colorado Springs, CO Created and maintained maps of the wildland urban interface and wildfire mitigation projects
2014	*GIS intern for Information Technology* – City of Colorado Springs, Colorado Springs, CO Developed and maintained maps for different city divisions

Teaching Experience

Teaching Associate (Instructor of Record) – University of California Santa Barbara (2018–2020)

- Geog 110: Introduction to Meteorology (Summer 2020)
- Geog 165: Waves and Tides in the Ocean (Summer 2018)

Teaching Associate (Instructor of Record) – California State University Los Angeles (2016–2017)

- Geog 1600: Introduction to Physical Geography (Fall 2016, Spring 2017)

Awards

2022	UCSB Department of Geography Excellence in Research Award
2021–2022	New Frontiers Graduate Fellow - NSF awards OCI-0725070 and ACI-1238993
2018–2021	NASA Earth and Space Science Fellowship #80NSSC18K1412
2017; '18; '19	Earth Research Institute Travel Scholarship
2017; '18; '19	Jack and Laura Dangermond Travel Scholarship
2019	AAG Climate Specialty Group Student Paper Competition: 2nd place
2017–2018	UCSB Regents Fellowship
2015–2017	NASA DIRECT-STEM Fellowship – MIRO #NNX15AQ06A
2017	CSULA Gamma Theta Upsilon Scholarship
2017	John David Rees Research Scholarship
2013–2014	UCCS Letters, Arts, and Sciences Research Grant
2014	UCCS Women in Geography Award
2010–2014	UCCS Honors Scholarship Program
2010–2014	UCCS Reach Your Peak Scholarship Program
2010–2014	UCCS Dean's and President's List

Publications

Murray, A. T., Carvalho, L., Church, R. L., Jones, C., Roberts, D., Xu, J., Zigner, K., & Nash, D. (2021). Coastal Vulnerability under Extreme Weather. *Applied Spatial Analysis and Policy*, *14*(3), 497–523. https://doi.org/10.1007/s12061-020-09357-0

Nash, D., Carvalho, L. M. V., Jones, C., & Ding, Q. (2021). Winter and spring atmospheric rivers in High Mountain Asia: climatology, dynamics, and variability. *Climate Dynamics*. https://doi.org/10.1007/S00382-021-06008-Z

Nash, D., Carvalho, L. M. V., Jones, C., & Ding, Q. (2022). Influence of zero degree line on Atmospheric Rivers in High Mountain Asia: WRF case studies of orographic precipitation extremes. *(in preparation)*.

Nash, D., & Carvalho, L. M. (2020). Brief Communication : An electrifying atmospheric river – understanding the thunderstorm event in Santa Barbara County during March 2019. *Natural Hazards and Earth System Sciences*, *20*, 1931–1940. https://doi.org/10.5194/nhess-20-1931-2020

Nash, D., Jones, C., & Carvalho, L. M. V. (2022). Extremes in the atmosphere, disasters on land: Simulating and evaluating hazardous atmospheric river-related precipitation in High Mountain Asia. *(in preparation)*.

Nash, D., Waliser, D. E., Guan, B., Ye, H., & Ralph, F. (2018). The Role of Atmospheric Rivers in Extratropical and Polar Hydroclimate. *Journal of Geophysical Research: Atmospheres*, *123*(13). https://doi.org/10.1029/2017JD028130

Nash, D., Ye, H., & Fetzer, E. (2017). Spatial and temporal variability in winter precipitation across the western United States during the satellite era. *Remote Sensing*, *9*(9). https://doi.org/10.3390/rs9090928

Presentations

Nash, D. (2016). Examining Atmospheric Rivers and Aerosols over California (poster). *CSULA Research Symposium*.

Nash, D. (2017). Atmospheric River Contributions to Extratropical Poleward Moisture Transports and Atmospheric Water Cycle (oral). *CSULA Research Symposium*.

Nash, D., & Carvalho, L. V. (2018a). Atmospheric Rivers Impact on High Asia Mountain Precipitation (poster). *AGU Fall Meeting*.

Nash, D., & Carvalho, L. V. (2018b). What is the impact of Atmospheric Rivers on High Mountain Asia Preciptiation? (poster). *NOAA's 43rd climate Diagnostic and Prediction Workshop*.

Nash, D., & Carvalho, L. V. (2019a). An Electrifying Atmospheric River: Understanding the Thunderstorm Event in Santa Barbara County during March 2019 (oral). *Earth Research Institute Climate Meeting*.

Nash, D., & Carvalho, L. V. (2019b). Atmospheric Rivers and Precipitation in High Mountain Asia (oral). *AGU Fall Meeting*.

Nash, D., & Carvalho, L. V. (2019c). Impacts on High Mountain Asia Precipitation (oral). *American Association of Geographers Annual Meeting*.

Nash, D., & Carvalho, L. V. (2019d). Synoptic-scale atmospheric circulation anomalies associated with winter atmospheric rivers in High Mountain Asia (oral). *Earth Research Institute Climate Meeting*.

Nash, D., & Carvalho, L. V. (2020a). Winter and Spring Atmospheric Rivers in High Mountain Asia (poster). *International Atmospheric River Conference*.

Nash, D., & Carvalho, L. V. (2020b). Winter and Spring Atmospheric Rivers in High Mountain Asia: Climatology, Dynamics and Variability (poster). *AGU Fall Meeting and International Atmospheric Rivers Conference*.

Nash, D., & Carvalho, L. V. (2021). Simulating and evaluating hazardous atmospheric river-related precipitation in High Mountain Asia (poster). *AGU Fall Meeting*.

Nash, D., & Gibbes, C. (2014). Examining post-fire landscape change using remote sensing (poster). *International Fire Conference*.

Nash, D., Mastrantonas, N., Schedftic, W., Mitchell, A. K., Joshi, J. R., DeFlorio, M. J., Subramanian, A. C., & Berner, J. (2022). Subseasonal predictions during the 2017 Oroville Dam Crisis: Role of atmospheric rivers and antecedent synoptic conditions (oral). *Workshop on Sub-seasonal to Seasonal Climate Forecasting for Water Management in the Western U.S.*

Nash, D., & Trefler, A. (2016). Using Satellite Observations to Explore Water Storage and Precipitation (oral). *Satellites and Education Conference*.

Nash, D., Waliser, D. E., Guan, B., Ye, H., & Ralph, F. (2017a). Atmospheric River Importance to Extratropical Climate and Hydrology (poster). *AGU Fall Meeting*.

Nash, D., Waliser, D. E., Guan, B., Ye, H., & Ralph, F. (2017b). How water vapor transport influences precipitation efficiency over high latitudes (oral). *American Association of Geographers Annual Meeting*.

Nash, D., Waliser, D. E., Guan, B., Ye, H., & Ralph, F. (2018). The Role of Atmospheric Rivers in Extratropical and Polar Hydroclimates (oral). *International Atmospheric River Conference*.

Nash, D., & Ye, H. (2016a). Spatial and Temporal Variability in Precipitation Characteristics in the Western United States (poster). *AGU Fall Meeting*.

Nash, D., & Ye, H. (2016b). Variability in Precipitation Characteristics in the Western United States (poster). *American Pacific Coast Geographers conference*.

Service

- Advanced Graduate Student Mentor (2021–2022), Dept. of Geography UCSB
- Mentor for Graduate Scholars Program (2021–2022), UCSB
- Mentor for out in STEM (2021), UCSB
- Mentored Undergraduate Research Project (2019), Dept. of Geography UCSB
- Alumnae Advisory Committee Recruitment Advisor (2019–2022), CA Zeta chapter of Pi Beta Phi
- Chair's Graduate Advisory Committee (2019–2022), Dept. of Geography UCSB
- Chair of the Lounge Committee (2019–2020), Dept. of Geography UCSB
- Member of the Events Committee (2017–2019), Dept. of Geography UCSB

- President of the Lambda Pi Chapter of Gamma Theta Epsilon Honor Society (2017), Dept. of Geography CSULA
- Member of the Theta Chi Chapter of Gamma Theta Epsilon Honor Society (2014), Dept. of Geography UCCS
- Member of the Colorado Epsilon Chapter of Pi Beta Phi (2011–2014), University of Colorado Colorado Springs

Abstract

Dynamics of Atmospheric Rivers in High Mountain Asia: Influences on Precipitation, Lightning and Landslides

by

Deanna Leigh Nash

Atmospheric Rivers (ARs), a global phenomenon, play an important role in the hydroclimate as they transport large amounts of moisture poleward via plumes in the lower troposphere across mid-latitudes and into Polar regions. Multiple studies have demonstrated that ARs are related to precipitation extremes, flooding, seasonal snowpack, and water availability where they occur. Despite ARs occurring about 10% of the time during the winter and spring in High Mountain Asia (HMA), little is known about these unique inland penetrating ARs, their resulting orographic precipitation and their association with precipitation-related hazards such as landslides and lightning. This research demonstrates the importance of HMA ARs to annual precipitation, summarizes their spatial and temporal variability in recent decades, and contrasts the synoptic and mesoscale conditions of three unique and hazardous ARs. The first part of this research explores the connection between ARs and lightning via a timely case study on an AR in Santa Barbara, CA that simultaneously occurred with over 8,000 lightning flashes in under 24 hours. Thermodynamic analysis revealed that orographic forcing and the warm conveyor belt lifted the abnormally high water vapor content in the AR in a convectively unstable atmosphere, resulting in hail formation and enhanced electrification. The second part of this research uses 40 years of the European Centre for Medium-Range Weather Forecasts (ECMWF) atmospheric reanalyses of the global climate (ERA5) to develop a climatology of ARs that reach HMA during winter and

spring and quantify their contribution to seasonal precipitation. Combined empirical orthogonal function (cEOF) and k-means clustering applied to meridional and zonal integrated vapor transport identified three distinct HMA AR types with unique circulation and precipitation patterns. Synoptic composites revealed that each HMA AR type results in above-average precipitation in Northwestern, Western, and Eastern HMA, respectively, when they occur. The differences in the precipitation patterns is largely due to the location and magnitude of the upper-level troughs and ridges, influencing the low-level moisture circulation in the ARs. Further, we found that large-scale climate modes, such as the El Niño Southern Oscillation, Arctic Oscillation, and Siberian High significantly influence the frequency of Northwestern and Western HMA ARs. During HMA ARs in recent decades, trends in moisture transport and the height of the freezing level have both increased significantly, a concern considering that during HMA ARs with a higher than average freezing level, there is significantly less frozen precipitation. The third part of this research contrasts the mesoscale characteristics of two Western HMA ARs that both resulted in extreme precipitation. With Climate Forecast System Reanalysis (CFSR) dynamically downscaled to 6.7 km spatial resolution, we show that the orientation of the AR axis relative to the topography increases the efficiency of the precipitation more than the amount or duration of the moisture within the AR. However, the 6.7 km data does not quite resolve the extreme precipitation associated with these ARs; therefore, the final part of this research uses the Advanced Weather Research and Forecasting (ARW-WRF, hereafter WRF) model to improve the accuracy of simulated extreme precipitation at a finer-scale resolution (3 km). This dissertation demonstrates the relevance of ARs to the winter and spring hydroclimate and precipitation-related hazards in HMA, and provides information that can be used for future projections of precipitation across multiple timescales.

Contents

List of Figures

List of Tables

Chapter 1

Introduction

D.L. NASH

1.1 Overview

1.1.1 Atmospheric Rivers

ARs, a term coined in the early 1990s, describes a phenomenon that explains how baroclinic eddies transport large amounts of water vapor via relatively infrequent, long conduits of strong moisture transport across mid-latitudes and into Polar Regions (Zhu & Newell, 1994). Many studies have shown the global importance of ARs to poleward moisture transport, climate, and water budgets (Guan & Waliser, 2017; Guan et al., 2018; Nash et al., 2018; Paltan et al., 2017; Waliser & Guan, 2017; Zhu & Newell, 1998). When zonally integrated, poleward integrated vapor transport (IVT) from ARs makes up over 90% of the total moisture transport in the mid to high latitudes (Guan & Waliser, 2015; Zhu & Newell, 1998). Since the original work done by Newell et al. (1992), there have been many studies that have focused on the regional impacts of ARs, particularly in western United States and Western Europe. Studies have found

that ARs are related to precipitation extremes, flooding, seasonal snowpack, and water availability in these regions (Dettinger, 2011; Guan et al., 2010, 2013; Lavers & Villarini, 2013; Ralph et al., 2006; Wick et al., 2013). Some studies have focused on the impact in other regions like Antarctica (Gorodetskaya et al., 2014), the Arctic Ocean and Greenland (Baggett et al., 2016; Hegyi & Taylor, 2018; Mattingly et al., 2018; Mattingly et al., 2020; Neff, 2018; Wernli & Papritz, 2018; Wille et al., 2019), South America (Ramos et al., 2019; Viale & Nuñez, 2011; Viale et al., 2018), North Africa (Akbary et al., 2019; Blamey et al., 2018; Dezfuli, 2020; Massoud et al., 2020), and East Asia (Naoi et al., 2020; Pan & Lu, 2020), finding that ARs play a role in modulating precipitation extremes.

ARs are usually identified by measuring IVT, which tells us about the flux of water vapor in each column of air, which is critical to understanding ARs. ARs generally occur in the region ahead of a cold front with an extratropical cyclone, obtaining their above-average water vapor content via moisture transport from the tropics as well as local moisture convergence associated with the warm conveyor belt and the cold front of the extratropical cyclone (Bao et al., 2006; Ralph et al., 2004; Rutz et al., 2014). Even though the official glossary definition of ARs from AMS (2018) states that "the water vapor in atmospheric rivers is supplied by tropical and/or extratropical moisture sources" it is a common misconception that tropical sources alone provide all the moisture within an AR. However, a study completed by Bao et al. (2006) concluded that local moisture convergence is the primary contributor to enhanced integrated water vapor (IWV) bands in the central and eastern Pacific, with evidence indicating that some bands include moisture transported from the tropics.

Based on the widely used AR detection algorithm developed by Guan and Waliser (2015), ARs are identified using a combination of geometry (e.g., length, width), intensity thresholds (e.g., usually above 85th percentile), and directional components (e.g.,

must be poleward), giving a series of AR objects on a 6-hourly, global basis. ARs make landfall, or cross from a major body of water to land, in a variety of regions across the globe, and cross the west coast of India from the Arabian Sea roughly 4 times a year (see Guan and Waliser, 2015, Fig. 8a). Using the Guan and Waliser (2015) AR detection algorithm, Fig. 1.1 shows the number of days an AR reaches HMA between 1979 and 2019, or passes through the 1 km elevation line indicated in Fig. 1.2. ARs occur on average 10 times a month during the winter and spring seasons, and up to 20 times a month during summer. Despite being relatively infrequent, when they reach the complex topography of HMA, ARs can result in higher-than-average orographic precipitation, making even those relatively few AR events critical to local water resources. A few studies have explored the thermodynamic and kinematics of atmospheric rivers as it relates to orographic precipitation, aiding in understanding of how atmospheric rivers transport large plumes of water vapor long distances without precipitating. ARs can occur simultaneously with the low-level jet, enhancing the water vapor flux. The AR is typically larger than the low-level jet (approximately 850 km wide and 3 km deep), and occurs in the lower-troposphere, with 75% of the IVT found below 650 hPa (Guan & Waliser, 2015; Guan et al., 2018; Ralph et al., 2017). The warm conveyor belt (WCB) is an area of ascending air within the warm sector of the extratropical cyclone. Water vapor in the AR, which can be sourced from intense vapor transport out of the tropics as well midlatitude convergence of water vapor along the path of the AR, can often be transported via winds into the WCB resulting in dynamical uplift (Dettinger et al., 2015). Some studies suggest that WCBs and ARs can form on their own without direct connection to each other (Dacre et al., 2015; Dettinger et al., 2015).

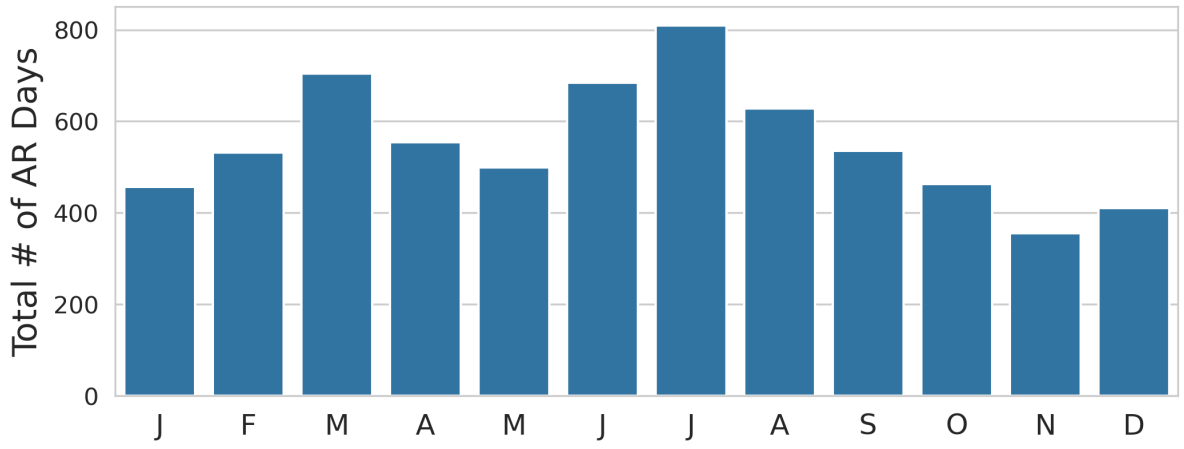

Figure 1.1: Frequency (total number of days) of ARs that reach HMA by passing the 1 km elevation height between 1979 and 2018.

1.1.2 High Mountain Asia Hydroclimate

There have been few studies that explore ARs specifically near southern Asia (e.g., Thapa et al. (2018) and Yang et al. (2018)), and they found that ARs contribute to extreme precipitation and are associated with flood events in the Nepal and Bay of Bengal areas. Both studies indicated the need for further investigation into mechanisms that govern ARs and their relationship with the two distinct precipitation regimes that modulate the local climate. In Southern Asia, precipitation and the resulting glacial melt in the spring and summer months provides water resources for hundreds of millions of people (Hewitt, 2005; Kääb et al., 2012). The Karakoram, a region located in the western Himalayas, receives approximately 50% of its annual precipitation during winter and spring months from extratropical cyclones, while Central Himalaya receives over 70% of its annual precipitation from summer monsoon flow (Bookhagen & Burbank, 2010; Norris et al., 2018; Norris et al., 2017). In addition to having two distinct precipitation regimes, there have been dynamical changes in these two regions that have impacted the local hydrological cycles. For example, in Central Himalaya, accelerated melting of alpine glaciers has been attributed to increased temperatures, decreasing

precipitation, and the weakening of the summer monsoon (Duan et al., 2006; Krishnan et al., 2013; Zhao et al., 2014). Meanwhile, glaciers in the Karakoram have been stable or advancing in a phenomenon known as the Karakoram Anomaly, attributed to increased wintertime precipitation, decreasing summer temperatures, and increases in extratropical cyclone frequency and intensity (Archer & Fowler, 2004; Bolch et al., 2012; Cannon et al., 2015; Forsythe, 2015; Gardelle et al., 2012; Hewitt, 2005; Kääb et al., 2012; Norris et al., 2018; Scherler et al., 2011).

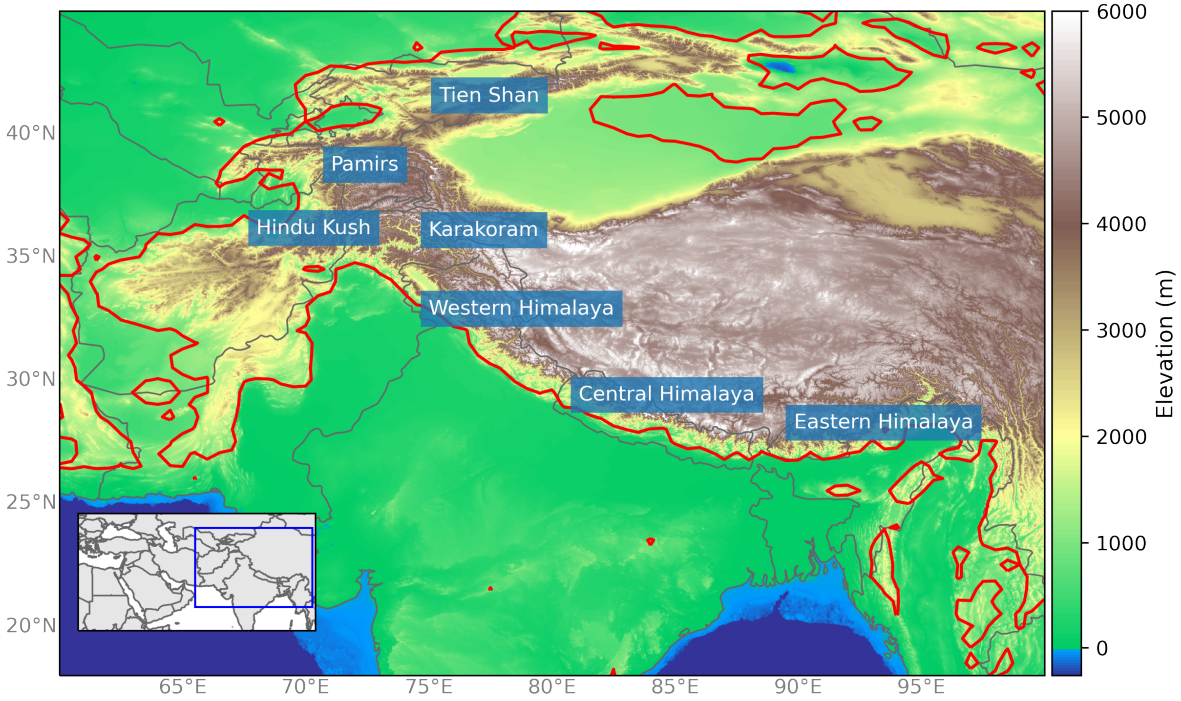

Figure 1.2: Study area with elevation (shaded; m) and names and locations of mountain ranges indicated by the blue labels. The red line is the 1 km elevation line, used to identify ARs that reach HMA.

Norris et al. (2017) described the interseasonal, intraseasonal, and diurnal patterns of precipitation in HMA by utilizing the Advanced Weather Research and Forecasting (ARW-WRF, hereafter WRF) model to simulate a 12-month period (April 2005 through March 2006). The WRF simulation performed well in the timing and intensity of win-

tertime extratropical cyclones, but had difficulty resolving summer nocturnal precipitation in the foothills and valleys of the Himalaya (Norris et al., 2017). Following that study, Norris et al. (2018) assessed the spatial patterns and trends of precipitation and temperature in HMA regarding the Karakoram Anomaly using the same WRF model configuration as Norris et al. (2017) to dynamically downscale global reanalysis for a 36-year period between 1979 and 2015. In recent decades, an anti-cyclonic warming trend during winter and summer has been observed over eastern and central Himalaya, while western Himalaya has been impacted by a cyclonic trend with no warming (Norris et al., 2018). While Norris et al. (2018) was not able to fully explain the Karakoram anomaly, the dynamically downscaled reanalyses in HMA over a 36-year period could be important in understanding the relationship between ARs and precipitation in this region, with an in depth exploration of the mesoscale flow patterns due to complex topography of HMA.

1.1.3 Natural Hazards in High Mountain Asia

India experiences a high frequency of lightning, mainly due to the increase in severe thunderstorms during pre-monsoon season (April to May). A study completed by Ramesh Kumar and Kamra (2012) found that the topography of the Himalayan range has a strong influence on lightning flash rates in the region. For example, south of the Himalayan range, an enhanced mountain breeze front and synoptic convective systems increase lightning frequency (Lal & Pawar, 2009; Pawar et al., 2015; Ramesh Kumar & Kamra, 2012). Pawar et al. (2015) analyzed a series of short duration thunderstorms with high peak flash rates in the foothills of northeastern India, and attributed the high lightning flash rates to the timing and location of the thunderstorms, explaining that the diurnal cycle of the mountain breeze increased moisture convergence in the valley

during the night. It is possible that ARs influence the frequency of lightning in HMA, and part of this research will explore the relationship between ARs and lightning.

Landslides are another hazard that often occur in HMA due to the location of Indian and Eurasian plate boundary. With climate change, studies estimate that extreme precipitation will increase near mountains and glaciers, which in turn increases the chances of landslide activity (Kirschbaum et al., 2020). Extreme rainfall is more likely during monsoon season, however, it does occur and result in devastating landslides during the winter and spring season. Figure 1.3 shows the location and fatality count of precipitation-triggered landslides that are associated with ARs in HMA, indicating the connection and impact of ARs on landslides in this region. This dissertation investigates extreme rainfall events during the winter and spring seasons that are associated with ARs and examines the role the ARs played in landslides that occurred on the same day. Understanding landslide activity is a complex geographic and geologic phenomenon, but other studies have already shown that extreme rainfall is the most significant trigger of landslides in HMA and that predictions of these landslides, particularly in the Karakoram, improve with better understanding of the large-scale moisture flux patterns (Hunt & Dimri, 2021; Kirschbaum et al., 2020).

One interesting new research aspect of ARs examines them from a categorical perspective. Ralph et al. (2019) developed a scale system to differentiate between weaker and stronger ARs in the Pacific Ocean, as the varying intensity changes the impact of AR on local precipitation. For example, different categories of ARs can provide a variety of benefits in the region they are occurring, such as increased reservoir levels, drought relief, water supply, while some ARs can cause various hazards (e.g., extreme precipitation, flooding, high winds) (Backes et al., 2015; Dettinger, 2013; Ralph & Dettinger, 2012; Ralph et al., 2019; Waliser & Guan, 2017). Though a general categorization of AR strength based on IVT values is useful, a more regional approach in High Mountain

Asia that includes other variables such as column temperature, rain/snow line information, topography, and prior conditions will be useful in understanding the impact of ARs on local water resources and natural hazards.

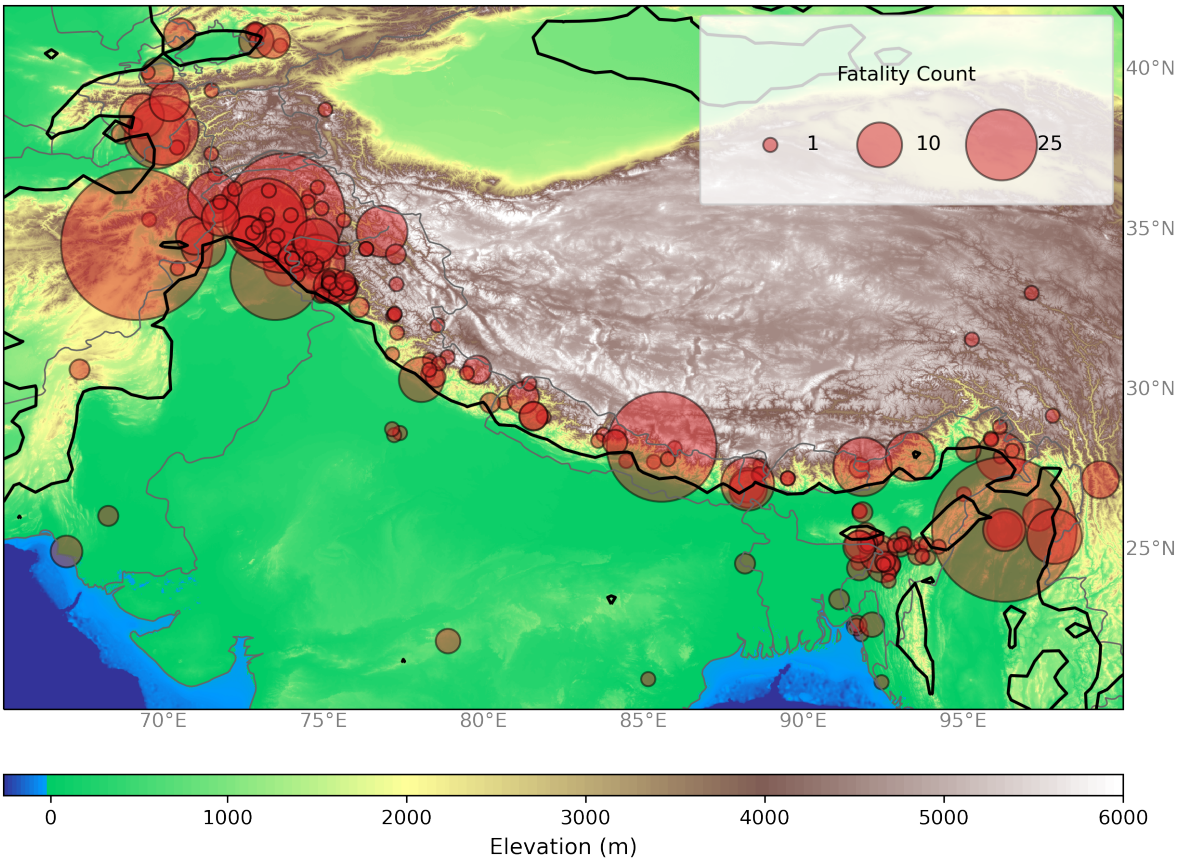

Figure 1.3: High Mountain Asia with elevation (shaded; m) and locations and fatality count (bubbles, fatality count) of landslides occurring on the same day as a HMA AR between 1988 and 2017 using the landslide data from Kirschbaum et al. (2010).

1.2 Dissertation Objectives

The hydroclimate of HMA is not well understood, and hundreds of millions of people rely on the water resources in this region. In addition, extreme precipitation events that occur in this region are not well predicted and result in damages to infrastruc-

ture, displaced populations, and fatalities. While we know quite a bit about ARs in other regions of the world, particularly in Western Europe and western United States, understanding the synoptic and mesoscale mechanisms of these unique, inland penetrating ARs will build on the current knowledge base of ARs, and potentially improve understanding about the relationship between ARs and orographic precipitation. **The main goal of this research was to assess the impact of ARs on High Mountain Asia's (HMA) hydroclimate from a climatological perspective by examining dynamic mechanisms and their relationship with precipitation, lightning and landslides.** In this dissertation, we classified the climatology of ARs in HMA, determined the synoptic scale, mesoscale, and thermodynamic conditions of HMA ARs, and investigated three AR case studies – one in western US, two in HMA – that resulted in extreme hazards. By completing the research objectives (outlined below), we worked to close current gaps in knowledge about the HMA hydroclimate and inland penetrating orographic ARs.

1. Examine synoptic and mesoscale features of a unique AR event in Santa Barbara, CA during March 2019 that resulted in over 8,000 lightning flashes in the southern California region in under 24 hours.

2. Investigate the regional climatology of ARs that reach HMA to understand their synoptic scale characteristics, impact on large-scale precipitation, and how climate modes such as ENSO, AO, and SH influence HMA AR frequency and broader circulation patterns.

3. Contrast the thermodynamic and mesoscale characteristics of two impactful AR events using 20 km and 6.7 km WRF simulations created by Norris et al. (2018) to determine the primary mechanisms of ARs associated with extreme orographic precipitation and lightning.

4. Evaluate the ability of multiple high-resolution WRF simulations to capture the spatial and temporal patterns of extreme precipitation associated with a particularly intense AR associated with multiple landslides in western HMA.

The first chapter of this dissertation is unique in that it focuses on an AR event that occurred in Santa Barbara, CA rather than HMA. This chapter demonstrates the important role of an AR in an extremely unique lightning storm in Southern California. The relationship between lightning and ARs is largely uncovered, and this timely case study examines the synoptic and mesoscale features that resulted in over 8,000 lightning flashes in southern California in under 24 hours. This study concludes that despite the very small amount of convective available potential energy (CAPE), the warm, moist air within the AR was lifted above the freezing level in a convectively unstable atmosphere, resulting in hail and high electrification. This case study provided a foundation for analysis for Chapter 4, where we explore the mesoscale characteristics of two HMA ARs that were associated with lightning, flooding, and extreme orographic precipitation.

The second chapter focuses on the synoptic characteristics of ARs that cross Southern Asia and reach HMA during the winter and spring months, contributing between 40-60% of total winter and spring precipitation. Combined empirical orthogonal function analysis (cEOF) and k-means clustering applied to meridional and zonal IVT in Southern Asia identifies three distinct HMA AR types with unique circulation and precipitation patterns. Additionally, this research describes the influence of large-scale climate modes, like El Niño Southern Oscillation, Arctic Oscillation, Siberian High, and Madden-Julian Oscillation on the frequency of the three HMA AR types.

The third chapter uses 36 years of dynamically downscaled reanalysis using WRF, created in Norris et al. (2018). We evaluate the 3-hourly, 6.7 horizontal resolution

model data against the large-scale circulation and precipitation patterns for the three AR subtypes determined in the previous chapter. We then use the WRF simulations to summarize trends in IVT and the height of the freezing level during the three HMA AR types defined in Nash et al. (2021). We then contrast the mesoscale conditions of two impactful Western HMA ARs - one that occurred with an above-average freezing level height and one with a below-average freezing level height. This work emphasizes the contribution of ARs to the rain to snow ratio, particularly focused on precipitation in the foothills, as the moisture from the AR is orographically forced. This illuminates the broader impact of these ARs on vital watershed landscapes such as the Karakoram and the Pamirs.

The final chapter of this dissertation evaluates the ability of multiple WRF simulations to capture the extreme maxima of orographic precipitation during a Western HMA AR that was associated with multiple landslides in February 2010. In addition to evaluating Norris' 6.7 km and 3-hourly WRF data, we dynamically downscale ERA5 to 9 and 3 km spatial resolution, and a 1-hourly temporal resolution and evaluate their ability to simulate the extreme precipitation associated with the February 2010 AR relative to NASA's Integrated Multi-satellitE Retrievals for GPM. We find that the finer-resolution dynamical simulations (3 km) greatly improve the representation of the orographic precipitation in complex terrain compared to the course-scale (6.7 km) simulations.

This dissertation demonstrates the broader importance of ARs on the winter and spring hydroclimate of HMA by identifying the synoptic characteristics of three unique HMA AR types and quantifying their contribution to seasonal precipitation (Nash et al., 2021). Roughly half of the annual precipitation in Southern Asia comes from winter and spring extratropical cyclones, and just a few impactful ARs occurring in the area ahead of the cold front of those cyclones can contribute significantly to those resources (Cannon et al., 2015; Nash et al., 2021, 2022; Norris et al., 2018). We show

that, in recent decades, increased water vapor transport and the height of the zero degree isotherm during HMA ARs is decreasing the ratio of frozen precipitation in HMA. Further, targeted, high-resolution simulations can be used to accurately represent orographic precipitation extremes associated with HMA ARs. The work completed here has increased the understanding of AR impacts in HMA, and can be applied to improve forecasts for water resources and natural hazards in a region vulnerable to changes in a warming climate.

1.3 Permissions and Attributions

1. The content of chapter 2 and A is the result of a collaboration with Leila Carvalho, and has previously appeared in Natural Hazards and Earth System Sciences (Nash & Carvalho, 2020). It is reproduced here with the permission of Copernicus Publications: https://nhess.copernicus.org/articles/20/1931/2020/.

2. The content of chapter 3 and appendix B is the result of a collaboration with Leila Carvalho, Charles Jones, and Qinghua Ding, and has previously appeared in Climate Dynamics (Nash et al., 2021). It is reproduced here with the permission of Springer Nature: https://link.springer.com/article/10.1007/s00382-021-06008-z.

References

Akbary, M., Salimi, S., Hosseini, S. A., & Hosseini, M. (2019). Spatio-temporal changes of atmospheric rivers in the Middle East and North Africa region. *International Journal of Climatology*, *39*, 3976–3986. https://doi.org/10.1002/JOC.6052

AMS. (2018). "atmospheric river". http://glossary.ametsoc.org/wiki/Atmospheric_river

Archer, D. R., & Fowler, H. J. (2004). Spatial and Temporal Variations in Precipitation in the Upper Indus Basin, Global Teleconnections and Hydrological Implications. *Hydrology and Earth System Sciences*, *8*(1), 47–61. https://doi.org/https://hal.archives-ouvertes.fr/hal-00304788

Backes, T. M., Kaplan, M. L., Schumer, R., & Mejia, J. F. (2015). A climatology of the vertical structure of water vapor transport to the Sierra Nevada in cool season atmospheric river precipitation events. *Journal of Hydrometeorology*, *16*(3), 1029–1047. https://doi.org/10.1175/JHM-D-14-0077.1

Baggett, C., Lee, S., & Feldstein, S. (2016). An investigation of the presence of atmospheric rivers over the North Pacific during planetary-scale wave life cycles and their role in Arctic warming. *Journal of the Atmospheric Sciences*, *73*(11), 4329–4347. https://doi.org/10.1175/JAS-D-16-0033.1

Bao, J. W., Michelson, S. A., Neiman, P. J., Ralph, F., & Wilczak, J. M. (2006). Interpretation of enhanced integrated water vapor bands associated with extratropical cyclones: Their formation and connection to tropical moisture. *Monthly Weather Review*, *134*, 1063–1080. https://doi.org/10.1175/MWR3123.1

Blamey, R. C., Ramos, A. M., Trigo, R. M., Tomé, R., & Reason, C. J. (2018). The Influence of Atmospheric Rivers over the South Atlantic on Winter Rainfall in South Africa. *Journal of Hydrometeorology*, *19*(1), 127–142. https://doi.org/10.1175/JHM-D-17-0111.1

Bolch, T., Kulkarni, A., Kääb, A., Huggel, C., Paul, F., Cogley, J. G., Frey, H., Kargel, J. S., Fujita, K., Scheel, M., Barjracharya, S., & Stoffel, M. (2012). The State and Fate of Himalayan Glaciers. *Science*, *336*(6079), 310–314. https://doi.org/10.1126/science.1215828

Bookhagen, B., & Burbank, D. W. (2010). Toward a complete Himalayan hydrological budget: Spatiotemporal distribution of snowmelt and rainfall and their impact on river discharge. *Journal of Geophysical Research: Earth Surface*, *115*(3), 1–25. https://doi.org/10.1029/2009JF001426

Cannon, F., Carvalho, L. M., Jones, C., & Bookhagen, B. (2015). Multi-annual variations in winter westerly disturbance activity affecting the Himalaya. *Climate Dynamics*, *44*(1-2), 441–455. https://doi.org/10.1007/s00382-014-2248-8

Dacre, H. F., Clark, P. A., Martinez-Alvarado, O., Stringer, M. A., & Lavers, D. A. (2015). How do atmospheric rivers form? *Bulletin of the American Meteorological Society*, *96*(8), 1243–1255. https://doi.org/10.1175/BAMS-D-14-00031.1

Dettinger, M. D. (2011). Climate change, atmospheric rivers, and floods in California - a multimodel analysis of storm frequency and magnitude changes. *JAWRA Journal of the American Water Resources Association*, *47*(3), 514–523. https://doi.org/10.1111/j.1752-1688.2011.00546.x

Dettinger, M. D. (2013). Atmospheric rivers as drought busters on the U.S. West Coast. *Journal of Hydrometeorology*, *14*(6), 1721–1732. https://doi.org/10.1175/JHM-D-13-02.1

Dettinger, M. D., Ralph, F., & Lavers, D. (2015). Setting the stage for a global science of atmospheric rivers. *Eos*, *97*(1), 7. https://doi.org/10.1029/2015eo038675

Dezfuli, A. (2020). Rare Atmospheric River Caused Record Floods across the Middle East. *Bulletin of the American Meteorological Society*, *101*(4), E394–E400. https://doi.org/10.1175/BAMS-D-19-0247.1

Duan, K., Yao, T., & Thompson, L. G. (2006). Response of monsoon precipitation in the Himalayas to global warming. *Journal of Geophysical Research: Atmospheres*, *111*(D19). https://doi.org/10.1029/2006JD007084

Forsythe, N. (2015). A detailed cloud fraction climatology of the upper indus basin and its implications for near-surface air temperature. *Journal of Climate*, *28*, 3537–3556. https://doi.org/10.1175/JCLI-D-14-00505.1

Gardelle, J., Berthier, E., & Arnaud, Y. (2012). Slight mass gain of Karakoram glaciers in the early twenty-first century. *Nature Geoscience*, *5*, 322–325. https://doi.org/10.1038/NGEO1450

Gorodetskaya, I. V., Tsukernik, M., Claes, K., Ralph, F., Neff, W. D., & Van Lipzip, N. P. M. (2014). The role of atmospheric rivers in anomalous snow accumulation in East Antarctica. *Geophysical Research Letters*, *41*, 6199–6206. https://doi.org/10.1002/2014GL060881

Guan, B., Molotch, N. P., Waliser, D. E., Fetzer, E. J., & Neiman, P. J. (2010). Extreme snowfall events linked to atmospheric rivers and surface air temperature via satellite measurements. *Geophysical Research Letters*, *37*(20), n/a–n/a. https://doi.org/10.1029/2010gl044696

Guan, B., Molotch, N. P., Waliser, D. E., Fetzer, E. J., & Neiman, P. J. (2013). The 2010/2011 snow season in California's Sierra Nevada: Role of atmospheric rivers and modes of large-scale variability. *Water Resources Research*, *49*(10), 6731–6743. https://doi.org/10.1002/wrcr.20537

Guan, B., & Waliser, D. E. (2015). Detection of atmospheric rivers: Evaluation and application of an algorithm for global studies. *Journal of Geophysical Research: Atmospheres*, *120*(24), 12514–12535. https://doi.org/10.1002/2015jd024257

Guan, B., & Waliser, D. E. (2017). Atmospheric rivers in 20 year weather and climate simulations: A multimodel, global evaluation. *Journal of Geophysical Research*, *122*, 5556–5581. https://doi.org/10.1002/2016JD026174

Guan, B., Waliser, D. E., & Ralph, F. (2018). An intercomparison between reanalysis and dropsonde observations of the total water vapor transport in individual atmospheric rivers. *Journal of Hydrometeorology*, *19*(2), 321–337. https://doi.org/10.1175/jhm-d-17-0114.1

Hegyi, B. M., & Taylor, P. C. (2018). The Unprecedented 2016–2017 Arctic Sea Ice Growth Season: The Crucial Role of Atmospheric Rivers and Longwave Fluxes. *Geophysical Research Letters*, *45*(10), 5204–5212. https://doi.org/10.1029/2017GL076717

Hewitt, K. (2005). The Karakoram Anomaly? Glacier Expansion and the 'Elevation Effect,' Karakoram Himalaya. *Mountain Research and Development*, *25*(4), 332–341. https://doi.org/10.1659/0276-4741(2005)025[0332:TKAGEA]2.0.CO;2

Hunt, K. M. R., & Dimri, A. P. (2021). Synoptic-scale precursors of landslides in the western Himalaya and Karakoram. *Science of The Total Environment*, *776*, 145895. https://doi.org/10.1016/J.SCITOTENV.2021.145895

Kääb, A., Berthier, E., Nuth, C., Gardelle, J., & Arnaud, Y. (2012). Contrasting patterns of early twenty-first-century glacier mass change in the Himalayas. *Nature*, *488*, 495–498. https://doi.org/10.1038/nature11324

Kirschbaum, D., Adler, R., Hong, Y., Hill, S., & Lerner-Lam, A. (2010). A global landslide catalog for hazard applications: Method, results, and limitations. *Natural Hazards*, *52*, 561–575. https://doi.org/10.1007/S11069-009-9401-4/TABLES/3

Kirschbaum, D., Kapnick, S. B., Stanley, T., & Pascale, S. (2020). Changes in Extreme Precipitation and Landslides Over High Mountain Asia. *Geophysical Research Letters*, *47*(4), e2019GL085347. https://doi.org/10.1029/2019GL085347

Krishnan, R., Sabin, T. P., Ayantika, D. C., Kitoh, A., Sugi, M., Murakami, H., Turner, A. G., Slingo, J. M., & Rajendran, K. (2013). Will the South Asian monsoon overturning circulation stabilize any further? *Climate Dynamics*, *40*(1-2), 187–211. https://doi.org/10.1007/s00382-012-1317-0

Lal, D. M., & Pawar, S. D. (2009). Relationship between rainfall and lightning over central Indian region in monsoon and premonsoon seasons. *Atmospheric Research*, *92*, 402–410. https://doi.org/10.1016/J.ATMOSRES.2008.12.009

Lavers, D. A., & Villarini, G. (2013). The nexus between atmospheric rivers and extreme precipitation across Europe. *Geophysical Research Letters*, *40*(12), 3259–3264. https://doi.org/10.1002/grl.50636

Massoud, E., Massoud, T., Guan, B., Sengupta, A., Espinoza, V., Luna, M. D., Raymond, C., & Waliser, D. (2020). Atmospheric Rivers and Precipitation in the Middle East and North Africa (MENA). *Water 2020, Vol. 12, Page 2863*, *12*(2863), 1–18. https://doi.org/10.3390/W12102863

Mattingly, K. S., Mote, T. L., & Fettweis, X. (2018). Atmospheric River Impacts on Greenland Ice Sheet Surface Mass Balance. *Journal of Geophysical Research: Atmospheres*, *123*(16), 8538–8560. https://doi.org/10.1029/2018JD028714

Mattingly, K. S., Mote, T. L., Fettweis, X., As, D. V., Tricht, K. V., Lhermitte, S., Pettersen, C., & Fausto, R. S. (2020). Strong summer atmospheric rivers trigger Greenland ice sheet melt through spatially varying surface energy balance and cloud regimes. *Journal of Climate*, *33*(16), 6809–6832. https://doi.org/10.1175/JCLI-D-19-0835.1

Naoi, M., Kamae, Y., Ueda, H., & Mei, W. (2020). Impacts of Seasonal Transitions of ENSO on Atmospheric River Activity over East Asia. *Journal of the Meteorological Society of Japan*, *98*(3), 655–668. https://doi.org/10.2151/JMSJ.2020-027

Nash, D., Carvalho, L. M. V., Jones, C., & Ding, Q. (2021). Winter and spring atmospheric rivers in High Mountain Asia: climatology, dynamics, and variability. *Climate Dynamics*. https://doi.org/10.1007/S00382-021-06008-Z

Nash, D., Carvalho, L. M. V., Jones, C., & Ding, Q. (2022). Influence of zero degree line on Atmospheric Rivers in High Mountain Asia: WRF case studies of orographic precipitation extremes. *(in preparation)*.

Nash, D., & Carvalho, L. M. (2020). Brief Communication : An electrifying atmospheric river – understanding the thunderstorm event in Santa Barbara County during March 2019. *Natural Hazards and Earth System Sciences*, *20*, 1931–1940. https://doi.org/10.5194/nhess-20-1931-2020

Nash, D., Waliser, D. E., Guan, B., Ye, H., & Ralph, F. (2018). The Role of Atmospheric Rivers in Extratropical and Polar Hydroclimate. *Journal of Geophysical Research: Atmospheres*, *123*(13). https://doi.org/10.1029/2017JD028130

Neff, W. (2018). Atmospheric rivers melt Greenland. https://doi.org/10.1038/s41558-018-0297-4

Newell, R. E., Newell, N. E., Zhu, Y., & Scott, C. (1992). Tropospheric rivers? A pilot study. *Geophysical Research Letters*, *19*(24), 2401–2404. https://doi.org/10.1029/92GL02916

Norris, J., Carvalho, L. M., Jones, C., & Cannon, F. (2018). Deciphering the contrasting climatic trends between the central Himalaya and Karakorum with 36 years of WRF simulations. *Climate Dynamics*, 1–22. https://doi.org/https://doi.org/10.1007/s00382-018-4133-3

Norris, J., Carvalho, L. M., Jones, C., Cannon, F., Bookhagen, B., Palazzi, E., & Tahir, A. A. (2017). The spatiotemporal variability of precipitation over the Himalaya: evaluation of one-year WRF model simulation. *Climate Dynamics*, *49*(5-6), 2179–2204. https://doi.org/10.1007/s00382-016-3414-y

Paltan, H., Waliser, D. E., Lim, W. H., Guan, B., Yamazaki, D., Pant, R., & Dadson, S. (2017). Global floods and water availability driven by atmospheric rivers. *Geophysical Research Letters*, *44*(20), 310–387. https://doi.org/10.1002/2017GL074882

Pan, M., & Lu, M. (2020). East Asia Atmospheric River catalog: Annual Cycle, Transition Mechanism, and Precipitation. *Geophysical Research Letters*, *47*, e2020GL089477. https://doi.org/10.1029/2020GL089477

Pawar, S. D., Gopalakrishnan, V., & Murugavel, P. (2015). Role of orography in inducing high lightning flash rate at the foothills of Himalaya Aeronomy. *Earth, Planets and Space*, *67*(51), 1–7. https://doi.org/10.1186/S40623-015-0221-3/FIGURES/5

Ralph, F., & Dettinger, M. D. (2012). Historical and National Perspectives on Extreme West Coast Precipitation Associated with Atmospheric Rivers during December 2010. *Bulletin of the American Meteorological Society*, *93*(6), 783–790. https://doi.org/10.1175/bams-d-11-00188.1

Ralph, F., Dettinger, M. D., Lavers, D., Gorodetskaya, I. V., Martin, A., Viale, M., White, A. B., Oakley, N., Rutz, J., Spackman, J. R., Wernli, H., & Cordeira, J. (2017). Atmospheric rivers emerge as a global science and applications focus. *Bulletin of the American Meteorological Society*, *98*(9), 1969–1973. https://doi.org/10.1175/BAMS-D-16-0262.1

Ralph, F., Neiman, P. J., Wick, G. A., Gutman, S. I., Dettinger, M. D., Cayan, D. R., & White, A. B. (2006). Flooding on California's Russian River: Role of atmospheric rivers. *Geophysical Research Letters*, *33*(13). https://doi.org/10.1029/2006gl026689

Ralph, F., Neiman, P. J., & Wick, G. A. (2004). Satellite and CALJET aircraft observations of atmospheric rivers over the Eastern North Pacific Ocean during the winter of 1997/98. *Monthly Weather Review*, *132*(7), 1721–1745. https://doi.org/10.1175/1520-0493(2004)132<1721:SACAOO>2.0.CO;2

Ralph, F., Wilson, A. M., Shulgina, T., Kawzenuk, B., Sellars, S., Rutz, J. J., Lamjiri, M. A., Barnes, E. A., Gershunov, A., Guan, B., Nardi, K. M., Osborne, T., & Wick,

G. A. (2019). ARTMIP-early start comparison of atmospheric river detection tools: how many atmospheric rivers hit northern California's Russian River watershed? *Climate Dynamics*, *52*, 4973–4994. https://doi.org/10.1007/s00382-018-4427-5

Ramesh Kumar, P., & Kamra, A. K. (2012). The spatiotemporal variability of lightning activity in the Himalayan foothills. *Journal of Geophysical Research: Atmospheres*, *117*(D24201), 1–15. https://doi.org/10.1029/2012JD018246

Ramos, A. M., Blamey, R. C., Algarra, I., Nieto, R., Gimeno, L., Tomé, R., Reason, C. J., & Trigo, R. M. (2019). From Amazonia to southern Africa: atmospheric moisture transport through low-level jets and atmospheric rivers. *Annals of the New York Academy of Sciences*, *1436*(1), 217–230. https://doi.org/10.1111/nyas.13960

Rutz, J. J., Steenburgh, W. J., & Ralph, F. (2014). Climatological Characteristics of Atmospheric Rivers and Their Inland Penetration over the Western United States. *Monthly Weather Review*, *142*, 905–921. https://doi.org/10.1175/MWR-D-13-00168.1

Scherler, D., Bookhagen, B., & Strecker, M. R. (2011). Spatially variable response of Himalayan glaciers to climate change affected by debris cover. *Nature Geoscience*, *4*, 156–159. https://doi.org/10.1038/NGEO1068

Thapa, K., Endreny, T. A., & Ferguson, C. R. (2018). Atmospheric Rivers Carry Non-monsoon Extreme Precipitation Into Nepal. *Journal of Geophysical Research: Atmospheres*, *123*, 5901–5912. https://doi.org/10.1029/2017JD027626

Viale, M., & Nuñez, M. N. (2011). Climatology of Winter Orographic Precipitation over the Subtropical Central Andes and Associated Synoptic and Regional Characteristics. *Journal of Hydrometeorology*, *12*, 481–507. https://doi.org/10.1175/2010JHM1284.1

Viale, M., Valenzuela, R., & Garreaud, R. D. (2018). Impacts of Atmospheric Rivers on Precipitation in Southern South America. *Journal of Hydrometeorology*, *19*, 1671–1687. https://doi.org/10.1175/JHM-D-18-0006.1

Waliser, D. E., & Guan, B. (2017). Extreme winds and precipitation during landfall of atmospheric rivers. *Nature Geoscience*, *10*(3), 179–183. https://doi.org/10.1038/ngeo2894

Wernli, H., & Papritz, L. (2018). Role of polar anticyclones and mid-latitude cyclones for Arctic summertime sea-ice melting. *Nature Geoscience*, *11*, 108–113. https://doi.org/https://doi.org/10.1038/s41561-017-0041-0

Wick, G. A., Neiman, P. J., Ralph, F., & Hamill, T. M. (2013). Evaluation of forecasts of the water vapor signature of atmospheric rivers in operational numerical weather prediction models. *Weather and Forecasting*, *28*(6), 1337–1352. https://doi.org/10.1175/waf-d-13-00025.1

Wille, J. D., Favier, V., Dufour, A., Gorodetskaya, I. V., Turner, J., Agosta, C., & Codron, F. (2019). West Antarctic surface melt triggered by atmospheric rivers. *Nature Geoscience*, *12*(11), 911–916. https://doi.org/10.1038/s41561-019-0460-1

Yang, Y., Zhao, T., Ni, G., & Sun, T. (2018). Atmospheric rivers over the Bay of Bengal lead to northern. *International Journal of Climatology*, *38*(August 2017), 1010–1021. https://doi.org/10.1002/joc.5229

Zhao, Y., Huang, A., Zhou, Y., Huang, D., Yang, Q., Ma, Y., Li, M., & Wei, G. (2014). Impact of the Middle and Upper Tropospheric Cooling over Central Asia on the Summer Rainfall in the Tarim Basin, China. *Journal of Climate*, *27*, 4721–4732. https://doi.org/10.1175/JCLI-D-13-00456.1

Zhu, Y., & Newell, R. E. (1994). Atmospheric rivers and bombs. *Geophysical Research Letters*, *21*(18), 1999–2002. https://doi.org/10.1029/94GL01710

Zhu, Y., & Newell, R. E. (1998). A proposed algorithm for moisture fluxes from atmospheric rivers. *Monthly Weather Review*, *126*, 10. https://doi.org/10.1175/1520-0493

Chapter 2

An Electrifying Atmospheric River: Understanding the Thunderstorm Event in Santa Barbara County during March 2019

D.L. NASH & L.M.V. CARVALHO

Abstract

On 5 March 2019 12 UTC, an Atmospheric River (AR) made landfall in Santa Barbara, CA and lasted approximately 30 hours. While ARs are typical winter storms in the area, the extraordinary amount of lightning strikes observed near coastal Santa Barbara made this event unique. The Earth Networks Global Lightning Network (ENGLN) detected 8,811 lightning flashes around southern California (30°N to 37°N and 130°W to 115°W) in 24 hours, which is roughly 2,500 times the climatological flash

rate in this region. The AR related thunderstorm resulted in approximately 23.18 mm accumulated precipitation in 30 hours in Santa Barbara. This article examines synoptic and mesoscale features conducive to this electrifying AR event, characterizing its uniqueness in the context of previous March events that made landfall in the region. We show that this AR was characterized by an unusual deep moist layer extending from low-to-mid troposphere in an environment with potential instability and low elevation freezing level. Despite the negligible convective available potential energy (CAPE) during the peak of the thunderstorm near Santa Barbara, the lifting of layers with high water vapor content in the AR via warm conveyor belt and orographic forcing in a convectively unstable atmosphere resulted in the formation of hail and enhanced electrification.

2.1 Introduction

Due to recent wildfire activity in Santa Barbara County (e.g. Thomas Fire during December 2017, Whittier Fire during July 2017, and Sherpa Fire during June and July 2016) this region is at high risk for post-fire debris flow when 15 minutes of rainfall has an intensity greater than or equal to 24 mm hour^{-1} (USGS, 2019). These conditions were observed during the devastating Montecito debris flow on the 9 January 2018 that resulted in 23 deaths, 246 structures destroyed, and 167 damaged structures (Oakley et al., 2018). On 1 March 2019, the National Weather Service (NWS) in Oxnard, CA forecasted 2 storms to hit Santa Barbara County (1-2 March 2019 and 5-6 March 2019). On 5 March 21 UTC, a mandatory evacuation order was issued for the Thomas, Whittier, and Sherpa fire burn areas due to the prediction of a subsequent severe storm and flood potential that existed for low-lying areas given increased ground saturation from the storm on 2 March 2019, impacting about 3,000 residents. While no significant

debris flows were triggered during this event, a combination of an Atmospheric River (AR) and an extreme number of lightning strikes made this storm exceptional. Figure 2.1a shows a photo of lightning strikes at the Santa Barbara Harbor during the storm taken by Santa Barbara County Fire Department's Mike Eliason.

The term Atmospheric River (AR), describes a phenomenon that explains how baroclinic eddies transport large amounts of water vapor via relatively infrequent, long conduits of strong moisture transport across mid-latitudes and into polar regions (Newell et al., 1992; Zhu & Newell, 1994). Many studies have focused on the regional impacts of ARs in western United States and have found that ARs bring large amounts of moisture to the west coast of North America and are related to precipitation extremes and flooding, particularly in the winter season (Dettinger et al., 2011; Guan et al., 2010, 2013; Harris & Carvalho, 2018; Ralph et al., 2006). Despite occurring less frequently than ARs in Northern California, the Southern California ARs have significant impact in the hydrological cycle of the region (Cannon et al., 2018; Harris & Carvalho, 2018; Oakley et al., 2018; Oakley & Redmond, 2014). Although ARs are often associated with extreme precipitation, flooding, and other hazardous events, they play a critical role in replenishing reservoirs and underground water resources, particularly in dry areas of Southern California. Studies show that just a few AR events each year can contribute the majority of the precipitation and streamflow that regulates the state's water resources (Cannon et al., 2018; Dettinger, 2013; Gershunov et al., 2017; Ralph et al., 2019). Ralph et al. (2019) have developed a scale to characterize ARs based on intensity and duration, pointing out that ARs can result in a wide spectrum of conditions from beneficial to hazardous. As of now, no studies have examined the relationship between ARs and lightning.

Lightning usually occurs when the electric charges in a cloud separate and exceed the intensity that the air can sustain (Price, 2013). Charges usually build up in the

mixed phase region of the clouds (0°C to -40°C) when there are enough updrafts to lift particles above the freezing level (Price & Rind, 1993). The correlation between cloud-top height and lightning rate is well documented and can be attributed to the deep vertical development of convective thunderstorms (Pessi & Businger, 2009; Price & Rind, 1993). Pessi and Businger (2009) documented that lightning activity can be associated with cold temperatures aloft or convection along cold fronts.

Although the thunderstorms on 5 March 2019 caused minimal damage (e.g. small lightning fires, power outages), this event was meteorologically significant because of the exceptional number of lightning strikes in such a short period. This study examines synoptic and mesoscale dynamics, as well as the thermodynamic characteristics of this AR and investigates the uniqueness of this event compared to past March ARs that made landfall in Santa Barbara.

2.2 Data and Methods

Climate Forecast System version 2 (CFSv2) (Saha et al., 2014) operational analysis was used in this study to evaluate the synoptic and mesoscale meteorological conditions between 10°N and 50°N and 150°W to 110°W between the dates 4 March 2019 18 UTC and 6 March 2019 18 UTC. CFSv2 data at 0.5° by 0.5° horizontal resolution was obtained at 37 pressure levels between 1000 and 1 hPa at a 6-hourly time scale. AR conditions are determined based on IVT (see appendix A for calculation) exceeding 250 kg m^{-1} s^{-1} at a fixed geographical point. The AR event in this study refers to the time that the AR conditions occurred in Santa Barbara, i.e. at the grid cell centered on 34.5°N and 119.5°W. The duration of the AR event is determined by the time (in hours) that the AR conditions are consecutively met. NASA's Modern Era Retrospective Reanalysis Version 2 (MERRA2) (Bosilovich et al., 2015; Gelaro et al., 2017) and the

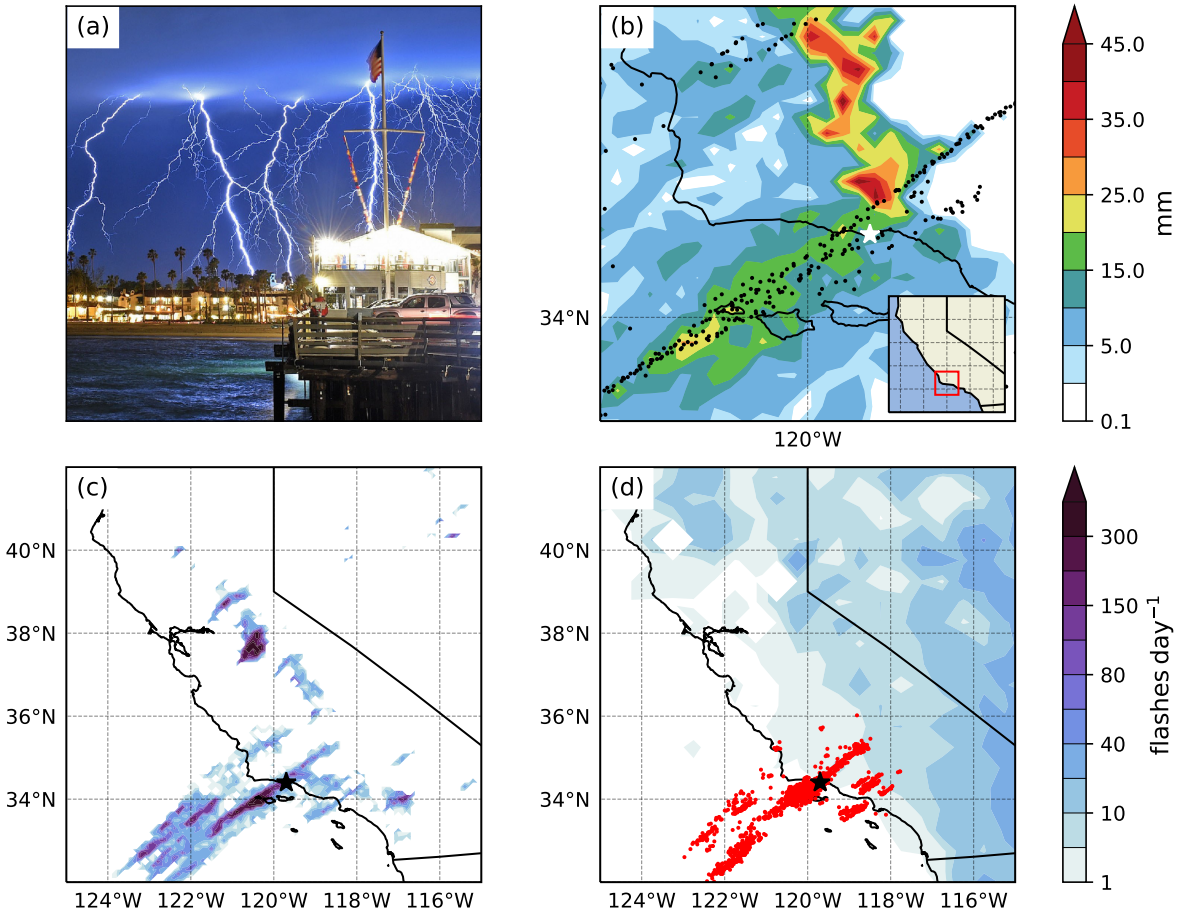

Figure 2.1: (a) Photo of lightning at the Santa Barbara Harbor in Santa Barbara, CA taken by Mike Eliason from the Santa Barbara County Fire Department during the storm at 6 March 2019 4 UTC. (b) NOAA NEXRAD L3 precipitation accumulation (shaded; mm) and locations of NOAA NEXRAD L3 Hail Signatures (black points) between 5 March 2019 12 UTC and 6 March 2019 23:59 UTC. The location of Santa Barbara is indicated by the white star. (c) ENGLN lightning strike frequency (shaded; flashes day^{-1}) on 6 March 2019. The location of Santa Barbara is indicated by the black star. (d) Climatological annual mean lightning density (shaded; flashes day^{-1}) between 1995 and 2014 using TRMM LIS-OTD lightning climatology and lightning strike locations (red points) between 4 and 5 UTC on 6 March 2019 based on ENGLN. The location of Santa Barbara is indicated by the black star.

global atmospheric river detection catalog that identifies atmospheric rivers on a global, 6-hourly basis were used to determine the anomalous characteristics of the March 2019 AR event compared to past ARs that made landfall in Santa Barbara. This AR detection algorithm was introduced in Guan and Waliser (2015) and refined in Guan and Waliser (2019). Here we analyzed ARs and their characteristics on a daily temporal scale at 0.5° by 0.625° spatial resolution between 1980 and 2018. The other calculated variables from CFSv2 are dew point (Td) and equivalent potential temperature (θ_E), which are calculated based on Bolton (1980, eq. 11, 43).

Lightning flash data obtained from Earth Networks Global Lightning Network (ENGLN) (EN, 2019) was used to quantify the location and number of lightning strikes between 4 March 2019 0 UTC and 7 March 2019 0 UTC near southern California (30°N to 37°N and 130°W to 115°W). The global lightning network, which includes more than 1,700 sensors, detects lightning flashes and provides various information about those flashes, including latitude, longitude, amplitude of the lighting, duration of the flash, and the number of in-cloud (IC) and cloud-to-ground (CG) lightning pulses within a given flash (EN, 2019). A lightning flash can be made up of one or more IC or CG lightning pulses, which connect regions of opposite polarity. To put the extremity of this lightning event into climatological context, an annual lightning strike climatology from Tropical Rainfall Measuring Mission Lightning Imaging Sensor and Optical Transient Detector (TRMM LIS-OTD) (Cecil et al., 2014) was used at a horizontal resolution of 0.5° by 0.5° between 1995 and 2014 from 20°N to 50°N and 140°W to 110°W. Comparing the two lightning sources has a certain level of uncertainty, since TRMM LIS-OTD and ENGLN do not overlap temporally. However, because this event had significantly above average lightning flash rates compared to the climatology, the possible error introduced by comparing two different data sets does not impact the results.

For precipitation, hourly precipitation data from National Oceanic and Atmospheric

Administration's Next Generation Radar Level 3 (NOAA's NEXRAD L3) was used between the dates 4 March 2019 18 UTC and 6 March 2019 23:59 UTC at roughly 1 km resolution (NOAA, 2019). To identify the approximate location, time, and diameter of hail, NOAA's NEXRAD L3 hail signature product was used. To identify cloud convection and cloud top height via cloud top temperature, the Cloud and Moisture Imagery (CMI) product from GOES-R (GOES-17) Advanced Baseline Imager Level 2 was obtained for 6 March between 3 UTC and 5 UTC at 5-minute temporal intervals and 10 km by 10 km spatial resolution (GOES-R, 2017).

2.3 Results and Discussion

2.3.1 March 2019 Event

An AR made landfall near Santa Barbara (34.5°N, 119.5°W) between 5 March 12 UTC and 6 March 18 UTC, resulting in total accumulated precipitation of approximately 23 mm around Santa Barbara according to NOAA NEXRAD L3 one-hour precipitation. While this was not enough precipitation to initiate debris flow, instances of hail were identified by the NOAA NEXRAD L3 hail signature product (see Fig. 2.1b). The presence of hail indicates strong updrafts and a low freezing level, which are conditions that also favor the development of lightning in a storm (Pruppacher & Klett, 1997). During this AR event, ENGLN detected 46,222 flashes of lightning with 85,032 combined IC and CG pulses around Southern California (30°N to 37°N and 130°W to 115°W) (EN, 2019). Among these, 8,811 flashes of lightning with 35,603 combined IC and CG pulses occurred in the 24 hour period following 6 March 0 UTC (Fig. 2.1c). TRMM LIS-OTD records an area annual average of 3.34 flashes per day in the region surrounding southern California (30°N to 37°N and 130°W to 115°W), making the 8,811 lightning flashes

in under 24 hours very extreme. In fact, even if this was the only lightning activity for 2019, it would represent over 2,500 times the climatological rate (Fig. 2.1d) (Cecil, 2015). Based on the AR database of Guan and Waliser (2019), on average 10 AR days are observed between December and March each year in Santa Barbara, with a total of 742 days associated with ARs that made landfall in the grid cells closest to Santa Barbara between 1980 and 2019. When compared to the TRMM LIS-OTD low resolution time series, between 1995 and 2014 there were approximately 350 landfalling AR events that coincided with lightning flashes, with the majority of events resulting in less than 60 flashes per day (Cecil, 2015).

2.3.2 Extratropical Cyclone and AR Conditions

Following an extratropical cyclone that made landfall at 1 March 12 UTC, a deep mid-level (500 hPa) trough developed into a closed low system, forming a pool of cold air centered at approximately 32°N and 140°W by 4 March 18 UTC (Fig. 2.2a). The surface low-pressure was located directly below the 500 hPa closed low on 4 March 18 UTC (Fig. 2.2a). This mid-level closed low moved eastward and northward, until 6 March 12 UTC when it was no longer closed (Fig. 2.2h). According to Oakley and Redmond (2014), 41-50% of precipitation in Santa Barbara between October and March is associated with closed lows. The surface low-pressure deepened from 1005 hPa to approximately 996.36 hPa by the peak event time at 6 March 2019 6 UTC; at this point it was centered around 38°N and 126°W, west of northern California (Fig. 2.2g). At the peak time of the event, 6 March 6 UTC, the jet streak exit region was located at 35°N and 122°W, directly northwest of Santa Barbara (Fig. A.1g). Pessi and Businger (2009) showed that most of the storms that have lightning activity over the North Pacific Ocean are associated with similar synoptic conditions as those observed

during the storm in March 2019.

These synoptic conditions provided the dynamical mechanisms necessary for subtropical moisture to be transported via an AR, shown as the area of IVT greater than 250 kg m^{-1} s^{-1} (Fig. 2.2). This AR made landfall at approximately 5 March 12 UTC on the west coast near Santa Barbara and lasted approximately 30 hours (Fig. 2.2d-i). The peak IVT value for this event within the AR was 1034 kg m^{-1} s^{-1} at 5 March 12 UTC (Fig 2.2d). In the grid cell closest to Santa Barbara (34.5°N and 119.5°W) the AR had a peak IVT value of 446 kg m^{-1} s^{-1} on 6 March 6 UTC (Fig. A.2a). Based on the duration (30 hours) and maximum instantaneous IVT intensity of the AR (446 kg m^{-1} s^{-1}), this event is categorized at AR-CAT 1 according to Ralph et al. (2019), indicating that this AR was most likely beneficial to the Santa Barbara area. This particular AR had IVT direction and magnitude characteristics similar to past ARs that made landfall in the Santa Barbara area (Fig. A.2b, c).

Equivalent potential temperature at 850 hPa (θ_E) (Fig. A.3) identifies the formation of the warm conveyor belt (WCB), or the ascending air within the warm sector of the extratropical cyclone and the overlap of the AR between 5 March 12 UTC and 6 March 12 UTC (Browning, 1986; Dettinger et al., 2015). At 6 March 6 UTC (Fig. A.3g), the cold front lies along the densely packed isotherms between the coast of California and 32°N and 124°W, and the warm front is located parallel to the coast of California. This placed the region of warm air advection and the WCB in the southern region of the domain between the two fronts where θ_E is around 320 K. Water vapor in the AR, which can be sourced from intense vapor transport out of the tropics as well midlatitude convergence of water vapor along the path of the AR, was transported via winds into the WCB (Fig. A.3) (Dettinger et al., 2015). The uplift of the moisture from the AR most likely occurred due to orographic uplift from interaction with complex topography as well as dynamic uplift from the WCB (Fig. A.3). It has been suggested that WCBs

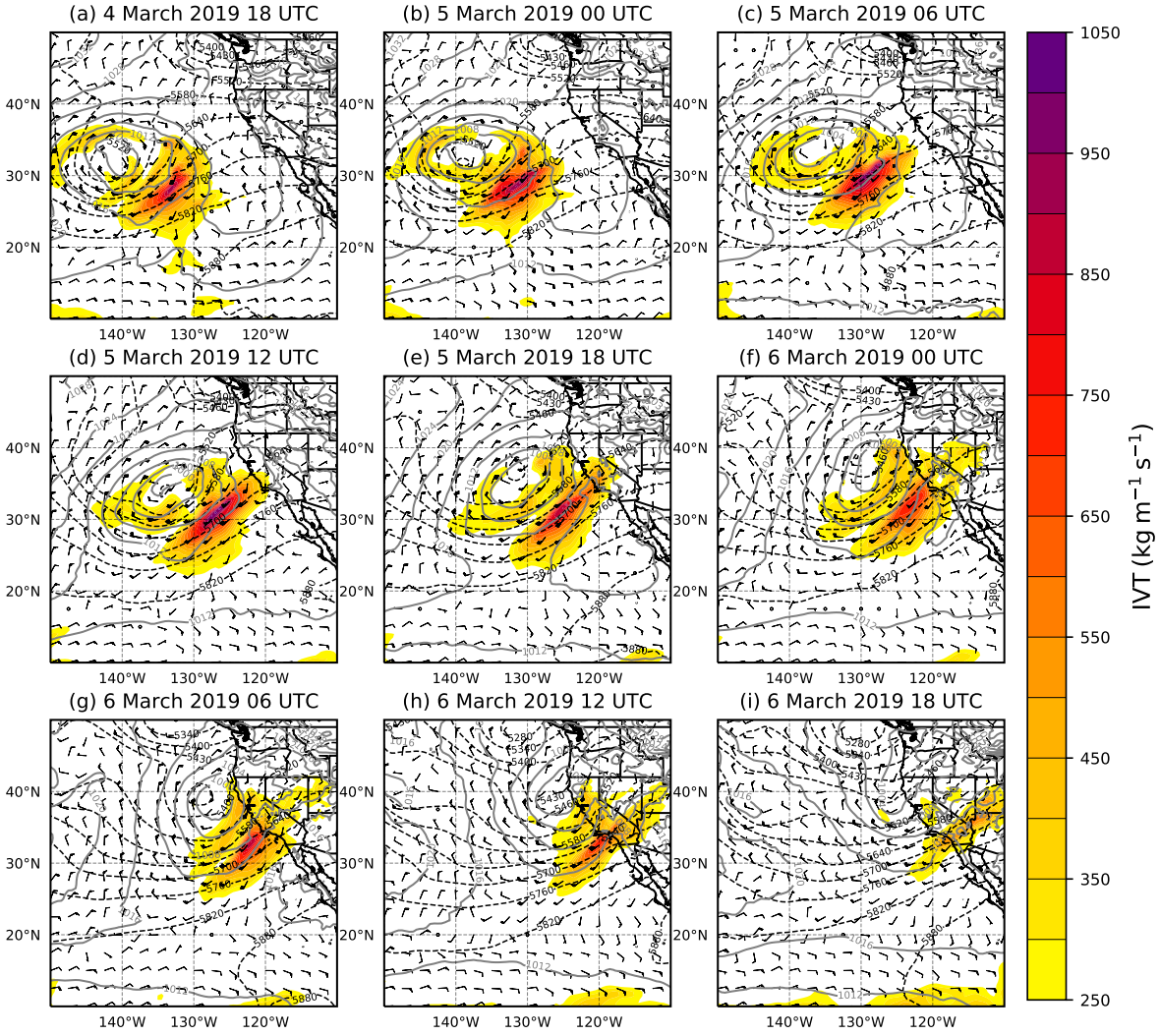

Figure 2.2: CFSv2 data showing IVT (shaded; kg m^{-1} s^{-1}), 850 hPa wind (barbs; knots), Mean sea level pressure (grey contours; hPa), and 500 hPa geopotential height (black dashed contours; m) at 6-hourly time steps between 4 March 2019 18 UTC and 6 March 2019 18 UTC. The time step closest to the peak of the event is shown in figure (g) at 6 March 2019 6 UTC in the bottom left corner.

and ARs can form on their own without direct connection to each other (Dacre et al., 2015; Dettinger et al., 2015). In this case, we observed an AR interacting with a WCB, along with updrafts and hail formation. The synoptic conditions of this event show that the cyclogenesis combined with the dynamical lift of the AR in a convectively unstable environment provided enough updraft to potentially aid in the electrification of the clouds via hail formation.

2.3.3 Thermodynamic Conditions

Wind in the skew(t) - log(p) diagram at 34.5°N 119.5°W (Fig. 2.3a) for the time closest to the peak of the event (6 March 6 UTC) indicates strong warm air advection below 800 hPa. This strong veering profile near the surface with increasing wind speeds with height intensifies the mesocyclone and maintains the storm. Most thunderstorms are associated with high values of Convective Available Potential Energy (CAPE), which measures the amount of energy available for convection. While this storm had values of surface-based CAPE up to 1000 J kg^{-1} as it made its way across the Pacific Ocean toward the west coast of California, there was little to no CAPE in Santa Barbara (10 J kg^{-1}) where lightning occurred at 6 March 6 UTC (Fig. 2.3a, A.4). However, like the extreme precipitation events in Cannon et al. (2018), additional dynamical forcing can develop convection even when CAPE is low. Although CAPE was low near Santa Barbara, the proximity of temperature and dew point profiles in the lower troposphere place the Lifting Condensation Level (LCL) very close to the surface (Fig. 2.3a).

Between 800 and 625 hPa, parcels are saturated, indicating the high moisture content of the AR (Fig. 2.3a, c). The equivalent potential temperature profile (Fig. 2.3b) shows decreasing θ_E with increasing height, indicating convective instability at the surface as well as in the midlevels between 800 and 600 hPa. A close inspection of the

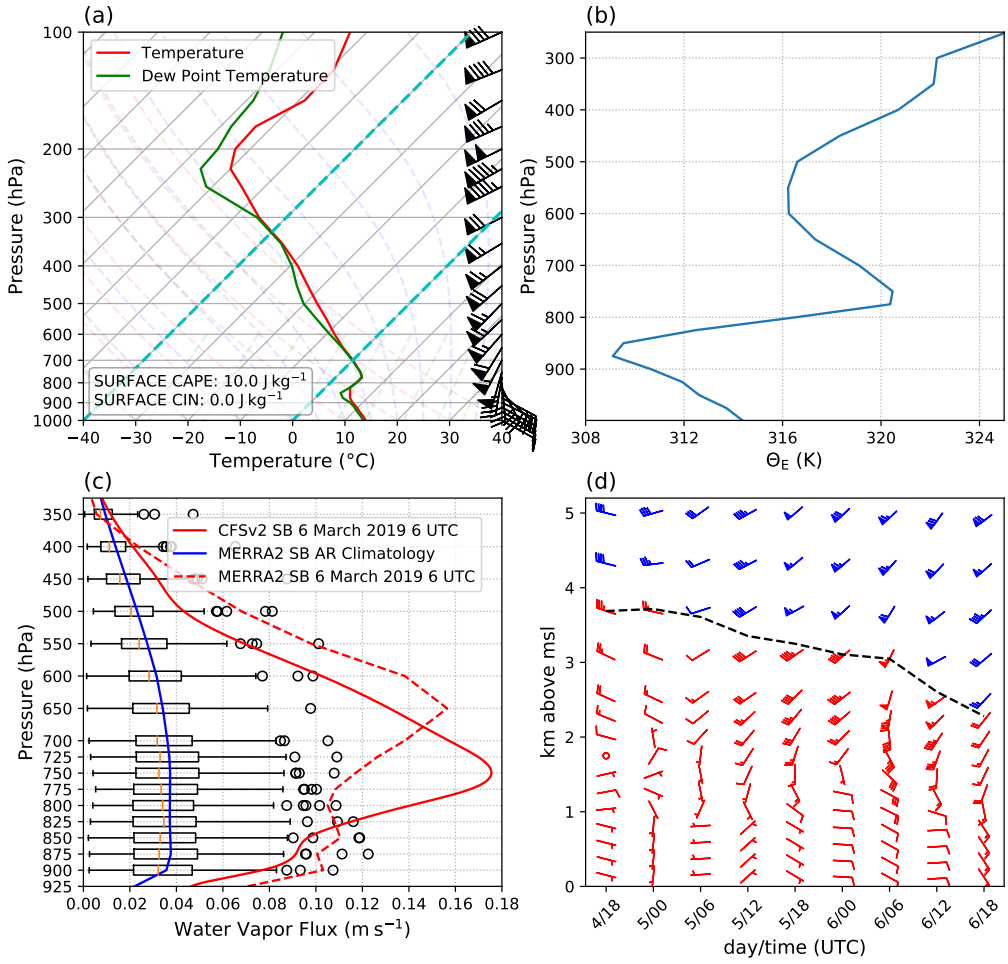

Figure 2.3: (a) Skew(t) - log(p) vertical profile of CFSv2 temperature (red line) and dew point (green line) at 34.5°N and 119.5°W at 6 March 2019 6 UTC. CFSv2 winds (knots; barbs) are indicated on the right side of the figure for each vertical level. Surface values of CAPE and Convective Inhibition (CIN) are shown in the bottom left corner. (b) CFSv2 Equivalent Potential Temperature θ_E (blue line; K) at 34.5°N and 119.5°W at 6 March 2019 6 UTC. (c) Climatological vertical profile of horizontal water vapor flux (m s^{-1}) based on MERRA2 at 34.5°N, 119.375°W for all days when AR conditions are met during the month of March between 1980 and 2015 (i.e. IVT >= 250 kg m^{-1} s^{-1}) at this location (blue line and box and whisker plots show the distribution of the 170 events), and vertical profile of horizontal water vapor flux (m s^{-1}) based on CFSv2 (red solid line) and MERRA2 (red dashed line) at the same location at 6 March 2019 6 UTC. (d) CFSv2 winds (knots, barbs) at vertical levels (km above mean sea level) at 34.5°N and 119.5°W at 6-hour intervals from 4 March 2019 18 UTC to 6 March 2019 18 UTC. The temperature (°C) is indicated by the color of the barb. Red barbs mean the temperature was greater than 0°C and blue barbs mean the temperature was less than 0°C. The height of the 0°C isotherm is indicated by the black dashed line.

θ_E profile at the location of the highest lightning flash density (Fig. A.4) indicates convective instability at nearly every 6-hour time step for the duration of the storm. The horizontal water vapor flux (m s^{-1}) calculated at each pressure level on 6 March 6 UTC at 34.5°N, 119.5°W, (Fig. 2.3c) indicates that the water vapor flux peaked at 0.17 m s^{-1} between 800 and 700 hPa. Similar results were found when using MERRA2, although with a slightly lower water vapor flux that occurred around 650 hPa (Fig. 2.3c). Compared to the climatological vertical profile of water vapor flux from the past March AR events in Santa Barbara, the AR on 6 March 2019 was extremely moist with maximum moisture peaking at a higher than average pressure level (Fig. 2.3c). The height (km above mean sea level) of the 0°C isotherm at 34.5°N, 119.5°W (Fig. 2.3d) is around 2.5 km above mean sea level during the peak of the storm, which is below the average height of the 0°C isotherm during past AR events in Santa Barbara (Fig. A.2d). The lifting of moist layers in these thermodynamic conditions either orographically or by the WCB resulted in conditionally unstable air and strong updrafts below freezing level (Fig. 2.3c, d). GOES-17 Cloud and Moisture Imagery Brightness Temperature (Fig. A.5) indicates vigorous convection via cold cloud temperatures that decrease to approximately -71°C near Santa Barbara at the time closest to the peak of the event. These cold top temperatures indicate a very strong updraft, which would result in hail formation when water droplets in the region of the updraft are carried above the freezing level (Pruppacher & Klett, 1997; Wallace & Hobbs, 2006). The lifting of the moist layers as well as the convective updrafts contributed to the formation of hail with an average size of 13.5 mm, which is co-located with cold cloud top temperatures (Fig. A.5), indicating the importance of deep convective updrafts for the development of the thunderstorms.

2.3.4 Lightning Conditions

Convective updraft in the lower troposphere are considered important for the build-up of regions with positive and negative net charges in the mixed-phase region of the cloud (0°C to -40°C), playing a role in the onset of lightning and thunder (Doswell, 2001; Pessi & Businger, 2009; Price, 2013; Price & Rind, 1993). Enhanced updrafts increase electrification and lightning rates because they transport droplets to below freezing levels increasing ice mass (Pessi & Businger, 2009). Downdrafts into the mixed-phase region of the cloud may aid in pushing hailstones downward and are important mechanisms for electrification of the storm (Price, 2013; Price & Rind, 1993). When the updrafted droplets and downdrafted hailstones collide, they can release latent heat, and potentially form graupel, a softer form of hail that is warmer than its environment (Doswell, 2001; Price & Rind, 1993). Particles in the mixed phase region of the cloud can collide with graupel and acquire positive charges when ascending (negative when descending). Over time, this process changes the storm cloud microphysics and electrical charges resulting in a negatively charged base and a positively charged top (Doswell, 2001; Price, 2013).

In the March 2019 storm, updrafts in the deep convective clouds, identified by overshooting cloud tops (Fig. A.5), could have transported smaller droplets to above the freezing level, (below 700 hPa), potentially allowing for the formation of hail with a positive charge (Fig. 2.3a, d, 2.1b, A.5). At the time closest to the peak of the event in Santa Barbara, dry air was entrained between 600 and 400 hPa as well as in the upper-levels between 300 and 200 hPa (Fig 2.3a), which could have enhanced downdrafts contributing in the formation of electrified hailstones.

According to Price and Rind (1993), the proportion of in-cloud (IC) to cloud-to-ground (CG) lightning pulses in thunderstorms is well correlated with the thickness of

the cloud region between 0°C and the top of the cloud. Therefore, as the thickness of the thunderstorm cloud increases, the ratio of IC to CG also increases. Here we use cloud-top height from GOES-R (GOES-17) Advanced Baseline Imager Level 2 (Fig. A.7) and the height of the 0°C isotherm (Fig. A.8) as a proxy for cloud thickness. Figure A.6a shows the number of IC pulses and CG pulses at every 15 minutes between 4 March 0 UTC and 7 March 0 UTC in the region of the extratropical cyclone. Between 4 March 0 UTC and 12 UTC, there are between 2000 and 3000 CG pulses and about 1000 to 2000 IC pulses centered around 26°N and 136°W. The second peak in lightning occurs at approximately 5 March 12 UTC with almost 4000 CG pulses and 3000 IC pulses centered around 30°N and 128°W (Fig. A.6a). The last peak of lightning frequency occurred between 6 March 0 UTC and 6 UTC with approximately 3000 IC pulses and less than 1000 CG pulses centered at 34°N and 120°W (Fig. A.6a). The cloud top height near the lightning throughout the event is between 9,000 m and 10,000 m (Fig. A.7). However, the 0°C isotherm near the lightning drops closer to the ground as time passes, indicating that the cloud thickness increases as the event progresses (Fig. A.8). The height of the IC pulses are below 5000 m before 5 March 12 UTC and between 7500 and 10000 m after 5 March 18 UTC (Fig. A.6b). The increased IC pulse height (Fig. A.6b) could be explained by the increased cloud thickness between the height of 0°C isotherm and the cloud top in the later half of the storm (after 5 March 18 UTC), similar to the findings of Price and Rind (1993).

2.4 Conclusions

On the coast of the Santa Barbara, CA, an extratropical cyclone and an AR made landfall at 5 March 2019 12 UTC. The AR intensified until its peak at 6 March 6 UTC, resulting in precipitation via uplift from the WCB and orographic forcing. This event

was associated with cold top clouds and vigorous convection that reached its peak at 6 March 2019 4 UTC. While the accumulated rainfall seen during this storm (about 23 mm) is not uncommon in winter storms associated with ARs making landfall in Southern California, this system exhibited extraordinary lightning activity for the region. In 30 hours between 5 March 12 UTC and 6 March 18 UTC, ENGLN detected 46,222 flashes of lightning with 85,032 combined IC and CG pulses around Southern California (30°N to 37°N and 130°W to 115°W). Of those, 1,486 lightning pulses occurred over Santa Barbara County in the 24 hours following 6 March 0 UTC, 533 of which were cloud-to-ground type.

The lightning activity can be considered highly unusual in a region that observes, on average less than 23 lightning flashes in the entire month of March. Although the system evolved as a typical winter storm associated with a cutoff low, it was exceptional due to the high water vapor content provided by the AR, particularly at mid-levels of the atmosphere. The AR developed in an troposphere cooler than average for an AR, as indicated by the low elevation of the 0°C isotherm (about 2.5 km above mean sea level). The AR provided higher than average horizontal water vapor flux between 800 and 600 hPa compared to other March landfalling ARs in Santa Barbara. Unlike most thunderstorms in the tropics, this event was not characterized by significant CAPE when the storm approached the coast. However, thermodynamic profiles indicated layers with potential instability near the surface and in the mid-troposphere throughout the life cycle of the thunderstorms. The uplift of saturated parcels in a convectively unstable atmosphere from the WCB and further by the orographic forcing resulted in enhanced updrafts. These updrafts transported droplets in a cold environment and high moisture availability from the AR, providing the ingredients to form hail. Downdrafts enhanced by entrainment between 600 and 400 hPa may have contributed to the downward transport of hail, helping to transform the charge distribution in the clouds

enhancing lightning activity. Understanding the dynamics of this storm provides the theoretical basis for future, systematic investigation of the relationship between ARs and unusual lightning scenarios in other regions. It also is critical to understand these processes in populated areas such as Santa Barbara, where lightning can significantly increase hazards during rainfall events.

References

Bolton, D. (1980). The Computation of Equivalent Potential Temperature. *Monthly Weather Review*, *108*, 1046–1053. https://doi.org/10.1175/1520-0493(1980)108<1046:TCOEPT>2.0.CO;2

Bosilovich, M. G., Akella, S., Coy, L., Cullather, R., Draper, C., Gelaro, R., Kovach, R., Liu, Q., Molod, A., Norris, P., Wargan, K., Chao, W., Reichle, R. H., Takacs, L., Vikhliaev, Y., Bloom, S., Collow, A., Firth, S., Labow, G., ... Suarez, M. (2015). MERRA-2: Initial Evaluation of the Climate. *NASA Technical Report NASA/TM-2015-104606*, *43*, 136. https://doi.org/https://gmao.gsfc.nasa.gov/pubs/docs/Bosilovich803.pdf

Browning, K. A. (1986). Conceptual Models of Precipitation Systems. *Weather and Forecasting*, *1*, 23–41. https://doi.org/https://doi.org/10.1175/1520-0434(1986)001<0023:CMOPS>2.0.CO;2

Cannon, F., Hecht, C. W., Cordeira, J. M., & Ralph, F. (2018). Synoptic and Mesoscale Forcing of Southern California Extreme Precipitation. *Journal of Geophysical Research: Atmospheres*, *123*(24), 714–13. https://doi.org/10.1029/2018JD029045

Cecil, D. J. (2015). LIS/OTD Gridded Lightning Climatology Data Collection Version 2.3.2015. *NASA EOSDIS Global Hydrology Resource Center Distributed Active Archive Center Huntsville, Alabama, U.S.A, accessed 20 August 2019*. https://doi.org/http:/dx.doi.org/10.5067/LIS/LIS-OTD/DATA311

Cecil, D. J., Buechler, D. E., & Blakeslee, R. J. (2014). Gridded lightning climatology from TRMM-LIS and OTD: Dataset description. *Atmospheric Research*, *135-136*, 404–414. https://doi.org/10.1016/J.ATMOSRES.2012.06.028

Dacre, H. F., Clark, P. A., Martinez-Alvarado, O., Stringer, M. A., & Lavers, D. A. (2015). How do atmospheric rivers form? *Bulletin of the American Meteorological Society*, *96*(8), 1243–1255. https://doi.org/10.1175/BAMS-D-14-00031.1

Dettinger, M. D. (2013). Atmospheric rivers as drought busters on the U.S. West Coast. *Journal of Hydrometeorology*, *14*(6), 1721–1732. https://doi.org/10.1175/JHM-D-13-02.1

Dettinger, M. D., Ralph, F., Das, T., Neiman, P. J., & Cayan, D. R. (2011). Atmospheric rivers, floods and the water resources of California. *Water*, *3*(4), 445–478. https://doi.org/10.3390/w3020445

Dettinger, M. D., Ralph, F., & Lavers, D. (2015). Setting the stage for a global science of atmospheric rivers. *Eos*, *97*(1), 7. https://doi.org/10.1029/2015eo038675

Doswell, C. A. (2001). Severe Convective Storms—An Overview. *Severe Convective Storms*, 1–26. https://doi.org/10.1007/978-1-935704-06-5{_}1

EN, E. N. (2019). Earth Networks Global Lightning Network. https://www.earthnetworks.com/product/weather-sensors/lightning/

Gelaro, R., McCarty, W., Suárez, M. J., Todling, R., Molod, A., Takacs, L., Randles, C. A., Darmenov, A., Bosilovich, M. G., Reichle, R. H., Wargan, K., Coy, L., Cullather, R., Draper, C., Akella, S., Buchard, V., Conaty, A., da Silva, A. M., Gu, W., … Zhao, B. (2017). The Modern-Era Retrospective Analysis for Research and Applications, Version 2 (MERRA-2). *Journal of Climate*, *30*(14), 5419–5454. https://doi.org/10.1175/jcli-d-16-0758.1

Gershunov, A., Shulgina, T., Ralph, F., Lavers, D. A., & Rutz, J. J. (2017). Assessing the climate-scale variability of atmospheric rivers affecting western North America. https://doi.org/10.1002/2017GL074175

GOES-R. (2017). NOAA GOES-R Series Advanced Baseline Imager (ABI) Level 2 Cloud and Moisture Imagery Products (CMIP) Band 13. https://doi.org/10.7289/V5736P36

Guan, B., Molotch, N. P., Waliser, D. E., Fetzer, E. J., & Neiman, P. J. (2010). Extreme snowfall events linked to atmospheric rivers and surface air temperature via satellite measurements. *Geophysical Research Letters*, *37*(20), n/a–n/a. https://doi.org/10.1029/2010gl044696

Guan, B., Molotch, N. P., Waliser, D. E., Fetzer, E. J., & Neiman, P. J. (2013). The 2010/2011 snow season in California's Sierra Nevada: Role of atmospheric rivers and modes of large-scale variability. *Water Resources Research*, *49*(10), 6731–6743. https://doi.org/10.1002/wrcr.20537

Guan, B., & Waliser, D. E. (2015). Detection of atmospheric rivers: Evaluation and application of an algorithm for global studies. *Journal of Geophysical Research: Atmospheres*, *120*(24), 12514–12535. https://doi.org/10.1002/2015jd024257

Guan, B., & Waliser, D. E. (2019). Tracking Atmospheric Rivers Globally: Spatial Distributions and Temporal Evolution of Life Cycle Characteristics. *Journal of Geophysical Research: Atmospheres*, *124*, 12523–12552. https://doi.org/10.1029/2019JD031205

Harris, S. M., & Carvalho, L. M. (2018). Characteristics of southern California atmospheric rivers. *Theoretical and Applied Climatology*, *132*(3-4), 965–981. https://doi.org/10.1007/s00704-017-2138-1

Newell, R. E., Newell, N. E., Zhu, Y., & Scott, C. (1992). Tropospheric rivers? A pilot study. *Geophysical Research Letters*, *19*(24), 2401–2404. https://doi.org/10.1029/92GL02916

NOAA. (2019). NOAA Next Generation Radar (NEXRAD) Level 3 Products Hail Signatures and One-Hour Precipitation. https://doi.org/10.7289/V5W9574V

Oakley, N. S., Cannon, F., Munroe, R., Lancaster, J. T., Gomberg, D., & Ralph, F. (2018). Brief communication: Meteorological and climatological conditions associated with the 9 January 2018 post-fire debris flows in Montecito and Carpinteria, California, USA. *Natural Hazards and Earth System Sciences*, *18*(11), 3037–3043. https://doi.org/10.5194/nhess-18-3037-2018

Oakley, N. S., & Redmond, K. T. (2014). A Climatology of 500-hPa closed lows in the northeastern pacific ocean, 1948-2011. *Journal of Applied Meteorology and Climatology*, *53*(6), 1578–1592. https://doi.org/10.1175/JAMC-D-13-0223.1

Pessi, A. T., & Businger, S. (2009). Relationships among Lightning, Precipitation, and Hydrometeor Characteristics over the North Pacific Ocean. *Journal of Applied Meteorology and Climatology*, *48*(4), 833–848. https://doi.org/10.1175/2008JAMC1817.1

Price, C. (2013). Lightning Applications in Weather and Climate Research. *Surveys in Geophysics*, *34*, 755–767. https://doi.org/10.1007/S10712-012-9218-7/FIGURES/2

Price, C., & Rind, D. (1993). What determines the cloud-to-ground lightning fraction in thunderstorms? *Geophysical Research Letters*, *20*(6), 463–466. https://doi.org/10.1029/93GL00226

Pruppacher, H., & Klett, J. (1997). *Microphysics of clouds and precipitation* (K. Acad, Ed.). Morwell Mass.

Ralph, F., Neiman, P. J., Wick, G. A., Gutman, S. I., Dettinger, M. D., Cayan, D. R., & White, A. B. (2006). Flooding on California's Russian River: Role of atmospheric rivers. *Geophysical Research Letters*, *33*(13). https://doi.org/10.1029/2006gl026689

Ralph, F., Wilson, A. M., Shulgina, T., Kawzenuk, B., Sellars, S., Rutz, J. J., Lamjiri, M. A., Barnes, E. A., Gershunov, A., Guan, B., Nardi, K. M., Osborne, T., & Wick, G. A. (2019). ARTMIP-early start comparison of atmospheric river detection tools: how many atmospheric rivers hit northern California's Russian River watershed? *Climate Dynamics*, *52*, 4973–4994. https://doi.org/10.1007/s00382-018-4427-5

Saha, S., Moorthi, S., Wu, X., Wang, J., Nadiga, S., Tripp, P., Behringer, D., Hou, Y. T., Chuang, H. Y., Iredell, M., Ek, M., Meng, J., Yang, R., Mendez, M. P., Van Den Dool, H., Zhang, Q., Wang, W., Chen, M., & Becker, E. (2014). The NCEP climate forecast system version 2. *Journal of Climate*, *27*(6), 2185–2208. https://doi.org/10.1175/JCLI-D-12-00823.1

USGS. (2019). Post-Fire Debris-Flow Hazards: Thomas Fire. https://landslides.usgs.gov/hazards/postfire_debrisflow/detail.php?objectid=178

Wallace, J. M., & Hobbs, P. V. (2006). *Atmospheric Science: An Introductory Survey*. Academic Press.

Zhu, Y., & Newell, R. E. (1994). Atmospheric rivers and bombs. *Geophysical Research Letters*, *21*(18), 1999–2002. https://doi.org/10.1029/94GL01710

Chapter 3

Winter and Spring Atmospheric Rivers in High Mountain Asia: Climatology, Dynamics, and Variability

D.L. NASH, L.M.V. CARVALHO, C. JONES, & Q. DING

Abstract

Atmospheric Rivers (ARs) that reach the complex terrain of High Mountain Asia (HMA) cause significant hydrological impacts for millions of people. While ARs are often associated with precipitation extremes and can cause floods and debris flows affecting populated communities, little is known about ARs that reach as far inland as HMA. This paper characterizes AR types and investigates dynamical mechanisms associated with the development of ARs that typically affect HMA. Combined empirical orthogonal function (cEOF) analysis using integrated water vapor transport (IVT) is applied to days where an AR reaches HMA. K-means cluster analysis applied to the

first two principal components uncovered three subtypes of AR events with distinct synoptic characteristics during winter and spring months. The first subtype increases precipitation and IVT in Western HMA and is associated with a zonally oriented wave train propagating within the westerly jet waveguide. The second subtype is associated with enhanced southwesterly IVT, anomalous upper-level cyclonic circulation centered on 45°E, and precipitation in Northwestern HMA. The third subtype shows anomalous precipitation in Eastern HMA and southwesterly IVT across the Bay of Bengal. Interannual variations in the frequency of HMA ARs and relationships with various teleconnection patterns show that western HMA AR subtypes are sensitive to well-known remote large-scale climate factors, such as the El Niño Southern Oscillation, Arctic Oscillation, and the Siberian High. These results provide synoptic characterization of the three types of ARs that reach HMA and reveal the previously unexplored significance of their contribution to winter and spring precipitation.

3.1 Introduction

Atmospheric Rivers (ARs), a term coined in the early 1990s, describes a phenomenon that explains how baroclinic eddies transport large amounts of water vapor via relatively infrequent, long conduits of strong moisture transport across mid-latitudes and into Polar Regions (Zhu & Newell, 1994). ARs obtain their high water vapor content from tropical or extratropical moisture sources, moisture convergence, or local evaporation and are often found in the area ahead of the cold front of extratropical cyclones (Dacre et al., 2015; Rutz et al., 2014). Many studies have shown the global importance of ARs to poleward moisture transport, climate, and water budgets (Guan & Waliser, 2017; Guan et al., 2018; Ma et al., 2020; Nash et al., 2018; Paltan et al., 2017; Waliser & Guan, 2017; Zhu & Newell, 1998). Poleward integrated vapor transport (IVT) from

ARs makes up over 90% of the total moisture transport in the mid to high latitudes (Guan & Waliser, 2015; Zhu & Newell, 1998). Studies have also shown ARs are related to precipitation extremes, flooding, seasonal snowpack, and water availability in the western United States and western Europe (Dettinger, 2011; Guan et al., 2010, 2013; Lavers & Villarini, 2013; Ralph et al., 2006; Wick et al., 2013). Moreover, ARs modulate extreme precipitation and anomalous snow accumulation in many other regions including Antarctica (Bozkurt et al., 2018; Gorodetskaya et al., 2014; Gorodetskaya et al., 2020), Australia and New Zealand (Kingston et al., 2016; Prince et al., 2021; Reid et al., 2021; Ye et al., 2020), the Arctic Ocean and Greenland (Baggett et al., 2016; Hegyi & Taylor, 2018; Mattingly et al., 2018; Mattingly et al., 2020; Neff, 2018; Wernli & Papritz, 2018; Wille et al., 2019), South America (Ramos et al., 2019; Viale & Nuñez, 2011; Viale et al., 2018), North Africa (Akbary et al., 2019; Blamey et al., 2018; Dezfuli, 2020; Massoud et al., 2020), and East Asia (Naoi et al., 2020; Pan & Lu, 2020).

While much is known about ARs that simply cross from oceanic regions to land and immediately result in precipitation, not much is understood about ARs that penetrate farther inland (Rivera et al., 2014; Rutz et al., 2014; Rutz et al., 2015), as is the case in Southern Asia. ARs in Southern Asia are unique as they spend most of their life cycle crossing land until they encounter the mountainous region surrounding the Tibetan Plateau referred to as High Mountain Asia (HMA). Yang et al. (2018) identified a series of ARs that formed near the equator over the Bay of Bengal between 1979 and 2016 and determined that many were associated with tropical cyclones, and while infrequent, a large proportion of these ARs led to extreme rainfall events in Northeast India, Bangladesh, and Myanmar. Thapa et al. (2018) detected ARs that crossed a transect in Nepal and found that 70% of these ARs were related to extreme rainfall during non-monsoon periods. Both studies indicated that further work is needed to

understand the synoptic conditions of ARs in Southern Asia and their modulation by various modes of large-scale climate variability in both monsoon and non-monsoon seasons.

This study aims to examine ARs that reach HMA and their resulting precipitation, which is important to improve our understanding of water resources in Southern Asia, where recent changes in the regional hydrological cycles have been clearly observed over the past decades but the consensus on the causes of these changes has not been reached. It is known that precipitation and the resulting glacial melt in HMA in the spring and summer months provides water resources for hundreds of millions of people in Southern Asia (Hewitt, 2005; Kääb et al., 2012). The Karakoram mountain range, located in the western Himalayas, receives approximately 50% of its annual precipitation during winter and spring months from extratropical cyclones or Winter Westerly Disturbances (WWDs) (Bookhagen & Burbank, 2010; Cannon et al., 2015; Carvalho et al., 2020; Norris et al., 2018; Norris et al., 2017). Glaciers in the Karakoram have been stable or advancing in a phenomenon known as the 'Karakoram Anomaly', attributed to increased wintertime precipitation, decreasing summer temperatures, and increases in extratropical cyclone frequency and intensity (Archer & Fowler, 2004; Bolch et al., 2012; Cannon et al., 2015; Forsythe et al., 2017; Gardelle et al., 2012; Hewitt, 2005; Kääb et al., 2012; Norris et al., 2018; Scherler et al., 2011). Meanwhile, in Central Himalaya, accelerated melting of alpine glaciers has been attributed to increased temperatures, decreasing precipitation, the weakening of the summer monsoon and decrease in nocturnal rains in the mountains induced by the amplification in the anabatic-katabatic winds (Duan et al., 2006; Krishnan et al., 2013; Norris et al., 2020; Zhao et al., 2014). In addition, over the past decades, HMA has been at risk for rainfall-related hazards such as floods, lightning, and landslides that impact nearby populations, infrastructure, and glaciers (Kirschbaum et al., 2019). The role of ARs in driving these

rainfall related phenomenon is currently unaddressed.

The objective of this paper is to characterize the climatology of ARs that bring moisture to HMA and result in distinctive regional patterns of precipitation during the non-monsoon months (December-March). This study also investigates the relationships between WWDs and ARs to better understand their interaction with topography and different large-scale climate drivers. To achieve this, we apply combined Empirical Orthogonal Function (cEOF) analysis to daily meridional and zonal IVT anomalies to analyze the variability in synoptic-scale atmospheric fields associated with ARs landfalling in HMA. We also examine the dynamic relationship between HMA ARs and a variety of well-known large-scale climate modes that are most representative and prevailing in the tropics, extratropics, and polar regions over a broad range of timescales, such as the Arctic Oscillation (AO), El Niño Southern Oscillation (ENSO), Siberian High (SH), and Madden-Julian Oscillation (MJO). The organization of this paper is as follows: Section 3.2 describes the data used for this analysis and Section 3.3 outlines the case selection and the methodology used for the cEOF and k-means cluster analysis associated with the AR cases selected. Section 3.4 outlines the climatology of HMA ARs and identifies synoptic AR subtypes. Moreover, we investigate the influence of climatic modes on the frequency of each ARs subtype and associated synoptic patterns. Results are summarized in Section 3.5.

3.2 Data

ARs are identified in this study using a combination of geometry (e.g., length, width), intensity thresholds (e.g., above 85th percentile in HMA), and directional components (e.g., must be poleward), on a 6-hourly global basis between 1979 and 2019 based on the widely used AR detection algorithm introduced in Guan and Waliser

(2015), and refined in Guan et al. (2018). The latest version of this algorithm includes tracking capabilities from one 6-hour time step to the next (Guan & Waliser, 2019). This AR catalog has been used in many studies and is particularly useful in this study due to the global spatial scale and the application of relative methods for IVT intensity thresholds (Lora et al., 2020; Rutz et al., 2019; Shields et al., 2018). The European Centre for Medium-Range Weather Forecasts (ECMWF) atmospheric reanalyses of the global climate (ERA5) is used here to examine geopotential height, winds, temperature at multiple pressure levels, as well as IVT and precipitation (Hersbach et al., 2020). One main issue in exploring precipitation in HMA is that rain gauges are unevenly distributed and mostly located in lower elevation areas (Andermann et al., 2011; Norris et al., 2017). In addition, complex topography causes challenges in remotely sensed precipitation products, such as systematic underestimation related to the ability of the IR sensors to distinguish between raining and non-raining clouds (Andermann et al., 2011; Behrangi et al., 2016; Maggioni et al., 2016; Palazzi et al., 2013). To account for the uncertainty in these data sets, this research compares precipitation from ERA5 with other precipitation data including the Integrated Multi-satellitE Retrievals for Global Precipitation Measurement (IMERG) V06B and APHRODITE's (Asian Precipitation - Highly-Resolved Observational Data Integration Towards Evaluation) daily gridded precipitation products (Hersbach et al., 2020; Huffman et al., 2020; Yatagai et al., 2012). In addition, the analysis was repeated using Modern Era Retrospective Reanalysis version 2 (MERRA2) and results were found extremely similar (not shown), indicating the robustness of the results and conclusions (Gelaro et al., 2017). Elevation of the HMA region was determined using the National Oceanic and Atmospheric Administration (NOAA) National Geophysical Data Center's ETOPO1 1 arc-minute (about 2km) global relief model (see Fig. 3.1) (Amante & Eakins, 2009). For consideration of AR days, the ETOPO1 data was upscaled to the resolution of the AR Catalog.

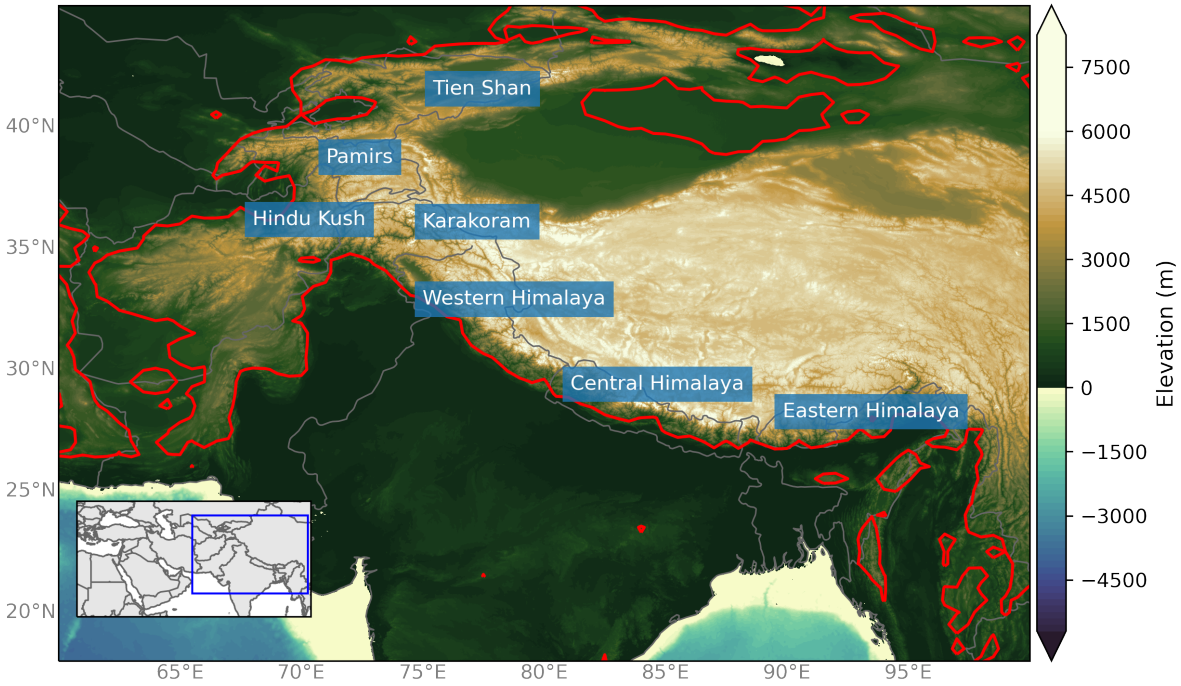

Figure 3.1: Topographical map of High Mountain Asia (HMA) using the NOAA National Geophysical Data Center's ETOPO1 1 arc-minute Global Relief Model showing the elevation (contours, m) for the HMA domain. The red line indicates 1000 m elevation using ETOPO1 global relief model upscaled to 0.5° horizontal resolution used for identifying HMA ARs. The labels show the relative locations of mountain ranges. The inset map indicates the domain used for the cEOF analysis with the blue bounding box indicated the extent of the topographical map.

We investigated climate modes that are known to influence water vapor content in the troposphere, position and intensity of the subtropical jet, Rossby wave activity, and the storm track in the Northern Hemisphere: AO, ENSO, SH, and MJO. The AO and ENSO indices used for this study were calculated by the National Weather Service Climate Prediction Center (www.cpc.ncep.noaa.gov). The ENSO index is based on the Oceanic Niño Index (3-month running mean of SSTAs in the Niño 3.4 region) (Trenberth, 1997). El Niño (La Niña) seasons are identified when the index exceeds +0.5°C (-0.5°C) for at least five consecutive months. The SH index was created by spatially averaging sea-level pressure over the region 80-120°E, 40-65°N during DJF between 1979 and 2019 and then standardized by subtracting the mean and dividing by the standard deviation of the time series (Panagiotopoulos et al., 2005). For both the AO and SH, conditions are considered positive (negative) when their respective index is 0.5 (-0.5) standard deviation above (below) zero. Due to the complexity of the MJO and the wide variety of indices used to identify MJO events, this study uses two different MJO indices. The first is the commonly used Real-time Multivariate MJO (RMM) index which uses cEOF analysis of normalized outgoing longwave radiation, 200 hPa zonal wind and 850 hPa zonal wind meridionally averaged at all longitudes between 15°S and 15°N (Wheeler & Hendon, 2004). MJO composites use phases in which the magnitude of the index is greater than one (Wheeler & Hendon, 2004). Daily RMM index values were obtained from the Centre for Australian Weather and Climate Research. The second is the MJO index of Jones (2009), which, in addition to using 20-200 day bandpass-filtered anomalies in the cEOF (same variables as RMM index), defines an MJO event as those that exceed an amplitude of one and have eastward propagation (Jones, 2009). These considerations improve the accuracy of the representation of the temporal evolution of MJO events (Jones, 2009).

3.3 Methods

3.3.1 AR events

To focus on ARs that reached HMA, days where an AR reached the 1000 m elevation threshold or higher (between 20°N and 40°N and 65°E and 97°E) were considered an AR day in HMA (see Fig. 3.1). While the number of AR events is sensitive to the choice of elevation threshold, the dynamics explaining these events are not affected. Between 1979 and 2019, we found a total of 1399 AR days in DJF and 1758 days in MAM intercepting the 1000 m elevation threshold. The independence of these events was assessed based on the results of the tracking capabilities from the Guan and Waliser (2019) AR detection algorithm v3. This method uses feature tracking and spatial overlapping from one 6-hour time step to the next to construct the AR tracks (see Guan and Waliser (2019) for more discussion). This resulted in a total of 2278 AR independent events in DJFMAM, which were used to assess the statistical significance tests performed in Section 3.4.3. Approximately half of the events in both DJF and MAM lasted less than 1 day while 10% of the events in both seasons were 5 days or longer. Because of the increased magnitude in water vapor and precipitation and the decreased magnitude in upper-level wind speeds in the spring season compared to the winter season, the seasons were initially separated for the cEOF and k-means cluster analysis. The subtypes of ARs in DJF were extremely similar to the subtypes found in MAM (not shown). Therefore, we discuss the results obtained for the entire DJFMAM season.

3.3.2 Combined EOF and k-means cluster analysis

A combined EOF analysis (cEOF) was performed to identify the main atmospheric patterns associated with ARs making landfall in HMA. The cEOF analysis was applied to daily meridional and zonal IVT anomalies using ERA5 reanalysis, in a domain extending between 20°E to 100°E and 10°N to 50°N for all selected AR days. Since EOF analysis is sensitive to the domain size and choice of variables, several tests were performed to find the optimum domain and the necessary number and type of variables to properly distinguish AR regimes (not shown). We found that despite some variation between number of ARs, variables, and domain choice for the cEOF analysis, results converged indicating the robustness of the analysis. The spatial loadings were calculated (see Appendix B.1 for details) and the distribution of the leading two cEOFs were analyzed (Wilks, 2019a). A k-means cluster analysis was further applied to highlight the prominent spatial differences between AR subtypes (see Appendix B.2 for details). Cluster analysis is a form of unsupervised learning that allows for an objective separation of data into groups based on the degree of similarity and differences in the spatial loadings (Wilks, 2019b). This methodology can bring out unique grouping of data that might not have been identified, making it a powerful tool for an objective stratification of distinct atmospheric patterns (Cheng & Wallace, 1993; Mercer et al., 2012; Peters & Schumacher, 2014). The results of the k-means clustering analysis are discussed in section 3.4.2.

3.4 Results

3.4.1 Climatology of ARs in High Mountain Asia

The climate of HMA from December to March is mainly influenced by Winter WWDs which are related to extratropical cyclones (Bookhagen & Burbank, 2010; Cannon et al., 2015; Lang & Barros, 2004). These disturbances are associated with the propagation of troughs and ridges in the upper-level jet stream that can result in precipitation if enough moisture is present when orographically forced (Cannon et al., 2016; Filippi et al., 2014; Singh et al., 1995). There are on average 70 WWDs related to extratropical cyclones per winter and spring season, but only 25% of WWDs result in large-scale precipitation (Hunt et al., 2018). Cannon et al. (2015) suggested that moisture advection was important for extreme precipitation events related to WWDs while Hunt et al. (2018) concluded that rainfall associated with WWDs is related to both orography and the intensity of the WWD. The mechanism behind extreme rainfall related to WWDs still remains elusive and we expect that water vapor transport from less frequent, but impactful ARs is critical to determine seasonal mean precipitation during the winter and spring months in HMA.

A seasonal climatology IVT and AR frequency over Southern Asia using ERA5 reanalysis and the global atmospheric river detection catalog (Guan & Waliser, 2015; Guan et al., 2018; Guan & Waliser, 2019) for the years between 1979 and 2019 is shown in Fig. 3.2. During winter (DJF) and spring (MAM) months, the highest frequency of ARs (right column) is observed in subtropical latitudes (between 30-40°N), which implies that ARs are associated with extratropical cyclones, otherwise known as WWDs. (Bookhagen & Burbank, 2010; Cannon et al., 2015; Lang & Barros, 2004; Norris et al., 2018). As expected, during the winter months (DJF) the highest IVTs are

observed in tropical latitudes. We also notice an anticyclonic circulation over India, which is typically observed during DJF. Between 30-40°N IVT is, on average, less than 200 kg m^{-1} s^{-1} and yet, during DJF there is an AR 8-10% of the time over Southwest Asia. In MAM, IVT begins to increase in subtropical latitudes (to about 150 kg m^{-1} s^{-1}) following the transition from anticyclonic to cyclonic circulation over India during the pre-monsoon season, which brings more moisture to subtropical latitudes associated with the intensification of the westerly flow between 20°N and 30°N. On average, we observe an AR during MAM about 8-12% of the time affecting Southwest Asia and 2-4% of the time in Southeast Asia. To quantify the relationship between extratropical cyclones related to WWD and HMA ARs, we used a catalog developed by Hunt et al. (2018) that identified WWDs over Pakistan and Northern India. This catalog, which extends from 1979 to 2015 identified approximately 2600 WWDs between the months of December to March, averaging about 12 WWDs per month. Therefore, compared to our 2278 AR events, WWDs are just as frequent as HMA ARs (Hunt et al., 2018). When we compared the days with ARs to the days with WWDs based on this catalog, we find that while 73% of ARs occur simultaneously with a given WWD day, only 42% of WWDs are associated with ARs.

Summer (JJA) ARs are typically associated with higher magnitudes of IVT from the Arabian Sea east across Southern India, through the Bay of Bengal and northeast from there. This strong westerly flow and high IVT (exceeding 500 kg m^{-1} s^{-1}) indicate a strong association with the summer monsoon flow. Therefore, during JJA, ARs typically affect the Indian Peninsula and adjacent oceans, with a frequency exceeding 10% of the time on average. The higher water vapor transport during the summer season is attributed to increased evaporation over the Indian Ocean and changes in circulation associated with the mature phase of the summer Indian monsoon (Carvalho et al., 2016; Goswami & Mohan, 2001; Yang et al., 2018; Zhao et al., 2016). In fall (SON) the

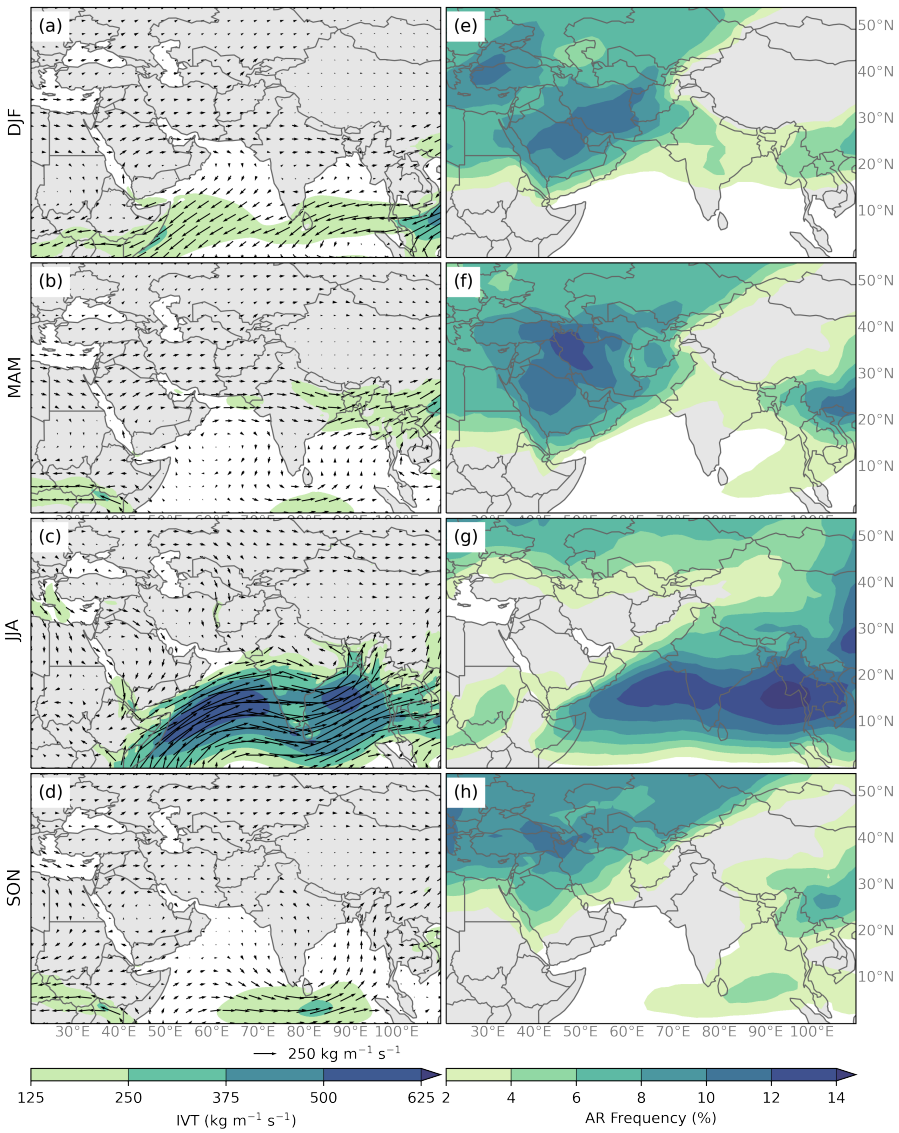

Figure 3.2: (a-d) The average IVT (shaded; kg m^{-1} s^{-1}) and IVT direction and magnitude (vectors; kg m^{-1} s^{-1}) for each season between 1979-2019 using ERA5 data. (e-h) The average AR frequency (shaded; percent of time steps) for each season between 1979-2019 using ERA5 data.

highest values of IVT (less than 150 kg m^{-1} s^{-1}) are observed in the low latitudes, south of the Indian Peninsula following the progress of the monsoon toward the Southern Hemisphere (e.g., (Carvalho et al., 2016)). There is an AR between 2-6% of the time during the fall affecting Southwest and Southeast Asia. The frequency of these events also increases over Eastern Europe in the mid-latitudes.

To determine the relative contribution of HMA ARs to precipitation, Fig. 3.3 shows the average seasonal total precipitation and the AR precipitation fraction. The AR precipitation fraction is the precipitation (in all grid cells) that occurs on HMA AR days that season compared to the total seasonal precipitation. During the winter (DJF) (Fig. 3.3a), precipitation is on average between 400-675 mm $season^{-1}$ and occurs primarily in the Pamir Mountains and along the Himalayas at elevations greater than 1000 m. Spring (MAM) (Fig. 3.3b) precipitation increases particularly in Eastern Himalaya, the Karakoram, the Pamirs, and Tien Shan Mountains (see Fig. 3.1 for location details). The contribution of precipitation during HMA ARs in DJF is around 60% and about 45% during MAM across HMA. In the area near Mumbai, HMA ARs contribute up to 80% of the total DJF seasonal precipitation (Fig. 3.3 and B.2). However, precipitation from ERA5 indicates high variability (standard deviation) in the high elevation regions and during the spring season (Fig. B.3). To check for consistencies, this analysis was repeated with IMERG-PM and APHRODITE (Fig. B.1). All three precipitation datasets show high precipitation totals along the Himalayas-particularly in the Karakoram and Eastern Himalaya regions but with varying magnitudes and spatial patterns. ERA5 overestimates precipitation compared to APHRODITE and IMERG-PM and had a higher variance in the eastern Himalayas compared to the other precipitation data sets. Despite these differences, all three precipitation datasets show that HMA AR days contribute roughly 60% of total DJF precipitation and around 40% of total MAM precipitation between 2000 and 2015 along HMA. Interestingly, there is roughly the same

contribution of AR events to the total precipitation during the summer monsoon (JJA) and post-monsoon (SON) seasons, indicating the importance of water vapor transport by tropical intraseasonal oscillations (ISOs) in contributing to the total precipitation over the region during the monsoon season.

The climatology in Figs. 3.2 and 3.3 show that winter months have much less precipitation in eastern Himalayas and overall a lower magnitude of IVT across Southern Asia compared to spring months. During the winter and spring months in Southern Asia, monsoon circulation weakens and temperatures on the Tibetan Plateau are much colder than temperature at the same altitude over the surrounding oceans, resulting in a typical winter monsoon pattern on India characterized by low-level northeastern winds over the southern Indian peninsula. Meanwhile, the westerly jet is strengthened but retreated equatorward to linger around 30°N. This increases the frequency of eastward propagating synoptic circulation systems along the jet such as WWDs from upstream regions toward HMA. (Bookhagen & Burbank, 2010; Krishnamurti & Bhalme, 1976; Wang, 2006). The waviness of the jet combined with topographic influence favors upper-level divergence ahead of the WWD, orographic lifting, and large-scale convection that may result in more interactions between ARs with local precipitation in HMA. In the spring, there is higher atmospheric moisture content due to increased temperatures and saturation vapor pressure in and around HMA at the lower levels, increasing convective instability and the occurrence of precipitation events (Bookhagen & Burbank, 2010; Wang, 2006). It has been shown that in the spring months preceding the monsoon season, the interaction of extratropical cyclones with the warm moist tropical air mass leads to enhanced moisture advection toward the mountains (Barlow et al., 2005; Cannon et al., 2017). These warmer, moister, and less stable atmospheric conditions combined with orographic forcing can work together to result in more active roles of ARs in triggering intense precipitation over HMA. It seems that more attention

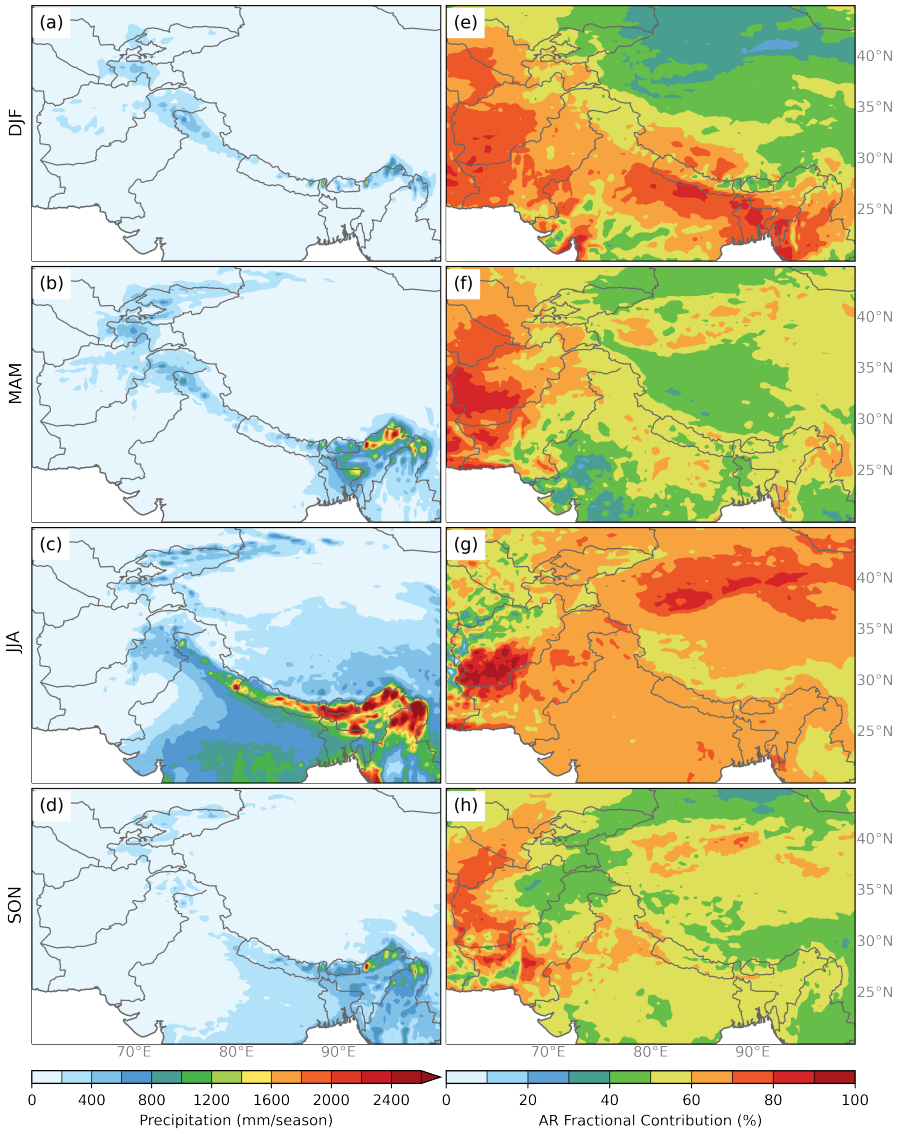

Figure 3.3: (a-d) The average ERA5 precipitation seasonal totals (shaded; mm season^{-1}) for DJF, MAM, JJA, and SON. For each grid cell the total seasonal precipitation is calculated per year, then averaged over all years between 1979-2019. (e-h) The AR precipitation fraction (shaded, % of total seasonal precipitation) for each season. The total seasonal precipitation that occurs within the AR object is calculated for each season. The AR precipitation fraction is then the total seasonal precipitation that occurs only within HMA ARs divided by the total seasonal precipitation, multiplied by 100 and then averaged over the years between 1979-2019.

should be placed on the impact of ARs, moisture availability and other key atmospheric variables that critically control moisture advection in the seasons.

3.4.2 Defining patterns of variability of AR events

Combined EOF (cEOF) analysis followed by k-means cluster analyses were applied to identify the main synoptic patterns associated with the occurrence of AR events (see section 3.3.2 and Appendix B.1). Daily meridional and zonal IVT anomalies from ERA5 reanalysis were used between 20°E to 100°E and 10°N to 50°N for the cEOF. To test the influence of seasonality on the cEOF and k-means cluster analysis we separated DJF and MAM AR days. While magnitudes of the resulting composites vary between the two seasons, the cEOF spatial patterns and the resulting synoptic conditions of the subtypes identified in the separate seasons were very similar. Therefore, results presented included cases in both seasons (hereafter, DJFMAM).

Figure 3.4a shows the fraction of the total percent of variance represented by each of the corresponding PCs. The first two PCs of the correlation matrix for the mean meridional and zonal IVT anomalies during HMA AR days in DJFMAM account for approximately 14% of the normalized DJFMAM IVT variance. According to the North (1984) test, only the first 2 cEOFs were sufficiently separated. PC3 and PC4, while not separated from each other, do appear to represent distinct variance and were included during the testing phase of the k-means clustering analysis to determine if they were necessary to retain. There was little variation in the final results when PC3 or PC4 were included in the k-means clustering analysis. Therefore, only the first two PCs were retained for the final analysis. The spatial loading patterns of the first four cEOFs (see Fig. 3.5) reflect the underlying circulation patterns in the atmosphere during these HMA AR events. For example, cEOF1 reflects the pattern of a strong anticyclonic

anomaly centered around the northeastern Arabian Sea with strong southwesterly flux across Southwest Asia that reaches roughly 40°N. While the second cEOF is also associated with above-average southwesterly flux over Southwest Asia the anticyclonic anomaly is located west of the anticyclone in cEOF1, and the IVT doesn't reach as far poleward as cEOF1. In addition, cEOF2 shows a cyclonic anomaly centered over the eastern Mediterranean Sea that appears to be interacting with the anticyclonic anomaly.

To objectively characterize spatial differences between AR subtypes we applied the k-means cluster analysis to the first two PCs (see section 3.3.2 and Appendix B.2). To estimate the optimal number of clusters, we examined the estimated kernel density function for the subspace of the first two PCs (Fig. 4b) (Peters & Schumacher, 2014). The kernel density estimate of the first two PC loadings exhibits one distinct maxima for all cases in DJFMAM approximately centered in a region with negative PC2 and biased toward a positive PC1 loading (yellow point, Fig. 3.4b). There are two additional less distinct maxima (green and red points, Fig. 3.4b) that are related to positive (red point) and negative (green point) PC2 loading. To ensure the robustness of the choice for the number of clusters, we also calculated the mean silhouette scores, which display how close each point in one cluster is to points in the neighboring clusters (Wilks, 2019b). A mean silhouette score of 1.0 would indicate that the sample is far away from other clusters. By reiteratively running the k-means clustering with k values from 1 to 15 and identifying the highest mean silhouette score, 3 was identified as the optimal k for both seasons (see Fig. 3.4c). Additionally, we performed sensitivity tests for k=2 and k=4 by performing numerous composites (not shown) and concluded that k=3 was the optimal number of clusters for the selected HMA AR cases. Figure 3.4d shows the kernel density estimate using the identified 3 clusters from the k-means cluster analysis with each subtype having a unique centroid. All subtypes had sufficient sample size to break them into 3 clusters (n=857, 886, and 1414 for AR Type 1, 2, and

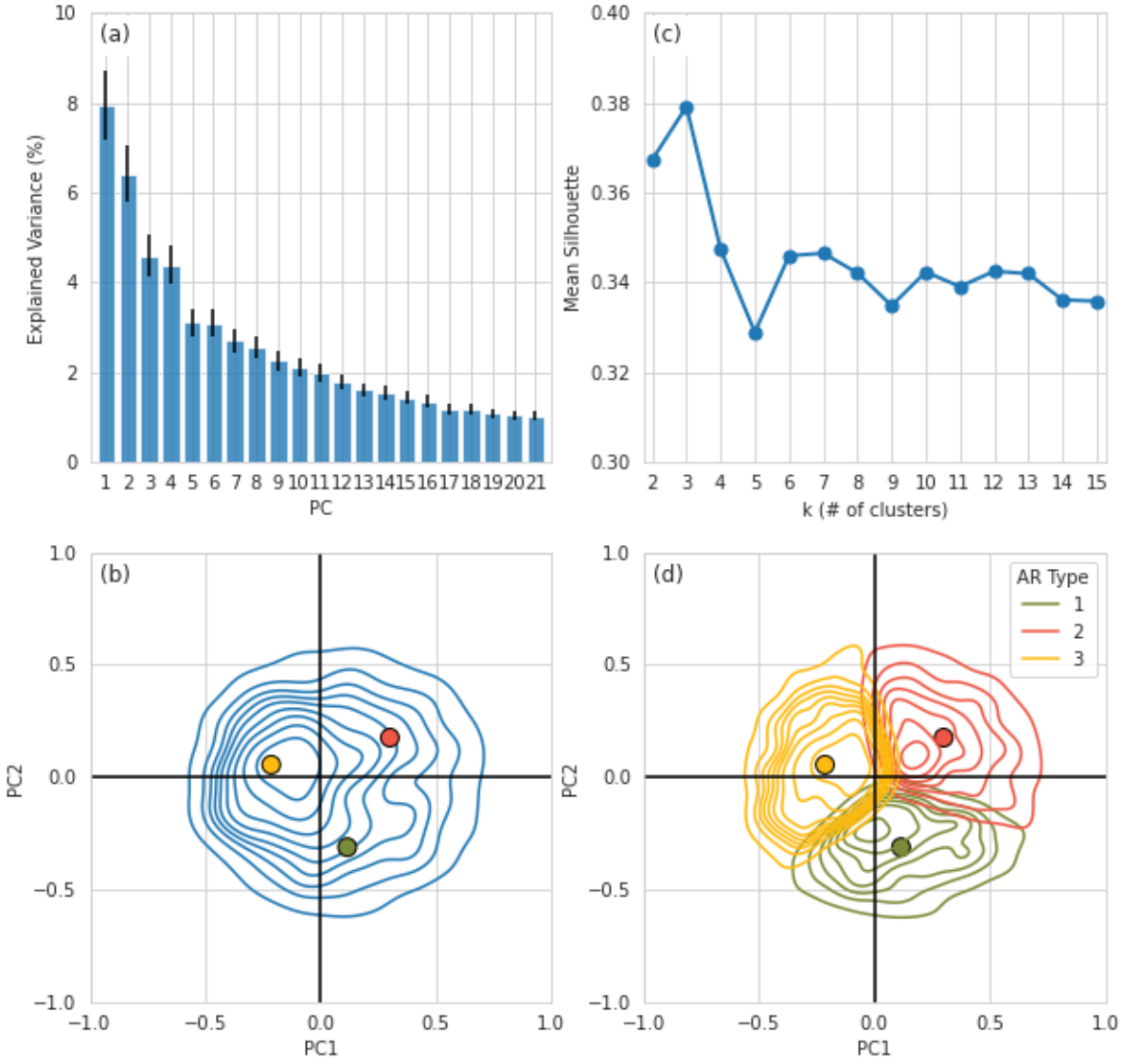

Figure 3.4: (a) Percent of variance explained by the first 21 DJFMAM PCs and their associated error calculated using the North Test (Wilks, 2019a). (b) Estimated kernel density function for PC1 and PC2 loadings for the ERA5 data analyzed for all AR events (contour lines) during DJFMAM. The three points indicate the PC loadings for three specific AR days that were categorized as different AR types during the k-means cluster analysis. (c) The mean silhouette score for clusters k=2 through k=15 (blue line). The ideal number of clusters chosen is where the mean silhouette score is the highest (Wilks, 2019b). (d) Same as (b) but broken down by AR Types after the k-means cluster analysis. The points in (d) are the same as those in (b).

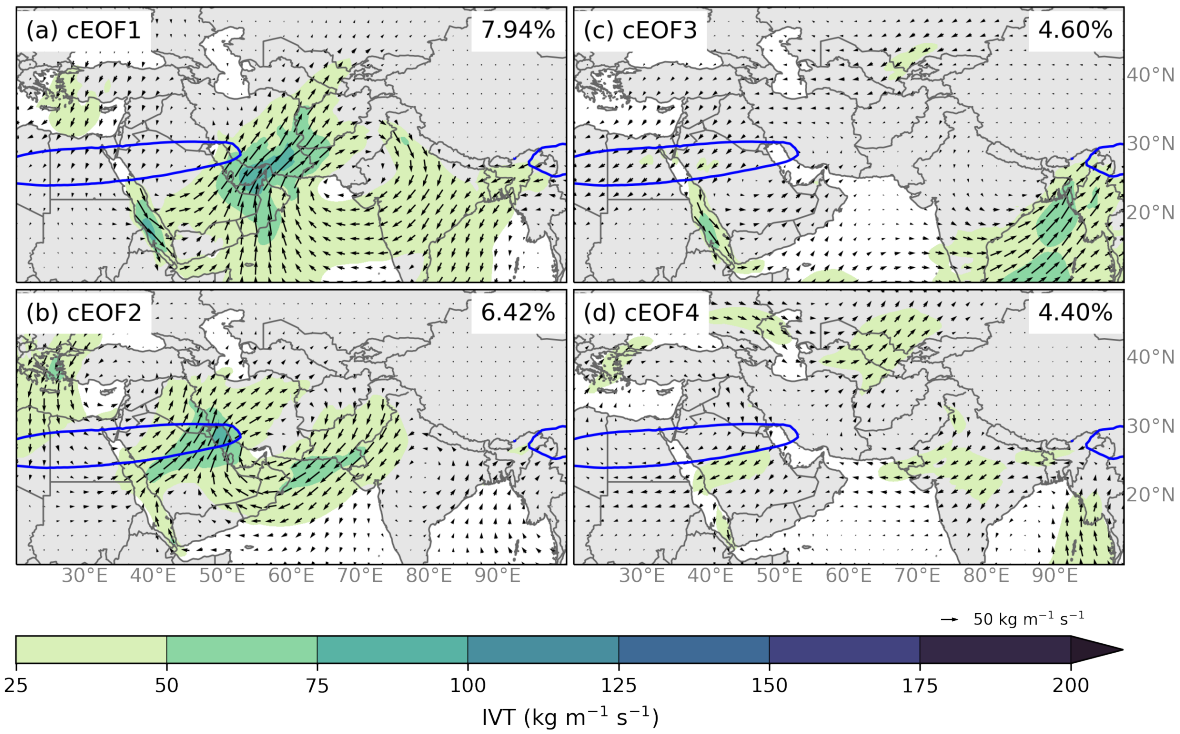

Figure 3.5: The first four eigenvectors of cEOF analysis for the mean IVT (shaded, kg m^{-1} s^{-1}), zonal, and meridional IVT (vectors, kg m^{-1} s^{-1}) anomalies during HMA AR days in DJFMAM at gridpoints in southern Asia. The percentages in the top right of each panel show the fraction of the total percent of variance represented by each of the corresponding cEOFs. The blue line indicates the mean position of the core of the 250 hPa subtropical jet ($\geq$40 m s^{-1}).

3, respectively).

To evaluate the temporal relationships among AR subtypes for both seasons, transition probabilities were computed to determine the likelihood of each AR Type transitioning to another AR Type or to a non-AR day. Figure 3.6a shows the probability that a Type 1 AR, Type 2 AR, Type 3 AR, and non-ARs will transition to another type of AR (or non-AR) the next day. In all cases there is a 45% to 50% chance that any AR Type will remain in the same AR type the next day. In some occasions, AR types transition from one type to another. For instance, the probability that Type 2 AR would transition to a Type 1 AR is higher than to Type 3, while the probability that Type 1 AR would transition to a Type 3 AR is higher than to Type 2. Nonetheless, ARs are typically transient (half of the ARs last 1 day or less) and there is between 20% to 40% chance that any AR type will transition to a non-AR the next day. The next section will describe how the results from the combined EOF and k-means cluster analysis were used to create synoptic composites for each of the unique AR subtypes.

3.4.3 Characterization of synoptic subtypes

Synoptic conditions associated with AR subtypes were characterized by performing composites of mean (Fig. 3.7) and anomalies (annual cycle removed) (Fig. 3.8) for IVT, 250 hPa geopotential heights and winds, and precipitation. The most notable differences between the three subtypes can be identified by the location and strength of the subtropical jet and geopotential anomalies, as well as the intensity and direction of the IVT. Type 1 ARs are associated with anticyclonic flow of above average IVT over southwest Asia and result in precipitation in Hindu Kush and Karakoram mountain regions. Type 2 ARs are characterized by southwesterly IVT over southwest Asia and above average precipitation in the Zagros, Pamir and Tien Shan mountain regions.

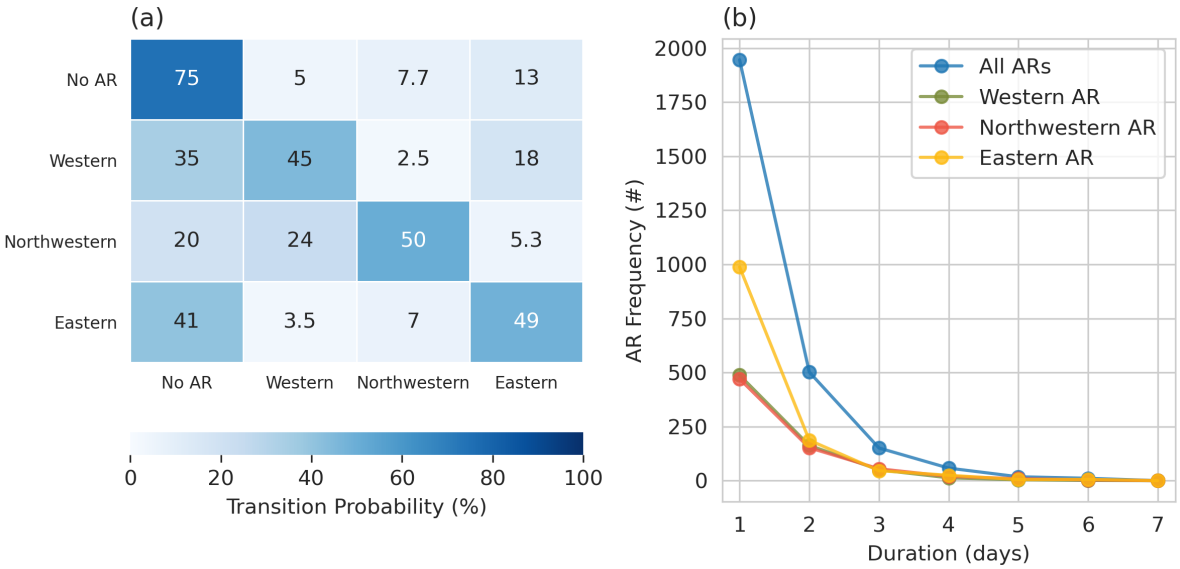

Figure 3.6: (a) The state transition probability matrix for DJFMAM days that start in state 0 (no AR, first row), state 1 (Western HMA AR, second row), state 2 (Northwestern HMA AR, third row) and state 3 (Eastern HMA AR, fourth row) and ends up in state 0 (no AR, first column), state 1 (Type 1 AR, second column), state 2 (Type 2 AR, third column), or state 3 (fourth column). The transition period is 1 day and the probability is given in percent. (b) The number of ARs and their respective duration (days). The blue line represents all ARs, green is Western HMA ARs (Type 1), red is Northwestern HMA ARs (Type 2), and yellow is Eastern HMA ARs (Type 3).

Type 3 ARs are characterized by southwesterly IVT that is mostly sourced from the Bay of Bengal and Northern India and results in precipitation across HMA, particularly in eastern Himalaya. For simplicity, we will refer to the ARs by the general location of the majority of their resulting anomalous precipitation. For example, Type 1 ARs will be referred to as Western HMA ARs, Type 2 ARs as Northwestern HMA ARs, and Type 3 as Eastern HMA ARs for the remainder of the paper. The seasonal frequencies of these events (see Fig. B.4) show that Western and Northwestern HMA ARs are most frequent in March, with all three types occurring up to 250 times between 1979 and 2019. This is important as March is considered a transition month and interannual variability in temperatures (particularly freezing levels) can impact the amount of rain versus the amount of snow. Eastern Himalayan ARs dominate in May, where there has been over 350 ARs between 1979 and 2019.

Western HMA ARs (Type 1, Fig. 3.7, first row) are identified by IVT with a westerly flow centered around 25°N and above-average precipitation in the Karakoram and Hindu Kush mountain regions with precipitation reaching between 16-20 mm day^{-1} in the Western Himalayas and the Karakoram. The subtropical jet for Western HMA ARs is weaker along HMA on average compared to Northwestern HMA ARs. Western HMA ARs are associated with anomalous trough and cyclonic circulation located at about 30°N and 60°E at 250 hPa and enhanced southwesterly moisture flux across northwestern India (see Fig. 3.8). Western HMA AR IVT has a more southwesterly orientation for the two days prior to the AR crossing the 1000 m threshold, but then has a more zonal orientation two days after, resulting in above average precipitation in the Karakoram and Western Himalayas (see Fig. B.5 and B.6). Some ARs that were identified in winter and spring months in Thapa et al. (2018) are considered Western HMA ARs (e.g., 5 Feb 2013, 5 Mar 1980, and 17-19 Feb 2003, among others). Thapa et al. (2018) concluded that these AR events are the main mechanism for bringing moisture into

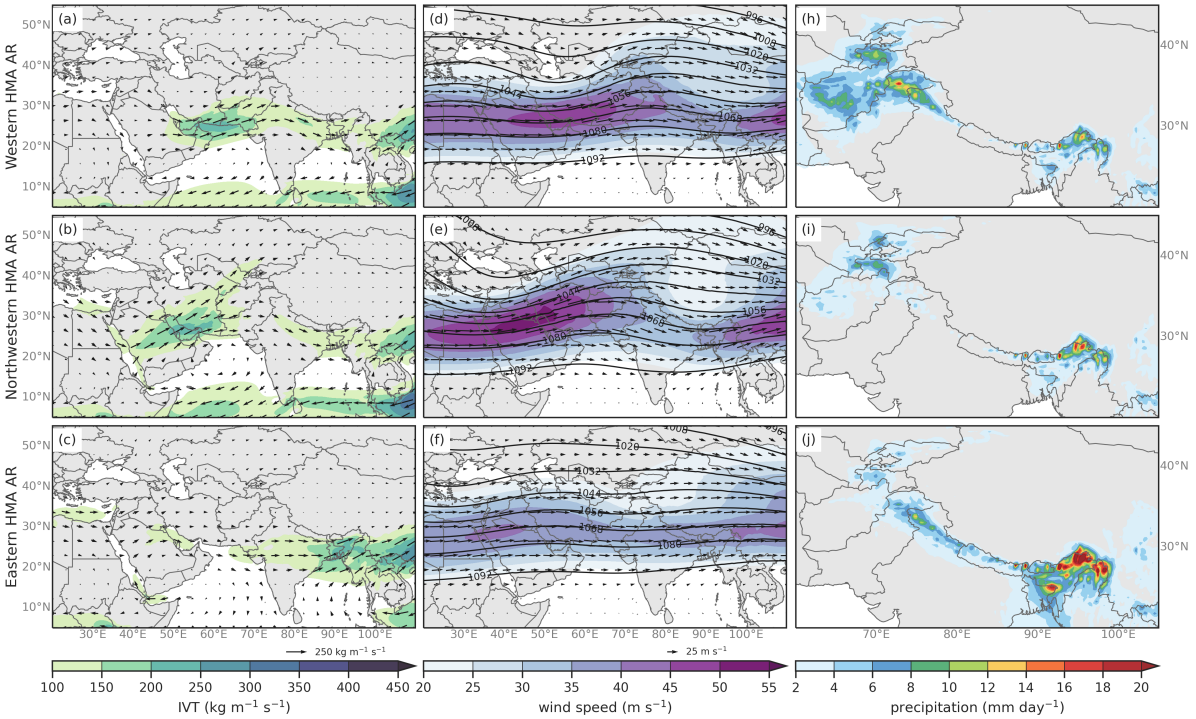

Figure 3.7: DJFMAM average composites of (left column) IVT (shaded, contours, kg m^{-1} s^{-1}), (middle column) 250 hPa wind speeds (shaded and vectors; m s^{-1}) and 250 hPa geopotential height (contours; dam), and (right column) precipitation (shaded; mm day^{-1}) for Western HMA ARs (Type 1, first row), Northwestern HMA ARs (Type 2, second row), and Eastern HMA ARs (Type 3, third row).

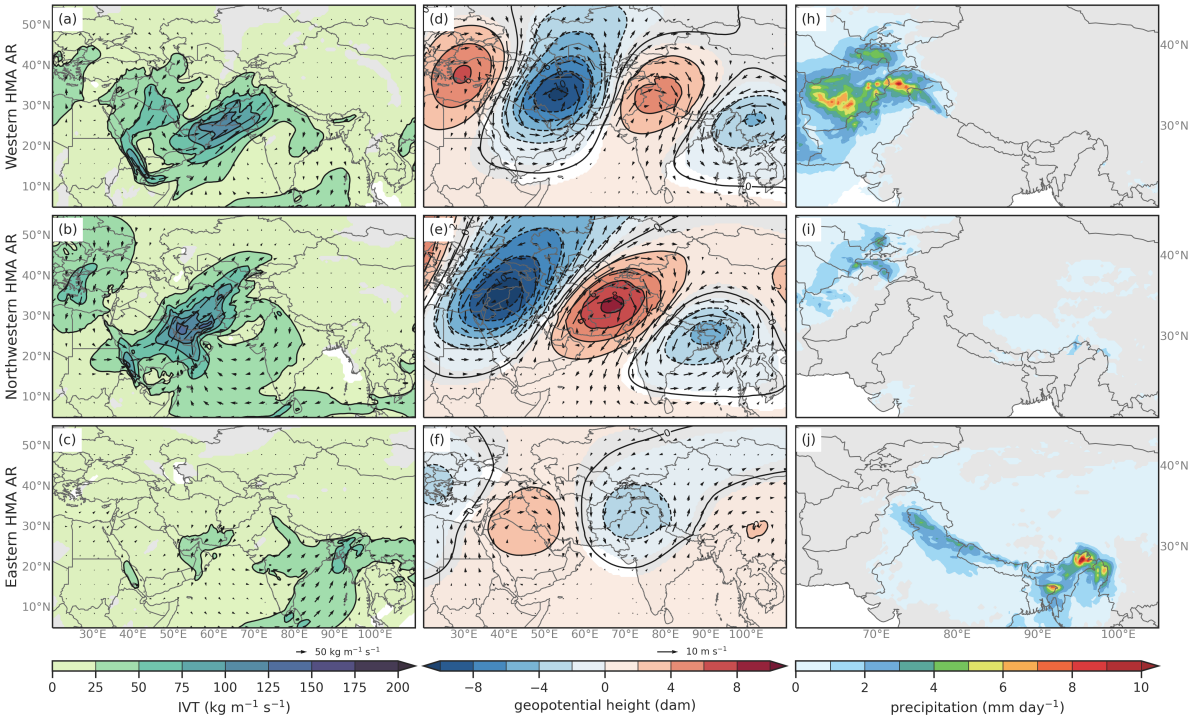

Figure 3.8: DJFMAM average anomaly composites of (left column) IVT (shaded, contours, kg m^{-1} s^{-1}), (middle column) 250 hPa wind speeds (shaded and vectors; m s^{-1}) and 250 hPa geopotential height (contours; dam), and (right column) precipitation (shaded; mm day^{-1}) for Western HMA ARs (Type 1, first row), Northwestern HMA ARs (Type 2, second row), and Eastern HMA ARs (Type 3, third row). Only values that are considered statistically significant at the 95% confidence interval are shaded.

HMA in non-monsoon months and they associate them with most extreme precipitation events in non-monsoon months. The detection algorithm employed in Thapa et al. (2018) focused on ARs that crossed a transect in Nepal, and they concluded that these types of ARs were less likely to occur in MAM compared to DJF due to lack of synoptic forcing. Our results show that Western HMA ARs are more likely to occur in MAM than DJF, though discrepancies between this work and Thapa et al. (2018) are most likely to differing detection algorithms and study region.

Northwestern HMA ARs (Type 2, Fig. 3.7, second row) are associated with enhanced southwesterly IVT that brings moisture from up near the Red Sea, across southwest Asia and the Persian Gulf and northwest into Hindu Kush, Pamirs, Karakoram, and Tien Shan regions. Northwestern ARs result in up to 8 mm of precipitation per day in the Pamirs, and up to 20 mm day^{-1} in Eastern Himalaya. Anomaly composites show that Northwestern ARs result in above-average precipitation in the Pamirs associated with a trough centered around 40°N and 40°E and a ridge centered at 30°N and 70°E that are 100 m below and above average heights respectively (see Fig. 3.8). The wave train from Central Europe to East Asia also appears to encourage northwesterly moisture flux from the Mediterranean Sea to the Red Sea, where the tilted trough then facilitates southwesterly vapor transport straight to the region surrounding Western Himalayas. In addition, anticyclonic IVT anomalies over the Arabian Sea funnel even more moisture poleward toward HMA. While there were no significant trends for HMA AR frequency, Smith and Bookhagen (2018) show evidence for increases in snow-water-equivalent storage in the northwestern region of HMA during DJF and in the high-elevation regions of the Pamirs and the Karakoram during MAM. These changes are attributed to increases in precipitation due to higher intensity WWDs in the most recent years and could be related to the 'Karakoram Anomaly' (Smith & Bookhagen, 2018). It is possible that Northwestern HMA ARs could be related to the growing

glaciers in the northwestern HMA region. Although we found no significant trend in the frequency of different AR Types, further work is needed to investigate how dynamical and thermodynamical features have changed in recent decades with regard to ARs. Precipitation in Eastern Himalayas during Northwestern HMA ARs could be attributed to the trough over Northeast India, which encourages the transport of moisture towards Eastern Himalayas. Roughly 15% of the time that there is a Northwestern HMA AR, an additional AR in Southern Asia transporting moisture to the Eastern Himalayas was identified. However, this moisture transport and resulting precipitation in Eastern Himalayas during Northwestern HMA ARs is not considered significantly above-average.

Some Northwestern HMA ARs have also been found to extend backwards across northern Africa. Massoud et al. (2020) documented an AR on January 25, 1994 that stretched over 12,000 km from western North Africa to the Karakoram. This was an anomalous case as the majority of the other ARs that impact the Middle East and Northern Africa were found to originate over the North Atlantic and dissipate in Iran where the Zagros Mountains in western Iran reach heights of 1250 m (Massoud et al., 2020). Another example of a Northwestern HMA AR that traversed northern Africa and ultimately ended in western Himalayas was documented in Dezfuli (2020) as well as Massoud et al. (2020). This AR, named "AR Dena", resulted in widespread flooding, particularly in Iran (Dezfuli, 2020). Dezfuli (2020) suggested that the moisture in the AR was enhanced due to warmer than normal marine basins that the AR passed over. While it is curious how Northwestern HMA ARs are able to traverse the complex topography of southwest Asia so far inland, the deep synoptic troughs along southern Iran and Pakistan appear to allow for moisture from marine basins, such as the Persian Gulf and Arabian Sea, to reinforce the aggregation of water vapor that is then transported all the way to the Pamir Mountains via cyclonic circulation as suggested in other regions where ARs persist inland (e.g., Cordeira et al., 2013; Dezfuli, 2020). Then, as

moisture-filled air in the AR is forced orographically, precipitation most likely develops on the windward side of the mountains.

Eastern HMA ARs (Type 3, Fig. 3.7, third row) are characterized by IVT from northern India extending eastward resulting in precipitation in the eastern Himalayas. The 250 hPa geopotential heights and winds for these ARs indicate the subtropical jet is located between 20°N and 35°N with a jet streak occurring across southwest Asia. Eastern HMA ARs coincide with a 250 hPa trough centered around 30°N and 75°E that is about 20 m below average height and ridge to the west of the trough that is about 20 m above average height (Fig. 3.8). These ARs are associated with above average southwesterly vapor transport from the Bay of Bengal region up to the Eastern Himalayas which most likely resulted in above average precipitation from terrain effects (see Fig. 3.8). Some ARs that were identified in winter and spring months in Yang et al. (2018) are considered Eastern HMA ARs in this analysis. Yang et al. (2018) suggests that the majority of these ARs are heavily influenced by tropical activity, where tropical cyclones can enhance longitudinal transport of water vapor in the ARs. Additionally, they concluded that a high proportion of December and January ARs in the Bay of Bengal led to extreme rainfall (Yang et al., 2018).

The synoptic conditions associated with all three HMA ARs have similarities with WWDs. What makes HMA ARs unique from WWDs is the enhanced moisture content within the AR. Cannon et al. (2015) investigated extreme precipitation events in the Karakoram and Central Himalaya and found that, while similar synoptic conditions were characteristic of WWDs for both regions, events that resulted in extreme precipitation in the Karakoram were independent from events that resulted in extreme precipitation in Central Himalaya. The main difference between the two types of events was the position of the trough, location of the moisture source, and precipitation. Our results show similar conditions for Western HMA ARs and Karakoram extreme precip-

itation, whereas Eastern HMA ARs resemble synoptic conditions that caused extreme precipitation in Central Himalaya in Cannon et al. (2015). Synoptic conditions during Northwestern HMA ARs resemble conditions leading (-2 days) extreme precipitation in the Karakoram region in Cannon et al. (2015), which aligns with the 24% probability that Northwestern HMA ARs transition to Western HMA AR within one-day (see Fig. 3.6). Further complicating matters, there can be more than one AR reaching HMA at any given time. For example, roughly 15-17% of any AR type occurs simultaneously with an additional AR in the Southern Asia region, indicating the complexity of HMA ARs compared to ARs in other regions of the world.

The median IVT within all three AR Types is roughly 200 kg m^{-1} s^{-1} and 50% of each AR type contains IVT between 100 and 300 kg m^{-1} s^{-1}. A little under half of the events for each AR type falls outside the interquartile range, with very few events reaching up to 700 kg m^{-1} s^{-1}, indicating the large variability of these ARs (see Fig.B.4b). Similarly, precipitation for each AR Type shows large variability, with less than 25% of each type contributing a maximum of 55-115 mm per AR event. In the area they are most likely to see above-average precipitation, the majority of ARs in each subtype results in less than 10 mm per event of precipitation (see Fig. B.4c). For example, for Eastern HMA ARs, if you area-average the total precipitation per AR event around Eastern HMA (24-30°N, 90-100°E), the majority of ARs contribute between 1 and 10 mm $event^{-1}$. This confirms what previous research has said about ARs - impactful ARs are relatively infrequent and just a few AR events per season can lead to significant contributions to water resources where they make landfall.

3.4.4 Climate Modulation

Using the HMA AR climatology presented in this research, we investigate the influence of ENSO, AO, SH, and MJO on the frequency and intensity of HMA ARs during the winter and spring seasons. On interannual timescales, ENSO, AO, and SH, among others, have been shown to influence some of the variability in precipitation and circulation in Southern Asia (Cannon et al., 2015; Gong & Ho, 2002; Gong et al., 2001; Wu & Wang, 2002; Yadav et al., 2009). The main goal of this section is to explore how these different climate modes modulate the frequency and intensity of HMA ARs.

ENSO warm phases have been shown to increase precipitation in western Himalaya during the winter, attributed to increased convergence over southeastern Asia due to increased subsidence over the maritime continent (Cannon et al., 2015; Yadav et al., 2009). During the warm phase of ENSO, when the tropical oceans are warmer than usual, anomalous upper-level convergence over southern Asia has been shown to intensify WWDs (Thapa et al., 2018; Yadav et al., 2009). Rana et al. (2019) explains that increased precipitation in Central Southwest Asia during winter season El Niño years is mainly attributed to a deepened trough over Central Southwest Asia with cyclonic circulation that enhances southwesterly flow and moist air advection from the Indian Ocean basin into Central Southwest Asia. Guan and Waliser (2015) found that El Niño conditions slightly increase NDJFM AR frequency in southwest and southern Asia but has no considerable impact on precipitation. AR frequency was shown to decrease significantly in southwest Asia during La Niña years in NDJFM (Guan & Waliser, 2015).

Here we evaluated the importance of the climate modes by calculating the difference in the proportion of HMA ARs for El Niño phase compared to La Niña phase, AO+ conditions compared to AO- conditions, SH+ conditions compared to SH- conditions

and MJO conditions compared to no MJO conditions (see Table 3.1). For example, we compute the seasonal proportions of HMA ARs for El Niño and La Niña conditions during 1979-2019; the null hypothesis is that El Niño and La Niña frequencies are equal. This is evaluated using a z test at the 5% significance level (see Appendix B.3 for equations). Significant differences at a 5% and 1% significance level in Table 3.1 are noted and indicate that Western and Northwestern HMA ARs are more frequent during El Niño compared to neutral and less frequent during La Niña conditions compared to neutral. However, ENSO related changes in frequency are considered significantly larger during La Niña conditions than during El Niño conditions. To investigate the impact of ENSO on the magnitude of IVT within the AR, we examined the distribution of the average IVT anomalies within the AR during the different types of HMA ARs for La Niña, neutral, and El Niño conditions (Fig. B.8a). There does not appear to be any dramatic difference in the average IVT magnitude within the ARs when comparing El Niño, neutral, and La Niña conditions. Eastern HMA ARs during La Niña seem to have larger variability in AR IVT, but few outliers, whereas Eastern HMA ARs during El Niño have less variability but larger outliers.

To understand why El Niño conditions favor increased frequency of Karakoram and Pamir ARs in contrast with La Niña, we compare DJFMAM averages of moisture and circulation fields for the two phases of the ENSO. Figures 3.9(a, d, g) shows the difference (El Niño minus La Niña) in the anomalies of IVT, 250 hPa geopotential height and winds, and precipitation and 500 hPa winds for Western HMA ARs and Fig. 3.9b, e, and h show differences for Northwestern HMA ARs. It is important to note that anomalies are relative to their respective AR Climatologies (see Fig. 3.8) and not the annual climatology. At upper levels, Western and Northwestern HMA ARs are related to weaker upper-level trough centered at 30°N and 40°E and a stronger ridge near 80°E during El Niño conditions compared to La Niña. This suggests that the El Niño

Table 3.1: Z scores used to test the difference in the proportion of AR days during DJFMAM 1979-2019 between the conditions of various climate indices and neutral conditions.**statistically significant at the 5% significance level **statistically significant at the 1% level.*

Conditions	W HMA AR	NW HMA AR	E HMA AR	All AR days
El Niño vs. La Niña	2.74**	3.97**	0.96	5.07**
El Niño vs. Neutral	0.93	0.07	-0.78	0.03
La Niña vs. Neutral	-2.29*	-4.46**	-1.89	-5.89**
AO+ vs. AO-	2.45*	5.24**	-0.77	4.52**
AO+ vs. Neutral	3.18**	3.28**	-2.91**	1.99*
AO- vs. Neutral	0.69	-2.02*	-2.1*	-2.54*
SH+ vs. Neutral	-0.05	0.02	-2.02*	-1.65
SH+ vs. SH-	-1.98*	-2.24*	0.05	-2.76**
SH- vs. Neutral	1.79	2.11*	-2.1*	0.91
MJO vs No MJO	1.35	-1.54	-0.7	-0.71

response in Central Asia favors an anticyclonic flow centered North of the Hindu Kush for Western HMA ARs and over the Hindu Kush for Northwestern HMA ARs. This increases transport of moisture to the high latitudes during Western and Northwestern HMA ARs, increasing precipitation in the Karakoram and Hindu Kush during Western HMA ARs and increasing precipitation in the Pamir region during Northwestern HMA ARs. While the upper-level blocking during El Niño is an important difference, the increased IVT in the higher latitudes during El Niño compared to La Niña indicates that the increased Northwestern HMA AR frequency seems influenced by atmospheric conditions that favor the enhancement in water vapor transport to relatively higher latitudes.

The positive (negative) phase of AO is characterized by negative (positive) 1000 hPa geopotential height anomalies in the Arctic and two zonal bands of positive (negative) 1000 hPa geopotential height anomalies in the midlatitudes, over the Pacific and Atlantic Oceans (Thompson & Wallace, 1998). Positive AO conditions encourage stronger upper-level westerlies, enhanced polar circulation, and the jet stream is typi-

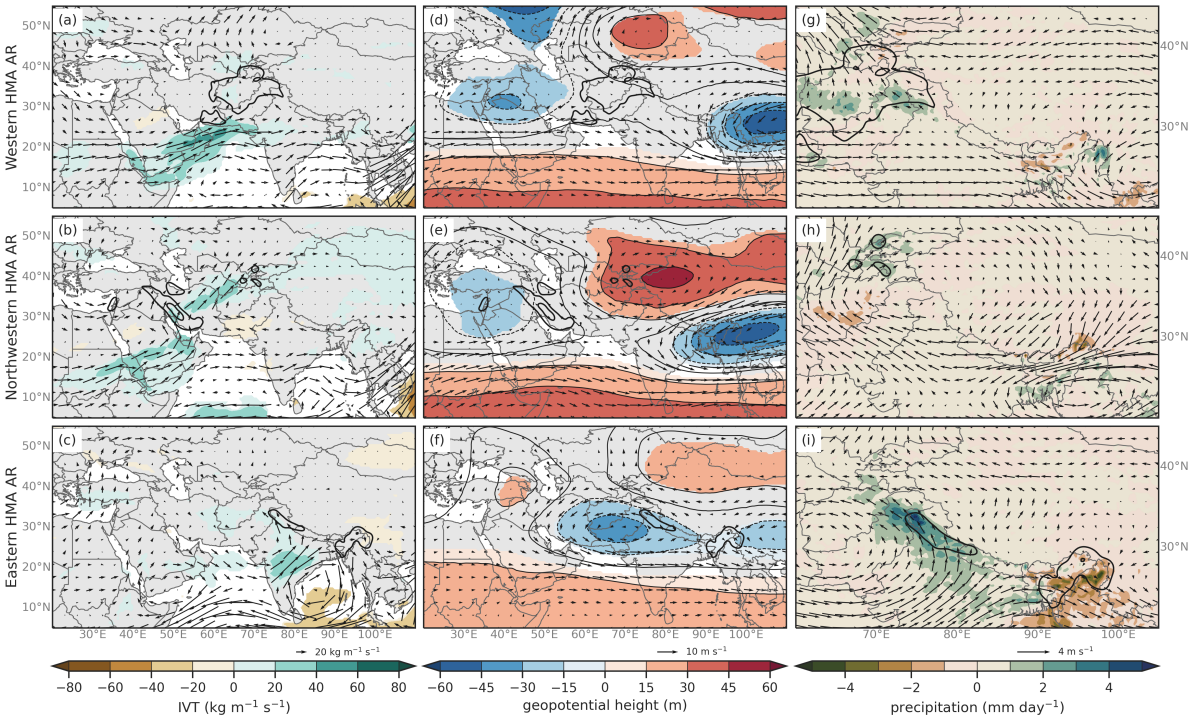

Figure 3.9: (a) Composite differences of IVT (shaded and vectors, kg m^{-1} s^{-1}) for Western HMA AR (Type 1) El Niño and La Niña conditions. Only differences in IVT that are considered at or above the 95% confidence level are shaded. (b) Same as (a) but for Northwestern HMA ARs (Type 2). (c) Same as (a) but for Eastern HMA ARs (Type 3). (d) Composite differences of 250 hPa geopotential heights (shaded and contours, m) and winds (vectors, m s^{-1}) between HMA AR days for Western HMA AR (Type 1) El Niño and La Niña conditions based on ERA5 for 1979-2019. Only differences in heights that are considered at or above the 95% confidence level are shaded. (e) Same as (d) but for Northwestern HMA ARs (Type 2). (f) Same as (d) but for Eastern HMA ARs (Type 3). (g) Composite differences of precipitation (shaded, mm day^{-1}) and 500 hPa wind direction (vectors, m s^{-1}) for Western HMA ARs (Type 1) El Niño and La Niña conditions. (h) Same as (g) but for Northwestern HMA ARs (Type 2). (i) Same as (g) but for Eastern HMA ARs (Type 3). The thick black contours in all plots are showing the mean anomaly composite rainfall (mm day^{-1}) for their respective AR Type with intervals at 2 mm day^{-1}, 6 mm day^{-1}, and 10 mm day^{-1}.

cally located further poleward. Cannon et al. (2015) showed that in HMA, positive AO conditions are associated with a poleward shift of the eastern extent of the subtropical jet, and an increase in magnitude in the jet to the west of the Karakoram. They indicated a strong positive relationship between the positive phase of AO and increased 200 hPa zonal winds in the midlatitudes. These increased zonal winds modify the jet position and increase WWD activity and precipitation over HMA (Cannon et al., 2015). Increased precipitation in northwest India during the positive phase of AO has also been noted by other studies (Thapa et al., 2018; Yadav et al., 2009). The negative phase of AO is usually associated with a weaker polar vortex and weaker upper-level westerlies that allows the jet stream to undulate more, increasing cold air advection from the Arctic and has been attributed to increased storminess in the midlatitudes (Cannon et al., 2015).

Z scores for differences in proportion of frequency of HMA ARs during AO+ and AO- conditions compared to neutral conditions indicate that Western and Nortwestern HMA ARs are significantly more frequent during positive AO conditions and less frequent during negative AO conditions compared to neutral. This is consistent with Guan and Waliser (2015), which found increased AR frequency over southwest Asia during the positive phase of AO, where Western and Northwestern HMA ARs typically enhance precipitation. Eastern HMA ARs are significantly less frequent during both AO+ and AO- conditions. Difference composites of 250 hPa geopotential height and winds, IVT, precipitation, and 500 hPa winds are shown in Fig. 3.10 for AO+ and AO-. All three AR types show increases in water vapor content between 20-40 kg m^{-1} s^{-1} along southwest Asia that could be attributed to an anticyclonic anomaly over the Arabian Sea (Fig. 3.10a-f). This may increase the amount of precipitation in the Karakoram and western Himalayas for Western and Eastern HMA ARs during AO+ conditions compared to AO- (see Fig. 3.10g, i). However, the anomalous trough and associated cyclonic circula-

tion near the Tien Shan region during Western ARs implies higher than average wind speeds potentially increase precipitation in the Tien Shan during AO+ compared to AO- conditions (see Fig. 3.10g). The location of the ridges and troughs during AO+ compared to AO- and the lower difference in IVT suggests that dynamics (likely through enhanced orographic lifting caused by strong winds) play a more important role than thermodynamics (increase in water vapor content) in influencing AR frequency during AO conditions.

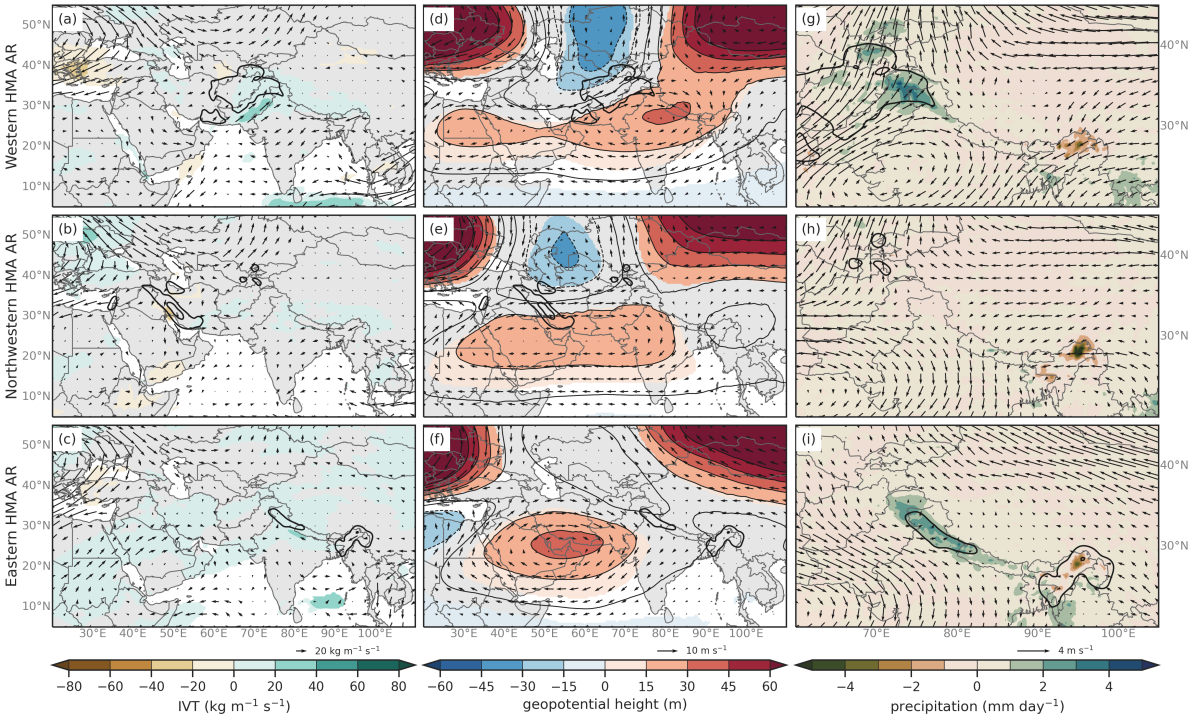

Figure 3.10: Same as Fig. 3.9, but for AO+ and AO- conditions.

The Siberian High is a high-pressure center located in the northeastern part of Eurasia that has been shown to strongly influence processes from surface temperatures to the middle troposphere and thus the climate in middle to high Eurasia during winter (Gong & Ho, 2002; Gong et al., 2001; Wu & Wang, 2002). Weakening of the SH encourages disturbances in the weaker subtropical jet, allowing for WWD to propagate

toward HMA, increasing precipitation in Central Himalayas (Cannon et al., 2015; Cohen & Entekhabi, 1999; Wu & Wang, 2002). Rana et al. (2019) shows that ridging that extends into central Asia and Europe during SH+ blocks eastward propagating westerly storm system, and restricts westerly flow to more southerly latitudes, resulting in increased precipitation in the southern region of Central Southwest Asia. Gong and Ho (2002) found that the SH explains 24% of the interannual variance in surface temperature over Eurasia, while AO explains roughly 30% of the variance, and that there are strong connections between AO and SH. They also found that 26% of precipitation variance over Eurasia was explained by AO, SH, and a few other prominent Eurasian climate modes, 9.8% of which SH contributed (Gong & Ho, 2002). They conclude that after AO, the Siberian High is the second most important influence on temperature and precipitation in Eurasia, making it important to understand the influence of SH on HMA AR frequency.

Table 1 indicates that Western and Northwestern HMA ARs are significantly more frequent during SH- compared to neutral. Figure 3.11a shows a significant decrease in water vapor content along the western basin of the Arabian Sea that is associated with enhanced ridging over Saudi Arabia during SH+ compared to SH negative during Western and Northwestern HMA ARs (Fig. 3.11b, e). Additionally, there is an increase in the magnitude of northwesterly winds around the Western Himalayas that would potentially decrease precipitation in these regions in SH+ compared to SH- (see Fig. 3.11g). Eastern HMA ARs are more frequent during SH+ compared to neutral (see Table 3.1), which is attributed to an anticyclonic anomaly in IVT over the Bay of Bengal increasing precipitation in Eastern Himalayas during SH+ conditions (see Fig. 3.11c, i).

The MJO, which is the primary mode of intraseasonal variability in the tropics (Madden & Julian, 1971, 1972), has been shown to influence precipitation and circulation

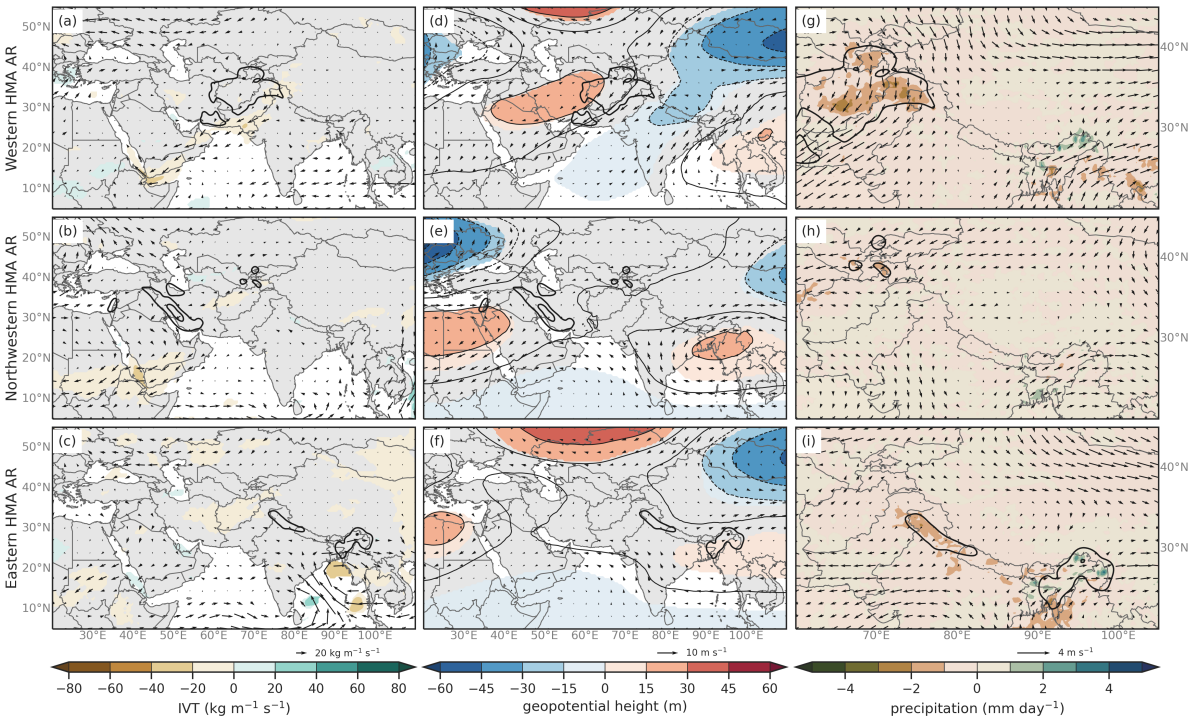

Figure 3.11: Same as Fig. 3.9, but for SH+ and SH- conditions.

regimes in HMA as well as ARs across the globe by forcing a Rossby wave response due to changes in convection and diabatic heating (Barlow et al., 2005; Cannon et al., 2017; Guan & Waliser, 2015; Guan et al., 2012; Ralph & Dettinger, 2011). Cannon et al. (2017) found that the MJO modifies the circulation and moisture availability within WWD, but no one phase favors extreme precipitation in High Mountain Asia. Guan and Waliser (2015) found that AR frequency increased in southwest Asia during NDJFM for MJO phases 1, 2, and 8 and only increased precipitation in HMA only during phase 8. They also found that AR frequency in southern Asia decreased significantly during MJO phases 4 and 5 with decreased precipitation in HMA during phase 5. According to z-scores from differences in proportion of HMA ARs, Eastern and Northwestern HMA ARs are less frequent when there is any active MJO phase compared to when there is no active MJO phase and Western HMA ARs are more frequent during any active

MJO phase, but no significant differences were found (see Table 3.1). Examining each MJO phase as well as the differences in circulation and water vapor did not yield any significant results. Although previous studies with distinct methodologies (Barlow et al., 2005; Cannon et al., 2017) have suggested links between the MJO and extreme precipitation in HMA, our results did not point to any strong connection in HMA AR frequency and MJO phase. Understanding the complexities of the impact of MJO on ARs is beyond the scope of this current analysis, and future work is needed to make significant conclusions on MJO and HMA ARs.

3.5 Discussion and Conclusions

The objective of this research was to identify the climatology of ARs that influence HMA and investigate their linkages with large-scale circulation and precipitation patterns in the winter and spring seasons. Using ERA5 reanalysis and a global AR catalog, this study revealed the climatology of ARs that reach HMA, and their relationship with precipitation regimes in southern Asia using combined EOF analysis with k-means clustering. While there is on average little to no vapor flux in Southern Asia during the winter and spring seasons, enhanced IVT during HMA ARs results in roughly 40-60% of the total seasonal precipitation. Three AR subtypes penetrate far inland across Southern Asia, reach HMA during the winter and spring, and result in different precipitation patterns.

The three AR types are delineated by the location of their above-average precipitation. Western HMA ARs are associated with low geopotential heights directly north of the Arabian Sea that results in enhanced IVT and increased precipitation in Western Himalayas and the Karakoram. IVT composites for Western HMA ARs identify an anticyclonic circulation center over the Arabian Sea that is responsible for transporting

water vapor poleward. Northwestern HMA ARs are characterized by a tilted trough axis and increased IVT that reaches as far as 40°N that increases precipitation in the Hindu Kush and the Pamirs. IVT during Northwestern HMA ARs has an anticyclonic circulation that covers most of the Arabian Sea and India. Eastern HMA ARs are associated with southwesterly moisture flux across the Bay of Bengal that results in above-average precipitation in Eastern Himalaya. Specifically, Eastern HMA ARs are associated with upper-level cyclonic circulation over the Tibetan Plateau and source moisture from the Arabian Sea and the Bay of Bengal regions related to anti-cyclonic circulation. Northwestern HMA ARs transition into Western HMA ARs 24% of the time, and Western HMA ARs transition into Eastern HMA ARs 18% of the time, indicating that while each subtype has its own unique characteristics, they are not all completely independent. Additionally roughly 15% of the time for any given AR type, there is a second AR located in the Southern Asia region. For example, if there is a Northwestern or Western HMA AR, there can also be an Eastern HMA AR 15% of the time, explaining the precipitation signatures in Eastern and Western HMA for all three synoptic composites.

Between 1979 and 2017, all three AR types have a history of being associated with extreme rainfall that can trigger flooding and/or landslide events that severely impacted the region. For example, in April 2016, an extreme rainfall event associated with a Northwestern HMA AR led to the occurrence of heavy flooding, lightning, and landslides in Kohistan, Pakistan, which resulted in over 100 fatalities (Kirschbaum et al., 2010). At least 56 landslides in the Global Landslide Catalog were associated with all three types of ARs (Kirschbaum et al., 2010). However, more landslides and extreme rainfall events may have been associated with HMA ARs, and a more thorough fine-scale analysis is needed to understand the meteorological influence of ARs on these extreme events.

This research further examined the relationship between HMA ARs and large-scale

climate modes such as the ENSO, AO, and SH. The relationships between these modes and HMA ARs are complex, but we find evidence that Western and Northwestern HMA ARs are more frequent during El Niño, AO+, and SH- conditions. We also described the impacts of each climate mode on the broader circulation and water vapor patterns in this region. Increased frequency in Western and Northwestern HMA ARs during El Niño and AO+ is attributed to the location of the wave train, identified by signatures in the upper-level jet. During El Niño compared to La Niña, precipitation and IVT are more likely to be higher than average for both Western and Northwestern HMA ARs. During AO+ compared to AO-, precipitation is likely to increase in the Karakoram and Pamirs, but decrease in Eastern Himalayas. During SH+ compared to SH-, precipitation is likely to decrease in the Hindu Kush and Pamirs regions while increasing in the Eastern Himalayan regions. During SH+, an upper-level ridge over Southwest Asia can block eastward propagating westerlies, which can funnel upper-level winds to a more equatorward track and encourages precipitation to the east of the Karakoram. Relationships between climate modes further complicate these results and the understanding of their influence on circulation patterns. For example, during the winter and spring months in the 40 years of the study, there were only 25 days where an El Niño occurred without the influence of a different climate mode (e.g. AO or SH). While it is very clear that different climate modes influence the frequency of all three types of ARs, future work should consider exploring the influence of ENSO, AO, and the SH on HMA ARs.

This work quantified the contribution of HMA ARs to winter and spring precipitation and illustrates the importance of ARs to the hydrological cycle in HMA by determining the regional climatology of ARs in HMA, as well as exploring the dynamical processes that relate ARs to precipitation regimes in Southern Asia. In addition to our findings regarding conditions of three different ARs and their interactions with

the HMA, our research points to a broader consideration: the importance of studying ARs in novel sites where ARs penetrate inland and can contribute greatly to the regional hydroclimate. The characterization of the HMA AR subtypes can be applied to future work to examine the mesoscale and thermodynamic characteristics of HMA ARs and exploring the long-term changes in the large-scale dynamics related to ARs. This can be used to uncover the relationship between ARs and local hazards such as landslides, floods, and other influences on HMA climate. Future modeling work to improve forecasting skill for ARs in this region could benefit from knowing the synoptic characteristics associated with each type of HMA AR and their potential impacts on regional precipitation. Understanding the role of ARs in local hydrology and the large-scale dynamics driving the ARs inland is critical to minimize uncertainty regarding the future of water resources in Southern Asia.

3.6 Declarations

3.6.1 Funding

This research was supported by NASA Headquarters under the NASA Earth and Space Science Fellowship Program - Grant 80NSSC18K1412.

3.6.2 Conflicts of interest/Competing Interests

The authors declare that they have no conflict of interest.

3.6.3 Availability of data and material

The AR data were provided by Bin Guan via https://ucla.box.com/ARcatalog. Development of the AR detection algorithm and databases was supported by NASA. ERA5 data on single levels (Hersbach et al., 2018b) and pressure levels (Hersbach et al., 2018a) were downloaded from the Copernicus Climate Change Service (C3S) Climate Data Store. The results contain modified Copernicus Climate Change Service information 2020. Neither the European Commission nor ECMWF is responsible for any use that may be made of the Copernicus information or data it contains. MERRA2 data (Gelaro et al., 2017; Global Modeling and Assimilation Office (GMAO), 2015), IMERG-PM v06 data (Huffman et al., 2019), APRHODITE data (Maeda et al., 2020; Yatagai et al., 2012) and NOAA topography data (Amante & Eakins, 2009) are all freely available online. The ENSO and AO indices were calculated by the National Weather Service Climate Prediction Center and can be found at https://cpc.ncep.noaa.gov/ENSO and https://www.cpc.ncep.noaa.gov/AO. The SH index was calculated using ERA5 mean sea level pressure data and the methods outlined in Panagiotopoulos et al. (2005). The MJO-RMM index can be found at http://www.bom.gov.au (Wheeler & Hendon, 2004). The MJO index referenced in Jones (2009) was provided by Charles Jones. The Westerly Disturbance Catalog from Hunt et al. (2018) can be found in the CEDA archive (Turner & Hunt, 2019). The Global Landslide Catalog is from Kirschbaum et al. (2010), Kirschbaum et al. (2015).

3.6.4 Code availability

The code for this analysis can be found at https://github.com/dlnash/AR_types.

3.6.5 Authors' contributions

DN conceptualized this article and participated in data collection, analysis, interpretation, and drafting of the article. LC participated in data interpretation and revision of the article. All authors participated in the revision and final version of the article.

3.6.6 Acknowledgements

The authors would like to thank Tessa Montini at University of California, Santa Barbara for feedback into these events. We would also like to thank the three anonymous reviewers for the comments and suggestions, which greatly improved the manuscript.

References

Akbary, M., Salimi, S., Hosseini, S. A., & Hosseini, M. (2019). Spatio-temporal changes of atmospheric rivers in the Middle East and North Africa region. *International Journal of Climatology*, *39*, 3976–3986. https://doi.org/10.1002/JOC.6052

Amante, C., & Eakins, B. W. (2009). ETOPO1 arc-minute global relief model: procedures, data sources and analysis. *NOAA Technical Memorandum NESDIS NGDC-24. National Geophysical Data Center, NOAA*. https://doi.org/10.7289/V5C8276M

Andermann, C., Bonnet, S., & Gloaguen, R. (2011). Evaluation of precipitation data sets along the Himalayan front. *Geochemistry, Geophysics, Geosystems*, *12*(7), 1–16. https://doi.org/10.1029/2011GC003513

Archer, D. R., & Fowler, H. J. (2004). Spatial and Temporal Variations in Precipitation in the Upper Indus Basin, Global Teleconnections and Hydrological Implications. *Hydrology and Earth System Sciences*, *8*(1), 47–61. https://doi.org/https://hal.archives-ouvertes.fr/hal-00304788

Baggett, C., Lee, S., & Feldstein, S. (2016). An investigation of the presence of atmospheric rivers over the North Pacific during planetary-scale wave life cycles and their role in Arctic warming. *Journal of the Atmospheric Sciences*, *73*(11), 4329–4347. https://doi.org/10.1175/JAS-D-16-0033.1

Barlow, M., Wheeler, M., Lyon, B., & Cullen, H. (2005). Modulation of Daily Precipitation over Southwest Asia by the Madden–Julian Oscillation. *Monthly Weather Review*, *133*(12), 3579–3594. https://doi.org/10.1175/MWR3026.1

Behrangi, A., Guan, B., Neiman, P. J., Schreier, M., & Lambrigtsen, B. (2016). On the Quantification of Atmospheric Rivers Precipitation from Space: Composite Assessments and Case Studies over the Eastern North Pacific Ocean and the Western United States. *Journal of Hydrometeorology*, *17*(1), 369–382. https://doi.org/10.1175/jhm-d-15-0061.1

Blamey, R. C., Ramos, A. M., Trigo, R. M., Tomé, R., & Reason, C. J. (2018). The Influence of Atmospheric Rivers over the South Atlantic on Winter Rainfall in South Africa. *Journal of Hydrometeorology*, *19*(1), 127–142. https://doi.org/10.1175/JHM-D-17-0111.1

Bolch, T., Kulkarni, A., Kääb, A., Huggel, C., Paul, F., Cogley, J. G., Frey, H., Kargel, J. S., Fujita, K., Scheel, M., Barjracharya, S., & Stoffel, M. (2012). The State and Fate of Himalayan Glaciers. *Science*, *336*(6079), 310–314. https://doi.org/10.1126/science.1215828

Bookhagen, B., & Burbank, D. W. (2010). Toward a complete Himalayan hydrological budget: Spatiotemporal distribution of snowmelt and rainfall and their impact on river discharge. *Journal of Geophysical Research: Earth Surface*, *115*(3), 1–25. https://doi.org/10.1029/2009JF001426

Bozkurt, D., Rondanelli, R., Marín, J. C., & Garreaud, R. (2018). Foehn Event Triggered by an Atmospheric River Underlies Record-Setting Temperature Along Continental Antarctica. *Journal of Geophysical Research: Atmospheres*, *123*(8), 3871–3892. https://doi.org/10.1002/2017JD027796

Cannon, F., Carvalho, L. M., Jones, C., Hoell, A., Norris, J., Kiladis, G. N., & Tahir, A. A. (2017). The influence of tropical forcing on extreme winter precipitation in the western Himalaya. *Climate Dynamics*, *48*(3-4), 1213–1232. https://doi.org/10.1007/s00382-016-3137-0

Cannon, F., Carvalho, L. M., Jones, C., & Norris, J. (2016). Winter westerly disturbance dynamics and precipitation in the western Himalaya and Karakorum: a wave-tracking approach. *Theoretical and Applied Climatology*, *125*, 27–44. https://doi.org/10.1007/s00704-015-1489-8

Cannon, F., Carvalho, L. M., Jones, C., & Bookhagen, B. (2015). Multi-annual variations in winter westerly disturbance activity affecting the Himalaya. *Climate Dynamics*, *44*(1-2), 441–455. https://doi.org/10.1007/s00382-014-2248-8

Carvalho, L. M. V., Norris, J., Cannon, F., & Jones, C. (2020). Climate Variability and Extreme Weather in High Mountain Asia: Observation and Modelling. *Himalayan weather and climate and their impact on the environment* (pp. 109–117). Springer. https://doi.org/https://doi.org/10.1007/978-3-030-29684-1{_}7

Carvalho, L. M., Jones, C., Cannon, F., & Norris, J. (2016). Intraseasonal-to-Interannual Variability of the Indian Monsoon Identified with the Large-Scale Index for the

Indian Monsoon System (LIMS). *Journal of Climate*, *29*(8), 2941–2962. https://doi.org/10.1175/jcli-d-15-0423.1

Cheng, X., & Wallace, J. M. (1993). Cluster Analysis of the Northern Hemisphere Wintertime 500-hPa Height Field: Spatial Patterns. *Journal of the Atmospheric Sciences*, *50*(16), 2674–2696. https://doi.org/10.1175/1520-0469(1993)050<2674:CAOTNH>2.0.CO;2

Cohen, J., & Entekhabi, D. (1999). Eurasian snow cover variability and Northern Hemisphere climate predictability. *Geophysical Research Letters*, *26*(3), 345–348. https://doi.org/10.1029/1998GL900321

Cordeira, J. M., Ralph, F., & Moore, B. J. (2013). The development and evolution of two atmospheric rivers in proximity to western north pacific tropical cyclones in october 2010. *Monthly Weather Review*, *141*(12), 4234–4255. https://doi.org/10.1175/MWR-D-13-00019.1

Dacre, H. F., Clark, P. A., Martinez-Alvarado, O., Stringer, M. A., & Lavers, D. A. (2015). How do atmospheric rivers form? *Bulletin of the American Meteorological Society*, *96*(8), 1243–1255. https://doi.org/10.1175/BAMS-D-14-00031.1

Dettinger, M. D. (2011). Climate change, atmospheric rivers, and floods in California - a multimodel analysis of storm frequency and magnitude changes. *JAWRA Journal of the American Water Resources Association*, *47*(3), 514–523. https://doi.org/10.1111/j.1752-1688.2011.00546.x

Dezfuli, A. (2020). Rare Atmospheric River Caused Record Floods across the Middle East. *Bulletin of the American Meteorological Society*, *101*(4), E394–E400. https://doi.org/10.1175/BAMS-D-19-0247.1

Duan, K., Yao, T., & Thompson, L. G. (2006). Response of monsoon precipitation in the Himalayas to global warming. *Journal of Geophysical Research: Atmospheres*, *111*(D19). https://doi.org/10.1029/2006JD007084

Filippi, L., Palazzi, E., Hardenberg, J. v., & Provenzale, A. (2014). Multidecadal Variations in the Relationship between the NAO and Winter Precipitation in the Hindu Kush–Karakoram. *Journal of Climate*, *27*(20), 7890–7902. https://doi.org/10.1175/JCLI-D-14-00286.1

Forsythe, N., Fowler, H. J., Li, X.-F., Blenkinsop, S., & Pritchard, D. (2017). Karakoram temperature and glacial melt driven by regional atmospheric circulation variability. *Nature Climate Change 2017 7:9*, *7*(9), 664–670. https://doi.org/10.1038/nclimate3361

Gardelle, J., Berthier, E., & Arnaud, Y. (2012). Slight mass gain of Karakoram glaciers in the early twenty-first century. *Nature Geoscience*, *5*, 322–325. https://doi.org/10.1038/NGEO1450

Gelaro, R., McCarty, W., Suárez, M. J., Todling, R., Molod, A., Takacs, L., Randles, C. A., Darmenov, A., Bosilovich, M. G., Reichle, R. H., Wargan, K., Coy, L., Cullather, R., Draper, C., Akella, S., Buchard, V., Conaty, A., da Silva, A. M., Gu, W., ... Zhao, B. (2017). The Modern-Era Retrospective Analysis for Research and Applications, Version 2 (MERRA-2). *Journal of Climate*, *30*(14), 5419–5454. https://doi.org/10.1175/jcli-d-16-0758.1

Global Modeling and Assimilation Office (GMAO). (2015). MERRA-2 inst6_3d_ana_Np: 3d, 6-Hourly, Instantaneous, Pressure-Level, Analysis, Analyzed Meteorological Fields V5.12.4. https://doi.org/10.5067/A7S6XP56VZWS

Gong, D. Y., & Ho, C. H. (2002). The Siberian High and climate change over middle to high latitude Asia. *Theoretical and Applied Climatology*, *72*(1-2), 1–9. https://doi.org/10.1007/s007040200008

Gong, D. Y., Wang, S. W., & Zhu, J. H. (2001). East Asian winter monsoon and Arctic Oscillation. *Geophysical Research Letters*, *28*(10), 2073–2076. https://doi.org/10.1029/2000GL012311

Gorodetskaya, I. V., Tsukernik, M., Claes, K., Ralph, F., Neff, W. D., & Van Lipzip, N. P. M. (2014). The role of atmospheric rivers in anomalous snow accumulation in East Antarctica. *Geophysical Research Letters*, *41*, 6199–6206. https://doi.org/10.1002/2014GL060881

Gorodetskaya, I. V., Silva, T., Schmithüsen, H., & Hirasawa, N. (2020). Atmospheric River Signatures in Radiosonde Profiles and Reanalyses at the Dronning Maud Land Coast, East Antarctica. *Advances in Atmospheric Sciences*, *37*(5), 455–476. https://doi.org/10.1007/s00376-020-9221-8

Goswami, B. N., & Mohan, R. S. A. (2001). Intraseasonal oscillations and interannual variability of the Indian summer monsoon. *Journal of Climate*, *14*(6), 1180–1198. https://doi.org/https://doi.org/10.1175/1520-0442(2001)014<1180:IOAIVO>2.0.CO;2

Guan, B., Molotch, N. P., Waliser, D. E., Fetzer, E. J., & Neiman, P. J. (2010). Extreme snowfall events linked to atmospheric rivers and surface air temperature via satellite measurements. *Geophysical Research Letters*, *37*(20), n/a–n/a. https://doi.org/10.1029/2010gl044696

Guan, B., Molotch, N. P., Waliser, D. E., Fetzer, E. J., & Neiman, P. J. (2013). The 2010/2011 snow season in California's Sierra Nevada: Role of atmospheric rivers and modes of large-scale variability. *Water Resources Research*, *49*(10), 6731–6743. https://doi.org/10.1002/wrcr.20537

Guan, B., & Waliser, D. E. (2015). Detection of atmospheric rivers: Evaluation and application of an algorithm for global studies. *Journal of Geophysical Research: Atmospheres*, *120*(24), 12514–12535. https://doi.org/10.1002/2015jd024257

Guan, B., & Waliser, D. E. (2017). Atmospheric rivers in 20 year weather and climate simulations: A multimodel, global evaluation. *Journal of Geophysical Research*, *122*, 5556–5581. https://doi.org/10.1002/2016JD026174

Guan, B., Waliser, D. E., Molotch, N. P., Fetzer, E. J., & Neiman, P. J. (2012). Does the Madden-Julian Oscillation Influence Wintertime Atmospheric Rivers and Snowpack in the Sierra Nevada? *Monthly Weather Review*, *140*, 325–342. https://doi.org/10.1175/MWR-D-11-00087.1

Guan, B., Waliser, D. E., & Ralph, F. (2018). An intercomparison between reanalysis and dropsonde observations of the total water vapor transport in individual atmospheric rivers. *Journal of Hydrometeorology*, *19*(2), 321–337. https://doi.org/10.1175/jhm-d-17-0114.1

Guan, B., & Waliser, D. E. (2019). Tracking Atmospheric Rivers Globally: Spatial Distributions and Temporal Evolution of Life Cycle Characteristics. *Journal of Geophysical Research: Atmospheres*, *124*, 12523–12552. https://doi.org/10.1029/2019JD031205

Hegyi, B. M., & Taylor, P. C. (2018). The Unprecedented 2016–2017 Arctic Sea Ice Growth Season: The Crucial Role of Atmospheric Rivers and Longwave Fluxes. *Geophysical Research Letters*, *45*(10), 5204–5212. https://doi.org/10.1029/2017GL076717

Hersbach, H., Bell, B., Berrisford, P., Biavati, G., Horányi, A., Muñoz Sabater, J., Nicolas, J., Peubey, C., Radu, R., Rozum, I., Schepers, D., Simmons, A., Soci, C., Dee, D., & Thépaut, J.-N. (2018a). ERA5 hourly data on pressure levels from 1979 to present. https://doi.org/10.24381/cds.bd0915c6

Hersbach, H., Bell, B., Berrisford, P., Biavati, G., Horányi, A., Muñoz Sabater, J., Nicolas, J., Peubey, C., Radu, R., Rozum, I., Schepers, D., Simmons, A., Soci, C., Dee, D., & Thépaut, J.-N. (2018b). ERA5 hourly data on single levels from 1979 to present. https://doi.org/10.24381/cds.adbb2d47

Hersbach, H., Bell, B., Berrisford, P., Hirahara, S., Horányi, A., Muñoz-Sabater, J., Nicolas, J., Peubey, C., Radu, R., Schepers, D., Simmons, A., Soci, C., Abdalla, S., Abellan, X., Balsamo, G., Bechtold, P., Biavati, G., Bidlot, J., Bonavita, M., ... Thépaut, J. N. (2020). The ERA5 global reanalysis. *Quarterly Journal of the Royal Meteorological Society*, *146*(730), 1999–2049. https://doi.org/10.1002/qj.3803

Hewitt, K. (2005). The Karakoram Anomaly? Glacier Expansion and the 'Elevation Effect,' Karakoram Himalaya. *Mountain Research and Development*, *25*(4), 332–341. https://doi.org/10.1659/0276-4741(2005)025[0332:TKAGEA]2.0.CO;2

Huffman, G. J., Stocker, E. F., Bolvin, D. T., Nelkin, E. J., & Tan, J. (2019). GPM IMERG Final Precipitation L3 Half Hourly 0.1 degree x 0.1 degree V06 (A. Savtchenko,

Ed.). *Greenbelt, MD, Goddard Earth Sciences Data and Information Services Center (GES DISC)*. https://doi.org/10.5067/GPM/IMERG/3B-HH/05

Huffman, G. J., Bolvin, D. T., Braithwaite, D., Hsu, K.-L., Joyce, R. J., Kidd, C., Nelkin, E. J., Sorooshian, S., Stocker, E. F., Tan, J., Wolff, D. B., & Xie, P. (2020). Integrated Multi-satellite Retrievals for the Global Precipitation Measurement (GPM) Mission (IMERG). In V. Levizzani, C. Kidd, D. B. Kirschbaum, C. D. Kummerow, K. Nakamura, & F. J. Turk (Eds.), *Satellite precipitation measurement: Volume 1* (pp. 343–353). Springer International Publishing. https://doi.org/10.1007/978-3-030-24568-9{_}19

Hunt, K. M., Turner, A. G., & Shaffrey, L. C. (2018). The evolution, seasonality and impacts of western disturbances. *Quarterly Journal of the Royal Meteorological Society*, *144*(710), 278–290. https://doi.org/10.1002/qj.3200

Jones, C. (2009). A homogeneous stochastic model of the Madden–Julian oscillation. *Journal of Climate*, *22*(12), 3270–3288. https://doi.org/10.1175/2008JCLI2609.1

Kääb, A., Berthier, E., Nuth, C., Gardelle, J., & Arnaud, Y. (2012). Contrasting patterns of early twenty-first-century glacier mass change in the Himalayas. *Nature*, *488*, 495–498. https://doi.org/10.1038/nature11324

Kingston, D. G., Lavers, D. A., & Hannah, D. M. (2016). Floods in the Southern Alps of New Zealand: the importance of atmospheric rivers. *Hydrological Processes*, *30*(26), 5063–5070. https://doi.org/10.1002/hyp.10982

Kirschbaum, D., Adler, R., Hong, Y., Hill, S., & Lerner-Lam, A. (2010). A global landslide catalog for hazard applications: Method, results, and limitations. *Natural Hazards*, *52*, 561–575. https://doi.org/10.1007/S11069-009-9401-4/TABLES/3

Kirschbaum, D., Stanley, T., & Zhou, Y. (2015). Spatial and temporal analysis of a global landslide catalog. *Geomorphology*, *249*, 4–15. https://doi.org/10.1016/j.geomorph.2015.03.016

Kirschbaum, D., Watson, C. S., Rounce, D. R., Shugar, D. H., Kargel, J. S., Haritashya, U. K., Amatya, P., Shean, D., Anderson, E. R., & Jo, M. (2019). The State of Remote Sensing Capabilities of Cascading Hazards Over High Mountain Asia. *Frontiers in Earth Science*, *7*(197), 1–37. https://doi.org/10.3389/FEART.2019.00197

Krishnamurti, T. N., & Bhalme, H. N. (1976). Oscillations of a monsoon system. Part I. Observational aspects. *Journal of the Atmospheric Sciences*, *33*(10), 1937–1954. https://doi.org/https://doi.org/10.1175/1520-0469(1976)033<1937:OOAMSP>2.0.CO;2

Krishnan, R., Sabin, T. P., Ayantika, D. C., Kitoh, A., Sugi, M., Murakami, H., Turner, A. G., Slingo, J. M., & Rajendran, K. (2013). Will the South Asian monsoon

overturning circulation stabilize any further? *Climate Dynamics*, *40*(1-2), 187–211. https://doi.org/10.1007/s00382-012-1317-0

Lang, T. J., & Barros, A. P. (2004). Winter storms in the central Himalayas. *Journal of the Meteorological Society of Japan*, *82*(3), 829–844. https://doi.org/10.2151/jmsj.2004.829

Lavers, D. A., & Villarini, G. (2013). The nexus between atmospheric rivers and extreme precipitation across Europe. *Geophysical Research Letters*, *40*(12), 3259–3264. https://doi.org/10.1002/grl.50636

Lora, J. M., Shields, C. A., & Rutz, J. J. (2020). Consensus and Disagreement in Atmospheric River Detection: ARTMIP Global Catalogues. *Geophysical Research Letters*, *47*(20), e2020GL089302. https://doi.org/10.1029/2020GL089302

Ma, W., Chen, G., & Guan, B. (2020). Poleward Shift of Atmospheric Rivers in the Southern Hemisphere in Recent Decades. *Geophysical Research Letters*, *47*(21), e2020GL089934. https://doi.org/10.1029/2020GL089934

Madden, R. A., & Julian, P. R. (1971). Detection of a 40-50 Day Oscillation in the Zonal Wind in the Tropical Pacific. *Journal of the Atmospheric Sciences*, *28*(5), 702–708. https://doi.org/10.1175/1520-0469(1971)028<0702:doadoi>2.0.co;2

Madden, R. A., & Julian, P. R. (1972). Description of Global-Scale Circulation Cells in the Tropics with a 40-50 Day Period. *Journal of the Atmospheric Sciences*, *29*(6), 1109–1123. https://doi.org/10.1175/1520-0469(1972)029<1109:dogscc>2.0.co;2

Maeda, M., Yasutomi, N., Yatagai, A., & (Eds)., N. C. f. A. R. S. (2020). The Climate Data Guide: APHRODITE: Asian Precipitation - Highly-Resolved Observational Data Integration Towards Evaluation of Water Resources. https://climatedataguide.ucar.edu/climate-data/aphrodite-asian-precipitation-highly-resolved-observational-data-integration-towards

Maggioni, V., Meyers, P. C., & Robinson, M. D. (2016). A Review of Merged High-Resolution Satellite Precipitation Product Accuracy during the Tropical Rainfall Measuring Mission (TRMM) Era. *Journal of Hydrometeorology*, *17*, 1101–1117. https://doi.org/10.1175/JHM-D-15-0190.1

Massoud, E., Massoud, T., Guan, B., Sengupta, A., Espinoza, V., Luna, M. D., Raymond, C., & Waliser, D. (2020). Atmospheric Rivers and Precipitation in the Middle East and North Africa (MENA). *Water 2020, Vol. 12, Page 2863*, *12*(2863), 1–18. https://doi.org/10.3390/W12102863

Mattingly, K. S., Mote, T. L., & Fettweis, X. (2018). Atmospheric River Impacts on Greenland Ice Sheet Surface Mass Balance. *Journal of Geophysical Research: Atmospheres*, *123*(16), 8538–8560. https://doi.org/10.1029/2018JD028714

Mattingly, K. S., Mote, T. L., Fettweis, X., As, D. V., Tricht, K. V., Lhermitte, S., Pettersen, C., & Fausto, R. S. (2020). Strong summer atmospheric rivers trigger Greenland ice sheet melt through spatially varying surface energy balance and cloud regimes. *Journal of Climate*, *33*(16), 6809–6832. https://doi.org/10.1175/JCLI-D-19-0835.1

Mercer, A. E., Shafer, C. M., Doswell, C. A., Leslie, L. M., & Richman, M. B. (2012). Synoptic composites of tornadic and nontornadic outbreaks. *Monthly Weather Review*, *140*(8), 2590–2608. https://doi.org/10.1175/MWR-D-12-00029.1

Naoi, M., Kamae, Y., Ueda, H., & Mei, W. (2020). Impacts of Seasonal Transitions of ENSO on Atmospheric River Activity over East Asia. *Journal of the Meteorological Society of Japan*, *98*(3), 655–668. https://doi.org/10.2151/JMSJ.2020-027

Nash, D., Waliser, D. E., Guan, B., Ye, H., & Ralph, F. (2018). The Role of Atmospheric Rivers in Extratropical and Polar Hydroclimate. *Journal of Geophysical Research: Atmospheres*, *123*(13). https://doi.org/10.1029/2017JD028130

Neff, W. (2018). Atmospheric rivers melt Greenland. https://doi.org/10.1038/s41558-018-0297-4

Norris, J., Carvalho, L. M., Jones, C., & Cannon, F. (2018). Deciphering the contrasting climatic trends between the central Himalaya and Karakorum with 36 years of WRF simulations. *Climate Dynamics*, 1–22. https://doi.org/https://doi.org/10.1007/s00382-018-4133-3

Norris, J., Carvalho, L. M., Jones, C., Cannon, F., Bookhagen, B., Palazzi, E., & Tahir, A. A. (2017). The spatiotemporal variability of precipitation over the Himalaya: evaluation of one-year WRF model simulation. *Climate Dynamics*, *49*(5-6), 2179–2204. https://doi.org/10.1007/s00382-016-3414-y

Norris, J., Carvalho, L. M., Jones, C., & Cannon, F. (2020). Warming and drying over the central Himalaya caused by an amplification of local mountain circulation. *npj Climate and Atmospheric Science*, *3*(1), 1–11. https://doi.org/10.1038/s41612-019-0105-5

North, G. R. (1984). Empirical orthogonal functions and normal modes. *Journal of the Atmospheric Sciences*, *41*(5), 879–887. https://doi.org/10.1175/1520-0469(1984)041<0879:EOFANM>2.0.CO;2

Palazzi, E., Von Hardenberg, J., & Provenzale, A. (2013). Precipitation in the Hindu-Kush Karakoram Himalaya: Observations and future scenarios. *Journal of Geophysical Research Atmospheres*, *118*, 85–100. https://doi.org/10.1029/2012JD018697

Paltan, H., Waliser, D. E., Lim, W. H., Guan, B., Yamazaki, D., Pant, R., & Dadson, S. (2017). Global floods and water availability driven by atmospheric rivers. *Geophysical Research Letters*, *44*(20), 310–387. https://doi.org/10.1002/2017GL074882

Pan, M., & Lu, M. (2020). East Asia Atmospheric River catalog: Annual Cycle, Transition Mechanism, and Precipitation. *Geophysical Research Letters*, *47*, e2020GL089477. https://doi.org/10.1029/2020GL089477

Panagiotopoulos, F., Shahgedanova, M., Hannachi, A., & Stephenson, D. B. (2005). Observed Trends and Teleconnections of the Siberian High: A Recently Declining Center of Action. *Journal of Climate*, *18*(9), 1411–1422. https://doi.org/10.1175/JCLI3352.1

Peters, J. M., & Schumacher, R. S. (2014). Objective categorization of heavy-rain-producing MCS synoptic types by rotated principal component analysis. *Monthly Weather Review*, *142*(5), 1716–1737. https://doi.org/10.1175/MWR-D-13-00295.1

Prince, H. D., Cullen, N. J., Gibson, P. B., Conway, J., & Kingston, D. G. (2021). A climatology of atmospheric rivers in New Zealand. *Journal of Climate*, *34*(11), 4383–4402. https://doi.org/10.1175/jcli-d-20-0664.1

Ralph, F., & Dettinger, M. D. (2011). Storms, Floods, and the Science of Atmospheric Rivers. *EOS*, *92*(32), 13–14. https://doi.org/https://doi.org/10.1029/2011EO320001

Ralph, F., Neiman, P. J., Wick, G. A., Gutman, S. I., Dettinger, M. D., Cayan, D. R., & White, A. B. (2006). Flooding on California's Russian River: Role of atmospheric rivers. *Geophysical Research Letters*, *33*(13). https://doi.org/10.1029/2006gl026689

Ramos, A. M., Blamey, R. C., Algarra, I., Nieto, R., Gimeno, L., Tomé, R., Reason, C. J., & Trigo, R. M. (2019). From Amazonia to southern Africa: atmospheric moisture transport through low-level jets and atmospheric rivers. *Annals of the New York Academy of Sciences*, *1436*(1), 217–230. https://doi.org/10.1111/nyas.13960

Rana, S., Mcgregor, J., & Renwick, J. (2019). Dominant modes of winter precipitation variability over Central Southwest Asia and inter - decadal change in the ENSO teleconnection. *Climate Dynamics*, *53*, 5689–5707. https://doi.org/10.1007/s00382-019-04889-9

Reid, K. J., Rosier, S. M., Harrington, L. J., King, A. D., & Lane, T. P. (2021). Extreme rainfall in New Zealand and its association with Atmospheric Rivers. *Environmental Research Letters*, *16*(4), 44012. https://doi.org/10.1088/1748-9326/abeae0

Rivera, E. R., Dominguez, F., & Castro, C. L. (2014). Atmospheric Rivers and Cool Season Extreme Precipitation Events in the Verde River Basin of Arizona. *Journal of Hydrometeorology*, *15*, 813–829. https://doi.org/10.1175/JHM-D-12-0189.1

Rutz, J. J., Steenburgh, W. J., & Ralph, F. (2014). Climatological Characteristics of Atmospheric Rivers and Their Inland Penetration over the Western United States.

Monthly Weather Review, *142*, 905–921. https://doi.org/10.1175/MWR-D-13-00168.1

Rutz, J. J., Shields, C. A., Lora, J. M., Payne, A. E., Guan, B., Ullrich, P., O'Brien, T., Leung, L. R., Ralph, F., Wehner, M., Brands, S., Collow, A., Goldenson, N., Gorodetskaya, I., Griffith, H., Kashinath, K., Kawzenuk, B., Krishnan, H., Kurlin, V., ... Viale, M. (2019). The Atmospheric River Tracking Method Intercomparison Project (ARTMIP): Quantifying Uncertainties in Atmospheric River Climatology. *Journal of Geophysical Research: Atmospheres*, *124*(24), 13777–13802. https://doi.org/10.1029/2019JD030936

Rutz, J. J., Steenburgh, W. J., & Ralph, F. (2015). The inland penetration of atmospheric rivers over western North America: A Lagrangian analysis. *Monthly Weather Review*, *143*(5), 1924–1944. https://doi.org/10.1175/MWR-D-14-00288.1

Scherler, D., Bookhagen, B., & Strecker, M. R. (2011). Spatially variable response of Himalayan glaciers to climate change affected by debris cover. *Nature Geoscience*, *4*, 156–159. https://doi.org/10.1038/NGEO1068

Shields, C. A., Rutz, J. J., Leung, L. Y., Ralph, F., Wehner, M., Kawzenuk, B., Lora, J. M., McClenny, E., Osborne, T., Payne, A. E., Ullrich, P., Gershunov, A., Goldenson, N., Guan, B., Qian, Y., Ramos, A. M., Sarangi, C., Sellars, S., Gorodetskaya, I., ... Nguyen, P. (2018). Atmospheric River Tracking Method Intercomparison Project (ARTMIP): Project goals and experimental design. *Geoscientific Model Development*, *11*(6), 2455–2474. https://doi.org/10.5194/GMD-11-2455-2018

Singh, P., Ramasastri, K. S., & Kumar, N. (1995). Topographical influence on precipitation distribution in different ranges of western Himalayas. *Nordic Hydrology*, *26*(4-5), 259–284. https://doi.org/10.2166/nh.1995.0015

Smith, T., & Bookhagen, B. (2018). Changes in seasonal snow water equivalent distribution in High Mountain Asia (1987 to 2009). *Science advances*, *4*(1), e1701550. https://doi.org/10.1126/sciadv.1701550

Thapa, K., Endreny, T. A., & Ferguson, C. R. (2018). Atmospheric Rivers Carry Nonmonsoon Extreme Precipitation Into Nepal. *Journal of Geophysical Research: Atmospheres*, *123*, 5901–5912. https://doi.org/10.1029/2017JD027626

Thompson, D. W. J., & Wallace, J. M. (1998). The Arctic Oscillation signature in the wintertime geopotential height and temperature fields. *Geophysical Research Letters*, *25*(9), 1297–1300. https://doi.org/http://dx.doi.org/10.1029/98GL00950

Trenberth, K. E. (1997). The definition of el nino. *Bulletin of the American Meteorological Society*, *78*(12), 2771–2778. https://doi.org/10.1175/1520-0477(1997)078<2771:TDOENO>2.0.CO;2

Turner, A. G., & Hunt, K. (2019). BITMAP: Tracks of western disturbances (1979-2015), Centre for Environmental Data Analysis. https://doi.org/http://dx.doi.org/10.5285/233cf64c54e946e0bb691a07970ec245

Viale, M., & Nuñez, M. N. (2011). Climatology of Winter Orographic Precipitation over the Subtropical Central Andes and Associated Synoptic and Regional Characteristics. *Journal of Hydrometeorology*, *12*, 481–507. https://doi.org/10.1175/2010JHM1284.1

Viale, M., Valenzuela, R., & Garreaud, R. D. (2018). Impacts of Atmospheric Rivers on Precipitation in Southern South America. *Journal of Hydrometeorology*, *19*, 1671–1687. https://doi.org/10.1175/JHM-D-18-0006.1

Waliser, D. E., & Guan, B. (2017). Extreme winds and precipitation during landfall of atmospheric rivers. *Nature Geoscience*, *10*(3), 179–183. https://doi.org/10.1038/ngeo2894

Wang, B. (2006). *The Asian Monsoon*. Praxis Publishing.

Wernli, H., & Papritz, L. (2018). Role of polar anticyclones and mid-latitude cyclones for Arctic summertime sea-ice melting. *Nature Geoscience*, *11*, 108–113. https://doi.org/https://doi.org/10.1038/s41561-017-0041-0

Wheeler, M. C., & Hendon, H. H. (2004). An all-season real-time multivariate MJO index: Development of an index for monitoring and prediction. *Monthly weather review*, *132*(8), 1917–1932. https://doi.org/10.1175/1520-0493(2004)132<1917:AARMMI>2.0.CO;2

Wick, G. A., Neiman, P. J., Ralph, F., & Hamill, T. M. (2013). Evaluation of forecasts of the water vapor signature of atmospheric rivers in operational numerical weather prediction models. *Weather and Forecasting*, *28*(6), 1337–1352. https://doi.org/10.1175/waf-d-13-00025.1

Wilks, D. S. (2019a). Chapter 13 - Principal Component (EOF) Analysis. In D. S. Wilks (Ed.), *Statistical methods in the atmospheric sciences (fourth edition)* (Fourth Edi, pp. 721–738). Elsevier. https://doi.org/https://doi.org/10.1016/B978-0-12-815823-4.00005-5

Wilks, D. S. (2019b). Chapter 16 - Cluster Analysis. In D. S. Wilks (Ed.), *Statistical methods in the atmospheric sciences (fourth edition)* (Fourth Edi, pp. 721–738). Elsevier. https://doi.org/https://doi.org/10.1016/B978-0-12-815823-4.00005-5

Wille, J. D., Favier, V., Dufour, A., Gorodetskaya, I. V., Turner, J., Agosta, C., & Codron, F. (2019). West Antarctic surface melt triggered by atmospheric rivers. *Nature Geoscience*, *12*(11), 911–916. https://doi.org/10.1038/s41561-019-0460-1

Wu, B., & Wang, J. (2002). Possible impacts of winter Arctic Oscillation on Siberian high, the East Asian winter monsoon and sea–ice extent. *Advances in Atmospheric Sciences*, *19*(2), 297–320. https://doi.org/10.1007/s00376-002-0024-x

Yadav, R. K., Rupa Kumar, K., & Rajeevan, M. (2009). Increasing influence of ENSO and decreasing influence of AO. *Journal of geophysical research*, *114*(D12). https://doi.org/10.1029/2008JD011318

Yang, Y., Zhao, T., Ni, G., & Sun, T. (2018). Atmospheric rivers over the Bay of Bengal lead to northern. *International Journal of Climatology*, *38*(August 2017), 1010–1021. https://doi.org/10.1002/joc.5229

Yatagai, A., Kamiguchi, K., Arakawa, O., Hamada, A., Yasutomi, N., & Kitoh, A. (2012). APHRODITE: Constructing a Long-Term Daily Gridded Precipitation Dataset for Asia Based on a Dense Network of Rain Gauges. *Bulletin of the American Meteorological Society*, *93*(9), 1401–1415. https://doi.org/10.1175/BAMS-D-11-00122.1

Ye, C., Zhang, H., Moise, A., & Mo, R. (2020). Atmospheric rivers in the Australia-Asian region: a BoM-CMA collaborative study. *Journal of Southern Hemisphere Earth Systems Science*, *70*, 3–16. https://doi.org/10.1071/ES19025

Zhao, T., Zhao, J., Hu, H., & Ni, G. (2016). Source of atmospheric moisture and precipitation over China's major river basins. *Frontiers of Earth Science*, *10*(1), 159–170. https://doi.org/10.1007/s11707-015-0497-4

Zhao, Y., Huang, A., Zhou, Y., Huang, D., Yang, Q., Ma, Y., Li, M., & Wei, G. (2014). Impact of the Middle and Upper Tropospheric Cooling over Central Asia on the Summer Rainfall in the Tarim Basin, China. *Journal of Climate*, *27*, 4721–4732. https://doi.org/10.1175/JCLI-D-13-00456.1

Zhu, Y., & Newell, R. E. (1994). Atmospheric rivers and bombs. *Geophysical Research Letters*, *21*(18), 1999–2002. https://doi.org/10.1029/94GL01710

Zhu, Y., & Newell, R. E. (1998). A proposed algorithm for moisture fluxes from atmospheric rivers. *Monthly Weather Review*, *126*, 10. https://doi.org/10.1175/1520-0493

Chapter 4

Influence of zero degree line on Atmospheric Rivers in High Mountain Asia: WRF case studies of orographic precipitation extremes

D.L. NASH, L.M.V. CARVALHO, C. JONES, & Q. DING

Abstract

Atmospheric Rivers (ARs) reach High Mountain Asia (HMA) roughly 10 days per month during the winter and spring, resulting in roughly 20 mm day^{-1} of precipitation. However, there are a few events each season that result in over 100 mm of precipitation, providing the vast majority of total winter precipitation, indicating that an individual AR event may significantly change water availability within the region in which it occurs. Furthermore, dynamical changes, such as the warming anticyclonic trend in

Central Himalaya, have influenced the frequency of ARs and their freezing level height when they reach HMA, impacting the resulting rain to snow ratio and ultimately water resources. To understand the mesoscale processes associated with the orographic precipitation during these extreme events, we compare two Northwestern-transitioned-to-Western HMA ARs associated with extreme precipitation during a below-average and above-average freezing level height. We use dynamically downscaled data from the Weather Research and Forecasting model at 20 km and 6.7 km spatial resolution to investigate the atmospheric flow interactions of ARs with the complex terrain of HMA. We show that there is less frozen precipitation during the AR with an above-average height of the 0°C isotherm, or zero degree line. Additionally, the axis of the AR relative to the complex topography is a better indicator of the resulting precipitation than the IVT magnitude in the AR. This study indicates the importance of exploring dynamical changes in HMA via ARs and the contribution of ARs and the freezing level to orographic precipitation, providing information for future work to improve forecasting skill in a region vulnerable to the impacts of climate change.

4.1 Introduction

In High Mountain Asia (HMA), precipitation and the resulting glacial melt in the spring and summer months simultaneously provide water resources for hundreds of millions of people, while also presenting risks for many extreme weather conditions (Hewitt, 2005; Kääb et al., 2012). Recent work has shown that Atmospheric Rivers (ARs), long conduits of strong moisture transport, are a significant contributor to total seasonal precipitation during winter and spring in HMA (Nash et al., 2021). ARs occur in a variety of locations across the globe and are associated with extreme precipitation, flooding, lightning, debris flows and anomalous snow accumulation (Cannon et al.,

2018; Nash & Carvalho, 2020; Oakley et al., 2018; Zhu & Newell, 1994, among others). In HMA, ARs contribute to extreme precipitation and are associated with flood events in the Nepal and Bay of Bengal areas (Thapa et al., 2018; Yang et al., 2018). Nash et al. (2021) found that there are three distinct types of ARs that reach HMA and result in above-average precipitation in Western, Northwestern, and Eastern HMA. There are typically between 9 and 11 HMA ARs per month in the winter and spring, contributing between 40-60% of total seasonal precipitation. However, a single strong AR event can provide up to a quarter of that precipitation, impacting water availability and rainfall-related risks. Scarce observational data and the course resolution of reanalysis (i.e., 27 km or greater) poses limitations to investigating mechanisms associated with ARs interactions with HMA.

The main objective of this study is to use Advanced Weather Research and Forecasting (ARW-WRF, hereafter WRF) simulations to investigate the mesoscale characteristics of two ARs that reached HMA that resulted in extreme precipitation (above 85th percentile) in western HMA during winter months. We focus on characteristics that are important to the extreme precipitation, such as water vapor flux and other thermodynamic characteristics of the core of the AR, the direction of the AR relative to HMA topography, the height of the freezing level, and the orographic mechanisms related to the precipitation in the foothills of HMA. We explore the thermodynamic and kinematics of atmospheric rivers as it relates to orographic precipitation in order to improve the understanding of how ARs transport large plumes of water vapor long distances without precipitating – particularly as HMA ARs that reach Northwestern and Western HMA can spend a significant portion of their life cycle over Southwest Asia. To facilitate this, we contrast two HMA ARs that both resulted in extreme precipitation, contributing significantly to the total seasonal precipitation, but had differing freezing level heights and outcomes with regard to precipitation-related hazards such as

lightning and landslides.

The organization of this paper is as follows: Section 4.2 describes the data used for this analysis and outlines WRF model set up. Section 4.3.2 describes thermodynamic trends during HMA AR events using 36 years of dynamically downscaled reanalyses over HMA. We evaluate changes in the freezing level and moisture, focusing on areas where HMA ARs typically result in above-average precipitation during the winter. Section 4.3.4 focuses on two extreme AR events that had similar overall characteristics, but had different freezing levels and precipitation amounts. Using the WRF model, we examine the mesoscale characteristics of two ARs associated with extreme precipitation (greater than 85th percentile) in Sections 4.3.5 and 4.3.6, emphasizing the differences between an AR event during a phase of below-average freezing level and an AR event during a phase of above-average freezing level. We compare the moisture and stability profiles along the core of the ARs and examine cross-sections of precipitation (both rain and snow). We summarize our results in Section 3.5.

4.2 Data and Methods

4.2.1 AR Detection: tARget v3

To detect ARs, we used the Tracking Atmospheric Rivers Globally as Elongated Targets (tARget) algorithm, version 3 which was applied to ERA-Interim data on a global, 6 hourly basis from 1979 to 2019 (Guan & Waliser, 2019). This AR detection algorithm is useful for the HMA region as it detects ARs via relative IVT intensity thresholds, which is particularly useful during the winter in HMA, as there is, on average, little to no moisture (Nash et al., 2021). Additionally, it has been used in multiple studies, including Nash et al. (2021) where combined Empirical Orthogonal Function and k-means

cluster analysis was applied to days an AR passed the 1000 m elevation threshold in HMA. Nash et al. (2021) determined that there are three main types of ARs that reach HMA in winter and spring months. We use the resulting classification of AR types in this study to focus on precipitation from Northwestern and Western HMA AR Types.

4.2.2 Model setup

This study uses 36 years of Climate Forecast System Reanalysis (see Saha et al., 2010) dynamically downscaled over HMA to 20 km and 6.7 km spatial resolution and 3-hourly temporal resolution using WRF model version 3.7.1 described in Norris et al. (2018). This data set extends from April 1979 to March 2015, and each year was run continuously from the beginning of March through the end of March the following year (e.g., from 1 March 1979 00 UTC to 1 April 1980 00 UTC) to capture the full winter and summer seasons. The first month of every year was discarded due to model spin-up, retaining 12 months per year of simulation. The simulations were performed with two domains with one-way interaction (i.e., no feedback and the inner domain did not affect the outer domain) of 20 km and 6.7 km (3:1 ratio), mapped with a Mercator projection (see Fig. 5.1 for a map of the domains). There were 50 vertical levels in the simulations from the surface to 50 hPa. Spectral nudging of zonal wave numbers 1-5 and meridional wave numbers 1-4 was applied to all vertical levels in the outer domain for temperature, winds, and geopotential height (Stauffer & Seaman, 1990; Stauffer et al., 1991). The physics options for the WRF simulations included the Thompson microphysics scheme (Thompson et al., 2008), fifth-generation Pennsylvania State University–National Center for Atmospheric Research Mesoscale Model (MM5) surface layer scheme (Monin & Obukhov, 1954), the Noah-MP (multi-physics) land surface model (Niu et al., 2011), the Rapid Radiative Transfer Model for GCMs

(RRTMG) scheme for longwave and shortwave radiation (Iacono et al., 2008), the Yonsei University boundary layer turbulence transfer scheme (Hong et al., 2006), and Kain-Fritch cumulus and shallow convection scheme on the outer domain only (Kain, 2004). For more information on the WRF model configuration for the 6.7 km output, please see Norris et al. (2017) and Norris et al. (2018).

We use the 20 km and 6.7 km WRF simulations to examine the trends of the height of the zero degree line (or 0°C isotherm) and integrated vapor transport (IVT) during Northwestern, Western, and Eastern HMA ARs during the winter months between 1979 and 2015. To calculate the height of the freezing level, we interpolated the height above ground level (m) to 0°C. IVT, a variable widely used in the detection and characterization of ARs (Guan & Waliser, 2015; Nash et al., 2021), was calculated by taking the 3-hourly model output, interpolating u and v wind components (m s^{-1}), and water vapor mixing ratio (kg kg^{-1}) to 20 pressure levels (1000, 975, 950, 925, 900, 875, 850, 825, 800, 775, 750, 700, 650, 600, 550, 500, 450, 400, 300, and 250 hPa). Then, using water vapor mixing ratio, we computed specific humidity (q) and then integrated u and v wind components with q at all pressure levels (see Appendix C.1 for equations). Additionally, we examined the mesoscale characteristics of two Western HMA ARs that resulted in extreme precipitation using the WRF output. For precipitation related variables (e.g., rain, snow, precipitation), model output from every three hours at 00 UTC, 03 UTC, 06 UTC, 09 UTC, 12 UTC, 15 UTC, and 21 UTC provided the accumulation from the initialization date of each year. This was then used to compute the mean values of precipitation for time step t by subtracting precipitation at time (t), from precipitation at time (t+1). For variables such as meridional and zonal wind and geopotential heights, the model data was interpolated to the given pressure level. A variety of variables (equivalent potential temperature, specific humidity, u, v, and w wind components) were used in vertical cross-section analysis, where we interpolated

the data to height above ground level along the identified cross-section.

4.2.3 Observations and gridded estimates

The European Centre for Medium-Range Weather Forecasts (ECMWF) atmospheric reanalysis of the global climate (ERA5) is used here at a 6-hourly and 0.5° resolutions to explore 250 hPa geopotential heights and IVT for the AR events at the synoptic scale because the outer domain of the WRF model output did not cover the spatial extent of the AR cases (Hersbach et al., 2018a, 2018b; Hersbach et al., 2020).

A daily time series of lightning flash rates from Tropical Rainfall Measuring Mission Lightning Imaging Sensor and Optical Transient Detector (TRMM LIS-OTD) (Cecil, 2015) is used at a horizontal resolution of 2.5° by 2.5° between 1995 and 2014 from 0-50°N and 20-110°E. It is important to keep in mind that this data is a smoothed estimate, as a 7.5° by 7.5° boxcar moving average, 111-day boxcar moving average, and 110-day digital filter were all applied. However, it does give a rough estimate of the lightning conditions during the identified AR events.

The landslide catalog created by Kirschbaum et al. (2010) identifies global landslides that were associated with extreme precipitation. We examine landslides that occurred within 20-45°N and 65-100°E, and consider a landslide associated with an AR if the AR reached HMA within 500 km of the landslide location on the same day.

4.3 Results

4.3.1 Evaluation of WRF Climatology relative to HMA ARs

Using the 36 years of dynamically downscaled WRF output in HMA from (Norris et al., 2018), we evaluated the ability of these simulations to capture the broad, synoptic

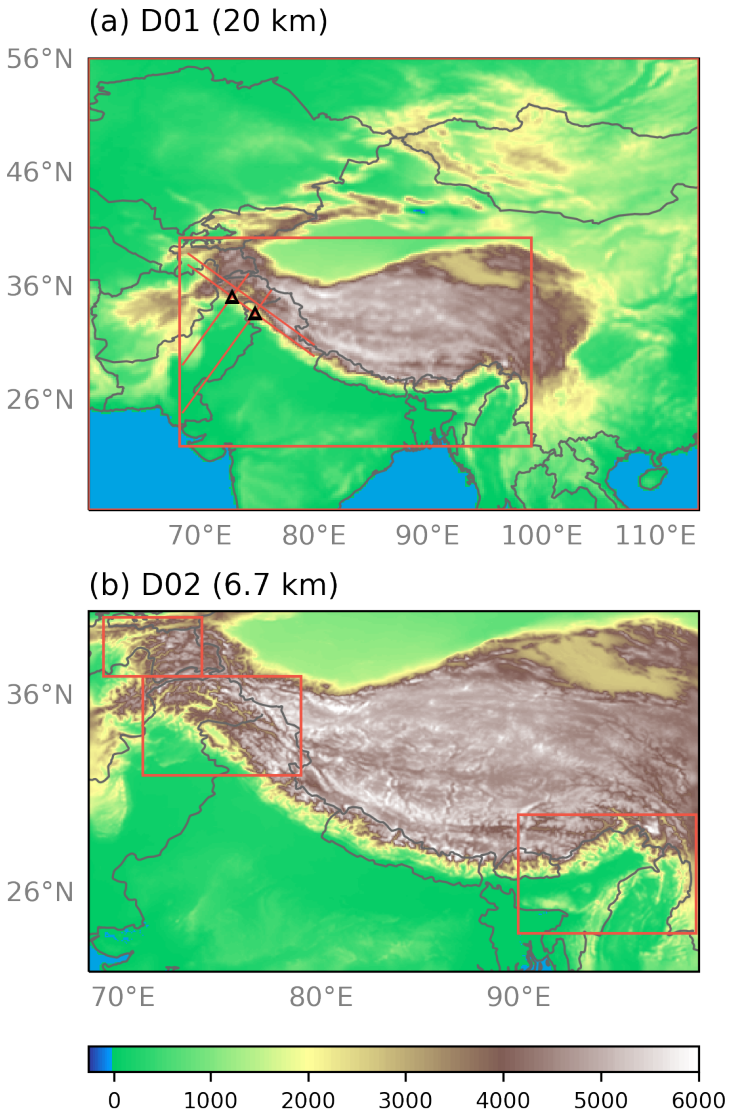

Figure 4.1: (a) WRF model outer domain (D01) for downscaling to 20 km grid spacing resolution. The red meridional lines indicate the location of the vertical cross-sections in Figs. 4.13 and 4.14, the red zonal lines indicate the location of the hovmoller diagrams (i.e., elevation by time diagrams) in Fig. 4.15 and 4.16, the black triangles indicate the location of the time x height diagrams in Fig. 4.17. The red box indicates the extent of the inner domain. (b) WRF model inner domain (D02) for downscaling to 6.7 km grid spacing resolution. The red boxes indicate the location of above average precipitation during the Northwestern, Western, and Eastern HMA AR Types and are used as subregions for analysis.

characteristics of the three HMA AR types identified in Nash et al. (2021) relative to ERA5. The WRF 20 km outer domain is much smaller than the extent of most HMA ARs. However, when compared to the synoptic composites using ERA5, the broad spatial patterns for precipitation, IVT, and 250 hPa geopotential heights are relatively similar. For all three HMA AR types, IVT is underestimated by about 75 kg m^{-1} s^{-1} in Central and Eastern HMA (Fig 4.2a-c). Upper level geopotential heights are overestimated by WRF north of HMA, and underestimated south of HMA, but bias values are less than 20 dekameters (Fig 4.2d-f). For Western HMA ARs, WRF 6.7 km precipitation has a positive bias of about 12 mm day^{-1} relative to ERA5 in Western Himalayas, the Karakoram, and parts of the Tien Shan (Fig 4.2h). However, for all three HMA AR types, WRF 6.7 km underestimated precipitation near the Eastern Himalayas by about 5 mm day^{-1} (Fig 4.2h-j). Overall, the WRF data is able to capture the broad synoptic patterns of the three HMA AR Types defined in Nash et al. (2021) and is sufficient for further analysis of HMA AR trends and mesoscale patterns.

4.3.2 Trend Analysis

During the winter, Norris et al. (2018) demonstrate that eastern HMA has experienced significant warming of the lower troposphere, while western HMA had no statistically significant trend. Associated with this warming trend is the weakening of the ridge over northwest HMA and a weakening of the trough over eastern HMA, increasing the frequency of extratropical cyclones in western HMA and decreasing their frequency in central Himalaya (Norris et al., 2018). In eastern HMA, Norris et al. (2018) show that there is a decreasing trend in 300 hPa cloud ice and snow in eastern and central HMA, in the same region of the warming trend. Western HMA displayed positive trends and higher magnitudes of cloud ice and liquid cloud, indicating the higher frequency of

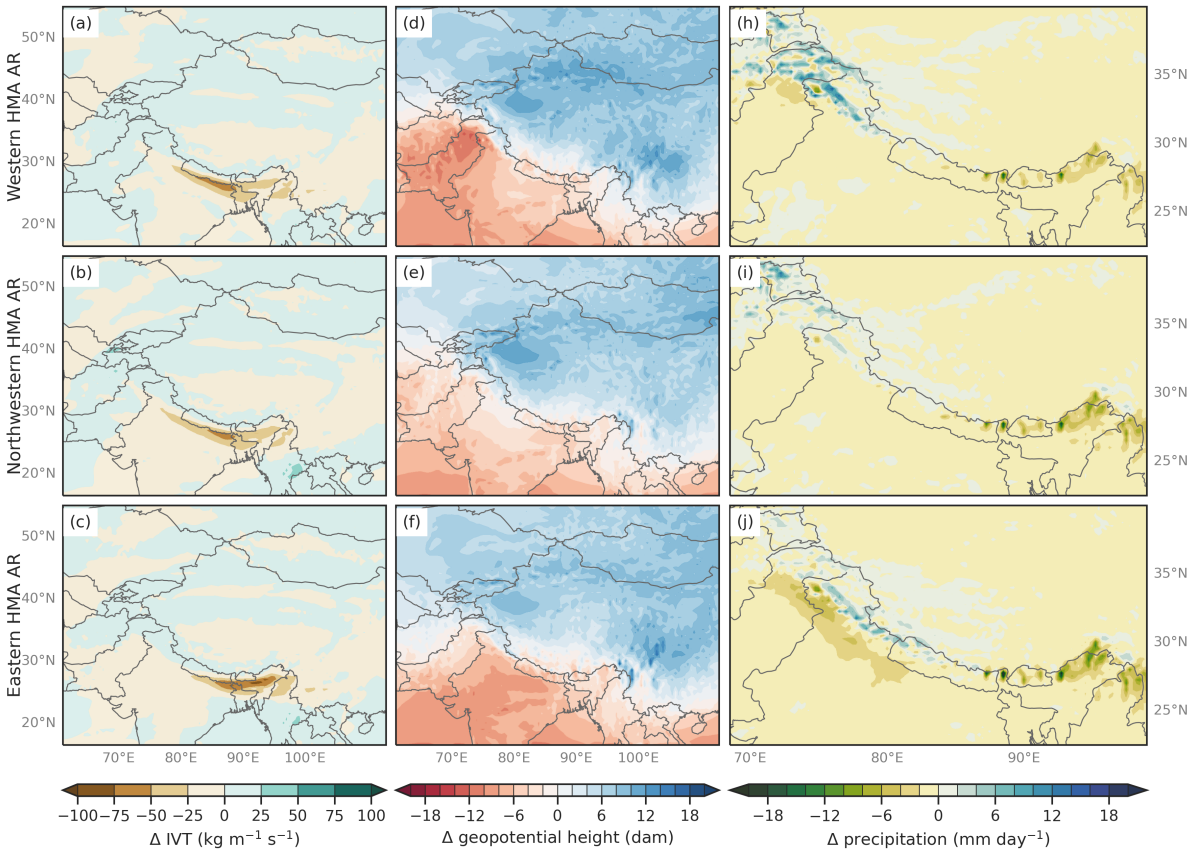

Figure 4.2: .(a) IVT bias from 20 km WRF model - 27 km ERA5 (shaded, kg m^{-1}, s^{-1}) for Western HMA ARs during DJF between 1 December 1979 and 28 February 2015. The model is regridded to match the reanalysis. (b) Same as (a) but for Northwestern HMA ARs. (c) Same as (a) but for Eastern HMA ARs. (d) Geopotential heights at 250 hPa bias for 20 km WRF model - 27 km ERA5 (shaded, dekameters) for Western HMA AR days during DJF between 1979 and 2015. (e) Same as (d) but for Northwestern HMA ARs. (f) Same as (d) but for Eastern HMA ARs. (g) Precipitation bias from 6.7 km WRF model - 27 km ERA5 (shaded, mm day^{-1}) for Western HMA AR days during DJF between 1979 and 2015. (h) Same as (g) but for Northwestern HMA ARs. (i) Same as (g) but for Eastern HMA ARs.

extratropical cyclones (Norris et al., 2018). Of the three types of HMA ARs, Northwestern and Western HMA ARs are primarily associated with extratropical cyclones, where the warm, moist air from the AR is advected in the area ahead of the cold front (Nash et al., 2021). Northwestern HMA ARs are associated with above-average precipitation in northwest HMA, primarily in the Tien Shan and Pamirs mountain ranges. Western HMA ARs are associated with above average precipitation in the Karakoram and Hindu Kush regions. Eastern HMA ARs bring moisture in from the Bay of Bengal and result in above-average precipitation in Eastern HMA. Espinoza et al. (2018) demonstrated that under the RCP 8.5 warming scenario, the frequency of HMA ARs is expected to increase by 6-8% while the intensity of IVT is expected to remain the same between 2073-2096. Kirschbaum et al. (2020) show that increases in extreme precipitation in HMA has the potential to increase landslides by 10-30% more in the years 2061-2100 across HMA, and even up to 70% more landslides in Central Himalaya. It is clear that ARs are associated with precipitation in HMA and increases in ARs could potentially increase precipitation and precipitation related hazards; therefore, it is important to understand the recent changes in AR properties to determine their influence on local warming and precipitation trends.

To characterize recent changes in HMA ARs, we examine seasonal trends in AR frequency, IVT, and the height of the zero degree isotherm using the dynamically downscaled WRF data. The nonparametric Mann-Kendall test is used to identify and plot significant trends for the months of December, January, and February (DJF) between 1979 and 2015 over HMA. When simply considering the number of ARs broken down by HMA AR type per year, we found no significant trends. However, when we looked at changes in AR frequency (based on the Guan and Walsier algorithm) in each winter month, we found contrasting trends. For example, during December, AR frequency is significantly decreasing over southwest Asia by about 1 day per year (Fig. 4.3a).

Meanwhile, in January and February, ARs have been increasing in frequency by about 0.25 days per year (Fig. 4.3b, c). Over Eastern and Central HMA, ARs have been significantly increasing in February by 0.25 to 0.5 days per year (Fig. 4.3b, c). Figure 4.4 shows changes in the moisture, or IVT using only days considered to have a HMA AR in DJF (see Nash et al. (2021) for more details on identifying HMA AR days). During Western HMA ARs, there has been a significant increase in IVT in western HMA of about 0.3 kg m^{-1} s^{-1} yr^{-1} (see Fig. 4.4a). Figs. 4.4a and b show that Eastern HMA has been experiencing a significant decrease in IVT (-0.2 kg m^{-1} s^{-1} yr^{-1}) during Western and Northwestern HMA ARs.

The height of the freezing level influences the fraction of frozen precipitation, as well as frequency of lightning flashes (Guan et al., 2016; Nash & Carvalho, 2020; Pawar et al., 2015). Latitude and elevation influence the height of the 0°C isotherm – for example, in DJF, between 1 and 3 km in HMA, the average height of the 0°C isotherm is between 2.5 and 3.5 km, while elevations higher than 3 km have an average 0°C isotherm of 4 km or greater. Between 25°N and 30°N, the average height of the 0°C isotherm is between 3 and 3.5 km, whereas poleward of 30°N, the average height is below 3 km. However, an upper-level cut-off low associated with high amplitude troughs can decrease the freezing height for the duration of a storm, potentially increasing the fraction of frozen precipitation relative to the total precipitation. On the other hand, because the moisture of ARs can be located relatively high up in the troposphere, they may increase the altitude of the freezing level, resulting in more rain and less snow falling at higher altitudes (Guan et al., 2016; Neiman et al., 2008; Neiman et al., 2011). The height of the freezing level has significantly increased across most of India during DJF between 1979 and 2015 (Fig. 4.5). The spatial extent of the increase of the height in the freezing level varies by AR type. For example, during Western HMA ARs (Fig. 4.5a), the height of the zero degree isotherm has increased across much of

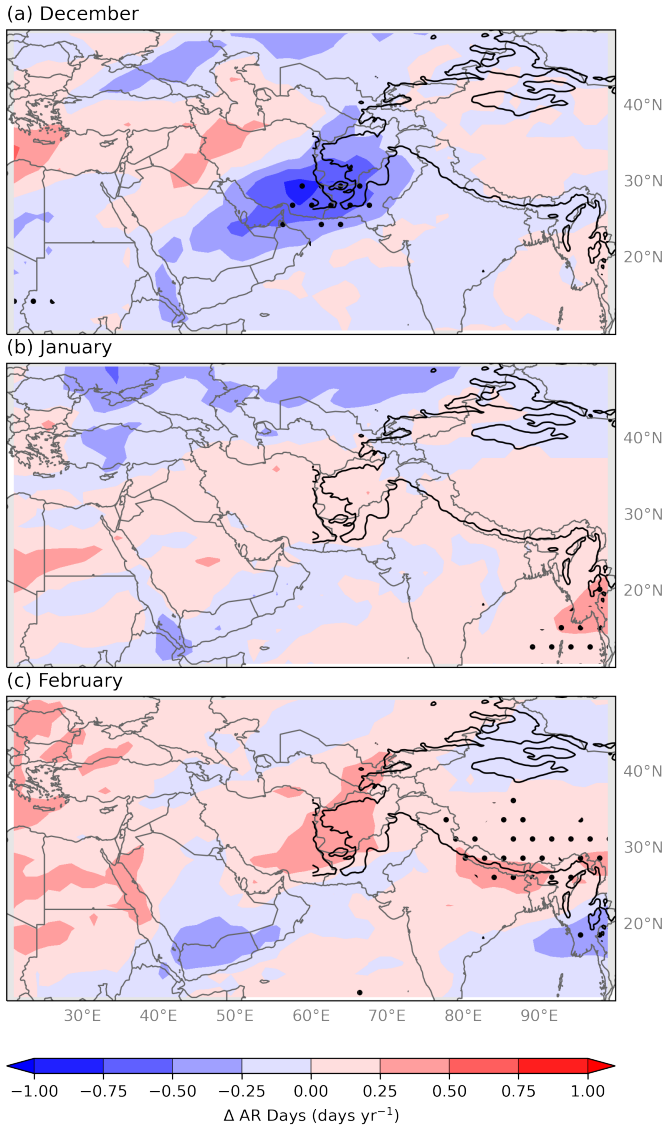

Figure 4.3: (a) AR frequency trends (shaded, number of AR days per year) over Asia during the month of December from 1979 to 2019. Stippling indicates trends that are considered statistically significant at the 5% significance level. (b) Same as (a) but for January. (c) Same as (a) but for February.

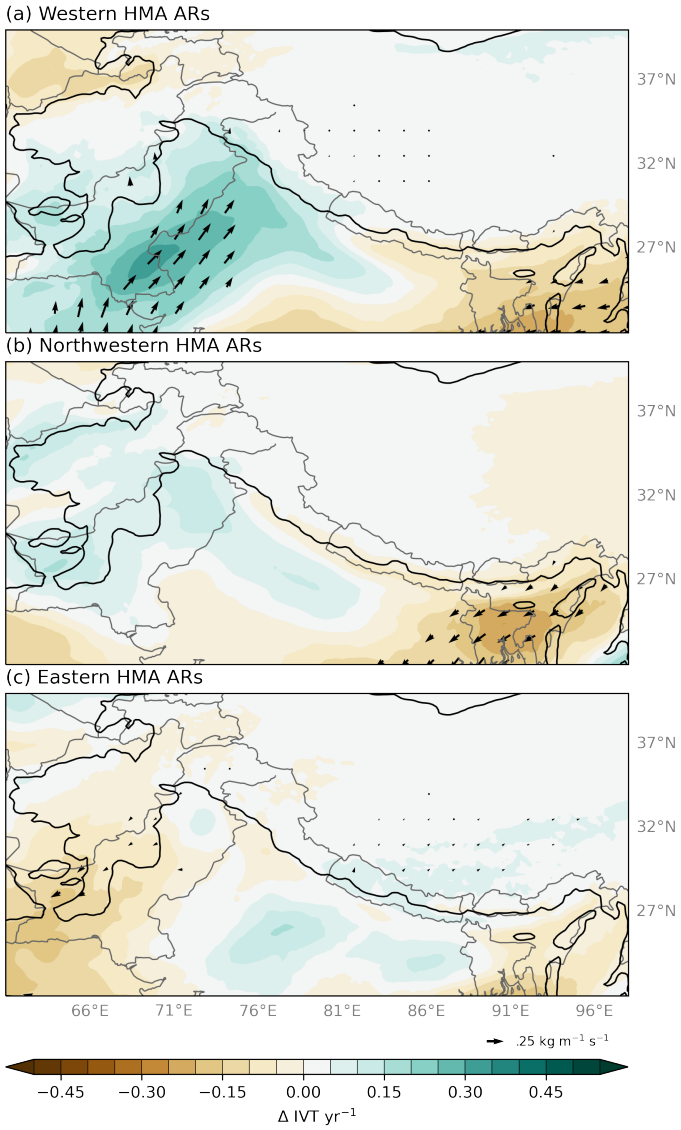

Figure 4.4: (a) Winter (DJF) seasonal trends in integrated vapor transport (IVT, kg m^{-1} s^{-1}) per year for Western HMA AR days based on 20 km WRF output for 1979-2015. IVT vectors indicate trends that are considered statistically significant at the 5% significance level. The black contour is the location of 1-km elevation. (b) Same as (a) but for Northwestern HMA ARs. (c) Same as (a) but for Eastern HMA ARs.

Central and Eastern HMA, while during Northwestern HMA ARs (Fig. 4.5b), the height of the zero degree isotherm has increased across most of India and southern Pakistan. During Eastern HMA ARs (Fig. 4.5c), increases in the height of the freezing level are confined to Eastern HMA. Overall in DJF, the height of the 0°C isotherm has significantly increased in Eastern and Central HMA and during all three AR types between 1979 and 2015.

To investigate the influence of the increases in moisture content and height of the 0°C isotherm on precipitation during HMA AR days between 1979 and 2015, we compare the fraction of frozen precipitation in HMA during above-average freezing level conditions and below-average freezing level conditions. We classified each HMA AR day as a below-average freezing level height, neutral freezing level height, or above-average freezing level height based on the average conditions within its respective subregion (see Fig. 4.1b for subregion extents). To classify AR days according to the height of the freezing level, we followed two steps. First, we identify the area with above-average precipitation during each HMA AR type (e.g., Western, Northwestern, and Eastern). Second, we calculate the daily average freezing level height for that region, separately for each AR type. For example, on 13 January 1981, there was a Western HMA AR and within the area where above-average precipitation usually occurs during Western HMA ARs (71-79°E and 32-37°N), the average height of the freezing level anomaly was greater than 1.5 times the standard deviation. Therefore, we classified that HMA AR as an event with above-average freezing level height. This was repeated for all HMA AR days between 1979 and 2015. Composites of the difference in the fraction of frozen precipitation between above and below-average freezing level heights, for each AR type, are shown in Fig. 4.6. During HMA AR days with below-average freezing level conditions, there is a significantly higher fraction of frozen precipitation compared to HMA AR days with above-average freezing level conditions (Fig.

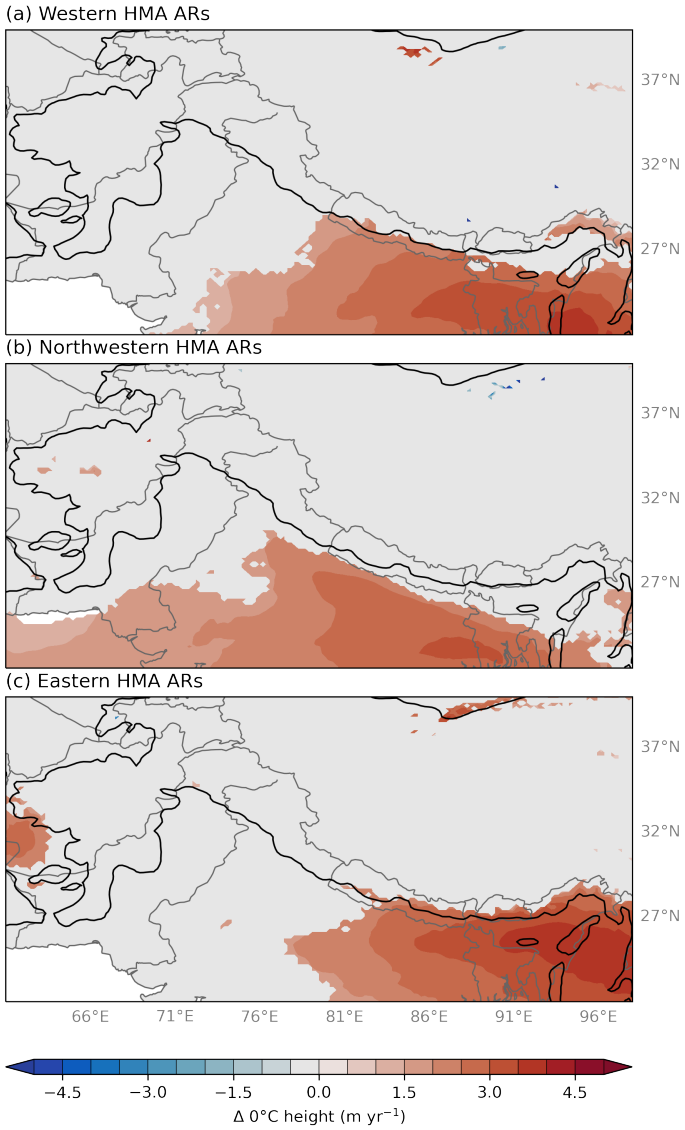

Figure 4.5: (a) Winter (DJF) seasonal trends in the height of the 0°C isotherm (shaded, m) per year for Western HMA AR days based on 20 km WRF output for 1979-2015. Data are only plotted where trends are considered statistically significant at the 5% significance level. The black contour is the location of 1-km elevation. (b) Same as (a) but for Northwestern HMA ARs. (c) Same as (a) but for Eastern HMA ARs.

4.6). Interestingly, the increased fraction of frozen precipitation extends beyond the region of above-average precipitation that we typically see during each type of HMA AR. This indicates the broader influence of ARs to precipitation across HMA. For example, during Western HMA AR days, we see there is 50% more frozen precipitation during below-average freezing level conditions across Western and Central HMA compared to above-average freezing level conditions (Fig. 4.6a). These results indicate the importance of the height of the 0°C isotherm during HMA ARs, and its relative impact on associated precipitation. To determine the local effect of the height of the 0°C isotherm on orographic precipitation during HMA ARs, we compare and contrast mesoscale conditions during a below-average freezing level AR and an above-average freezing level AR.

4.3.3 Case Study Selection

Figure 4.7 shows, for all HMA ARs between 1979 and 2019, the maximum total precipitation in different subregions and the average IVT within the AR for the duration of each event, based on ERA5. The colors indicate the duration (in hours) of each AR event. Based on the location of above-average precipitation during each HMA AR Type, we chose the subregions to evaluate here (see Nash et al. (2021)) and included Northwestern HMA (66-74°E and 37-40°N), Western HMA (71-79°E and 32-37°N), Eastern Himalaya (90-100°E and 24-30°N) (see Fig. 4.1 for subregion extents). We evaluated multiple precipitation metrics, including 85th percentile and area-average precipitation, while excluding grid cells from each area that had less than 20 mm of precipitation per event to focus on the regions that are receiving higher than average precipitation. Unsurprisingly, the precipitation maximum gave the clearest picture of how IVT influences precipitation during HMA ARs and is what is shown in Fig. 4.7.

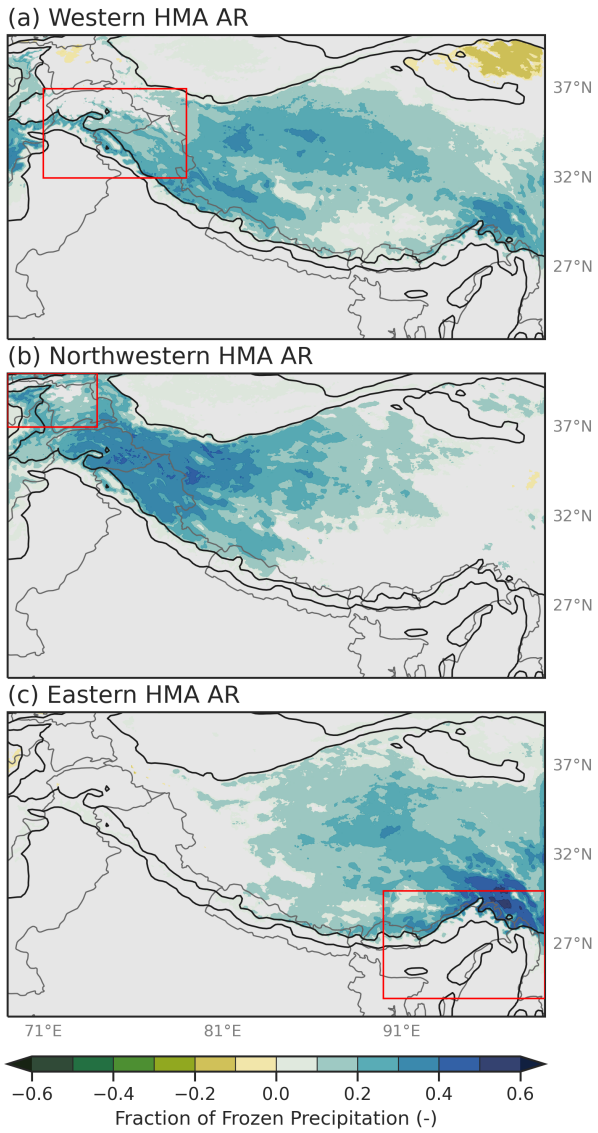

Figure 4.6: (a) Composite differences of fraction of frozen precipitation (shaded, -) for Western HMA ARs below-average freezing level conditions and above-average freezing level conditions within the red box. Only differences in the fraction of frozen precipitation that are considered at or above the 95% confidence level are shaded. (b) Same as (a) but for Northwestern HMA ARs. (c) Same as (a) but for Eastern HMA ARs.

Only precipitation in Eastern Himalayas during Eastern HMA shows a linear relationship (e.g., precipitation increases as IVT increases) (Fig. 4.7c). This is attributed to the fact that Eastern ARs spend a larger proportion of their life cycle over a body of water, which in this case is the Bay of Bengal. This follows what we know to be true about ARs that make landfall on the west coast of the US or Europe – that IVT is a good indicator of precipitation (i.e., the higher the IVT, the more likely it is that precipitation will be higher). This aligns well with the AR Category scale defined in Ralph et al. (2019), which assigns a category to an AR based on the duration of the IVT being above a certain threshold, the magnitude of the IVT, and the duration of the AR. For example, a category 5 AR that is considered "extreme" and defined as "primarily hazardous" would have a maximum IVT magnitude above 1000 kg m^{-1} s^{-1} and would sustain above 250 kg m^{-1} s^{-1} for 48 hours or longer.

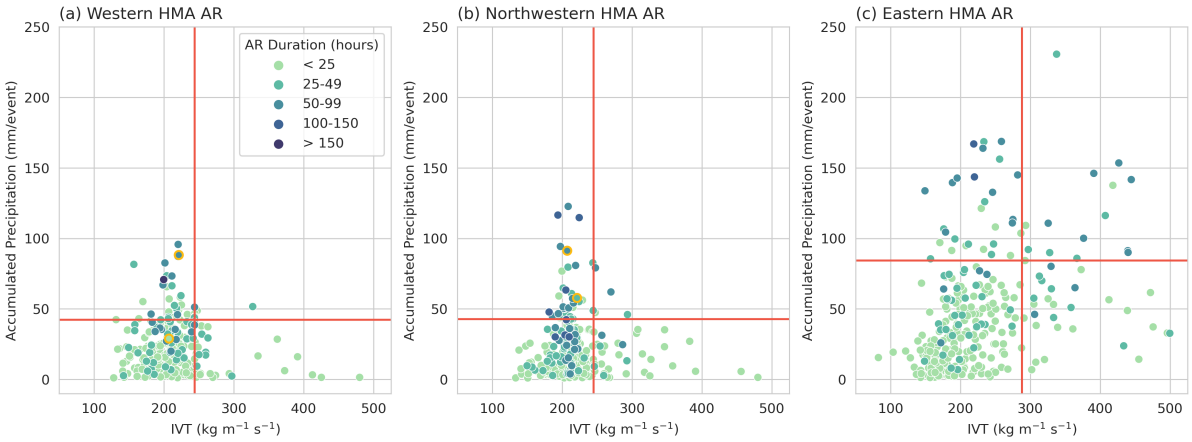

Figure 4.7: (a) Scatter plot showing ERA-Interim average IVT (kg m^{-1} s^{-1}) within the AR object for the duration of the AR event compared to the ERA5 maximum-total precipitation (mm $event^{-1}$) in the region that accumulates above-average precipitation for Western HMA ARs (see Fig. 4.1b for subregion locations). The duration (hours) of the AR event is indicated by the shading. The circles with yellow highlight indicate the case studies chosen in Section 4.3.4. (b) Same as (a) but for Northwestern HMA ARs. (c) Same as (a) but for Eastern HMA ARs.

The assumption that higher IVT magnitude leads to higher precipitation does not

appear to hold for Northwestern and Western HMA ARs (Fig. 4.7a, b). There are very few events that have above 85th percentile IVT and above 85th percentile precipitation. Rather, there are quite a few events that are just below the 85th percentile threshold for IVT that have a wide range of precipitation values, suggesting that there is a preferential IVT value for Western and Northwestern HMA ARs when it comes to extreme precipitation. Most ARs that reach western and northwestern HMA during DJF have an average IVT of about 220 kg m^{-1} s^{-1}. In considering the duration of AR compared to maximum precipitation, we see that the longer duration ARs result in higher precipitation totals, however the relationship is not statistically significant, which suggests that characteristics such as AR direction relative to the topography hold more importance in this region during the dry winter season compared to the amount and duration of IVT. This is really important when considering predictability of events. Most current long-term prediction work for precipitation in the United States emphasizes the importance of ARs as a predicting tool, relying on the assumption that higher magnitude IVT and longer sustained IVT will mean more precipitation for the West Coast (DeFlorio et al., 2019). It is possible that future work regarding the prediction of ARs on multiple time scales will need to focus on different characteristics of the ARs as predictors for precipitation, such as their axis relative to topography. This indicates the importance of determining the mesoscale characteristics of HMA ARs that are associated with precipitation extremes.

Using the 85th percentile as the guide for AR events that resulted in extreme precipitation and freezing level height classification, we chose two AR cases to determine the synoptic and mesoscale characteristics that resulted in extreme precipitation. Both cases began as a Northwestern HMA AR and transitioned to a Western HMA AR. The first AR case occurred from 10 January 2002 12 UTC to 13 January 2002 12 UTC (duration of 72 hours). During the January 2002 AR, locations across Western HMA

received up to 100 mm of precipitation, but there were no reported landslides or damages (Fig. 4.8a). The second AR case occurred from 4 February 2010 00 UTC to 8 February 2010 18 UTC, and had a below-average freezing level height in both Northwestern and Western HMA. Figure 4.8c shows the 90-hour AR event resulted in around 200 mm of precipitation in western HMA, reaching 450 mm in some locations. Three precipitation-related landslides occurred between 6-8 February and appear to be associated with this AR (locations identified as yellow squares in Fig. 4.8c). There were many devastating impacts from these landslides, including at least sixteen deaths, destruction of many houses and buildings, and isolation of many communities due to highway closures and damage (Kirschbaum et al., 2010). The February 2010 AR event occurred during El Niño conditions, while the January 2002 AR occurred during neutral conditions; however, we do not believe the difference in ENSO conditions between these two events significantly impacted the overall results of this analysis. Nash et al. (2021) found that while there was a significant increase in the frequency of Northwestern and Western HMA ARs during El Niño conditions compared to La Niña conditions, there was no significant difference in IVT for El Niño conditions compared to neutral conditions. Figure 4.8f shows the difference in the fraction of frozen precipitation between the two AR events and indicates that there was more frozen precipitation during the February 2010 AR with the lower freezing level compared to the January 2002 AR with a higher freezing level. To assess the variation between individual AR events, we repeated the following analysis for most Northwestern and Western HMA AR cases with above 85th percentile precipitation (not shown) and support similar conclusions based on the two AR cases described here. Therefore, the remainder of this paper focuses on the synoptic and mesoscale conditions for the January 2002 and February 2010 cases to determine the underlying mechanisms that contributed to these differing outcomes.

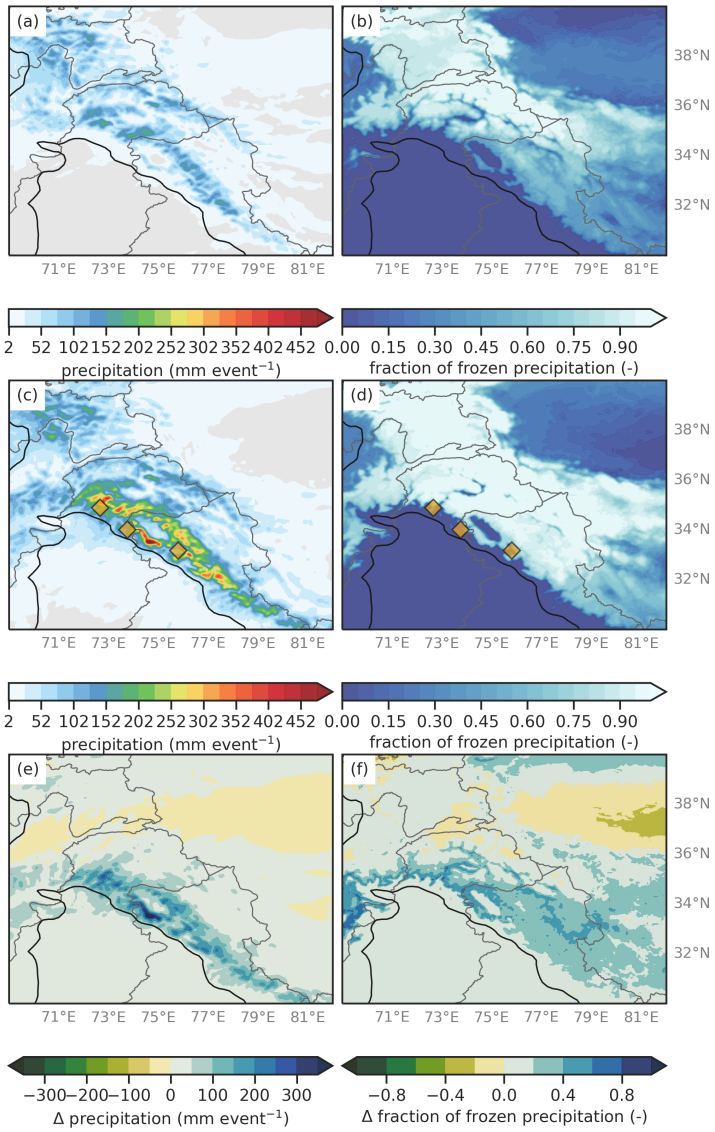

Figure 4.8: WRF 6.7 km precipitation (shaded, mm event^{-1}) for the duration of the (a) January 2002 AR and (c) February 2010 AR. The black contour is the location of 1-km elevation, and the yellow diamonds indicate the location of a precipitation-triggered landslide during the AR event. The average fraction of frozen precipitation (shaded, -) for the (c) January 2002 AR and (d) February 2010 AR. (e) The difference in precipitation (shaded, mm event^{-1}) between the February 2010 AR and the January 2002 AR. (f) The difference in the fraction of frozen precipitation (shaded, -) between the February 2010 AR and the January 2002 AR.

4.3.4 Synoptic Characteristics of the HMA AR Case Studies

Figures 4.9 and 4.11 show the ERA5 IVT (kg m^{-1} s^{-1}) and 250 hPa geopotential heights (dekameters) and Figures 4.10 and 4.12 show the WRF precipitation (mm $hour^{-1}$) and IVT (contours every 250 kg m^{-1} s^{-1}) every 6 hours for the duration of the AR event $\pm$ 1 day to capture the onset and end of the events. ERA5 is used to describe the underlying synoptic conditions of the AR events (e.g., 250 hPa geopotential heights and IVT), as the outer domain of the WRF simulation does not cover the large spatial extent of the ARs. When compared to the WRF output, ERA5 IVT and 250 hPa geopotential heights were consistent. Because both of these AR events were quasi-stationary, 6-hourly results were sufficient to capture the large scale dynamics.

January 2002 Event

On 10 January 2002 00 UTC (Fig. 4.9a), a cyclone associated with an upper-level trough centered at 35°E and 35°N propelled moisture in the area ahead of the cold front that appears to be sourced from the Red Sea and Persian Gulf. At the onset of the January 2002 AR event, there was no anticyclone over the Arabian Sea, unlike the February 2010 case. By 12 UTC on 10 January (Fig. 4.9c), an anticyclone did form over the very northern basin of the Arabian Sea, adding to the moisture of the AR all the way through 13 January 00 UTC (Fig. 4.9m). The IVT of this AR reached above 500 kg m^{-1} s^{-1}, but was contained to a small core within the AR. The anticyclone centered at 60°E and 30°N aided in the moisture of the AR reaching Northwestern HMA at latitudes greater than 40°N on 12 January (Figs. 4.9i-l). For most of 12 January, the moisture from the AR across western HMA is northwesterly, resulting in less than 2 mm per hour of precipitation. Starting on 13 January 00 UTC (Fig. 4.9m), the upper level trough disappears, turning the orientation of the IVT to have more zonal flow. Most of the

precipitation for this event occurs in western HMA between 13 January 00 UTC and 14 January 06 UTC, when the head of the AR transitions from westerly to southerly, forcing some moisture directly perpendicular to the topography of western HMA (Fig. 4.10m-r). For the most part, the flow of this AR is zonal, resulting in less precipitation than during the February 2010 event.

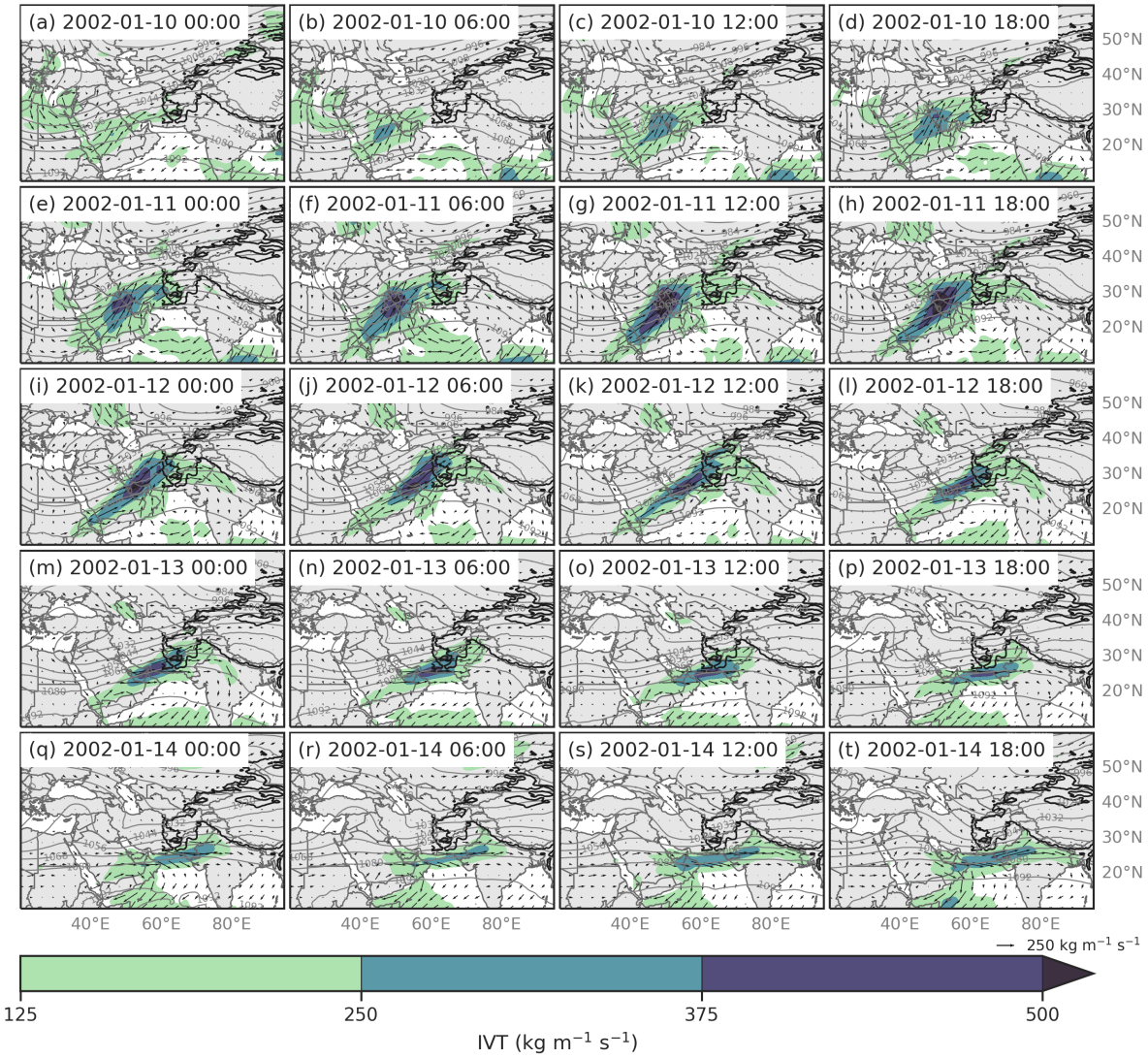

Figure 4.9: (a) ERA5 IVT (shaded and vectors, kg m^{-1} s^{-1}) and 250 hPa geopotential heights (contours, m) at 10 January 2002 00 UTC. The black contour is the location of 1-km elevation. (b-t) Same as (a) but for every 6 hours between 10 January 06 UTC to 14 January 18 UTC.

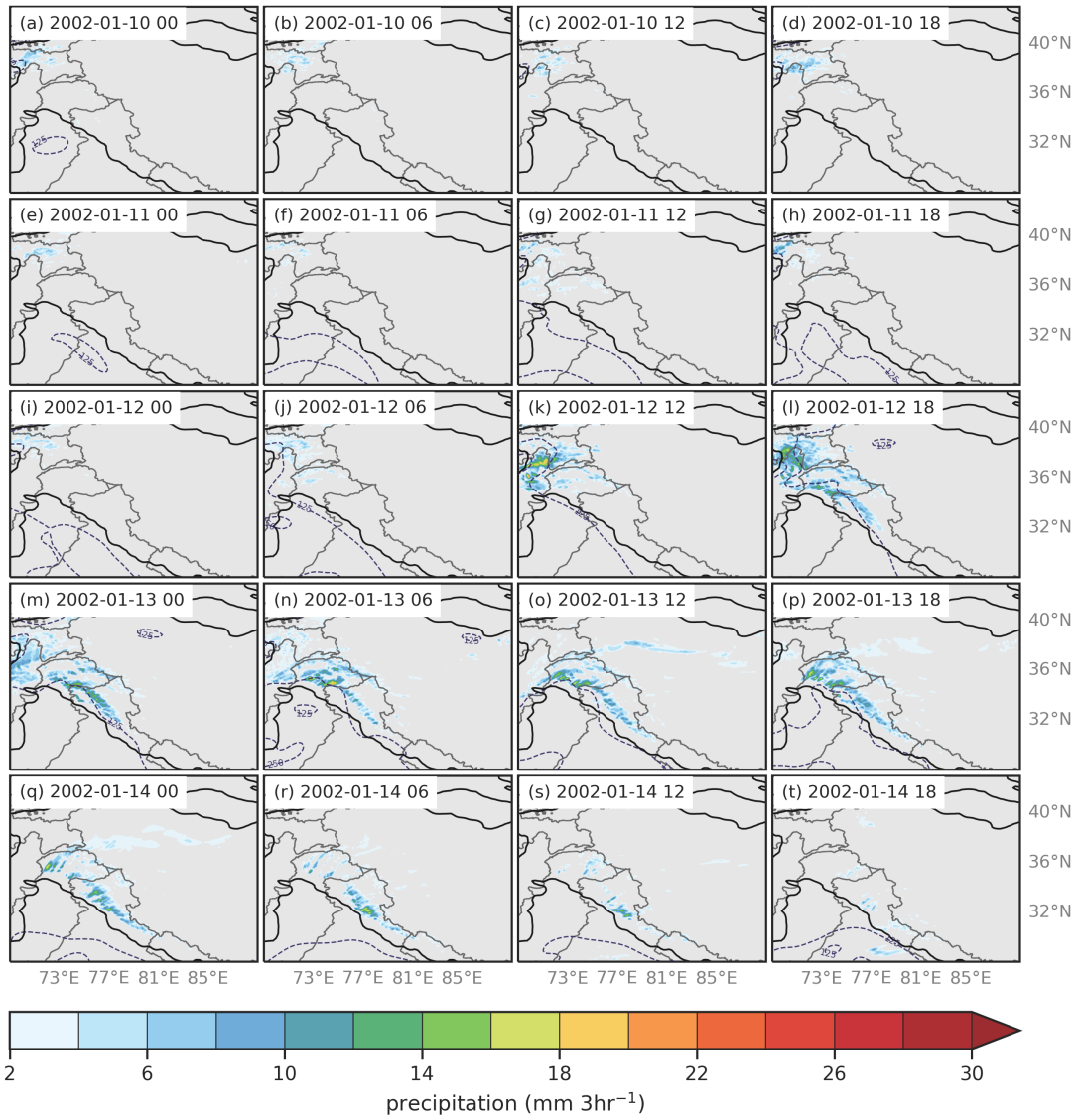

Figure 4.10: (a) WRF 6.7 km precipitation (shaded, mm 3-hr^{-1}) and IVT (dashed contour, kg m^{-1} s^{-1}) at 10 January 2002 00 UTC. The black contour is the location of 1-km elevation. (b-t) Same as (a) but for every 6 hours between 10 January 06 UTC to 14 January 18 UTC.

February 2010 Event

On 4 February 2010 00 UTC (Fig. 4.11a), an upper level closed low centered at about 35°E and 40°N with characteristics typical of a midlatitude weather system or a winter westerly disturbance aided in the formation of an AR in the area ahead of the cold front. The moisture in this AR was likely sourced from the Red Sea, Persian Gulf, and anticyclonic flow over the Arabian Sea. By 5 February 2010 00 UTC (Fig. 4.11e), the AR had formed into the more long, thin, filamentary feature that is typically associated with ARs. The moisture in the core of the AR had intensified from 250 kg m^{-1} s^{-1} to about 500 kg m^{-1} s^{-1} and had reached the Hindu Kush, Pamirs, and Tien Shan mountain ranges. The onset of precipitation starts when the moisture from the AR reaches these high elevation regions during 5 February (Fig. 4.12g-h). Between 5-6 February (Figs. 4.11e-l), the upper level trough northwest of the Hindu Kush weakened while the ridge over the Arabian Sea remained in place, aiding in funneling the moisture from the AR into northwest HMA, western HMA, and Central Himalayas, decreasing the IVT within the AR to less than 375 kg m^{-1} s^{-1} and reducing the precipitation across western HMA. By 7 February 2010 00 UTC (Fig. 4.11m), the anticyclone over the Arabian Sea had shifted eastward to sit directly over India for the next few days, encouraging additional moisture from the Bay of Bengal to be anticyclonically circulated around India and back up into the AR, increasing the moisture content within the AR back up to above 500 kg m^{-1} s^{-1} and increasing the precipitation rate across the Hindu Kush and Western HMA to above 7 mm per hour (Fig. 4.12m). A new anticyclonic circulation that appeared centered at 50°E and 10°N on 8 February (Fig. 4.11q-t) provided additional moisture for the AR from the Arabian Sea, but the relatively stationary midlatitude conditions (i.e., trough centered at 60°E and ridge centered at 80°E) were more important to pull the moisture all the way to HMA for such an extended period of time. The precipitation

in Western HMA was at it's most intense during 8 February, when the orientation of the AR was perpendicular to the topography. By 9 February 6 UTC, the upper level trough and ridge shifted eastward and weakened so that the AR began to quickly dissipate (Fig. 4.11v).

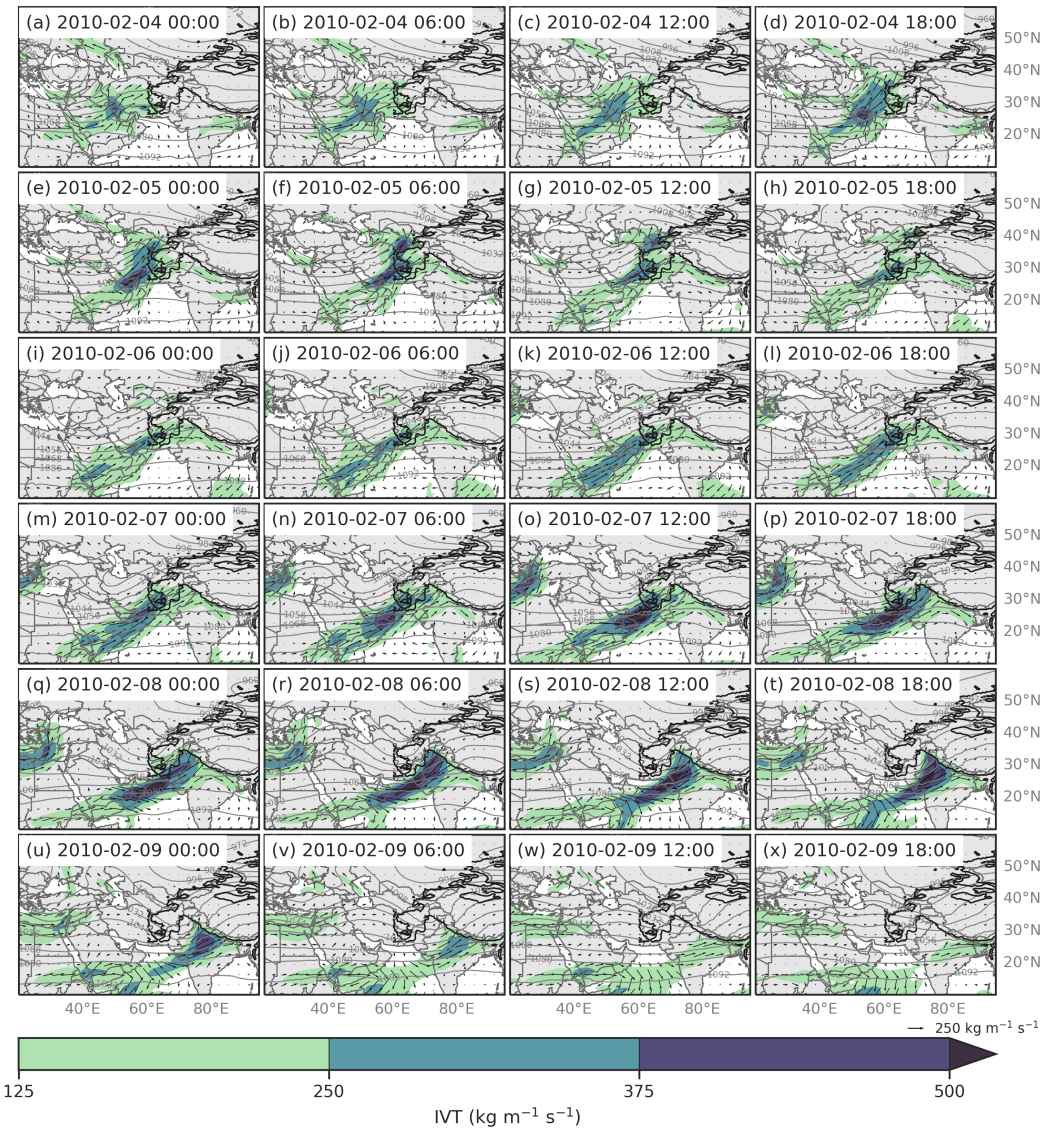

Figure 4.11: (a) ERA5 IVT (shaded and vectors, kg m^{-1} s^{-1}) and 250 hPa geopotential heights (contours, m) at 4 February 2010 00 UTC. The black contour is the location of 1-km elevation. (b-x) Same as (a) but for every 6 hours between 4 January 06 UTC to 9 February 18 UTC.

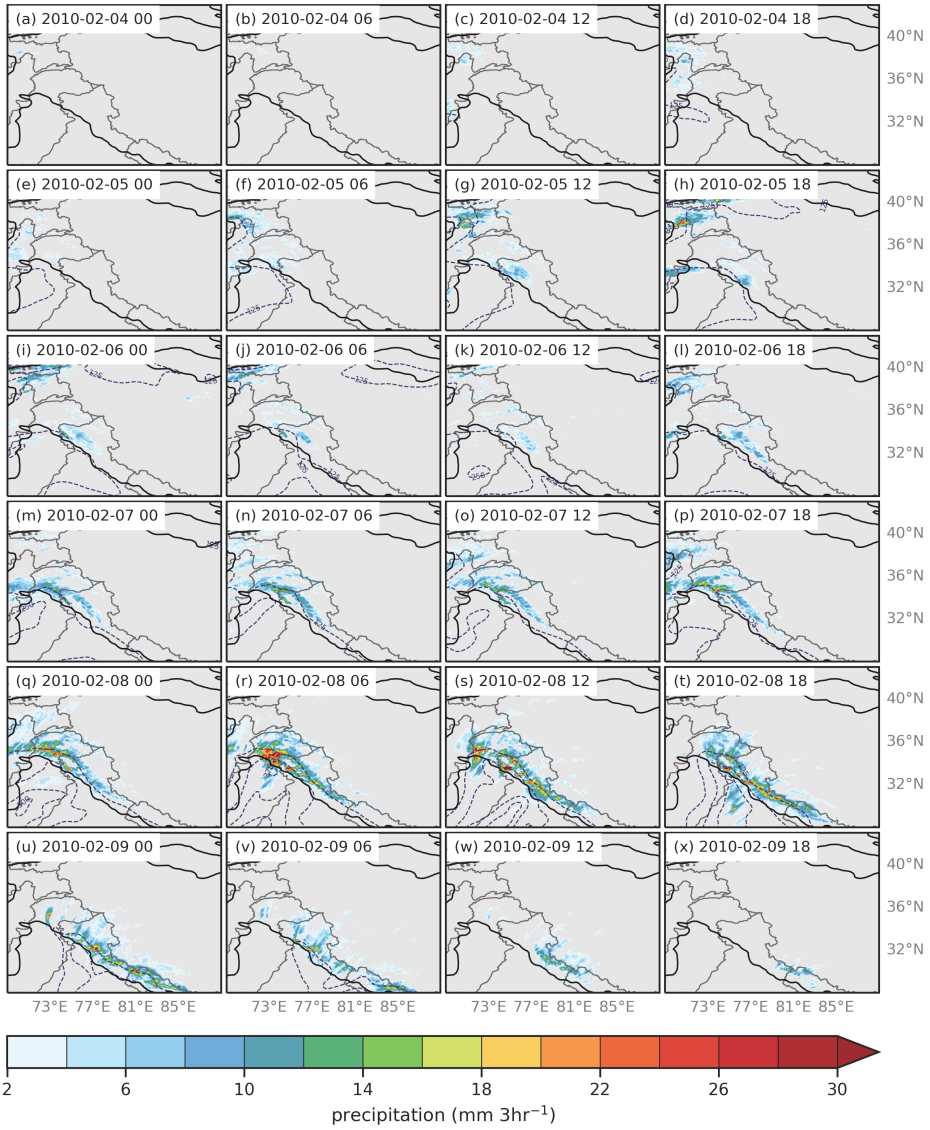

Figure 4.12: (a) WRF 6.7 km precipitation (shaded, mm 3-hr^{-1}) and IVT (dashed contour, kg m^{-1} s^{-1}) at4 February 2010 00 UTC. The black contour is the location of 1-km elevation. (b-x) Same as (a) but for every 6 hours between 4 January 06 UTC to 9 February 18 UTC.

Both events show that the majority of their precipitation falls in western HMA when the IVT becomes terrain locked in the "notch" or area that is enclosed on three sides by high elevation mountains. The terrain in the area of this western HMA notch, identified in Lang and Barros (2004), combined with the location of the subtropical jet, increases the likelihood that an extratropical cyclone remains quasi-stationary in this area, increasing the orographic precipitation in western HMA. The precipitation patterns during both our AR events are consistent with the January 1999 extreme precipitation event, described in Norris et al. (2015) as a western notch pattern. This is unsurprising, considering that the classification completed in Nash et al. (2021) identified 10 January 1999 as a Western HMA AR type. This indicates the utility provided by the HMA AR Types from Nash et al. (2021) in identifying winter precipitation variability in HMA.

4.3.5 Mesoscale Characteristics of the HMA AR Case Studies

The following discussion investigates the mesoscale conditions for the differing ARs to better understand the possible mechanisms for the differing orographic precipitation amounts and types (i.e., snow, rain) in western HMA. We expected that the precipitation simulated for these AR events required a general combination of lift, moisture, and instability. Using along AR cross-sections (see yellow lines in Figs. 4.13a and 4.14a), we show the horizontal water vapor flux (m s^{-1}), equivalent potential temperature contours (K), potential temperature contours (K), vertical velocity (m s^{-1}), snow-water mixing ratio (g kg^{-1}), and water vapor mixing ratio (g kg^{-1}) interpolated to height above ground level (km) at 13 January 2002 00 UTC and 8 February 2010 00 UTC. Results for other times during the AR events were consistent with the times shown here; therefore, we only show the day of peak IVT for each event to allow for easier comparison

between the two dates.

On 13 January 2002 00 UTC, the IVT has a more zonal component as it crosses the Hindu Kush, and then turns into more of a southwesterly flow in western HMA, getting caught in the western notch (Fig. 4.13a, h). The western cross-section (4.13b) shows that the IVT within the AR south of 29.8°N extends from the surface to 8 km, peaking at 0.04 m^{-1} s^{-1} between 4-7 km. The moisture in the AR appears to be following the isentropes as they slope down at 29.8°N and then gently slope upward between 31.4°N and 34.4°N. Vertical velocity (Fig. 4.13e) shows that there is upward motion on the windward side of each peak, accompanied by negative vertical velocity on the lee side of the slopes. The above-average freezing level, which is above 4 km until about 31.4°N keeps the snow-water mixing low (Fig. 4.13h). However, unlike the February 2010 case, there is no rainfall in the foothills. We think this is because most of the moisture from the AR is above the height of the freezing level north of 31.4°N, so all the precipitation falls as snow, coinciding with the snow water mixing ratio of up to 0.3 g kg^{-1} (Fig. 4.13h). The eastern cross-section (Fig. 4.13c) shows moisture near the ocean surface south of 25.7°N and the moisture from the AR is aloft between 4 and 8 km north of 25.7°N, as this area is downwind of the zonally advecting AR. There is a peak in snowfall that coincides with the first tall mountain peak and snow water mixing ratio up to 0.6 g kg^{-1} (Fig. 4.13i), north of 32.6°N that implies that the moisture was forced orographically.

The westernmost cross-section for the February 2010 case (Fig. 4.14b) shows that the moisture from the AR is already aloft at 29.8°N, with a maximum of water vapor flux at 0.16 m s^{-1} around 3 km in elevation. Compared to the climatological vertical profile of water vapor flux from the past AR events that reached Western HMA, the February 2010 AR was extremely moist with maximum moisture peaking at a higher than average pressure level. At 29.8°N (roughly above the first mountain peak), the

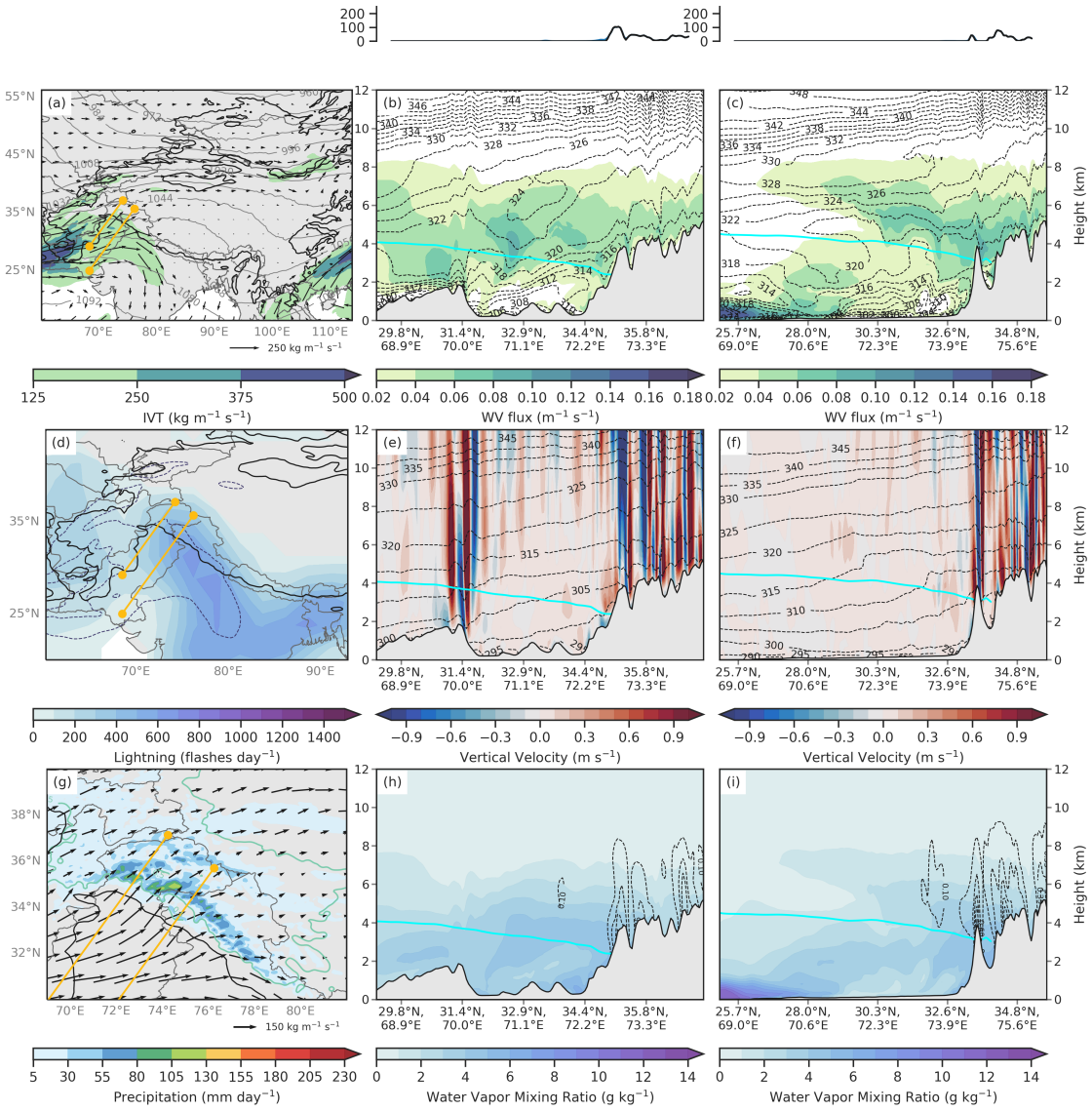

Figure 4.13: (a) WRF 20 km IVT (shaded and vectors, kg m^{-1} s^{-1}) on 13 January 2002 00 UTC. The black contour is 1-km elevation. The left yellow line indicates the cross-section for (b) and the right yellow line is the cross-section (c). (b) WRF 6.7 km water vapor flux (shaded, m s^{-1}) and θ_E (dashed contour, K) interpolated to height above ground level (km). The cyan line is the height of the 0°C isotherm. The line plot above is WRF 6.7 km total precipitation (mm, blue line) and snow (mm, black line) along the same cross-section. (d) TRMM LIS-OTD lightning (shaded, flashes day^{-1}) and WRF 20 km IVT (dashed contours, every 125 kg m^{-1} s^{-1}). (e) WRF 6.7 km potential temperature (dashed contour, K) and vertical velocity (shaded, m s^{-1}). (g) WRF 6.7 km precipitation (shaded, mm day^{-1}), fraction of frozen precipitation (blue contour, at 0.5 and 1.0), and IVT (dashed contours, every 125 kg m^{-1} s^{-1}). (h) WRF 6.7 km snow water mixing ratio (contour, g kg^{-1}) and water vapor mixing ratios (shaded, g kg^{-1}). (c, f, i) Same as (b, e, h) but for the eastern cross-section.

air is unstable at 3 km and 4.25 km in elevation, supporting the moist air aloft (Fig. 4.14e). There is a maximum in vertical velocity on the lee side of the slope just south of 31.4°N associated with a vertically homogeneous theta-e zone, and a maximum of snow-water mixing ratio, where a very minimal amount of rainfall occurs (Fig. 4.13b, e, h). The moisture in the AR moves below 2 km on the lee side of the slope around 31.5°N before it is orographically lifted to 4 km on the second main peak it encounters at 34.4°N (Fig. 4.14b). Just south of 34.4°N there is a peak in rainfall in the foothills (about 100 mm) as the moisture is orographically lifted. There is an area of potential instability in the foothills north of 34.4°N, diagnosed by the tightly packed isentropes (theta-e) as well as another vertical velocity maximum (Fig. 4.14b, e). This, along with the sharp decrease in the freezing level height, may explain the peak in snowfall just north of 34.4°N, with a snow-water mixing ratio greater than 0.35 g kg^{-1} (Fig. 4.14h). It is around the location of the transition from rainfall to snowfall where one of the landslides occurred on 8 February 2010 at 73°E, 34°N, unsurprising with almost 250 mm of snow falling in under 3-hours. There is another small peak in snowfall as the remaining moisture is orographically lifted in the steep terrain south of 35.8°N that is associated with a maximum of snow water mixing ratio above 1 g kg^{-1} (Fig. 4.14h).

In the eastern cross-section for February 2010 (Fig. 4.14c), there is a layer of moisture close to the surface south of 25°N, that is slightly lifted, most likely due to the moisture in the AR making landfall, or crossing from ocean to land. Additionally, there is moisture aloft between 4 and 6 km but once it reaches 28°N, it descends to 2-4 km as it moves closer to HMA, falling below the zero degree isotherm, following the isentropes (theta-e) (Fig. 4.14c). Snow-water mixing ratio within this moisture aloft reaches 0.6 g kg^{-1} and water vapor mixing ratio is below 4 g kg^{-1} (Fig. 4.14i). Then, similar to the western cross-section, there is an area of potential instability in the foothills north of 32.6°N, providing lift for the moisture and resulting in rainfall and

then snowfall when the height of the freezing level decreases. Orographic lift of the remaining moisture results in a secondary peak of snow, south of 34.8°N (Fig. 4.14c).

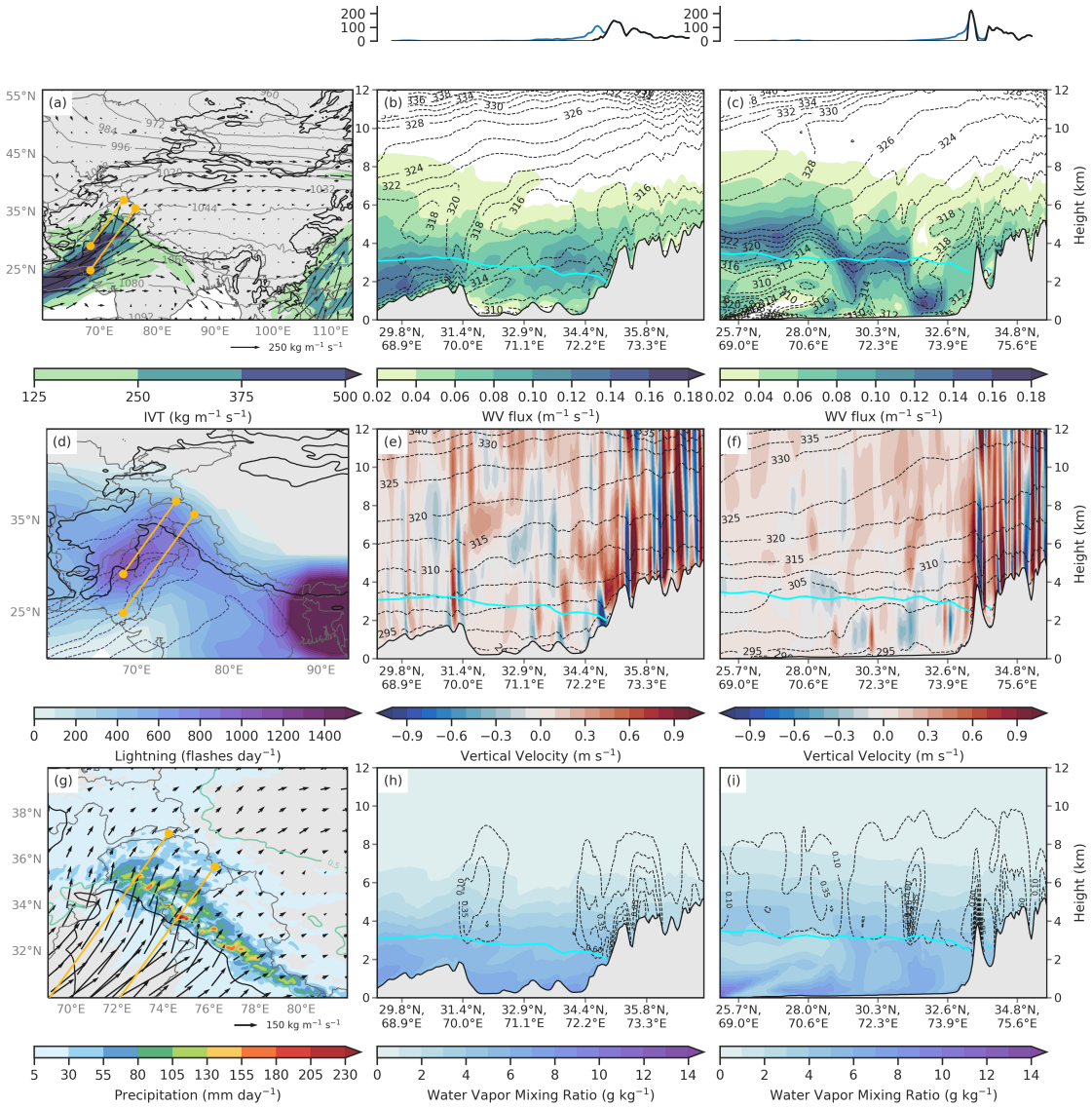

Figure 4.14: Same as Fig. 4.13 but for 8 February 2010 00 UTC.

The main differences between the two AR cases are the orientation of the AR axis, where the moisture during February 2010 was southerly, and directly perpendicular to the terrain, while the moisture during January 2010 was zonal (Figs. 4.13g and 4.14g). However, in January 2010, there are still indications that the moisture became terrain

locked in the western HMA notch, resulting in 100 mm precipitation totals in some locations (Fig. 4.13g). With the higher elevation freezing level in the January 2002 case, it does appear that there was significantly less frozen precipitation compared to the February 2010 case, despite increased rainfall in the February 2010 case (Fig. 4.13h, i and 4.14h, i). The cross-sections for both cases show that the freezing level descends as the latitude increases, but the moisture above the freezing level in the January 2002 case provides context for the lack of rainfall in the foothills (Fig. 4.13b). The February 2010 case, which had a lower than average freezing level in western HMA, had more rainfall than the January 2002 case, which seems to be because the moisture in the February 2010 AR was lower than the moisture in the January 2002 cases respective each to their own freezing level height (Fig. 4.14b). It also appears that the height of the freezing level influenced the number of lightning flashes during each event where, in western HMA, there were roughly 10,000 lightning flashes for the duration of the January AR while 25,000 lightning flashes occurred during the February 2010 AR (Fig. 4.13d and 4.14d). Similar to Nash and Carvalho (2020), the lowered height of the freezing level during the February 2010 case potentially increased the number of lightning flashes in western HMA. This also aligns with previous studies, who recognized that in addition to terrain slope, an increase in the ice within clouds increases the lightning flash rate (Blyth et al., 2001; Dye et al., 2000; Lal & Pawar, 2009; Pawar et al., 2015).

4.3.6 Thermodynamic Characteristics of the HMA AR Case Studies

To facilitate discussion of the orographic impacts on moisture and precipitation, we focus on zonally oriented cross-sections along the areas of topography that appear to receive most of their precipitation during Western HMA AR events (for cross-section

locations, see Fig. 4.1a). The locations of the cross-sections fall roughly within the Foothill Zone and Montane Zone of HMA, or around 1 km and 3 km respectively. We consider the temporal evolution of IVT and precipitation along these cross-sections in Fig. 4.15 where IVT (kg m^{-1} s^{-1}) is shaded and precipitation (mm hr^{-1}) is contoured and Fig. 4.16 breaks down the differences between snow (shaded, mm hr^{-1}) and rain (contoured, mm hr^{-1}). Noticeably, IVT maximums and precipitation maximums do not always align, with the IVT maximum occurring in the lower elevations while precipitation maximums occur in higher elevations (Fig. 4.15). For both events, there was more snow compared to rain, and the rain occurred at lower elevation than snow (Fig. 4.16). The duration of IVT greater than 50 kg m^{-1} s^{-1} is longer during the February 2010 event compared to the January 2002 event, which was expected given that the February 2010 event lasted about 18 hours longer than the January 2002 event (Fig. 4.15). Coinciding with IVT values greater than 50 kg m^{-1} s^{-1}, precipitation duration was longer during the February 2010 event compared to the January 2002 event (Fig. 4.15). Both events have similar IVT maximums (February 2010 at 300 kg m^{-1} s^{-1}, and January 2002 at 250 kg m^{-1} s^{-1}) at 33.9°N and 74.7°E for less than 3 hours in the Foothill Zone (Fig. 4.15a, c). Another notable difference is that the onset of the February 2010 AR was relatively uniform along both cross-sections, with a slight delay in onset in the eastern region of Western High Mountain Asia while the onset of the January 2002 AR began sooner in the western region of the cross-section and the onset in the eastern region over 48 hours later (Fig. 4.15). This is likely because the orientation of the IVT within the AR was more southerly in the western region and more westerly in the eastern region during the January 2002, delaying the onset east of 70.8°E. Another interesting observation is that the diurnal cycle seems to influence the timing of the rainfall more than the snow in the foothills, with increased rainfall around 6 UTC each day (Fig. 4.16a, c).

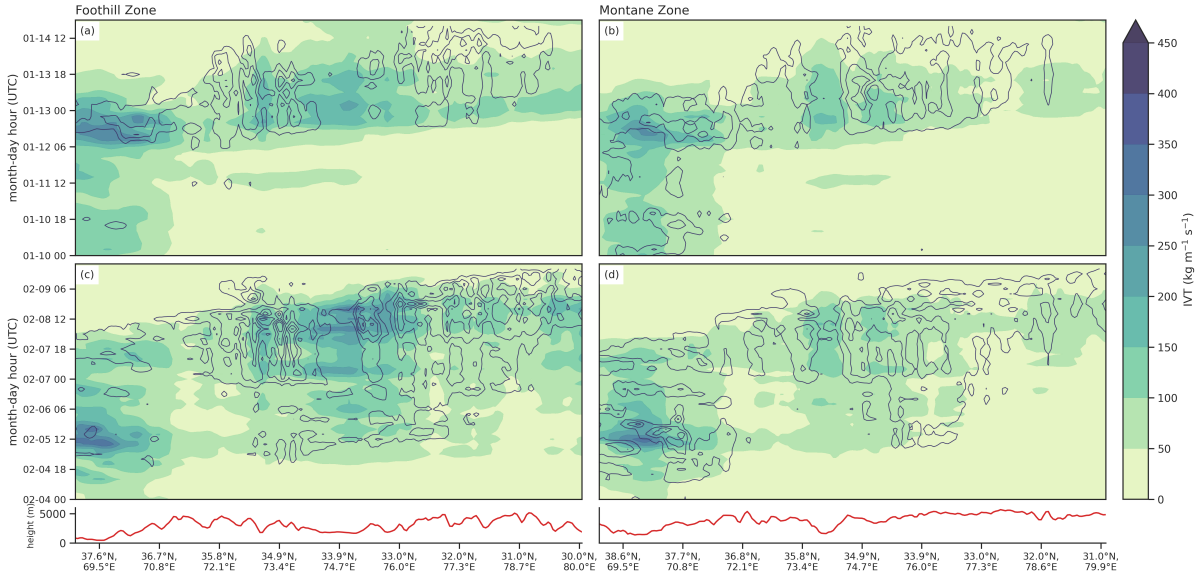

Figure 4.15: (a) WRF 6.7 km IVT (shaded, kg m^{-1} s^{-1}) and precipitation (contour, mm hr^{-1}) along the zonally oriented cross-section (extent shown in Fig. 4.1) every 3 hours in the Foothill Zone for the January 2002 AR event. (b) Same as (a) but along the cross-section in the Montane Zone. (c) Same as (a) but for the February 2010 AR event. (d) Same as (b) but for the February 2010 AR event. The elevation (red line, m), latitudes, and longitudes of their respective cross-sections are on the bottom of the figure for reference.

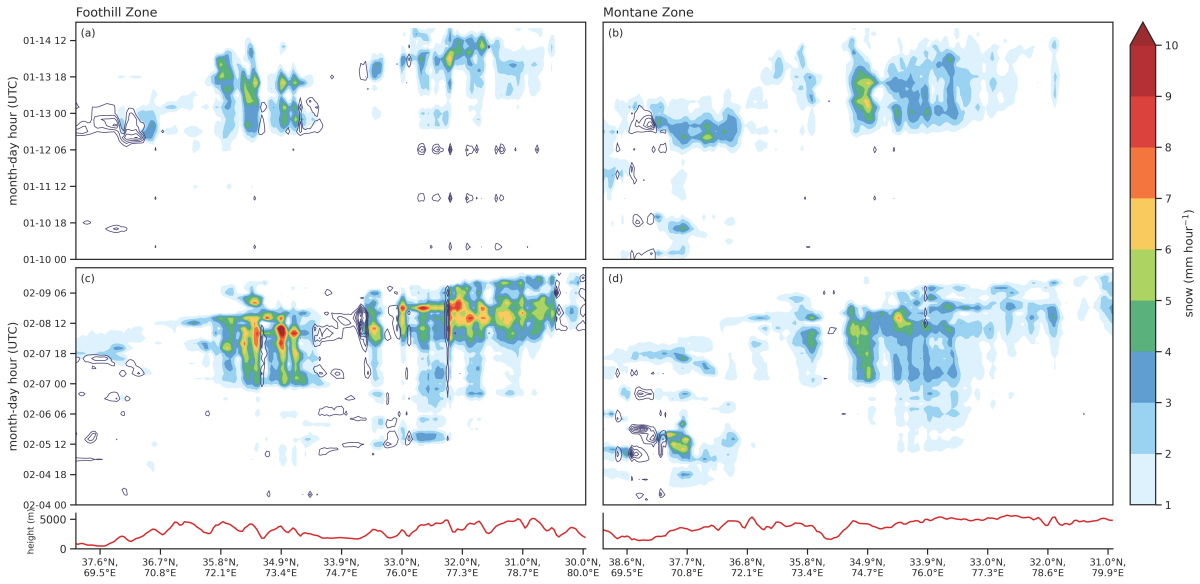

Figure 4.16: (a) WRF 6.7 km Snow (shaded, mm hr^{-1}) and rainfall (contour, mm hr^{-1}) along the zonally oriented cross-section (extent shown in Fig. 4.1) every 3 hours in the Foothill Zone for the January 2002 AR event. (b) Same as (a) but along the cross-section in the Montane Zone. (c) Same as (a) but for the February 2010 AR event. (d) Same as (b) but for the February 2010 AR event. The elevation (red line, m), latitudes, and longitudes of their respective cross-sections are on the bottom of the figure for reference.

Focusing on two locations that appear to be hot spots for precipitation during these ARs with differing elevations (locations are black triangles in Fig. 4.1a), Fig. 4.17 shows the precipitation rate (mm hour^{-1}), water vapor flux (m^{-1} s^{-1}, and equivalent potential temperature (K) every 3 hours interpolated to height above ground level (km). The grid cell nearest 32.18°N and 72.82°E has an elevation of 3.61 km and accumulated 160 mm of precipitation during the January 2002 event and over 450 mm of snow during the February 2010 event (Fig. 4.8a, b). Most of the water vapor flux during the February 2010 event is below 8 km, while water vapor flux during the January 2002 event reaches 9 km in elevation. Both events have a maximum water vapor flux of 0.07 m^{-1} s^{-1} around 4.5 km in elevation (Fig. 4.17c, g). At the grid cell closest to 33.73°N, 74.82°E where the elevation is 2.12 km, both AR events saw higher water vapor flux of 0.14 m^{-1} s^{-1} during the February 2010 AR and 0.08 m^{-1} s^{-1} during the January 2002 AR peaking below 5 km (Fig. 4.17d, h). The water vapor flux quickly intensifies on 8 February 2010, with a rain rate of 20 mm hour^{-1} (Fig. 4.17f, h). For both locations on 5 February 2010, the low-level moisture advection (between 4-6 km) from the AR increases theta-e 16°K in less than 12 hours between 0 and 12 UTC. (Fig. 4.17c, d, g, h). Theta-e oscillates in the low levels as moisture convergence results in precipitation, and once the condensed water vapor cools and precipitates on 8 February 2010, theta-e decreases about 10°K per 12 hours between 12 UTC and 0 UTC (Fig. 4.17g, h). Moisture increase from advection has a much shorter duration during January 2002, where theta-e decreases about 6°K between 4-8 km by 12 January 2002 13 UTC and then increases about 6-8°K by 13 January 2002 11 UTC (Fig. 4.17c, d). If we look at the rain rates at 33.73°E, 74.82°N during the February 2010 AR (Fig. 4.17f), we see the same diurnal patterns we identified in Fig. 4.16.

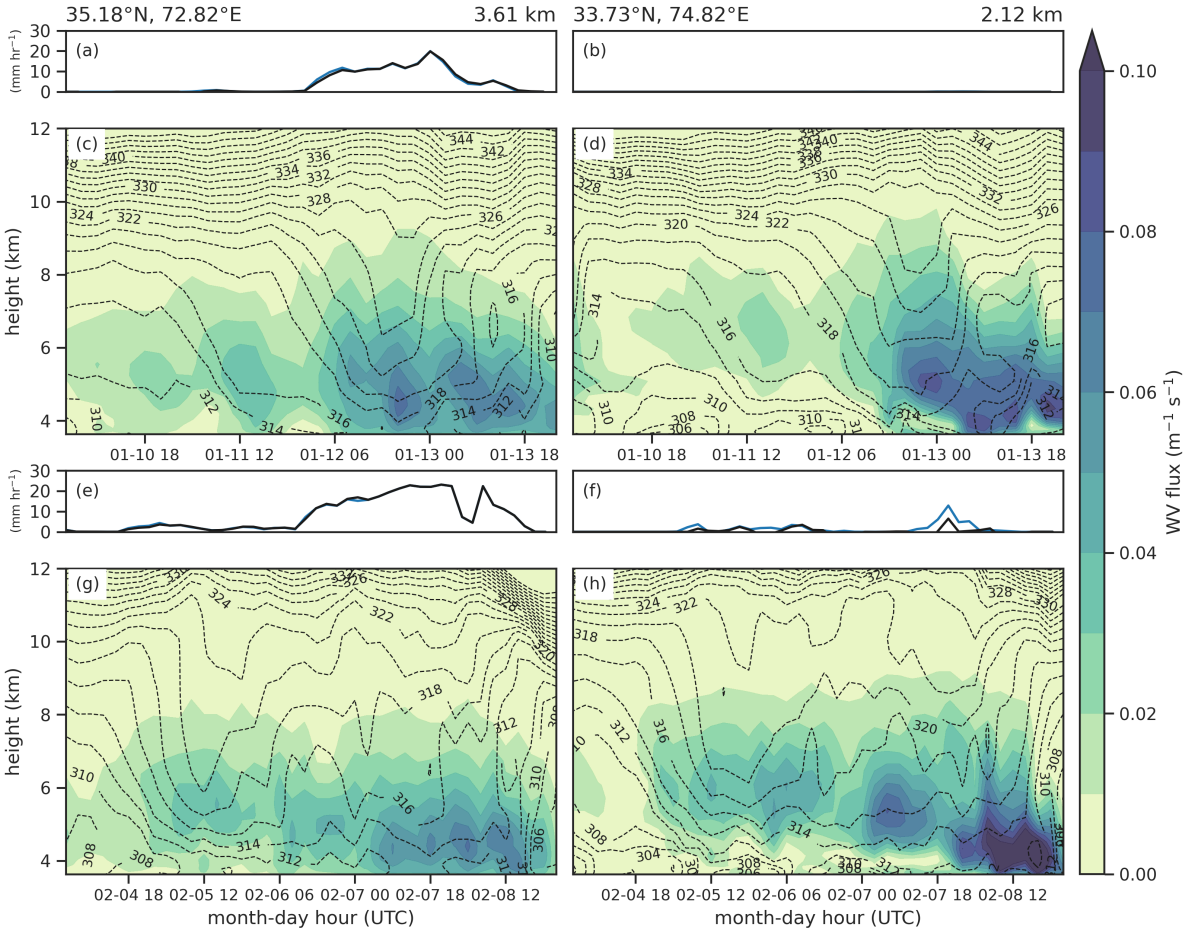

Figure 4.17: (a) WRF 6.7 km precipitation (blue line, mm hr^{-1}) and snow (black line, mm hr^{-1}) at the grid cell closest to 35.18°N, 72.82°E for the duration of the January 2002 AR event. (b) Same as (a) but for the grid cell closest to 33.73°, 74.82°E. (c) WRF 6.7 km water vapor flux (shaded, m^{-1} s^{-1}) and equivalent potential temperature (contours, K) at the grid cell closest to 35.18°N, 72.82°E every 3 hours for the duration of the January 2002 AR. (e) Same as (a) but for the February 2010 AR. (f) Same as (b) but for the February 2010 AR. (g) Same as (c) but for the February 2010 AR. (h) Same as (d) but for the February 2010 AR. For the spatial locations of the grid cells, see the black triangles in Fig. 4.1.)

4.4 Conclusions

Between 1979 and 2015, the frequency of ARs crossing southwest Asia has increased during January and February. Additionally, southerly IVT has significantly increased in western HMA during winter Western HMA ARs, indicating that in recent decades, there has been an increase in the frequency and intensity of Western HMA ARs. Considering the warming temperature trend across HMA, combined with the large fraction of total winter precipitation ARs contribute across HMA, it is imperative to examine the mesoscale features of these ARs to determine their local influence on orographic precipitation and associations with precipitation-related hazards such as lightning and landslides. We show that the height of the 0°C isotherm has been increasing all across HMA, significantly so across central and eastern HMA, and that there is significantly more frozen precipitation during HMA ARs occurring with a below-average freezing level height compared to HMA ARs with an above-average freezing level height. Focusing on two impactful western HMA ARs, we compare and contrast their mesoscale characteristics to determine the influence of the height of the freezing level on orographic precipitation. Additionally, we show what mechanisms are important for improving the efficiency of AR-related precipitation in western HMA.

The first AR occurred in February 2010, lasted for about 5 days, resulted in about 250 mm of precipitation, reaching 450 mm in some locations, and was related to three separate landslide events along the windward ridge of western HMA. The second AR occurred in January 2002, lasted for about 3 days, resulted in about 100 mm of precipitation across western HMA, and was not related to any identified landslides. Both events had secondary bands of precipitation (up to 100 mm) that formed on ridges downwind. We selected these cases because they both were Northwestern HMA AR types that transitioned to Western HMA AR types, and they resulted in above 85th

percentile of precipitation for western and/or northwestern HMA. One of the main differences between the February 2010 case and the January 2002 case was that the height of the freezing level in western HMA during the AR was above-average during the January 2002 case and below-average during the February 2010 case, which potentially resulted in a higher fraction of frozen precipitation during the February 2010 case compared to the January 2002 AR. Our results show that both events were quasi-stationary, with a trough located in NW HMA and anti-cyclonic circulation over India terrain-locking and orographically lifting the moisture within the AR plume, resulting in extreme precipitation. However, the trough at the time of peak IVT in the January 2002 case was west of the trough during the time of peak IVT in the February 2010 case, so that by the time the plume of AR moisture became terrain-locked in the western HMA notch, the IVT magnitude was lower, and the upper level geopotential heights were more zonal. This reflected in the mesoscale analysis as the February 2010 case having southerly AR moisture flowing directly perpendicular to the topography, while the AR moisture in the January 2002 case was much more southwesterly. Similar to the findings in Norris et al. (2015), it appears that the orientation of the axis of the AR and the duration of the AR appear to influence the efficiency of the orographic precipitation more than the amount of IVT.

The moisture in the February AR was much lower in elevation relative to the freezing height level (3 km), centered just below 4 km in the lower latitudes, while the majority of the moisture in the January 2002 AR was above the height of the freezing level (4 km), between 4 and 6 km. This is perhaps the main reason that we see more rainfall in the foothills during the February 2010 case, despite the lower than average freezing level. Once the moisture in both cases reached the mountains, it ascended and as a result, snow fell along the windward side of multiple peaks until the moisture from the AR was gone. The lowered freezing level in the February AR may have influenced

the frequency of lightning flashes in this region, as there were almost 25,000 lightning flashes in western HMA during this event. We also show that there were up to 10,000 lighting flashes during the January 2002 AR, highlighting the connection between ARs and lightning that was introduced in Nash and Carvalho (2020).

This work illustrates the importance of the height of the freezing level and other mesoscale mechanisms on local, orographic precipitation during Western HMA ARs. We show that in recent decades, along with the increase of the height of the freezing level across HMA, the frequency and intensity of Western HMA ARs has increased, and that when the height of the 0°C isotherm is above-average, there is significantly less frozen precipitation. Our research shows the impact of ARs as they cross HMA and result in extreme precipitation if the orientation of the AR axis is perpendicular to the complex topography. We uncovered more information on the relationship between ARs and precipitation-triggered landslides in our analysis of the February 2010 AR. We show the water vapor flux along the AR in the February 2010 event is orographically lifted in a potentially unstable environment near the foothills of HMA, resulting in a combination of rain and snow of about 100 mm $hour^{-1}$, potentially triggering multiple landslides across western HMA. However, the 6.7 km spatial resolution simulation is not fine scale enough to resolve the complex orographic processes, and further downscaling to 3 or 1 km resolution may be necessary to fully resolve all the meteorological characteristics of this particular event. Improved understanding of the meteorological characteristics during these extreme HMA ARs could potentially improve landslide predictability in western HMA.

4.4.1 Declarations and Funding

This research is part of the Blue Waters sustained-petascale computing project, which is supported by the National Science Foundation (awards OCI-0725070 and ACI-1238993) the State of Illinois, and as of December 2019, the National Geospatial-Intelligence Agency. Blue Waters is a joint effort of the University of Illinois at Urbana-Champaign and its National Center for Supercomputing Applications. NASA Headquarters under the NASA Earth and Space Science Fellowship Program - Grant 80NSSC18K1412 supported a portion of this research. The 20 km and 6.7 km WRF simulations were supported by the Climate and Large-scale Dynamics Program, from the National Science Foundation (NSF award-AGS 1116105).

References

Blyth, A. M., Christian, H. J., Driscoll, K., Gadian, A. M., & Latham, J. (2001). Determination of ice precipitation rates and thunderstorm anvil ice contents from satellite observations of lightning. *Atmospheric Research*, *59-60*, 217–229. https://doi.org/10.1016/S0169-8095(01)00117-X

Cannon, F., Hecht, C. W., Cordeira, J. M., & Ralph, F. (2018). Synoptic and Mesoscale Forcing of Southern California Extreme Precipitation. *Journal of Geophysical Research: Atmospheres*, *123*(24), 714–13. https://doi.org/10.1029/2018JD029045

Cecil, D. J. (2015). LIS/OTD Gridded Lightning Climatology Data Collection Version 2.3.2015. *NASA EOSDIS Global Hydrology Resource Center Distributed Active Archive Center Huntsville, Alabama, U.S.A, accessed 20 August 2019*. https://doi.org/http:/dx.doi.org/10.5067/LIS/LIS-OTD/DATA311

DeFlorio, M. J., Waliser, D. E., Ralph, F., Guan, B., Goodman, A., Gibson, P. B., Asharaf, S., Monache, L. D., Zhang, Z., Subramanian, A. C., Vitart, F., Lin, H., & Kumar, A. (2019). Experimental Subseasonal-to-Seasonal (S2S) Forecasting of Atmospheric Rivers Over the Western United States. *Journal of Geophysical Research: Atmospheres*, *124*(21), 11242–11265. https://doi.org/10.1029/2019JD031200

Dye, J. E., Ridley, B. A., Skamarock, W., Barth, M., Venticinque, M., Defer, E., Blanchet, P., Thery, C., Laroche, P., Baumann, K., Hubler, G., Parrish, D. D., Ryerson, T., Trainer, M., Frost, G., Holloway, J. S., Matejka, T., Bartels, D., Fehsenfeld, F. C., ... Zerr, R. (2000). An overview of the Stratospheric-Tropospheric Experiment:

Radiation, Aerosols, and Ozone (STERAO)-Deep Convection experiment with results for the July 10, 1996 storm. *Journal of Geophysical Research: Atmospheres*, *105*(D8), 10023–10045. https://doi.org/10.1029/1999JD901116

Espinoza, V., Waliser, D. E., Guan, B., Lavers, D. A., & Ralph, F. (2018). Global Analysis of Climate Change Projection Effects on Atmospheric Rivers. *Geophysical Research Letters*, *45*(9), 4299–4308. https://doi.org/10.1029/2017GL076968

Guan, B., & Waliser, D. E. (2015). Detection of atmospheric rivers: Evaluation and application of an algorithm for global studies. *Journal of Geophysical Research: Atmospheres*, *120*(24), 12514–12535. https://doi.org/10.1002/2015jd024257

Guan, B., & Waliser, D. E. (2019). Tracking Atmospheric Rivers Globally: Spatial Distributions and Temporal Evolution of Life Cycle Characteristics. *Journal of Geophysical Research: Atmospheres*, *124*, 12523–12552. https://doi.org/10.1029/2019JD031205

Guan, B., Waliser, D. E., Ralph, F., Fetzer, E. J., & Neiman, P. J. (2016). Hydrometeorological characteristics of rain-on-snow events associated with atmospheric rivers. *Geophysical Research Letters*, *43*(6), 2964–2973. https://doi.org/10.1002/2016GL067978

Hersbach, H., Bell, B., Berrisford, P., Biavati, G., Horányi, A., Muñoz Sabater, J., Nicolas, J., Peubey, C., Radu, R., Rozum, I., Schepers, D., Simmons, A., Soci, C., Dee, D., & Thépaut, J.-N. (2018a). ERA5 hourly data on pressure levels from 1979 to present. https://doi.org/10.24381/cds.bd0915c6

Hersbach, H., Bell, B., Berrisford, P., Biavati, G., Horányi, A., Muñoz Sabater, J., Nicolas, J., Peubey, C., Radu, R., Rozum, I., Schepers, D., Simmons, A., Soci, C., Dee, D., & Thépaut, J.-N. (2018b). ERA5 hourly data on single levels from 1979 to present. https://doi.org/10.24381/cds.adbb2d47

Hersbach, H., Bell, B., Berrisford, P., Hirahara, S., Horányi, A., Muñoz-Sabater, J., Nicolas, J., Peubey, C., Radu, R., Schepers, D., Simmons, A., Soci, C., Abdalla, S., Abellan, X., Balsamo, G., Bechtold, P., Biavati, G., Bidlot, J., Bonavita, M., ... Thépaut, J. N. (2020). The ERA5 global reanalysis. *Quarterly Journal of the Royal Meteorological Society*, *146*(730), 1999–2049. https://doi.org/10.1002/qj.3803

Hewitt, K. (2005). The Karakoram Anomaly? Glacier Expansion and the 'Elevation Effect,' Karakoram Himalaya. *Mountain Research and Development*, *25*(4), 332–341. https://doi.org/10.1659/0276-4741(2005)025[0332:TKAGEA]2.0.CO;2

Hong, S. Y., Noh, Y., & Dudhia, J. (2006). A New Vertical Diffusion Package with an Explicit Treatment of Entrainment Processes. *Monthly Weather Review*, *134*(9), 2318–2341. https://doi.org/10.1175/MWR3199.1

Iacono, M. J., Delamere, J. S., Mlawer, E. J., Shephard, M. W., Clough, S. A., & Collins, W. D. (2008). Radiative forcing by long-lived greenhouse gases: Calculations

with the AER radiative transfer models. *Journal of Geophysical Research: Atmospheres*, *113*(D13), 13103. https://doi.org/10.1029/2008JD009944

Kääb, A., Berthier, E., Nuth, C., Gardelle, J., & Arnaud, Y. (2012). Contrasting patterns of early twenty-first-century glacier mass change in the Himalayas. *Nature*, *488*, 495–498. https://doi.org/10.1038/nature11324

Kain, J. S. (2004). The Kain–Fritsch Convective Parameterization: An Update. *Journal of Applied Meteorology and Climatology*, *43*(1), 170–181. https://doi.org/10.1175/1520-0450(2004)043

Kirschbaum, D., Adler, R., Hong, Y., Hill, S., & Lerner-Lam, A. (2010). A global landslide catalog for hazard applications: Method, results, and limitations. *Natural Hazards*, *52*, 561–575. https://doi.org/10.1007/S11069-009-9401-4/TABLES/3

Kirschbaum, D., Kapnick, S. B., Stanley, T., & Pascale, S. (2020). Changes in Extreme Precipitation and Landslides Over High Mountain Asia. *Geophysical Research Letters*, *47*(4), e2019GL085347. https://doi.org/10.1029/2019GL085347

Lal, D. M., & Pawar, S. D. (2009). Relationship between rainfall and lightning over central Indian region in monsoon and premonsoon seasons. *Atmospheric Research*, *92*, 402–410. https://doi.org/10.1016/J.ATMOSRES.2008.12.009

Lang, T. J., & Barros, A. P. (2004). Winter storms in the central Himalayas. *Journal of the Meteorological Society of Japan*, *82*(3), 829–844. https://doi.org/10.2151/jmsj.2004.829

Monin, A. S., & Obukhov, A. M. (1954). Basic laws of turbulent mixing in the surface layer of the atmosphere. *Originally published in Tr. Akad. Nauk SSSR Geophiz. Inst*, *24*(151), 163–187.

Nash, D., Carvalho, L. M. V., Jones, C., & Ding, Q. (2021). Winter and spring atmospheric rivers in High Mountain Asia: climatology, dynamics, and variability. *Climate Dynamics*. https://doi.org/10.1007/S00382-021-06008-Z

Nash, D., & Carvalho, L. M. (2020). Brief Communication : An electrifying atmospheric river – understanding the thunderstorm event in Santa Barbara County during March 2019. *Natural Hazards and Earth System Sciences*, *20*, 1931–1940. https://doi.org/10.5194/nhess-20-1931-2020

Neiman, P. J., Ralph, F., Wick, G. A., Lundquist, J. D., & Dettinger, M. D. (2008). Meteorological characteristics and overland precipitation impacts of atmospheric rivers affecting the west coast of North America based on eight years of SSM/I satellite observations. *Journal of Hydrometeorology*, *9*(1), 22–47. https://doi.org/10.1175/2007jhm855.1

Neiman, P. J., Schick, L. J., Ralph, F., Hughes, M., & Wick, G. A. (2011). Flooding in Western Washington: The Connection to Atmospheric Rivers*. *Journal of Hydrometeorology*, *12*(6), 1337–1358. https://doi.org/10.1175/2011jhm1358.1

Niu, G. Y., Yang, Z. L., Mitchell, K. E., Chen, F., Ek, M. B., Barlage, M., Kumar, A., Manning, K., Niyogi, D., Rosero, E., Tewari, M., & Xia, Y. (2011). The community Noah land surface model with multiparameterization options (Noah-MP): 1. Model description and evaluation with local-scale measurements. *Journal of Geophysical Research: Atmospheres*, *116*(D12), 12109. https://doi.org/10.1029/2010JD015139

Norris, J., Carvalho, L. M. V., Jones, C., & Cannon, F. (2015). WRF simulations of two extreme snowfall events associated with contrasting extratropical cyclones over the western and central Himalaya. *Journal of Geophysical Research: Atmospheres*, *120*(8), 3114–3138. https://doi.org/10.1002/2014JD022592

Norris, J., Carvalho, L. M., Jones, C., & Cannon, F. (2018). Deciphering the contrasting climatic trends between the central Himalaya and Karakorum with 36 years of WRF simulations. *Climate Dynamics*, 1–22. https://doi.org/https://doi.org/10.1007/s00382-018-4133-3

Norris, J., Carvalho, L. M., Jones, C., Cannon, F., Bookhagen, B., Palazzi, E., & Tahir, A. A. (2017). The spatiotemporal variability of precipitation over the Himalaya: evaluation of one-year WRF model simulation. *Climate Dynamics*, *49*(5-6), 2179–2204. https://doi.org/10.1007/s00382-016-3414-y

Oakley, N. S., Cannon, F., Munroe, R., Lancaster, J. T., Gomberg, D., & Ralph, F. (2018). Brief communication: Meteorological and climatological conditions associated with the 9 January 2018 post-fire debris flows in Montecito and Carpinteria, California, USA. *Natural Hazards and Earth System Sciences*, *18*(11), 3037–3043. https://doi.org/10.5194/nhess-18-3037-2018

Pawar, S. D., Gopalakrishnan, V., & Murugavel, P. (2015). Role of orography in inducing high lightning flash rate at the foothills of Himalaya Aeronomy. *Earth, Planets and Space*, *67*(51), 1–7. https://doi.org/10.1186/S40623-015-0221-3/FIGURES/5

Ralph, F., Rutz, J. J., Cordeira, J. M., Dettinger, M. D., Anderson, M., Reynolds, D., Schick, L. J., & Smallcomb, C. (2019). A scale to characterize the strength and impacts of atmospheric rivers. *Bulletin of the American Meteorological Society*, *100*(2), 269–289. https://doi.org/10.1175/BAMS-D-18-0023.1

Saha, S., Moorthi, S., Pan, H.-L., Wu, X., Wang, J., Nadiga, S., Tripp, P., Kistler, R., Woollen, J., Behringer, D., Liu, H., Stokes, D., Grumbine, R., Gayno, G., Wang, J., Hou, Y.-t., Chuang, H.-y., Juang, H.-M. H., Sela, J., ... Goldberg, M. (2010). The NCEP Climate Forecast System Reanalysis. *Bulletin of the American Meteorological Society*, 1015–1058. https://doi.org/10.1175/2010BAMS3001.1

Stauffer, D. R., & Seaman, N. L. (1990). Use of Four-Dimensional Data Assimilation in a Limited-Area Mesoscale Model. Part I: Experiments with Synoptic-Scale Data. *Monthly Weather Review*, *118*, 1250–1277. https://doi.org/https://doi.org/10.1175/1520-0493(1990)118<1250:UOFDDA>2.0.CO;2

Stauffer, D. R., Seaman, N. L., & Binkowski, F. S. (1991). Use of Four-Dimensional Data Assimilation in a Limited-Area Mesoscale Model Part II: Effects of Data Assimilation within the Planetary Boundary Layer. *Monthly Weather Review*, *119*, 734–754. https://doi.org/https://doi.org/10.1175/1520-0493(1991)119<0734:UOFDDA>2.0.CO;2

Thapa, K., Endreny, T. A., & Ferguson, C. R. (2018). Atmospheric Rivers Carry Non-monsoon Extreme Precipitation Into Nepal. *Journal of Geophysical Research: Atmospheres*, *123*, 5901–5912. https://doi.org/10.1029/2017JD027626

Thompson, G., Field, P. R., Rasmussen, R. M., & Hall, W. D. (2008). Explicit Forecasts of Winter Precipitation Using an Improved Bulk Microphysics Scheme. Part II: Implementation of a New Snow Parameterization. *Monthly Weather Review*, *136*(12), 5095–5115. https://doi.org/10.1175/2008MWR2387.1

Yang, Y., Zhao, T., Ni, G., & Sun, T. (2018). Atmospheric rivers over the Bay of Bengal lead to northern. *International Journal of Climatology*, *38*(August 2017), 1010–1021. https://doi.org/10.1002/joc.5229

Zhu, Y., & Newell, R. E. (1994). Atmospheric rivers and bombs. *Geophysical Research Letters*, *21*(18), 1999–2002. https://doi.org/10.1029/94GL01710

Chapter 5

Extremes in the atmosphere, disasters on land: Simulating and evaluating hazardous atmospheric river-related precipitation in High Mountain Asia

D.L. NASH, C. JONES, & L.M.V. CARVALHO

Abstract

Atmospheric Rivers (ARs) are relatively infrequent corridors of water vapor in our atmosphere that contribute both to beneficial water resources and hazardous weather conditions via precipitation across the globe. ARs reach High Mountain Asia (HMA), impact seasonal precipitation totals, and result in extreme weather events such as flooding, landslides, and lightning storms. Yet, the effects of ARs on water resources and hazards in HMA are not well established. A 36-year regional climate simulated by

the Weather Research and Forecasting (WRF) model described the mesoscale characteristics of a Western HMA AR that occurred in February 2010 and resulted in over 450 mm of precipitation and 3 landslides in western HMA. While the 20 km and 6.7 km simulation was able to realistically capture the mean precipitation for this devastating event, it had difficulty resolving the spatial and extreme extents of the precipitation during this AR. This paper provides multiple nested high-resolution (e.g., 9 and 3 km) downscaling simulations for the February 2010 Western HMA AR to investigate the optimal WRF configuration and parameterization needed to resolve the atmospheric flow interactions of ARs with the complex terrain of HMA. The accuracy of simulated extreme precipitation, relative to gridded observations provided by NASA's Integrated Multi-satellitE Retrievals for GPM (IMERG-PM), notably improves by increasing model resolution. We show that 3 km simulations improve precipitation estimates by 75% relative to coarser 6.7 km simulations. This targeted dynamical downscaling framework is able to capture local extreme precipitation and key fine-scale characteristics of one of the more extreme Western HMA ARs, and will be important to utilize to aid in understanding AR-related extremes.

5.1 Introduction

In High Mountain Asia (HMA), precipitation and the resulting glacial melt in the spring and summer months simultaneously provides water resources for hundreds of millions of people, while also presenting risks for many extreme weather conditions (Hewitt, 2005; Kääb et al., 2012). Atmospheric Rivers (ARs) occur in a variety of locations across the globe and are associated with extreme precipitation, flooding, lightning, debris flows and anomalous snow accumulation (Cannon et al., 2018; Nash & Carvalho, 2020; Oakley et al., 2018; Zhu & Newell, 1994, among others). In HMA,

ARs contribute to extreme precipitation and are associated with flood events in the Nepal and Bay of Bengal areas (Thapa et al., 2018; Yang et al., 2018). Recent work has shown that Atmospheric Rivers (ARs) are a significant contributor to total seasonal precipitation during winter and spring months in HMA, and a single AR event can contribute up to 25% of the total seasonal winter precipitation (Nash et al., 2021, 2022). However, due to the scarcity of observation stations, and the complex topography of HMA, precipitation estimates may be inaccurate, particular in higher elevations during the winter where snow is the main form of precipitation, highlighting the need for finer-scale simulations (Bookhagen & Burbank, 2010; Norris et al., 2015; Norris et al., 2017).

Norris et al. (2017) evaluated Advanced Weather Research and Forecasting (ARW-WRF, hereafter WRF) simulations of the full annual range of mesoscale precipitation for the entire Himalayan arc between 1 April 2005 00 UTC and 1 April 2006 00 UTC and found that for the 6.7 km simulations, WRF had considerable skill in simulating the timing of winter storms on the windward side of the mountains. However, in areas of complex topography, the model had a considerable wet bias when compared to the rain-gauges. Norris et al. (2017) highlight the need for improved observations for snow in the higher elevations of HMA, as the rain-gauges cannot accurately capture snowfall. Norris et al. (2018) found that compared to the 6.7 km simulations, further downscaling to a 2.2 km domain did not capture any spatio-temporal precipitation patterns. However, Huang et al. (2020) found that high-resolution dynamical simulations of ARs are necessary to accurately show fine-scale orographic precipitation processes driven by ARs, particularly in regions of complex topography. For this study, we complete a series of downscaling experiments during an impactful AR that occurred in February 2010 in western HMA, resulting in over 450 mm of precipitation in some regions. We demonstrate that finer-scale resolution simulations improve the represen-

tation of the precipitation in an area with steep and narrow topographical features that are prominent in HMA.

In our previous chapter, using 6.7 km WRF simulations generated in Norris et al. (2018), we contrast the mesoscale characteristics of two extreme precipitation events in HMA associated with ARs, and we show that the orientation of the AR axis is critical to the amount of precipitation that occurs. We identified three precipitation-triggered landslides that occurred within the vicinity of the February AR event (Kirschbaum et al., 2010). However, the 6.7 km spatial resolution simulation was not fine scale enough to resolve the complex orographic processes, and further downscaling is necessary to fully resolve all the meteorological characteristics of this particular event. Here, we simulate the February 2010 AR event at 9 and 3 km spatial resolution and hourly temporal resolution to improve the simulated orographic precipitation processes. We show that the improvement from finer-scale simulations is important to shed some light on the interactions between orographic precipitation related to ARs and precipitation triggered landslides in the Kashmir and Khyber Pakhtunkhwa regions in western HMA. The main objective of this study is to evaluate 3 km WRF simulations using multiple parameterization schemes to determine if we can improve the simulated precipitation during the extreme western HMA AR event in February 2010.

5.2 Data

To detect ARs, we used the Tracking Atmospheric Rivers Globally as Elongated Targets (tARget) algorithm, version 3 which was applied to ERA-Interim data on a global, 6 hourly basis from 1979 to 2019 (Guan & Waliser, 2019). This AR detection algorithm is useful for the HMA region as it detects ARs via relative IVT intensity thresholds, which is particularly useful during the winter and spring in HMA, as there is, on average, little

to no moisture (Nash et al., 2021). Additionally, it was used in multiple studies, including Nash et al. (2021) where they applied cEOF and k-means cluster analysis to days an AR passed the 1000 m elevation threshold in HMA. Nash et al. (2021) determined that there are three main types of ARs that reach HMA in winter, and used the resulting classification of AR types to identify the synoptic characteristics of the February 2010 AR event analyzed here.

This study uses 36 years of Climate Forecast System Reanalysis (Saha et al., 2010) dynamically downscaled over HMA to 20 km and 6.7 km spatial resolution and 3-hourly temporal resolution using the Advanced Weather Research and Forecasting (ARW-WRF, hereafter WRF) model version 3.7.1 created in Norris et al. (2018). Norris et al. (2018) generated these simulations specifically to analyze the mechanisms and trends associated with the contrasting regions of the Karakoram and Central Himalaya between April 1979 to March 2015. Here, it is used to evaluate precipitation and IVT during the February 2010 AR event. For more information on the WRF model configuration for the 6.7 km output, please see Norris et al. (2017) and Norris et al. (2018).

The European Centre for Medium-Range Weather Forecasts (ECMWF) atmospheric reanalyses of the global climate (ERA5) is used here to derive the initial and boundary conditions for the downscaling experiments and case studies with a 0.25° spatial resolution and hourly temporal resolution (Hersbach et al., 2020). The parameters and description of the setup for the WRF experiments can be found in Section 5.3.1.

Precipitation observations in HMA are limited, particularly when focusing on extreme conditions because rain-gauge data is sparse and unreliable and there is no precipitation radar (Norris et al., 2015). Precipitation data from Integrated Multi-satellitE Retrievals for Global Precipitation Measurement (IMERG-PM) V06B is used for comparison to WRF's simulated precipitation distribution during HMA AR events. Combined infrared and microwave data from multiple satellites are used to estimate precipita-

tion at 0.1° spatial resolution with half-hourly temporal resolution (Huffman et al., 2020). Despite its finer spatial resolution compared to the previous generation of Tropical Rainfall Measuring Mission (TRMM), this data still has known deficiencies, and is too coarse for capturing orographic precipitation structures in the complex topography of HMA. Multiple studies have shown that IMERG-PM underestimates frozen precipitation in areas with sparse station data or in areas of complex topography (Behrangi et al., 2016; Huang et al., 2020). We will show that this underestimation leads to discrepancies between this observation and the simulated precipitation, particularly in higher elevations. Despite its limitations, IMERG-PM is the most reliable long-term gridded precipitation estimate, and is useful in comparing the broader spatial patterns and timing of precipitation during these AR events.

For model verification in the vertical levels, we used raw radiosonde data from 4-9 February 2010 for 00 and 12 UTC from the University of Wyoming Department of Atmospheric Sciences Weather online data archive from the New Delhi station (station number 42182), located at 28.58°N and 77.20°E. Figure 5.1 shows the location of the radiosonde location for reference. We performed comparisons with WRF for temperature, dew point, wind speed, specific humidity, and water vapor flux at standard pressure levels from 925 to 100 hPa. We omitted soundings without standard pressure levels from model validation.

5.3 Methods

5.3.1 WRF Setup

We performed simulations for the 4-9 February 2010 AR event beginning 36 hours before the AR made landfall in HMA (identified using the same criteria for Nash et al.

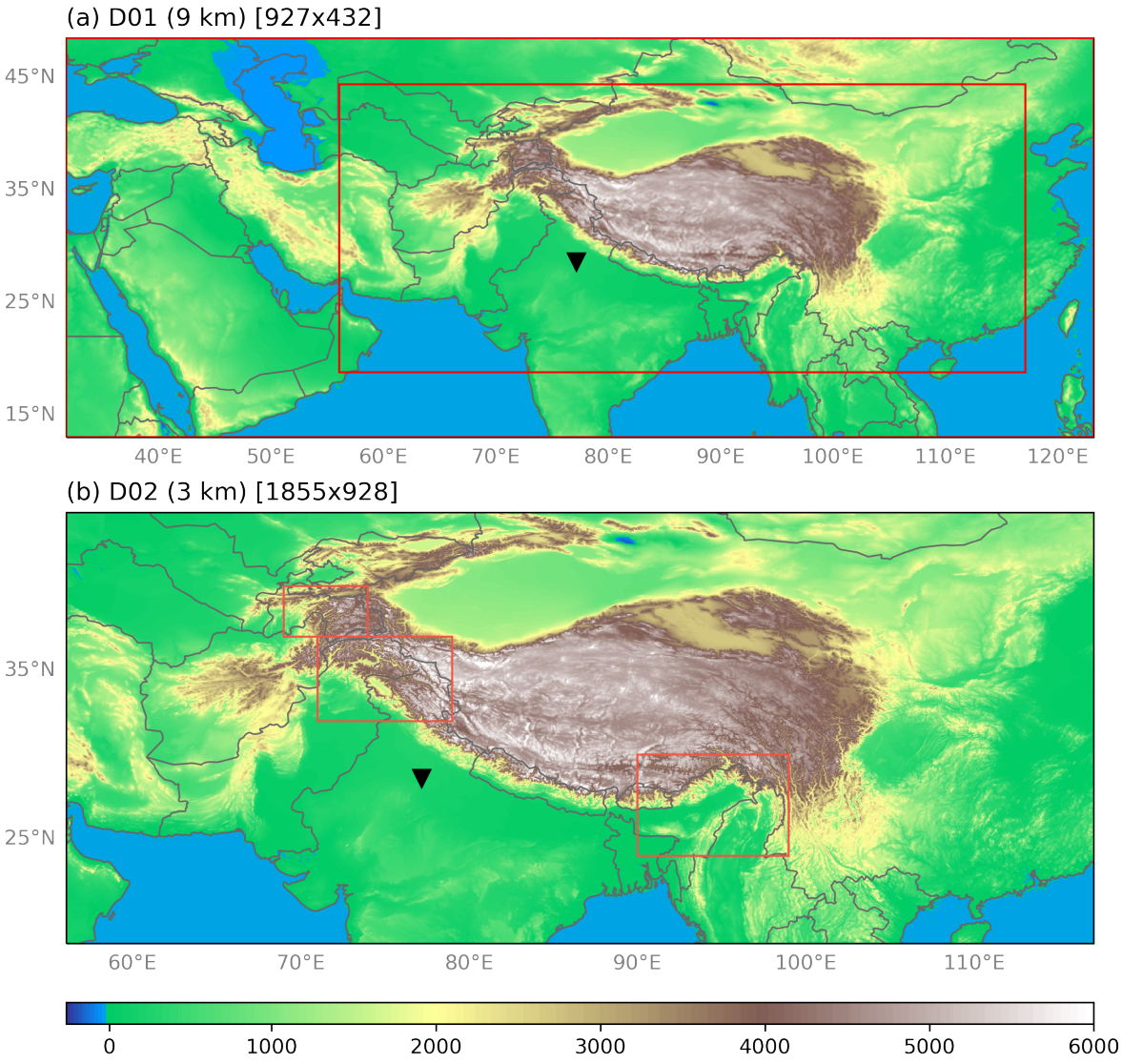

Figure 5.1: Elevation (shaded, m) for WRF model domains used for downscaling to 3 km. Domains D01 and D02 have 9 km (927 by 432) and 3 km (1855 by 928) grid spacing resolution (number of grid cells), respectively. We represent the New Delhi radiosonde station with a black triangle (station number 42182). The numbers in the brackets indicate the number of grid points in the x and y direction for each domain.

(2021)) and ended when there was no longer an AR according to the tARget algorithm. Using version 4.2.2 of the WRF model (Skamarock et al., 2008), we completed simulations with two domains with one-way interaction (i.e., no feedback and the inner domain did not affect the outer domain) of 9 km and 3 km (3:1 ratio), mapped with a Mercator projection (see Fig. 5.1 for a map of the domains). The time steps were 45 s and 15 s. Hourly ERA5 reanalysis provided the initial and lateral boundary conditions. Our reference scheme is the same parameterization scheme that was used in Norris et al. (2018), as Nash, Carvalho, Jones, et al. (2022) found it to capture the broad spatial precipitation patterns during HMA AR events (for more details, see Table 5.1).

We ran a series of experiments with additional microphysics and land surface model schemes to confirm that the performance of specific schemes were appropriate for capturing AR-related precipitation extremes in HMA. We chose schemes for our experiments based on the following criteria: 1) they are commonly used in the WRF community; 2) they have excellent performance in precipitation in High Mountain Asia or in AR-related precipitation in previous studies. We completed the experiments by changing one parameterization scheme at a time, and then evaluating the skill of that experiment with the model verification strategy outlined in the next section. We ran two additional simulations, one where we kept all parameterizations the same except for changing the microphysics from Thompson to Morrison 2-moment (referred to as MP1) (Morrison et al., 2009; Thompson et al., 2008), and one where we changed the Land Surface Model from Noah MP to Noah LSM (referred to as LSM1) (Chen & Dudhia, 2001; Niu et al., 2011).

Each 3 km simulation started on 3 February 2010 00 UTC, with the first 24 hours discarded as spin-up time. We turned off cumulus parameterization for the 3 km domain, as it is only valid for domains with greater than 9 km spatial resolution (Huang

Table 5.1: WRF model setup for the parameterization experiments.

Timing	
Simulation Period	3 February 2010 00 UTC to 9 February 2010 00 UTC
Time step	45 s, 15 s
Maps and grids	
Map projection	Mercator
Horizontal grid spacing	9 km (927 x 432), 3 km (1927 x 928)
Vertical levels	55 eta-levels
Model top	50 hPa
Forcing strategy	
Forcing data	ERA5 (0.25°, hourly)
Initialization	Once
Runs starting time	3 February 2010 00 UTC
Runs duration	144 hr
Spin-up time	12 hr
Physical parameterization schemes	
Longwave radiation	RRTMG (Iacono et al., 2008)
Shortwave radiation	RRTMG (Iacono et al., 2008)
Cumulus (CU)	Kain-Fritcsh Convection - outer domain only (Kain, 2004)
Microphysics (MP)	Thompson (Thompson et al., 2008)
Planetary boundary layer (PBL)	Yonsei University BL (Hong et al., 2006)
Land Surface Model (LSM)	Noah-MP (Niu et al., 2011)
Surface layer	MM5 (Monin and Obukhov, 1954)

et al., 2020; Norris et al., 2017; Skamarock et al., 2019). In our downscaling experiments, the outer domain has a large spatial extent compared to previous case study experiments, extending from eastern Africa to eastern Asia to encapsulate the entirety of the HMA AR, as it reached 2000 km or longer. WRF uses a terrain-following vertical coordinate (with 55 levels used in these simulations from the surface to 50 hPa), and we interpolated all output onto pressure levels.

5.3.2 Verification Strategy

For the model validation against the radiosonde observations, we take the model output every 12 hours (e.g., 00 UTC and 12 UTC) and all variables (equivalent potential temperature, temperature, dew point, wind components, specific humidity, and water vapor flux) were interpolated to standard pressure levels from 925 hPa to 100 hPa at the grid cell closest to the location of the radiosonde station identified in Section 5.2. To validate precipitation for each simulation, hourly model output at 00 UTC, 01 UTC, ... 23 UTC, provided the hourly accumulation from 4 February 2010 00 UTC. This was then used to compute the mean values of precipitation for time step t by subtracting precipitation at time (t), from precipitation at time (t+1). Integrated water Vapor Transport (IVT) is a variable widely used in the detection and characterization of ARs (Guan & Waliser, 2015; Nash et al., 2021). This was calculated by taking hourly model output, interpolating u and v wind components (m s^{-1}), and water vapor mixing ratio (kg kg^{-1}) to 20 pressure levels (1000, 975, 950, 925, 900, 875, 850, 825, 800, 775, 750, 700, 650, 600, 550, 500, 450, 400, 300, and 250 hPa). Only data at pressure levels above ground level were used for each grid cell in the integration. Then, using water vapor mixing ratio, we computed specific humidity (q) and then integrated u and v wind components with q at all pressure levels above ground level (see Appendix

C.1 for equations).

For each parameterization experiment, statistical measures for model performance include mean bias, root-mean-square error (RMSE) and correlation coefficient. We calculated these metrics for two-dimensional fields of precipitation and IVT, as well as for vertical fields of variables outlined in Section 5.3.2. Mean bias shows the deviation of the model from the observation, but can be misleading since the observation and model are not the same spatial resolution. For example, when interpolating the latitude and longitude grids to the same resolution, the values can be offset, giving you strong negative or positive biases in those grid cells. The observation was regridded to the finer-scale model resolution for any verification methods. Mean absolute error is the average magnitude of the error, which, when combined with mean bias, can give a more accurate picture of the overall difference in values. RMSE gives information about the variability of the error distribution because it is more sensitive to outliers (Chai & Draxler, 2014; Wang et al., 2021; Willmott & Matsuura, 2005). The correlation coefficient is a measure of how the model and observation change together. Using these evaluation criteria, we discuss the best scheme for simulating the AR-related extreme precipitation in Western HMA during February 2010.

5.4 Results

5.4.1 Summary of AR Case

Here I will summarize the synoptic, mesoscale, and thermodynamic characteristics that we found are important to simulating the extreme precipitation related to the February 2010 AR case. This AR occurred from 4 February 2010 00 UTC to 8 February 2010 18 UTC (duration of 90 hours), and had a below-average freezing level height

in both Northwestern and Western HMA for the duration of the event. The AR began as a Northwestern HMA AR Type from 4-6 February, then transitioned to a Western HMA AR Type on 6 February. The IVT flow was primarily southwesterly, but around 7 February 12 UTC, the moisture in the AR near HMA was synoptically forced to be more southerly, due to the positioning of the upper level trough and ridge. The moisture was orographically forced into western HMA and was considered cross-barrier flow because the moisture in the IVT was directly perpendicular to the topography. Up to 450 mm of precipitation (mostly snow) fell in some areas of western HMA from this event and there were three landslides that occurred (two on 6 February, one on 8 February) that resulted in multiple fatalities as well as the destruction of several buildings and roads (Kirschbaum et al., 2010). The moisture was well confined to the lower levels (below 4 km) and the orographic lift and long enduring IVT resulted in the extreme precipitation in western HMA.

5.4.2 Model Evaluation

The main goal of the WRF model evaluation is to assess the ability of the simulation to represent the main IVT characteristics (length, width, direction, and magnitude) during extreme AR events. Additionally, we assess the capability of the simulation to capture the extreme precipitation in the foothills and montane regions (between 1 and 3 km elevation) of HMA during the February 2010 Western HMA AR. Last, we evaluate orographically forced vertical motion, via low-level winds and moisture, and convective instability during these AR events.

Figure 5.2 shows the spatial bias of IVT for the 20 km WRF output, and the 3 km experiments relative to ERA5 at the 00 UTC time steps from 6-9 February. We repeated this analysis for every available time step and the results were consistent, and only

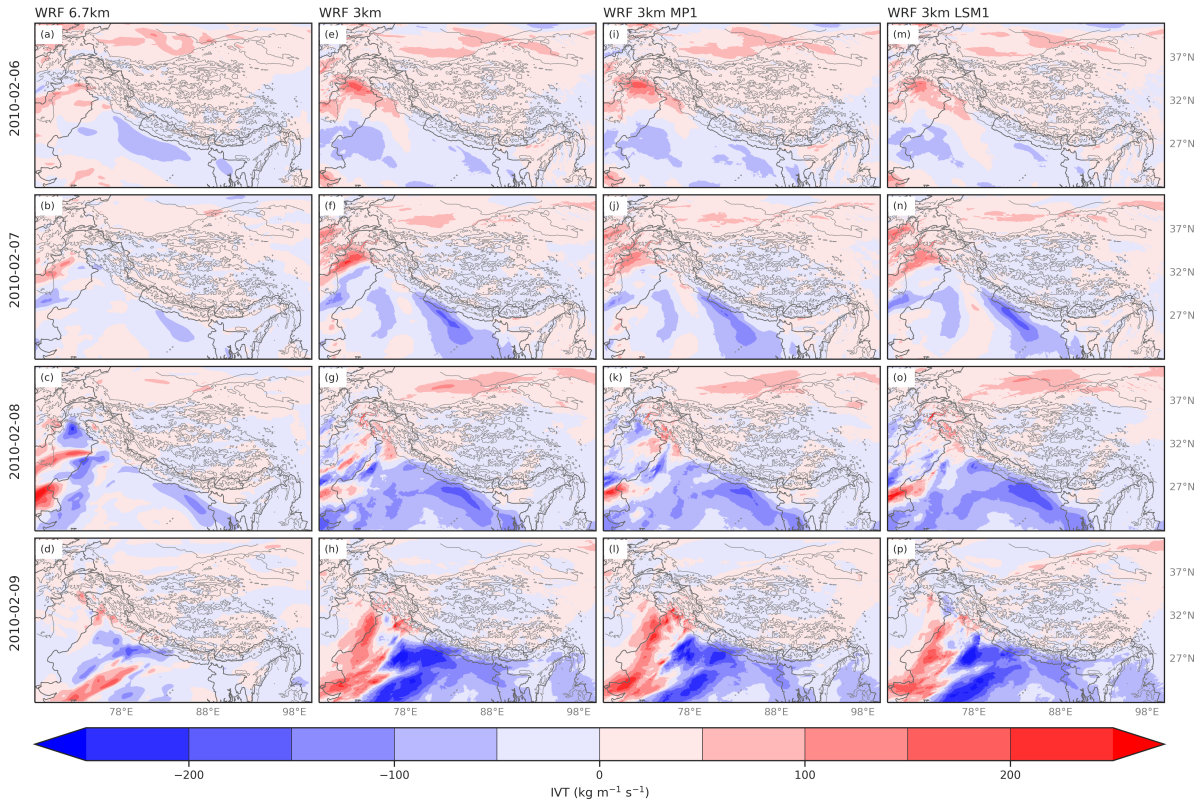

Figure 5.2: (a-d) IVT bias (shaded, kg m^{-1} s^{-1}) of WRF 20 km output – ERA5 27 km (regridded to match model) for the February 2010 AR event in Western HMA. Elevation (gray contours, km) is shown every 2 km from 1 km to 10 km. (e-h) Same as (a-d) but for WRF 3 km output using the benchmark parameterizations. (i-l) Same as (a-d) but for WRF 3 km output using the MP1 parameterizations. (m-p) Same as (a-d) but for WRF 3 km output using the LSM1 parameterizations.

show the 00 UTC time step of each day for brevity. The 6.7 km simulation shows a wet bias of about 100 kg m^{-1} s^{-1} in regions with an elevation greater than 1 km (Fig. 5.2a-d). For the 3 km simulations, there is a westward displacement of the AR IVT, which shows up as a moist bias in western HMA and a dry bias in central HMA (Fig. 5.2e-p). This is probably because we directly compared the 3 km simulations to 27 km ERA5, resulting in strong bias in offset grid cells, as described in Section 5.3.2. It also could be related to directly downscaling ERA5 to 9 km resolution, rather than a coarser scale parent domain of 27 km. Wang et al. (2021) found that WRF produced large-scale distortion in circulation patterns when they directed downscaled from ERA5 to 10 km resolution, compared to their simulations with a 30 km parent domain and a 10 km inner domain with two-way nesting. However, in the time series of the area-average IVT (see Fig. 5.3), the 3 km simulations outperform the 6.7 km simulation as they are able to capture not only the IVT magnitude estimated by ERA5 (Fig. 5.3a-c), but the broader timing and intensity of IVT with an overestimation of 25 kg m^{-1} s^{-1} of IVT at times in Western and Northwestern HMA (Fig. 5.3d, e). This is perhaps unsurprising, as ERA5 provided the initial conditions for the 3 km simulations, while CFSR was used for the 6.7 km simulation. The 6.7 km simulation underestimates the magnitude of IVT in these regions – potentially due to the differing data for initial conditions or perhaps due to the coarser resolution (Fig. 5.3). There is a minimal difference in IVT values between the 3 km reference simulation and the MP1 and LSM1 simulations. The spatial RMSE and Pearson R Correlation for IVT is shown in Fig. 5.4. The maps show that the 6.7 km simulation had higher Pearson R correlation coefficients (> 0.8) and lower RMSE values (< 75 kg m^{-1} s^{-1}) compared to both 3 km simulations (Fig. 5.4a, e). The 3 km simulations had very minor differences between each other, with lower correlation in the Hindu Kush region ($r=0.4$) and higher RMSE (between 75-100 kg m^{-1} s^{-1}) in the foothills and valley regions of Western HMA (Fig. 5.4b-d, f-h).

When evaluating the average temporal coefficients of Pearson R and RMSE for IVT in the three HMA subregions (see Fig. 5.5), there was no clear indication that one simulation outperformed the others, however the correlation values were below 0.6 on 7 and 8 February in Northwestern HMA (Fig. 5.5b) and RMSE increased over time in Western HMA (Fig. 5.5d). The 3 km MP1 simulation had slightly higher average RMSE scores and slightly lower Pearson R coefficients for all three subregions compared to the 6.7 km simulation (Fig. 5.5). Even though the 6.7 km simulation had the lower RMSE scores (Fig. 5.5d-f), the Pearson R coefficients were quite similar to the 3 km simulations (Fig. 5.5a-c).

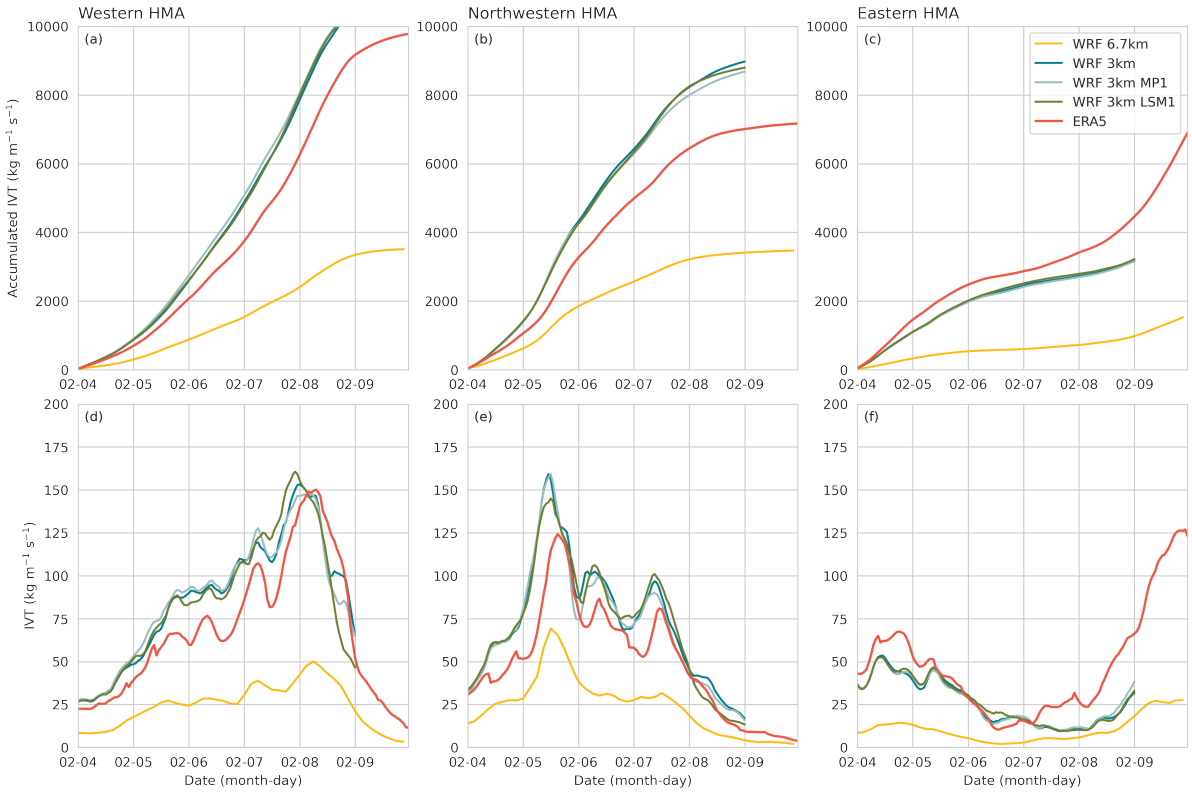

Figure 5.3: (top row) Average accumulated IVT (kg m^{-1} s^{-1}) within (a) Western HMA between 32-37°N, 71-79°E and (b) Northwestern HMA between 37-40°N, 66-74°E, and (c) Eastern HMA for the February 2010 AR event for the WRF 6.7 km simulation (yellow line), WRF 3 km benchmark simulation (navy blue line), WRF 3 km MP1 simulation (light blue line), WRF 3 km LSM1 simulation (green line), and IVT from ERA5 (red line). (d-f) Same as (a-c) but for average IVT rate (kg m^{-1} s^{-1}).

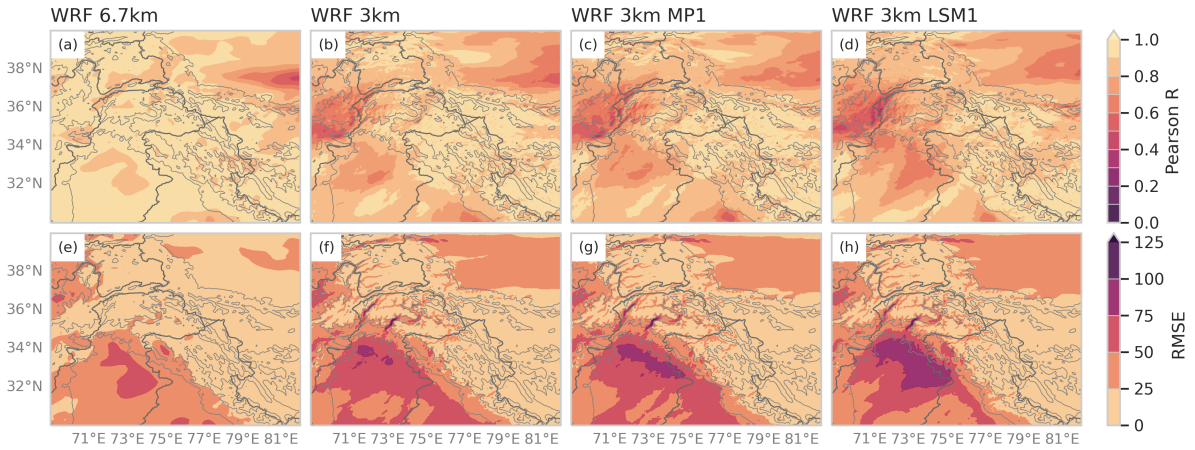

Figure 5.4: The calculated Pearson R correlation coefficient for (a) WRF 6.7 km 3-hourly IVT (kg m^{-1} s^{-1}), (b) WRF 3 km benchmark 1-hourly IVT, and (c) WRF 3 km MP1 1-hourly IVT, and (d) WRF 3 km LSM1 1-hourly IVT relative to ERA5 IVT. The calculated RMSE for (e) WRF 6.7 km 3-hourly IVT, (f) WRF 3 km benchmark 1-hourly IVT, (g) WRF 3 km MP1 1-hourly IVT, and (h) WRF 3 km LSM1 1-hourly IVT (kg m^{-1} s^{-1}) relative to ERA5 hourly IVT.

One thing that may directly improve the simulation of IVT include reinitializing the model every day of the integration, rather than a continuous integration from start of AR event to end of AR event. Wang et al. (2021) found that in order to keep the synoptic-scale forcing as close to the observation, the model needed to be re-initialized every day of the simulation. However, Norris et al. (2018) ran the model for a continuous 12-month period rather than re-initializing every day, and IVT during this AR event is well represented by that simulation. One main difference between the Norris et al. (2018) scheme and our reference scheme is that spectral nudging was not used in the parent domain, which may have influenced the larger-scale synoptic patterns, including IVT. Another modification that could be made is adding a 27 km parent domain, and nesting the 9-and-3 km domains, similar to the methodology used in Wang et al. (2021) for the High Asia Reanalysis.

Precipitation bias (see Fig. 5.6) between the WRF simulations and IMERG-PM shows that Norris' 6.7 km WRF simulations overestimated precipitation in the higher

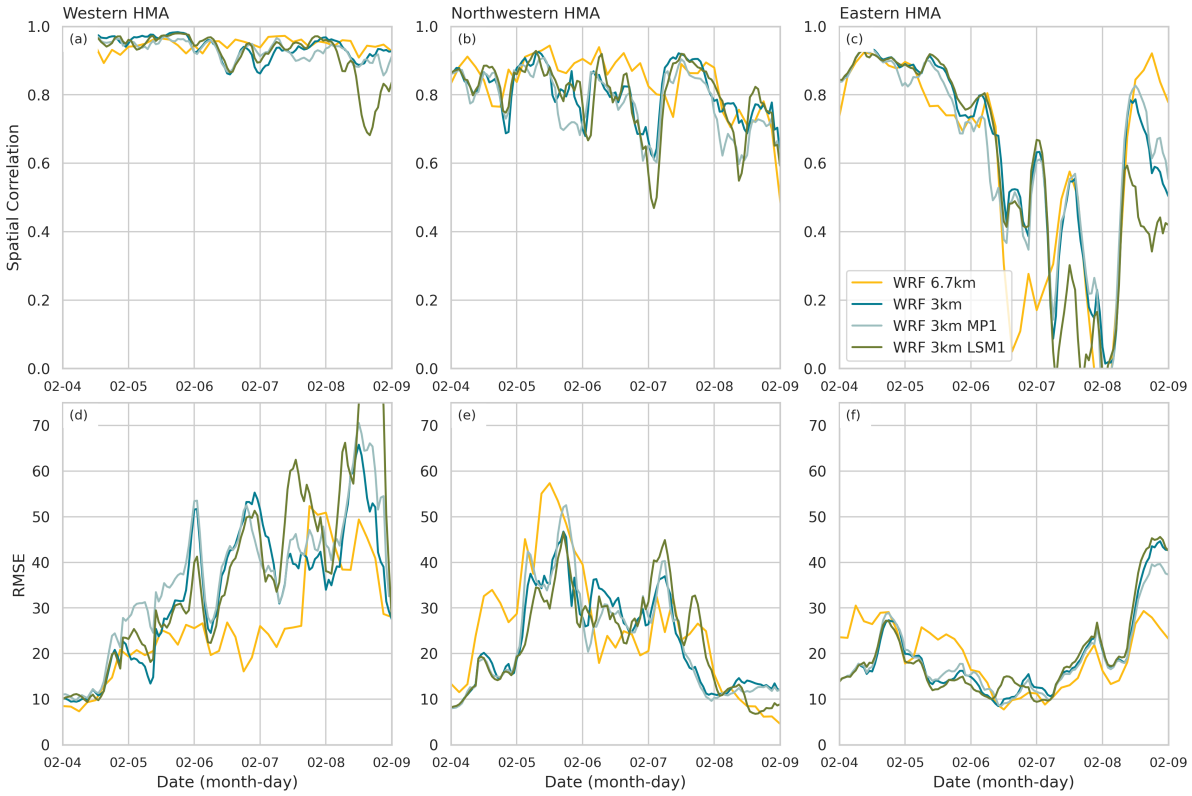

Figure 5.5: Pearson R correlation coefficient between ERA5 IVT (kg m^{-1} s^{-1}) and WRF simulations within (a) Western HMA between 32-37°N, 71-79°E and (b) Northwestern HMA between 37-40°N, 66-74°E, and (c) Eastern HMA for the February 2010 AR event between ERA5 IVT and the WRF 6.7 km simulation (yellow line), WRF 3 km benchmark simulation (navy blue line), WRF 3 km MP1 simulation (light blue line), and WRF 3 km LSM1 simulation (green line). (c-e) Same as (a-c) but for RMSE.

elevation regions by about 20 mm hour^{-1} (Fig. 5.6a-c), while all the 3 km simulations only overestimated precipitation in elevations greater than 1 km by about 5 mm hour^{-1} (Fig. 5.6d-l). This suggests further downscaling directly improved simulated precipitation, and differing microphysics had less of an influence. Figure 5.7a-c shows the accumulated precipitation and Fig. 5.7d-f shows the precipitation rate for the duration of the AR in the subregions where the precipitation during Western, Northwestern, and Eastern HMA ARs was above-average in Nash et al. (2021). In Western HMA, precipitation accumulation was similar across all simulations, with every simulation capturing the relative maximum of precipitation with a dry bias of about 5-10 mm (Fig. 5.7a). In Northwestern HMA, the 3 km simulations more accurately captured the accumulated precipitation, while the 6.7 km simulation overestimated the precipitation in this region by about 20 mm (Fig. 5.7b). All simulations overestimated the precipitation rate (by about 0.5 mm hr^{-1}) in both Western and Northwestern HMA, but were able to relatively capture the broader intensity timing represented by IMERG-PM (Fig. 5.7d, e). When examining the Pearson R correlation and RMSE coefficients, precipitation showed below 0.4 correlation, particularly in higher elevation regions for all simulations (Fig. 5.8a-d). However, when comparing the RMSE between the 6.7 km and 3 km simulations, the 3 km simulations had lower RMSE (below 4 mm in Western HMA and below 2 mm in Northwestern HMA), particularly in elevations between 1 and 3 km (Figs. 5.8e-h and 5.9d-e). RMSE seems a more accurate portrayal of precipitation skill compared to Pearson R correlation coefficient for this particular case study.

Figure 5.10 provides a summary of the average IVT and precipitation Pearson R correlation coefficients and RMSE values for both precipitation and IVT in the three HMA subregions for each of the simulations. Overall, all the 3 km simulations have lower RMSE and higher Pearson R correlation coefficients for precipitation, indicating that the finer resolution simulations provide a more accurate representation of pre-

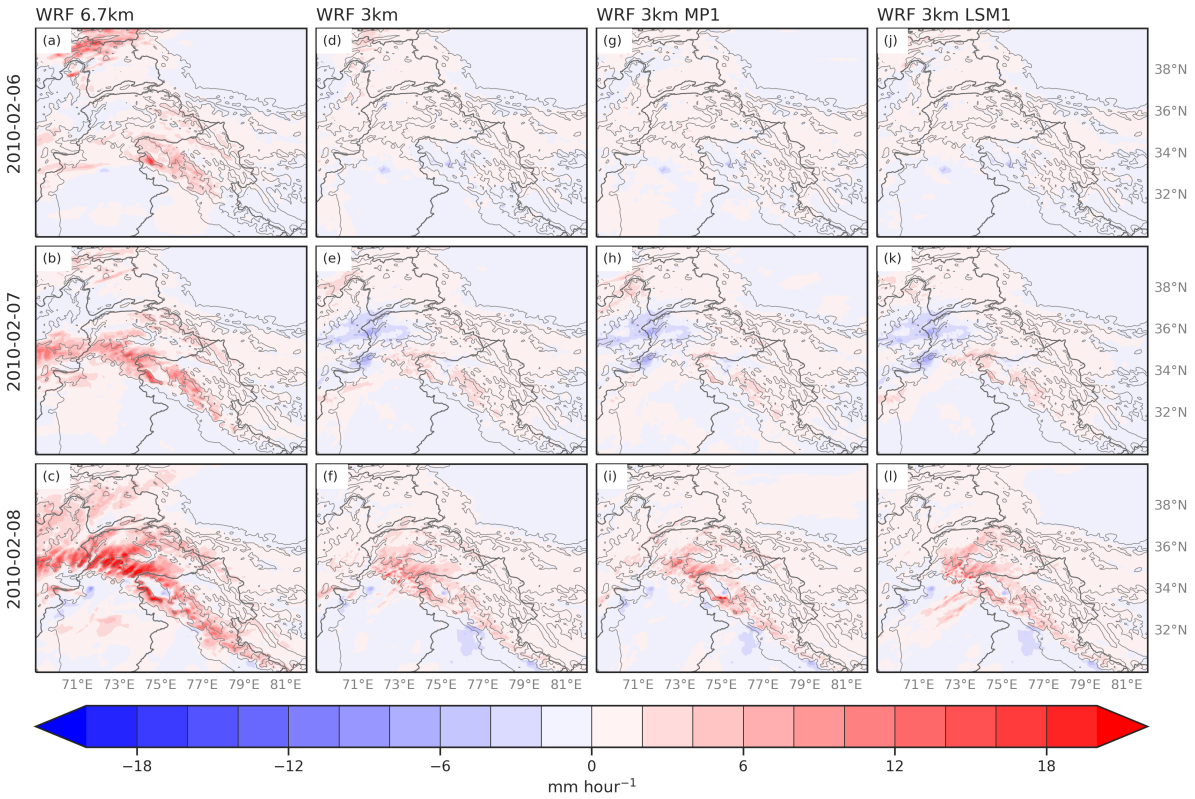

Figure 5.6: (a-c) Precipitation bias (shaded, mm hour^{-1}) of WRF 6.7 output - IMERG-PM 11 km (regridded to match model) for the February 2010 AR event in Western HMA. Elevation (gray contours, km) is shown every 2 km from 1 km to 10 km. (d-f) Same as (a-c) but for WRF 3 km output using the benchmark parameterizations. (g-i) Same as (a-c) but for WRF 3 km output using the MP1 parameterizations. (j-l) Same as (a-c) but for WRF 3 km output using the LSM1 parameterizations.

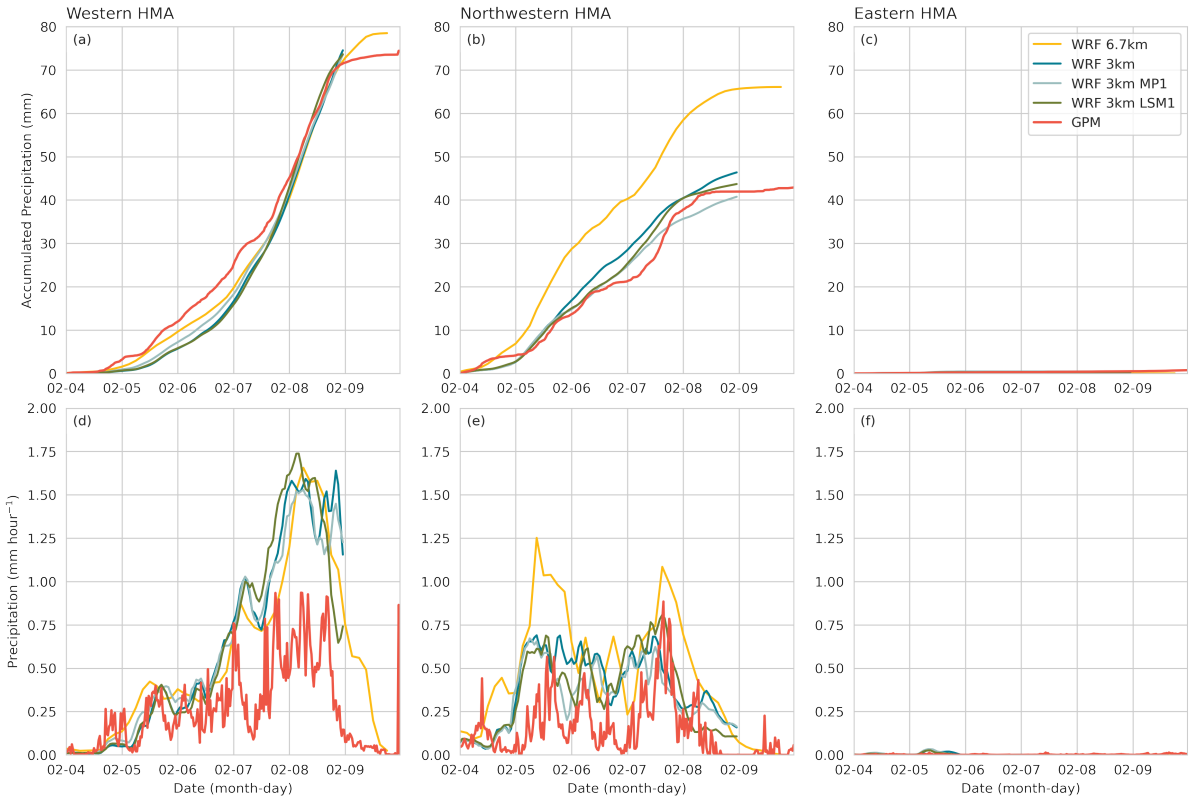

Figure 5.7: Same as Fig. 5.3, but for (a-c) average accumulated precipitation (total mm) and (d-f) average precipitation rate (mm hr^{-1}).

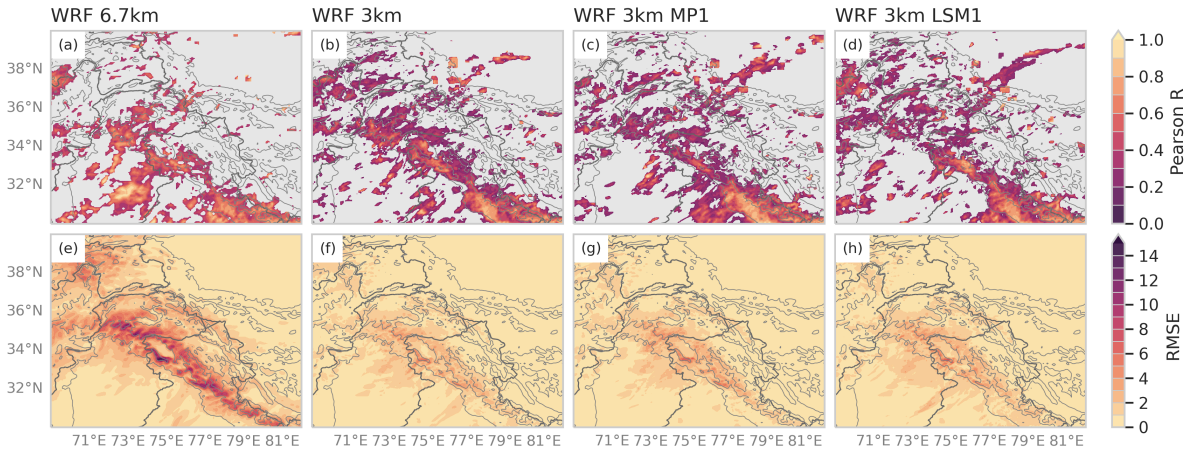

Figure 5.8: Same as Fig. 5.4 but for simulated precipitation (mm hr^{-1}) relative to IMERG-PM observations.

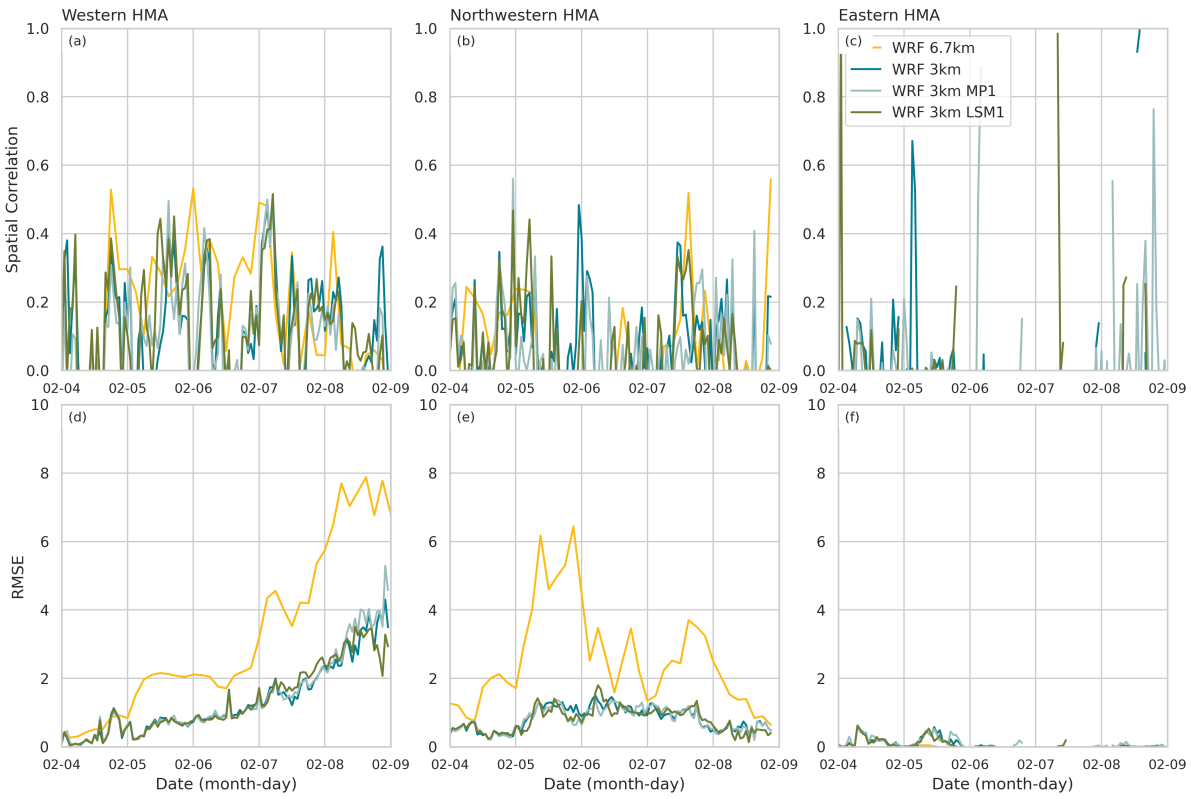

Figure 5.9: Same as Fig. 5.5, but for simulated precipitation (mm hr^{-1}) relative to IMERG-PM observations.

cipitation when compared to IMERG-PM observations (see Fig. 5.10a, b). The 6.7 km simulation did have a higher Pearson R correlation coefficient (r=0.15) in western HMA compared to the 3 km simulations (r=0.11, 0.09, 0.12), but the difference is quite small. There is little difference between the Pearson R precipitation coefficients for the different 3 km simulations, but the reference 3 km simulation had a slightly higher Pearson R coefficient in Northwestern HMA, while the WRF 3 km LSM1 simulation had the highest Pearson R correlation coefficient in Western HMA (Fig. 5.10a, b). For IVT, the 6.7 km simulation had lower RMSE compared to the 3 km simulations, particularly in Western HMA (Fig. 5.10c). The reference WRF 3 km simulation had the highest IVT Pearson R correlation coefficient in all three subregions (Fig. 5.10d). Wang et al. (2021) tested various parameterization schemes for evaluating precipitation for the High Asia Reanalysis and found that Morrison 2-moment microphysics Morrison et al. (2009) outperformed their other schemes because it uses double-moment for rain, ice, snow, and graupel while Thompson et al. (2008) only uses double moment for rain and ice. In this specific case, Morrison 2-moment microphysics (WRF 3 km MP1) does not improve the simulated precipitation. The choice of Land Surface Model (LSM) in WRF simulations primarily influences variations in surface heat fluxes. However, previous studies note that different LSMs influenced simulated circulation patterns in the lower troposphere in HMA (Norris et al., 2015). For example, Wang et al. (2021) indicated that Noah-MP may need a longer spin-up time compared to Noah-LSM to properly resolve precipitation, and resulted in a cold bias with a shorter spin-up time (Barlage et al., 2015; Cai et al., 2014; Gao et al., 2015). Our results show no significant differences when comparing Noah-MP (WRF 3 km reference) to Noah LSM (WRF 3 km LSM1) for either precipitation or IVT (Fig. 5.10.

To evaluate the vertical characteristics during this AR event, we compare observations from the New Delhi radiosonde station every 12 hours for the duration of the AR

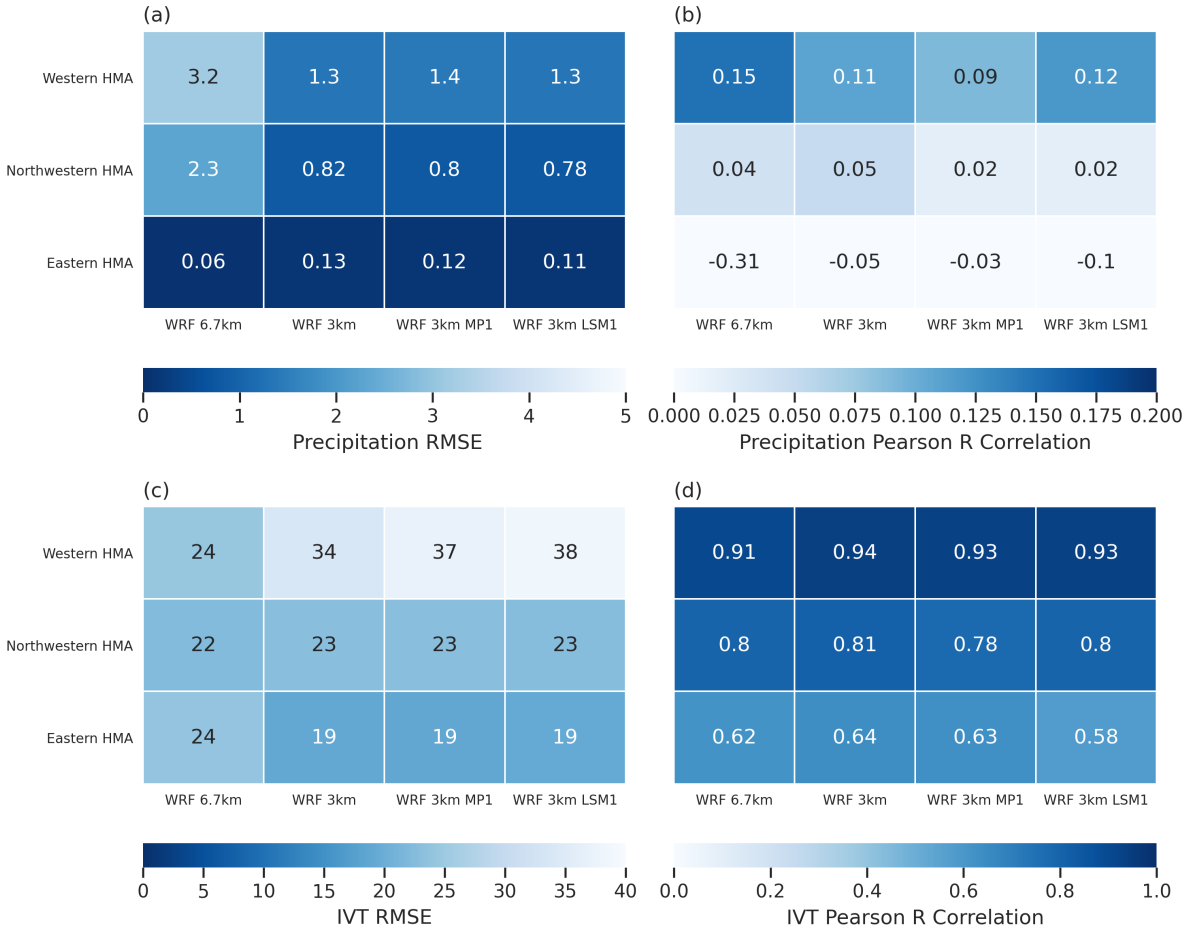

Figure 5.10: Regional (a) RMSE and (b) temporal correlation coefficients of average simulated precipitation relative to IMERG-PM observations. For the extents of the subregions, see Fig. 5.1. For more information on the parameterization schemes of the simulations, see Table 5.1. (c) Same as (a) but for IVT (kg m^{-1} s^{-1}). (d) Same as (b) but for IVT (kg m^{-1} s^{-1}).

event. We compute the bias at all standard pressure levels between 925 and 100 hPa for temperature (°C), dew point (°C), wind speed (m s^{-1}), equivalent potential temperature (K), specific humidity (kg kg^{-1}), and water vapor flux (m^{-1} s^{-1}) (see Fig. 5.11). At the New Delhi station, the 6.7 km simulation outperformed the 3 km simulations below 700 hPa for dew point, theta-e, specific humidity and water vapor flux (Fig. 5.11b, d-f). This supports the evaluation of the RMSE for IVT (Fig. 5.4e-h), indicating that the finer scale simulations overestimated the moisture within the AR in western HMA. Comparing the 3 km simulations, the reference 3 km scheme and the MP1 scheme outperformed the LSM1 simulation in moisture variables below 700 hPa (Fig. 5.11b, d-f). There was not a noticeable difference in the 3 km simulations for all variables, except that the MP1 simulation outperformed the other 3 km simulations in water vapor flux between 950 and 700 hPa (Fig. 5.11f). In the mid-levels between 700 and 400 hPa, all 4 simulations were similar, with less than a 1°C cool bias in temperature and warm biases of about 5°C in dew point (Fig. 5.11a, b). Noticeably, all four simulations had similar negative wind speed bias at all pressure levels, with a negative bias decreasing with height up to -35 m s^{-1} at 200 hPa (Fig. 5.11c).

5.5 Conclusions

We dynamically downscale an extreme Western HMA AR event that occurred between 4-9 February 2010 using nested WRF simulations at 9 and 3 km forced by ERA5 reanalysis. Comparing these finer-scale simulations to previously generated 6.7 km WRF output, we find that the 6.7 km WRF output is too coarse to explicitly resolve precipitation maximums related to this AR event. The climatological 6.7 km simulation generated in Norris et al. (2018) overestimated precipitation in the higher elevation regions and underestimated precipitation in the foothills compared to IMERG-PM v06.

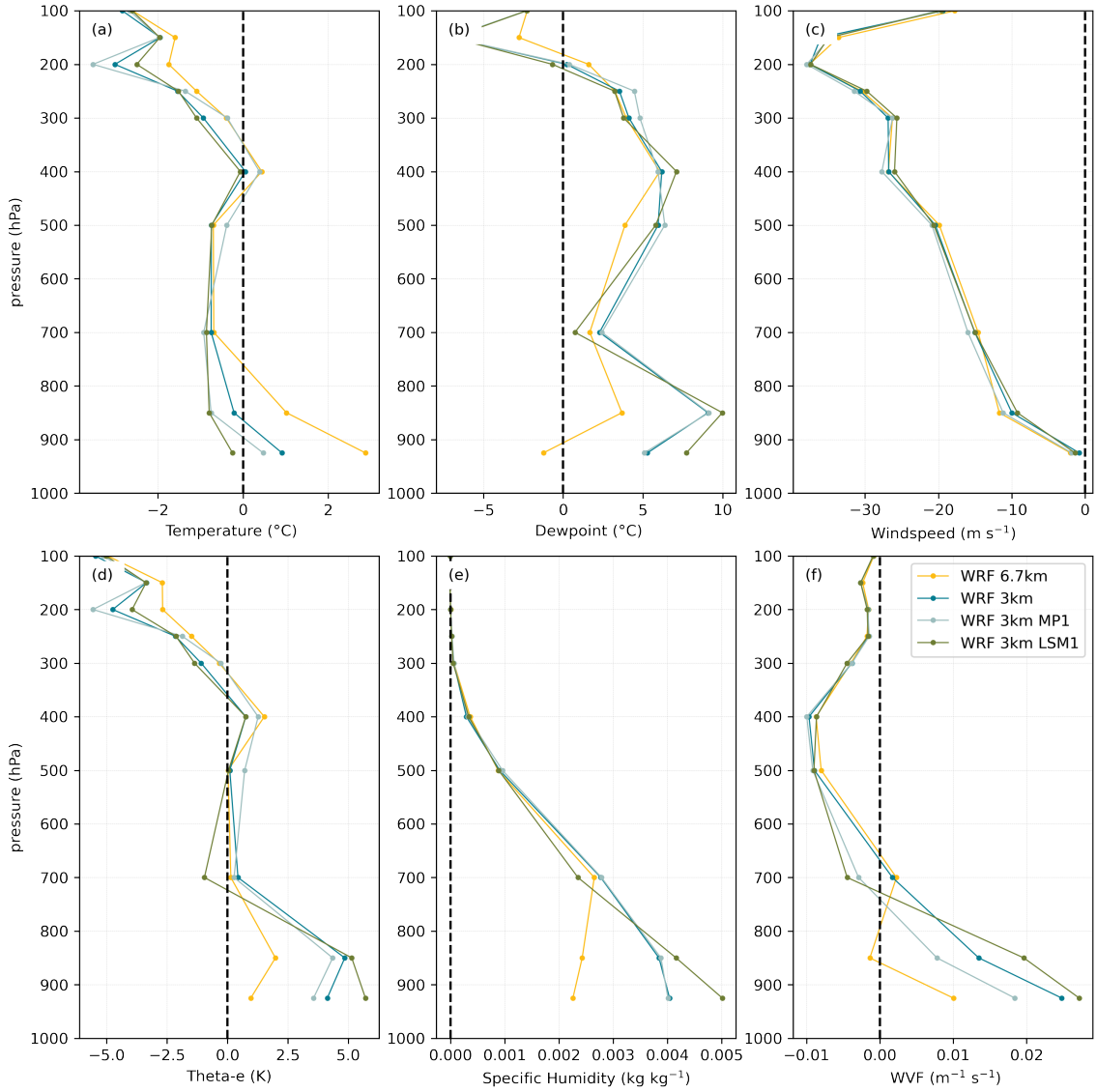

Figure 5.11: Bias for (a) surface temperature (°C), (b) dew point (°C), (c) wind speed (m s^{-1}), (d) equivalent potential temperature (K), (e) specific humidity (kg kg^{-1}), and water vapor flux (m s^{-1}) at standard pressure levels between observed radiosonde values and WRF 6.7 km simulation (yellow line), WRF 3 km benchmark simulation (navy blue line), WRF 3 km MP1 simulation (light blue line), and WRF 3 km LSM1 simulation (green line) at the New Delhi Station (see Fig. 5.1 for location).

We show that finer scale simulations decreases the moist bias in higher elevation regions from 20 mm to about 5 mm (about a 75% decrease in precipitation bias).

We also evaluated the impact of downscaling to 3 km on IVT and found that the 6.7 km simulation outperformed the 3 km simulations. This most likely is due to the fact that our 3 km simulations did not use spectral nudging in the parent domain, as was done for the 6.7 km simulation (Norris et al., 2018). It also may have been due to comparing ERA5's 27 km IVT to the very fine scale 3 km simulations, or an effect of directly downscaling ERA5 from 27 km to 9 km. To determine if there was an influence on simulated extreme precipitation and IVT using different WRF parameterizations, we tested the Morrison 2-moment microphysics scheme and the Noah-LSM. While we did not see a significant difference in 3 km simulated precipitation or IVT with our different microphysics or land surface model simulations compared to our reference simulation, it could be important to run additional parameterization tests.

Leung and Qian (2009) evaluated how well WRF simulated heavy precipitation and floods related to ARs in the US and found that the 5-class mixed phase cloud microphysics scheme provided realistic estimates of extreme wintertime precipitation amounts and spatial distribution Hong et al. (2004) found that the 5-class mixed phase cloud microphysics scheme better represented the ice cloud-radiation feedback, which improved surface precipitation and large-scale mean temperature. Testing this additional microphysics scheme could be important to try as this study focused on wintertime orographic precipitation associated with an AR. In addition to testing the simulation with 5-class mixed phase cloud microphysics scheme, we recommend adding two more domains to the simulation, including an inner domain with 1-km spatial resolution and an additional parent domain of 27 km. Additional downscaling to 1 km will help determine the ideal spatial resolution for resolving extreme precipitation. The additional parent domain of 27 km would be used to determine the influence of directly

downscaling from ERA5 to 9 km parent domain, similar to the tests ran in Wang et al. (2021). This may improve the spatial positioning of the AR in the 3 km simulations, reducing the overall bias we observed.

Our results suggest the importance of fine spatial resolution (3 km or less) in the representation of extreme orographic precipitation during winter HMA AR events. While it is difficult to specifically choose one specific parameterization scheme, it appears that the parameterizations defined in Norris et al. (2015), used to generate the 36 years of 6.7 km WRF data, and is used in this study as our reference 3 km WRF simulation improves model performance when simulating extreme winter orographic precipitation during HMA ARs (Norris et al., 2018). These findings highlight the importance of better-resolved fine scale simulations in capturing AR-related precipitation extremes. While coarse scale simulations and reanalysis are able to accurately capture the broad synoptic patterns and the filamentary IVT features related to HMA ARs, the fine-scale spatial features specific to terrain-locked, quasi-stationary ARs are limited to higher-resolution simulations. This is relevant for uncovering the impact of ARs on natural hazards, such as the three landslides that occurred within the 90 hours of this AR. Finer-scale resolution simulations are necessary to capture the extreme orographic precipitation that trigger landslides in HMA. It is also important to accurately simulate these precipitation extremes related to ARs, even when they are not associated with natural hazards, because, as shown in this February 2010 AR event and the January 2002 event (Nash, Jones, et al., 2022), a single AR can contribute up to almost a quarter of the total seasonal precipitation in HMA, having long-lasting impacts on water availability. In the future, high-resolution mesoscale simulations have the potential to provide specific projections of extreme precipitation from short-term forecasting to seasonal outlooks that impacts water-related adaptation policies.

5.5.1 Declarations and Funding

This research is part of the Blue Waters sustained-petascale computing project, which is supported by the National Science Foundation (awards OCI-0725070 and ACI-1238993) the State of Illinois, and as of December 2019, the National Geospatial-Intelligence Agency. Blue Waters is a joint effort of the University of Illinois at Urbana-Champaign and its National Center for Supercomputing Applications. NASA Headquarters under the NASA Earth and Space Science Fellowship Program – Grant 80NSSC18K1412 supported a portion of this research. The 20 km and 6.7 km WRF simulations were supported by the Climate and Large-scale Dynamics Program, from the National Science Foundation (NSF award-AGS 1116105).

References

Barlage, M., Tewari, M., Chen, F., Miguez-Macho, G., Yang, Z. L., & Niu, G. Y. (2015). The effect of groundwater interaction in North American regional climate simulations with WRF/Noah-MP. *Climatic Change*, *129*, 485–498. https://doi.org/10.1007/S10584-014-1308-8

Behrangi, A., Guan, B., Neiman, P. J., Schreier, M., & Lambrigtsen, B. (2016). On the Quantification of Atmospheric Rivers Precipitation from Space: Composite Assessments and Case Studies over the Eastern North Pacific Ocean and the Western United States. *Journal of Hydrometeorology*, *17*(1), 369–382. https://doi.org/10.1175/jhm-d-15-0061.1

Bookhagen, B., & Burbank, D. W. (2010). Toward a complete Himalayan hydrological budget: Spatiotemporal distribution of snowmelt and rainfall and their impact on river discharge. *Journal of Geophysical Research: Earth Surface*, *115*(3), 1–25. https://doi.org/10.1029/2009JF001426

Cai, X., Yang, Z. L., David, C. H., Niu, G. Y., & Rodell, M. (2014). Hydrological evaluation of the noah-MP land surface model for the Mississippi River Basin. *Journal of geophysical research*, *119*, 23–38. https://doi.org/10.1002/2013JD020792

Cannon, F., Hecht, C. W., Cordeira, J. M., & Ralph, F. (2018). Synoptic and Mesoscale Forcing of Southern California Extreme Precipitation. *Journal of Geophysical Research: Atmospheres*, *123*(24), 714–13. https://doi.org/10.1029/2018JD029045

Chai, T., & Draxler, R. R. (2014). Root mean square error (RMSE) or mean absolute error (MAE)? -Arguments against avoiding RMSE in the literature. *Geoscientific Model Development*, *7*(3), 1247–1250. https://doi.org/10.5194/GMD-7-1247-2014

Chen, F., & Dudhia, J. (2001). Coupling an Advanced Land Surface–Hydrology Model with the Penn State–NCAR MM5 Modeling System. Part I: Model Implementation and Sensitivity. *Monthly Weather Review*, *129*(4), 569–585. https://doi.org/10.1175/1520-0493(2001)129

Gao, Y., Jianwei, X., & Chen, D. (2015). Evaluation of WRF Mesoscale Climate Simulations over the Tibetan Plateau during 1979–2011. *Journal of Climate*, *28*, 2823–2841. https://doi.org/10.1175/JCLI-D-14-00300.1

Guan, B., & Waliser, D. E. (2015). Detection of atmospheric rivers: Evaluation and application of an algorithm for global studies. *Journal of Geophysical Research: Atmospheres*, *120*(24), 12514–12535. https://doi.org/10.1002/2015jd024257

Guan, B., & Waliser, D. E. (2019). Tracking Atmospheric Rivers Globally: Spatial Distributions and Temporal Evolution of Life Cycle Characteristics. *Journal of Geophysical Research: Atmospheres*, *124*, 12523–12552. https://doi.org/10.1029/2019JD031205

Hersbach, H., Bell, B., Berrisford, P., Hirahara, S., Horányi, A., Muñoz-Sabater, J., Nicolas, J., Peubey, C., Radu, R., Schepers, D., Simmons, A., Soci, C., Abdalla, S., Abellan, X., Balsamo, G., Bechtold, P., Biavati, G., Bidlot, J., Bonavita, M., … Thépaut, J. N. (2020). The ERA5 global reanalysis. *Quarterly Journal of the Royal Meteorological Society*, *146*(730), 1999–2049. https://doi.org/10.1002/qj.3803

Hewitt, K. (2005). The Karakoram Anomaly? Glacier Expansion and the 'Elevation Effect,' Karakoram Himalaya. *Mountain Research and Development*, *25*(4), 332–341. https://doi.org/10.1659/0276-4741(2005)025[0332:TKAGEA]2.0.CO;2

Hong, S.-Y., Dudhia, J., & Chen, S.-H. (2004). A Revised Approach to Ice Microphysical Processes for the Bulk Parameterization of Clouds and Precipitation. *Monthly Weather Review*, *132*(1), 103–120. https://doi.org/https://doi.org/10.1175/1520-0493(2004)132<0103:ARATIM>2.0.CO;2

Huang, X., Swain, D. L., Walton, D. B., Stevenson, S., & Hall, A. D. (2020). Simulating and Evaluating Atmospheric River-Induced Precipitation Extremes Along the U.S. Pacific Coast: Case Studies From 1980–2017. *Journal of Geophysical Research: Atmospheres*, *125*(4). https://doi.org/10.1029/2019JD031554

Huffman, G. J., Bolvin, D. T., Braithwaite, D., Hsu, K.-L., Joyce, R. J., Kidd, C., Nelkin, E. J., Sorooshian, S., Stocker, E. F., Tan, J., Wolff, D. B., & Xie, P. (2020). Integrated Multi-satellite Retrievals for the Global Precipitation Measurement (GPM) Mission (IMERG). In V. Levizzani, C. Kidd, D. B. Kirschbaum, C. D. Kum-

merow, K. Nakamura, & F. J. Turk (Eds.), *Satellite precipitation measurement: Volume 1* (pp. 343–353). Springer International Publishing. https://doi.org/10.1007/978-3-030-24568-9{_}19

Kääb, A., Berthier, E., Nuth, C., Gardelle, J., & Arnaud, Y. (2012). Contrasting patterns of early twenty-first-century glacier mass change in the Himalayas. *Nature*, *488*, 495–498. https://doi.org/10.1038/nature11324

Kirschbaum, D., Adler, R., Hong, Y., Hill, S., & Lerner-Lam, A. (2010). A global landslide catalog for hazard applications: Method, results, and limitations. *Natural Hazards*, *52*, 561–575. https://doi.org/10.1007/S11069-009-9401-4/TABLES/3

Leung, L. R., & Qian, Y. (2009). Atmospheric rivers induced heavy precipitation and flooding in the western U.S. simulated by the WRF regional climate model. *Geophysical Research Letters*, *36*(3), n/a–n/a. https://doi.org/10.1029/2008gl036445

Morrison, H., Thompson, G., & Tatarskii, V. (2009). Impact of Cloud Microphysics on the Development of Trailing Stratiform Precipitation in a Simulated Squall Line: Comparison of One- and Two-Moment Schemes. *Monthly Weather Review*, *137*(3), 991–1007. https://doi.org/10.1175/2008MWR2556.1

Nash, D., Carvalho, L. M. V., Jones, C., & Ding, Q. (2021). Winter and spring atmospheric rivers in High Mountain Asia: climatology, dynamics, and variability. *Climate Dynamics*. https://doi.org/10.1007/S00382-021-06008-Z

Nash, D., Carvalho, L. M. V., Jones, C., & Ding, Q. (2022). Influence of zero degree line on Atmospheric Rivers in High Mountain Asia: WRF case studies of orographic precipitation extremes. *(in preparation)*.

Nash, D., & Carvalho, L. M. (2020). Brief Communication : An electrifying atmospheric river – understanding the thunderstorm event in Santa Barbara County during March 2019. *Natural Hazards and Earth System Sciences*, *20*, 1931–1940. https://doi.org/10.5194/nhess-20-1931-2020

Nash, D., Jones, C., & Carvalho, L. M. V. (2022). Extremes in the atmosphere, disasters on land: Simulating and evaluating hazardous atmospheric river-related precipitation in High Mountain Asia. *(in preparation)*.

Niu, G. Y., Yang, Z. L., Mitchell, K. E., Chen, F., Ek, M. B., Barlage, M., Kumar, A., Manning, K., Niyogi, D., Rosero, E., Tewari, M., & Xia, Y. (2011). The community Noah land surface model with multiparameterization options (Noah-MP): 1. Model description and evaluation with local-scale measurements. *Journal of Geophysical Research: Atmospheres*, *116*(D12), 12109. https://doi.org/10.1029/2010JD015139

Norris, J., Carvalho, L. M. V., Jones, C., & Cannon, F. (2015). WRF simulations of two extreme snowfall events associated with contrasting extratropical cyclones over

the western and central Himalaya. *Journal of Geophysical Research: Atmospheres*, *120*(8), 3114–3138. https://doi.org/10.1002/2014JD022592

Norris, J., Carvalho, L. M., Jones, C., & Cannon, F. (2018). Deciphering the contrasting climatic trends between the central Himalaya and Karakorum with 36 years of WRF simulations. *Climate Dynamics*, 1–22. https://doi.org/https://doi.org/10.1007/s00382-018-4133-3

Norris, J., Carvalho, L. M., Jones, C., Cannon, F., Bookhagen, B., Palazzi, E., & Tahir, A. A. (2017). The spatiotemporal variability of precipitation over the Himalaya: evaluation of one-year WRF model simulation. *Climate Dynamics*, *49*(5-6), 2179–2204. https://doi.org/10.1007/s00382-016-3414-y

Oakley, N. S., Cannon, F., Munroe, R., Lancaster, J. T., Gomberg, D., & Ralph, F. (2018). Brief communication: Meteorological and climatological conditions associated with the 9 January 2018 post-fire debris flows in Montecito and Carpinteria, California, USA. *Natural Hazards and Earth System Sciences*, *18*(11), 3037–3043. https://doi.org/10.5194/nhess-18-3037-2018

Saha, S., Moorthi, S., Pan, H.-L., Wu, X., Wang, J., Nadiga, S., Tripp, P., Kistler, R., Woollen, J., Behringer, D., Liu, H., Stokes, D., Grumbine, R., Gayno, G., Wang, J., Hou, Y.-t., Chuang, H.-y., Juang, H.-M. H., Sela, J., ... Goldberg, M. (2010). The NCEP Climate Forecast System Reanalysis. *Bulletin of the American Meteorological Society*, 1015–1058. https://doi.org/10.1175/2010BAMS3001.1

Skamarock, W. C., Klemp, J. B., Dudhia, J., Gill, D. O., Barker, D. M., Wang, W., & Powers, J. G. (2008). *A description of the advanced research WRF Version 3, NCAR technical note, Mesoscale and Microscale Meteorology Division* (tech. rep.). National Center for Atmospheric Research. Boulder, CO, USA.

Skamarock, W. C., Klemp, J. B., Dudhia, J., Gill, D. O., Liu, Z., Berner, J., Wang, W., Powers, J. G., Duda, M. G., Barker, D. M., & Huang, X.-Y. (2019). *A description of the advanced research WRF model version 4* (tech. rep.). National Center for Atmospheric Research. Boulder, CO, USA. https://opensky.ucar.edu/islandora/object/technotes:576/datastream/PDF/download/citation.pdf

Thapa, K., Endreny, T. A., & Ferguson, C. R. (2018). Atmospheric Rivers Carry Nonmonsoon Extreme Precipitation Into Nepal. *Journal of Geophysical Research: Atmospheres*, *123*, 5901–5912. https://doi.org/10.1029/2017JD027626

Thompson, G., Field, P. R., Rasmussen, R. M., & Hall, W. D. (2008). Explicit Forecasts of Winter Precipitation Using an Improved Bulk Microphysics Scheme. Part II: Implementation of a New Snow Parameterization. *Monthly Weather Review*, *136*(12), 5095–5115. https://doi.org/10.1175/2008MWR2387.1

Wang, X., Tolksdorf, V., Otto, M., & Scherer, D. (2021). WRF-based dynamical downscaling of ERA5 reanalysis data for High Mountain Asia: Towards a new version

of the High Asia Refined analysis. *International Journal of Climatology*, *41*(1), 743–762. https://doi.org/10.1002/JOC.6686

Willmott, C. J., & Matsuura, K. (2005). Advantages of the mean absolute error (MAE) over the root mean square error (RMSE) in assessing average model performance. *Climate Research*, *30*(1), 79–82. https://doi.org/10.3354/CR030079

Yang, Y., Zhao, T., Ni, G., & Sun, T. (2018). Atmospheric rivers over the Bay of Bengal lead to northern. *International Journal of Climatology*, *38*(August 2017), 1010–1021. https://doi.org/10.1002/joc.5229

Zhu, Y., & Newell, R. E. (1994). Atmospheric rivers and bombs. *Geophysical Research Letters*, *21*(18), 1999–2002. https://doi.org/10.1029/94GL01710

Chapter 6

Conclusions

D.L. NASH

6.1 Summary

Atmospheric Rivers (ARs) are a synoptic scale global phenomenon that impact local precipitation regimes where they occur and are associated with precipitation-related hazards such as floods, lightning, and landslides (Dettinger, 2011; Gorodetskaya et al., 2014; Guan et al., 2010; Lavers et al., 2011; Lavers & Villarini, 2013; Nash et al., 2021; Nash & Carvalho, 2020; Nash et al., 2018; Neiman et al., 2008; Ralph et al., 2006; Thapa et al., 2018; Wernli & Papritz, 2018; Yang et al., 2018). In High Mountain Asia (HMA) the complex precipitation regimes provide water resources for millions of people and can simultaneously result in hazardous conditions such as lightning, floods, and landslides. This dissertation demonstrates that ARs are critical to understanding precipitation regimes in HMA. By increasing our understanding of the synoptic scale, mesoscale, and thermodynamic of HMA ARs, we can potentially improve precipitation forecasts, potentially decreasing damages to infrastructure, displaced populations, and fatalities during hazardous events and increasing understanding of local water re-

sources. **This dissertation contributes insight on the interconnected relationship between inland penetrating orographic ARs, the HMA hydroclimate, and their relationship with precipitation-related hazards using the following research objectives:**

1. Examine synoptic and mesoscale features of a unique AR event in Santa Barbara, CA during March 2019 that resulted in over 8,000 lightning flashes in the southern California region in under 24 hours (Chapter 2).

2. Investigate the regional climatology of ARs that reach HMA to understand their synoptic scale characteristics, impact on large-scale precipitation, and how climate modes such as ENSO, AO, and SH influence HMA AR frequency and broader circulation patterns (Chapter 3).

3. Contrast the thermodynamic and mesoscale characteristics of two impactful AR events using 20 km and 6.7 km WRF simulations created by Norris et al. (2018) to determine the primary mechanisms of ARs associated with extreme orographic precipitation and lightning (Chapter 4).

4. Evaluate the ability of multiple high-resolution WRF simulations to capture the spatial and temporal patterns of extreme precipitation associated with a particularly intense AR associated with multiple landslides in western HMA (Chapter 5).

6.2 Key Results

Chapter 2 describes the synoptic and thermodynamic conditions of an AR event that occurred in Santa Barbara, CA in March 2019 and resulted in over 8,000 lightning

flashes in under 24 hours. Despite low levels of convective available potential energy (CAPE), hail and electrification resulted from orographically forcing the above-average water vapor in the AR in a convectively unstable atmosphere above the freezing level. This case study provided a foundation for analysis for Chapter 4, where we contrast two HMA ARs with differing freezing levels that were associated with lightning, landslides, and extreme orographic precipitation.

Chapter 3 develops a climatology of ARs that spend a significant portion of their lifecycle crossing Southwest Asia and reach the complex topography before they precipitate out. Despite their low IVT content (usually less than 200 kg m^{-1} s^{-1}), HMA ARs contribute between 40-60% of total winter and spring precipitation in areas with an elevation greater than 1 km. We classified three distinct HMA AR types with unique circulation and precipitation patterns using combined empirical orthogonal function analysis (cEOF) and k-means clustering analysis. Synoptic composites revealed that each HMA AR type results in above-average precipitation in Northwestern, Western, and Eastern HMA, giving each of them their respective names. During Western HMA ARs, an anticyclonic circulation center over the Arabian Sea transports water vapor poleward and increases precipitation Western Himalayas and the Karakoram. Northwestern HMA ARs are characterized by a tilted trough axis and increased IVT that reaches as far as 40°N that increases precipitation in the Hindu Kush and the Pamirs. Roughly a quarter of the time, a Northwestern HMA AR will transition to a Western HMA AR, increasing precipitation in both regions. Eastern HMA ARs are associated with southwesterly moisture flux across the Bay of Bengal that results in above-average precipitation in Eastern Himalaya. Additionally, this research found that Western and Northwestern HMA AR frequency increases during El Niño conditions and positive Arctic Oscillation conditions.

Chapter 4 used 36 years of dynamically downscaled reanalysis (6.7 km spatial res-

olution, 3-hourly temporal resolution) to evaluate the mesoscale conditions during the three HMA AR types. Trend analysis revealed that, during ARs, the height of the freezing level and magnitude of IVT has increased significantly since 1979 across HMA. We found a significant decrease in the fraction of frozen precipitation during AR days of above-average freezing level compared to AR days of below-average freezing level. To investigate this relationship further, we contrasted the mesoscale conditions of two impactful Northwestern-transitioned-to-Western HMA ARs - one that occurred with an above-average freezing level height and one with a below-average freezing level height. We found that the synoptic placement of the upper level trough and lower level anticyclonic circulation is critical to orientation of the AR axis relative to the topography. Western HMA ARs with more southwesterly flow are more likely to get terrain-locked in the western HMA notch, resulting in higher amounts of orographic precipitation, while ARs with more zonal flow will result in less extreme precipitation. Similar to the results in Chapter 2, the AR with the below-average freezing level height had a much higher lightning flash frequency. Further conclusions on the relationship between lightning and HMA ARs will be delayed until more accurate lightning data can be provided. This work also emphasizes the role of the height of the freezing level during HMA ARs in the contribution to frozen precipitation. This chapter illuminates the local impact of these ARs on vital watersheds, precipitation-triggered landslides, and lightning in HMA.

The final chapter of this dissertation uses High Performance Computing resources provided by Blue Waters and Frontera supercomputers to complete multiple high-resolution WRF simulations. We evaluate the ability of simulations with differing spatial resolutions and physics parameterizations to resolve the features of extreme precipitation and IVT during a Western HMA AR that was associated with multiple landslides in February 2010. We validated Norris' 6.7 km WRF model data, 3 km WRF model

data (using same physics parameterizations as Norris et al. (2018)), 3 km WRF simulations with a difference microphysics scheme, and 3 km simulations with a different land surface model against precipitation provided by NASA's Integrated Multi-satellitE Retrievals for GPM. We find that the finer-resolution dynamical simulations (3 km) improves the representation of the orographic precipitation in complex terrain by 75% compared to the course-scale (6.7 km) simulations. We also validated IVT against the ERA5 reanalysis and found that a reconfiguration of the WRF domains (e.g., adding a 27 km parent domain and including spectral nudging) for the 3 km simulation is needed to keep low-level moisture circulation fields closer to the reanalysis. This chapter justifies the need for further and future downscaling of HMA ARs to improve our understanding of their impact on precipitation extremes.

6.3 Suggestions for future work

There are three types of HMA ARs that contribute roughly 40-60% of total winter and spring precipitation in Western, Northwestern, and Eastern HMA, respectively (Nash et al., 2021). While a little over half of the annual precipitation in HMA comes from winter and spring extratropical cyclones, just a few of those co-occurring with impactful ARs can contribute significantly to those totals (Cannon et al., 2015; Hunt et al., 2018; Nash et al., 2021, 2022; Norris et al., 2018). We show that the fraction of frozen precipitation is significantly lower during AR days with an above-average freezing level, and both water vapor transport and the height of the zero degree isotherm during HMA ARs has significantly increased since 1979. This illuminates the need for future work investigating the influence of the 0°C isotherm during AR events. We also found that in HMA, the orientation of the AR relative to topography plays a more important role in AR precipitation totals than IVT content. This has unique implications

for the future development of an AR-risk categorization, similar to that in Ralph et al. (2019), emphasizing the importance of AR direction and local topography. We needed finer-scale simulations to accurately represent extreme orographic precipitation during HMA ARs, highlighting the importance of dynamical downscaling for future forecasting efforts. This dissertation increased the overall understanding of AR impacts in HMA - however, this is just the beginning of our understanding of the complex relationship between HMA and ARs. Further work will improve forecasts for precipitation and natural hazards in a region vulnerable to changes in a warming climate. Future and ongoing research efforts regarding HMA ARs include the following:

1. Investigate the relationship between ARs and lightning on a global scale using data from the Geostationary Lightning Mapper (GLM) on the National Oceanic and Atmospheric Administration's (NOAA) Geostationary Operational Environmental Satellite version 16 (GOES-16). Because this satellite is geostationary, the extent does not cover HMA. However, further work could be done to illustrate the relationship between ARs and lightning.

2. Using the synoptic conditions of the HMA AR subtypes identified in Chapter 3, develop a probabilistic forecast model of HMA ARs that could be used for subseasonal-to-seasonal predictions of AR frequency in HMA. Gibson et al. (2020) used a similar framework in S2S predictions of ARs and drought conditions in the western US, and would be useful in HMA.

3. Further investigation into the land-sea interaction of air parcels within HMA ARs would be useful in determining the moisture sourcing for the ARs and improve understanding of evaporation contribution vs. tropical moisture exports.

4. As suggested in Chapter 5, additional parameterization tests and further down-

scaling (e.g., 1 km spatial resolution) could support the conclusions that downscaling is important to resolving extreme maxima of AR-related precipitation and determine the influence of finer-scale simulations on these features.

5. The framework developed in Chapter 5 could be applied to the mesoscale analysis and AR case studies completed in Chapter 4, to resolve fine-scale features such as localized orographically forced vertical motion and further illustrate the differences between hazardous and beneficial HMA ARs.

References

Cannon, F., Carvalho, L. M., Jones, C., & Bookhagen, B. (2015). Multi-annual variations in winter westerly disturbance activity affecting the Himalaya. *Climate Dynamics*, *44*(1-2), 441–455. https://doi.org/10.1007/s00382-014-2248-8

Dettinger, M. D. (2011). Climate change, atmospheric rivers, and floods in California - a multimodel analysis of storm frequency and magnitude changes. *JAWRA Journal of the American Water Resources Association*, *47*(3), 514–523. https://doi.org/10.1111/j.1752-1688.2011.00546.x

Gibson, P. B., Waliser, D. E., Guan, B., DeFlorio, M. J., Ralph, F., & Swain, D. L. (2020). Ridging Associated with Drought across the Western and Southwestern United States: Characteristics, Trends, and Predictability Sources. *Journal of Climate*, *33*(7), 2485–2508. https://doi.org/10.1175/JCLI-D-19-0439.1

Gorodetskaya, I. V., Tsukernik, M., Claes, K., Ralph, F., Neff, W. D., & Van Lipzip, N. P. M. (2014). The role of atmospheric rivers in anomalous snow accumulation in East Antarctica. *Geophysical Research Letters*, *41*, 6199–6206. https://doi.org/10.1002/2014GL060881

Guan, B., Molotch, N. P., Waliser, D. E., Fetzer, E. J., & Neiman, P. J. (2010). Extreme snowfall events linked to atmospheric rivers and surface air temperature via satellite measurements. *Geophysical Research Letters*, *37*(20), n/a–n/a. https://doi.org/10.1029/2010gl044696

Hunt, K. M., Turner, A. G., & Shaffrey, L. C. (2018). The evolution, seasonality and impacts of western disturbances. *Quarterly Journal of the Royal Meteorological Society*, *144*(710), 278–290. https://doi.org/10.1002/qj.3200

Lavers, D. A., Allan, R. P., Wood, E. F., Villarini, G., Brayshaw, D. J., & Wade, A. J. (2011). Winter floods in Britain are connected to atmospheric rivers. *Geophysical Research Letters*, *38*(23), 1–8. https://doi.org/10.1029/2011gl049783

Lavers, D. A., & Villarini, G. (2013). The nexus between atmospheric rivers and extreme precipitation across Europe. *Geophysical Research Letters*, *40*(12), 3259–3264. https://doi.org/10.1002/grl.50636

Nash, D., Carvalho, L. M. V., Jones, C., & Ding, Q. (2021). Winter and spring atmospheric rivers in High Mountain Asia: climatology, dynamics, and variability. *Climate Dynamics*. https://doi.org/10.1007/S00382-021-06008-Z

Nash, D., Carvalho, L. M. V., Jones, C., & Ding, Q. (2022). Influence of zero degree line on Atmospheric Rivers in High Mountain Asia: WRF case studies of orographic precipitation extremes. *(in preparation)*.

Nash, D., & Carvalho, L. M. (2020). Brief Communication : An electrifying atmospheric river – understanding the thunderstorm event in Santa Barbara County during March 2019. *Natural Hazards and Earth System Sciences*, *20*, 1931–1940. https://doi.org/10.5194/nhess-20-1931-2020

Nash, D., Waliser, D. E., Guan, B., Ye, H., & Ralph, F. (2018). The Role of Atmospheric Rivers in Extratropical and Polar Hydroclimate. *Journal of Geophysical Research: Atmospheres*, *123*(13). https://doi.org/10.1029/2017JD028130

Neiman, P. J., Ralph, F., Wick, G. A., Kuo, Y.-H., Wee, T.-K., Ma, Z., Taylor, G. H., & Dettinger, M. D. (2008). Diagnosis of an intense atmospheric river impacting the Pacific Northwest: storm summary and offshore vertical structure observed with COSMIC satellite retrievals. *Monthly Weather Review*, *136*(11), 4398–4420. https://doi.org/10.1175/2008mwr2550.1

Norris, J., Carvalho, L. M., Jones, C., & Cannon, F. (2018). Deciphering the contrasting climatic trends between the central Himalaya and Karakorum with 36 years of WRF simulations. *Climate Dynamics*, 1–22. https://doi.org/https://doi.org/10.1007/s00382-018-4133-3

Ralph, F., Neiman, P. J., Wick, G. A., Gutman, S. I., Dettinger, M. D., Cayan, D. R., & White, A. B. (2006). Flooding on California's Russian River: Role of atmospheric rivers. *Geophysical Research Letters*, *33*(13). https://doi.org/10.1029/2006gl026689

Ralph, F., Wilson, A. M., Shulgina, T., Kawzenuk, B., Sellars, S., Rutz, J. J., Lamjiri, M. A., Barnes, E. A., Gershunov, A., Guan, B., Nardi, K. M., Osborne, T., & Wick, G. A. (2019). ARTMIP-early start comparison of atmospheric river detection tools: how many atmospheric rivers hit northern California's Russian River watershed? *Climate Dynamics*, *52*, 4973–4994. https://doi.org/10.1007/s00382-018-4427-5

Thapa, K., Endreny, T. A., & Ferguson, C. R. (2018). Atmospheric Rivers Carry Non-monsoon Extreme Precipitation Into Nepal. *Journal of Geophysical Research: Atmospheres*, *123*, 5901–5912. https://doi.org/10.1029/2017JD027626

Wernli, H., & Papritz, L. (2018). Role of polar anticyclones and mid-latitude cyclones for Arctic summertime sea-ice melting. *Nature Geoscience*, *11*, 108–113. https://doi.org/https://doi.org/10.1038/s41561-017-0041-0

Yang, Y., Zhao, T., Ni, G., & Sun, T. (2018). Atmospheric rivers over the Bay of Bengal lead to northern. *International Journal of Climatology*, *38*(August 2017), 1010–1021. https://doi.org/10.1002/joc.5229

Appendix A

Chapter 2 Appendix

A.1 Calculation of IVT for CFSv2

Integrated water vapor transport (IVT), a variable widely used for the detection and identification of ARs (e.g. (Dettinger et al., 2015; Guan & Waliser, 2015; Ralph et al., 2019)) is derived from specific humidity and wind fields at 17 pressure levels between 1,000 and 300 hPa inclusive from the CFSv2 operational analysis. IVT is calculated in the zonal (x) and meridional (y) direction using the following equations:

$$IVT_x = -\frac{1}{g}\int_{1000}^{300} uqdp \tag{A.1}$$

$$IVT_y = -\frac{1}{g}\int_{1000}^{300} vqdp \tag{A.2}$$

where g is the gravitational acceleration, u is zonal wind, v is meridional wind, q is specific humidity, p is pressure, and the column integration is between pressure levels 1000 and 300 hPa inclusive.

A.2 Supplemental Material

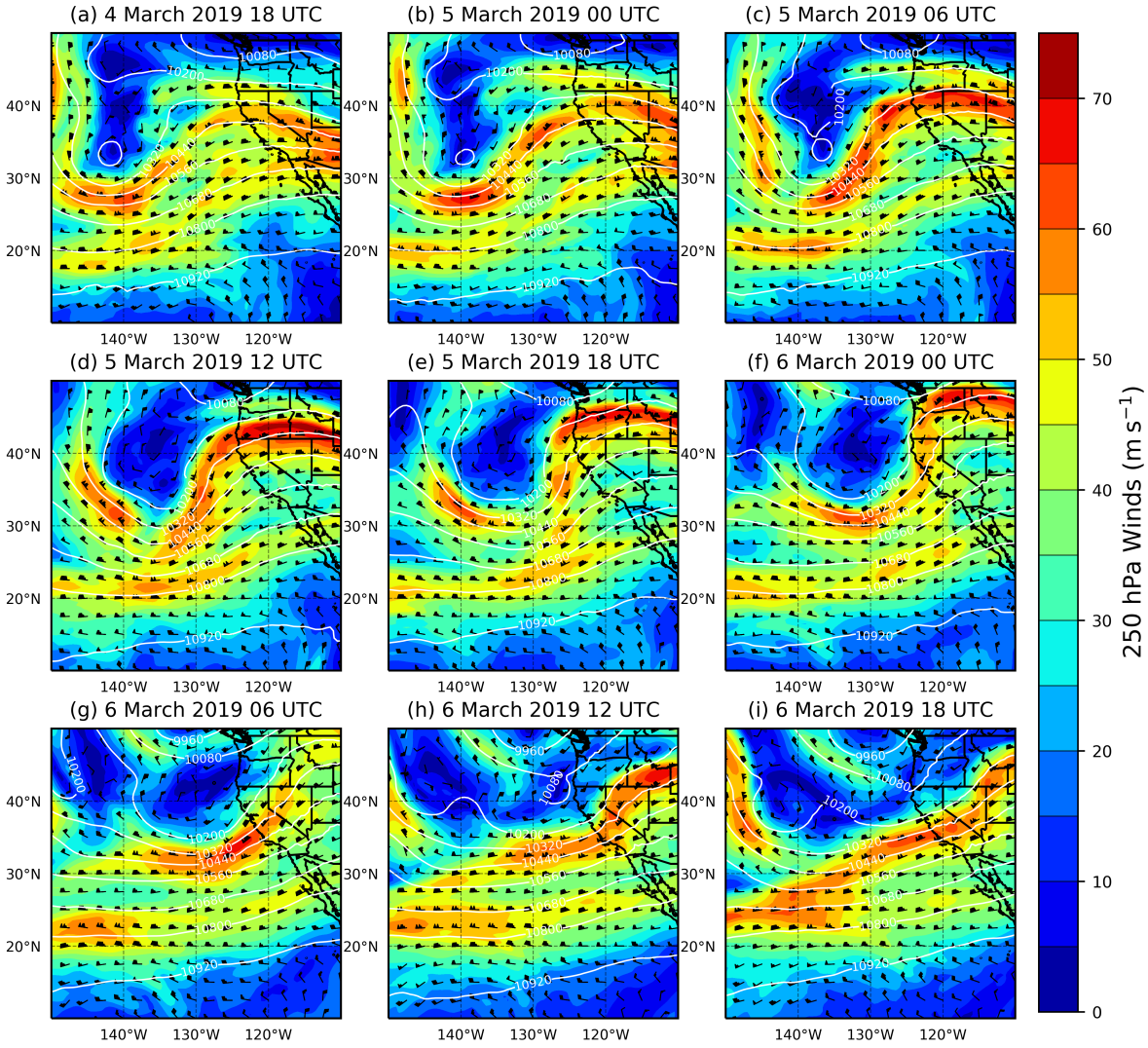

Figure A.1: CFSv2 250 hPa winds (barbs, knots), 250 hPa wind magnitude (shaded; m s^{-1}) and 250 hPa geopotential height (white contours; m) at 6-hourly timesteps between 4 March 2019 18 UTC and 6 March 2019 18 UTC.

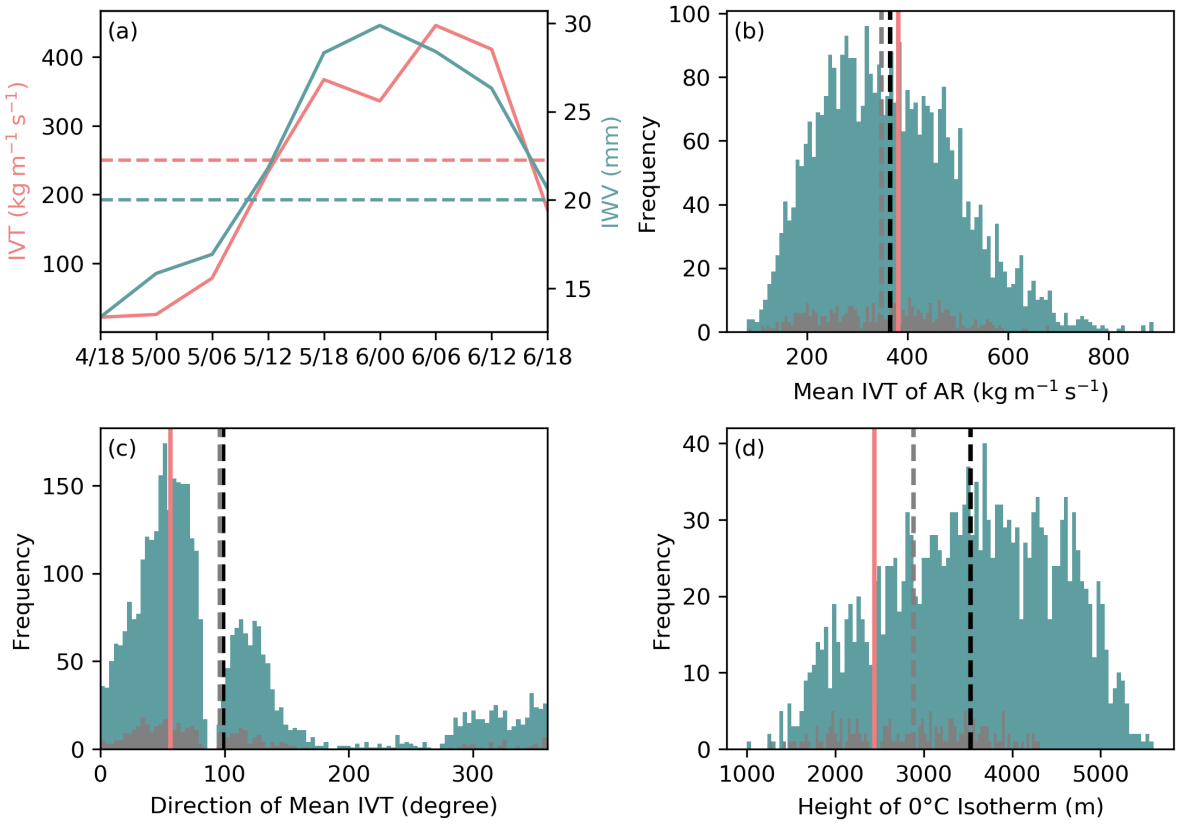

Figure A.2: (a) CFSv2 IVT (red line; kg m^{-1} s^{-1}) and IWV (blue line; mm) at the grid cell closest to Santa Barbara (34.5°N, 119.5°W) at each 6-hour time step between 4 March 2019 18 UTC and 6 March 2019 18 UTC. The minimum thresholds for the location to be considered part of an AR event are indicated by the dotted lines. (b) Mean IVT of the AR objects that made landfall in Santa Barbara in all the months (blue lines) and only March (grey lines) between January 1980 and May 2019 based on the AR Catalog from Guan and Waliser (2015). The mean IVT for the AR Event on March 5 is shown by the red solid line. The means of the distributions are shown in the dotted line. (c) Same as (b) but for direction of mean IVT propagation (azimuth is 0°if IVT is directed to the north). (d) Same as (b) but for the height of the 0°C Isotherm (m) interpolated from MERRA2 temperature and geopotential height.

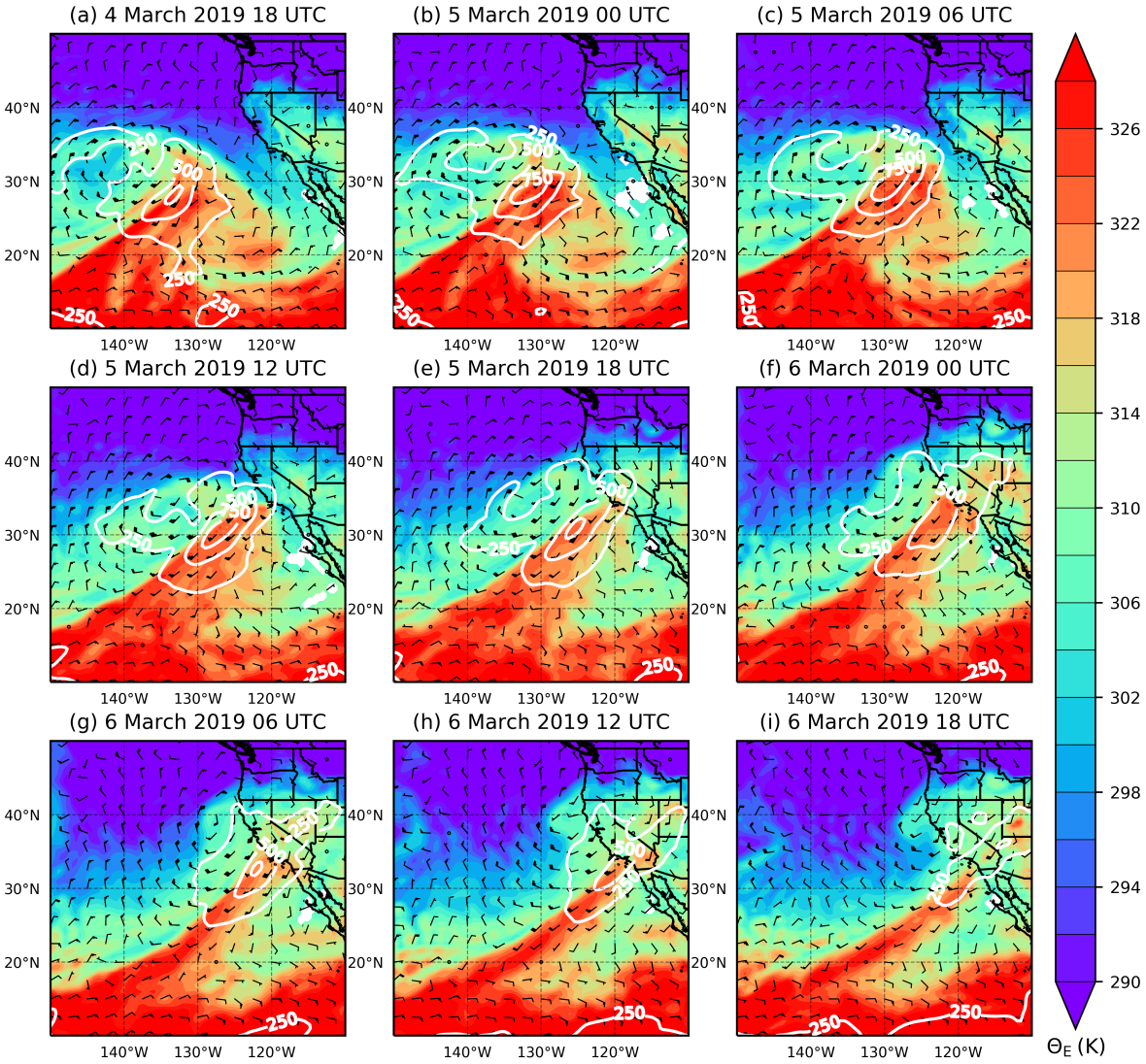

Figure A.3: Figure S3. CFSv2 850 hPa Equivalent Potential Temperature (shaded; K), 850 hPa winds (barbs; knots), and IVT greater than 250 kg m^{-1} s^{-1} (white contours; every 250 kg m^{-1} s^{-1}) for each 6-hour time step between 4 March 2019 18 UTC and 6 March 2019 18 UTC.

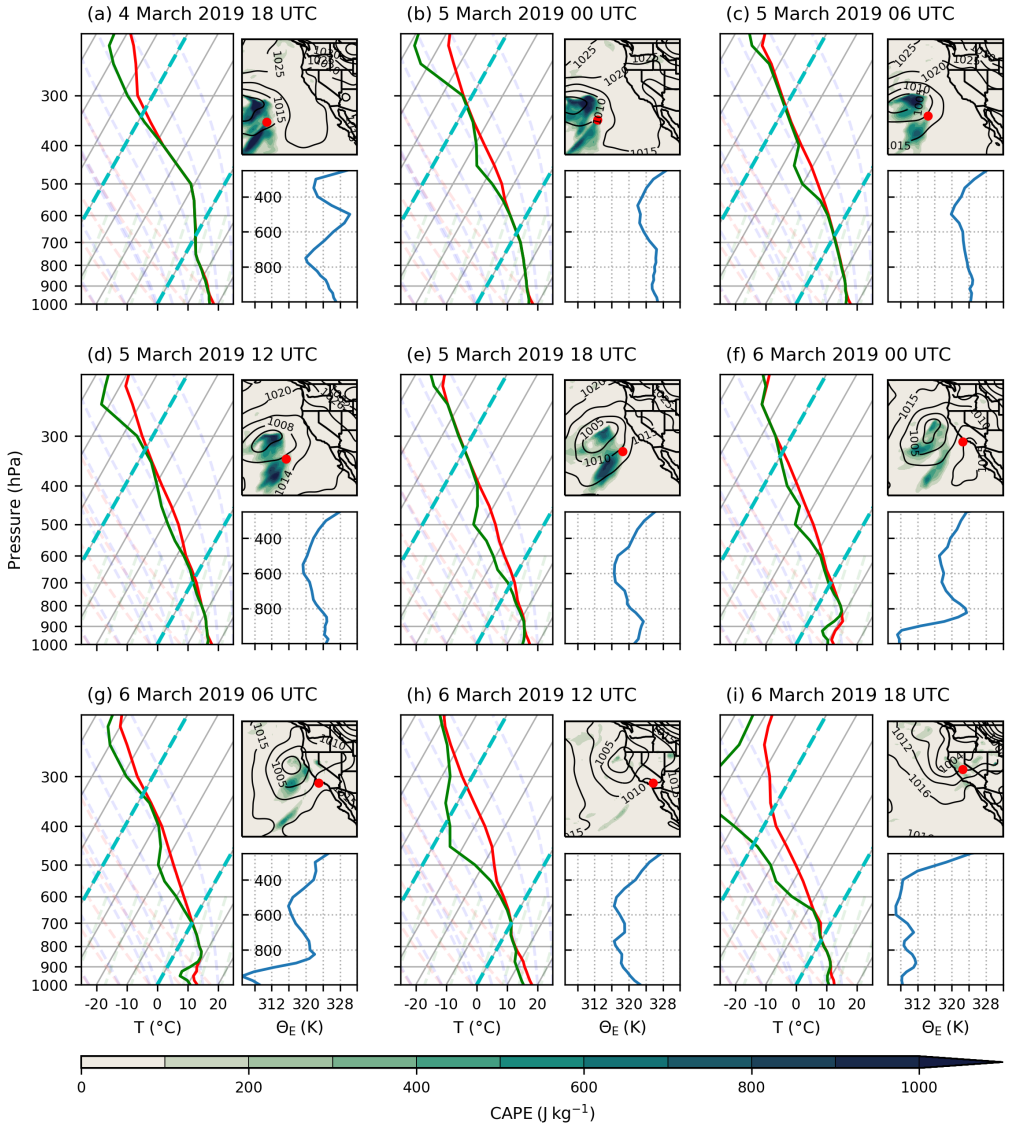

Figure A.4: *(left panel)* Skew(t) - log(p) vertical profile of CFSv2 temperature (red line) and dew point (green line) at the grid cell with the highest flash density (per 6 hours); *(right top panel)* CFSv2 CAPE (shaded, J kg^{-1}) and MSLP (black dashed contours; hPa) with the location of the highest flash density indicated by the red dot; *(right bottom panel)* CFSv2 Equivalent Potential Temperature (blue line; K) at the grid cell with the highest flash density for each 6-hour time step between (a) 4 March 2019 18 UTC and (i) 6 March 2019 18 UTC.

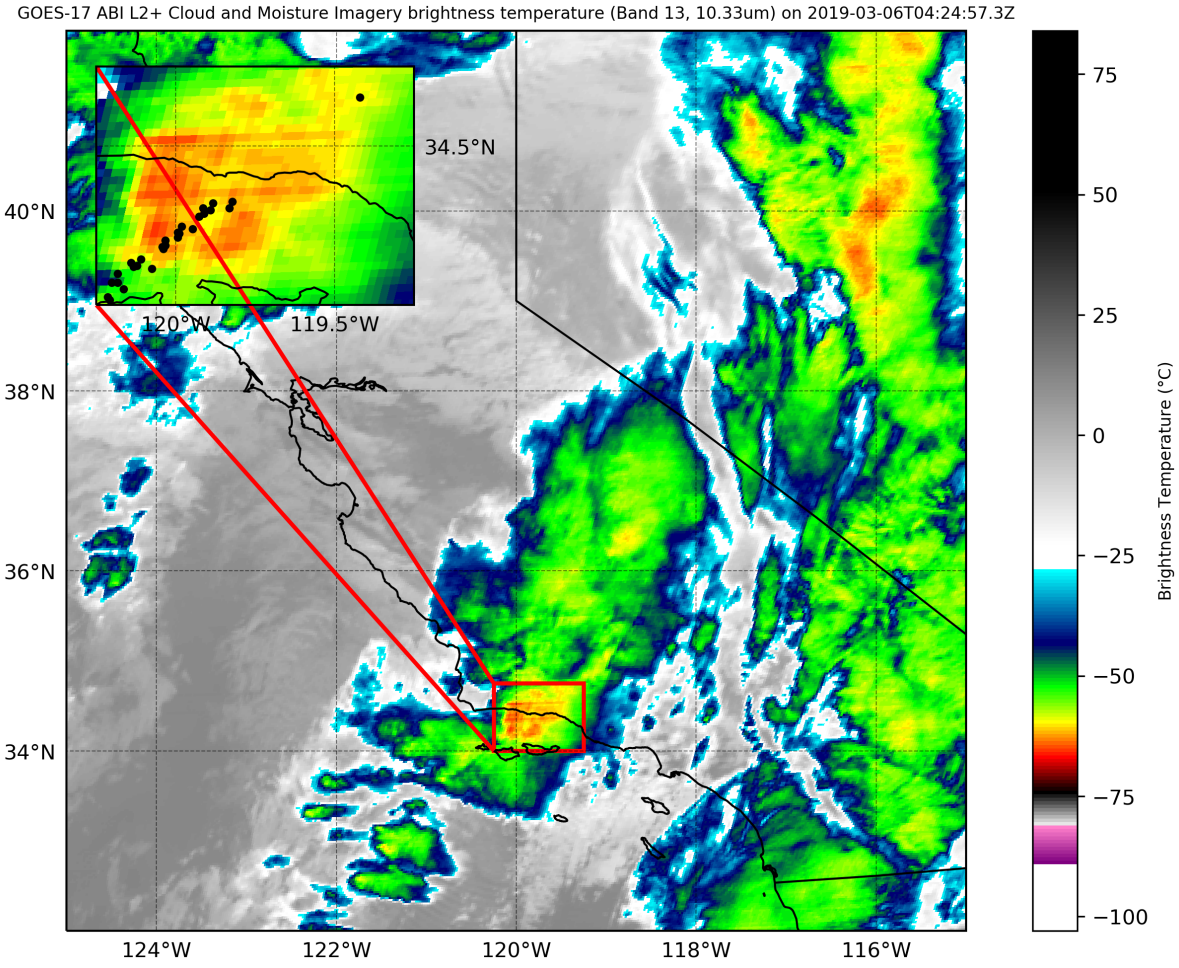

Figure A.5: Infrared brightness temperatures (shaded, °C) derived from band 13 of the GOES17 ABI L2 Cloud and Moisture Imagery Brightness Temperature at 6 March 2019 4:24 UTC. Detailed infrared brightness temperatures around Santa Barbara (outlined in red) are shown in the top left area of the map. Locations of NOAA NEXRAD L3 Hail Signatures (black points) identified between 4:15 UTC and 4:45 UTC on 6 March 2019 are shown on the inset map.

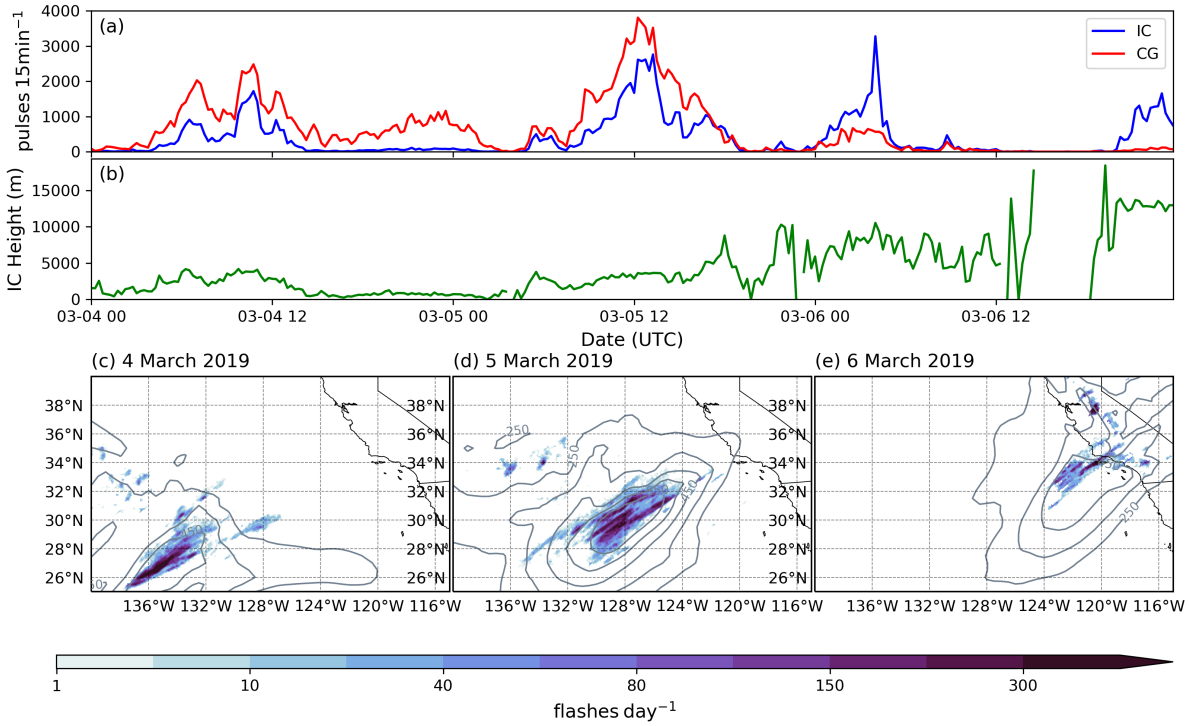

Figure A.6: (a) ENGLN number of flashes per 15 minutes between 4 March 2019 0 UTC and 7 March 0 UTC for in-cloud (IC) flashes (blue line) and cloud-to-ground (CG) flashes (red line). (b) ENGLN average IC lightning flash height (green line; m) between 4 March 2019 0 UTC and 7 March 0 UTC. (c) ENGLN lightning flash count (shaded, flashes day^{-1}) interpolated to 0.1°and IVT greater than 250 kg m^{-1} s^{-1} (grey contours; every 100 kg m^{-1} s^{-1}) for the 24-hour period of 4 March 2019. (d) Same as (c), but for the 24-hour period of 5 March 2019. (e) Same as (c), but for the 24-hour period of 6 March 2019.

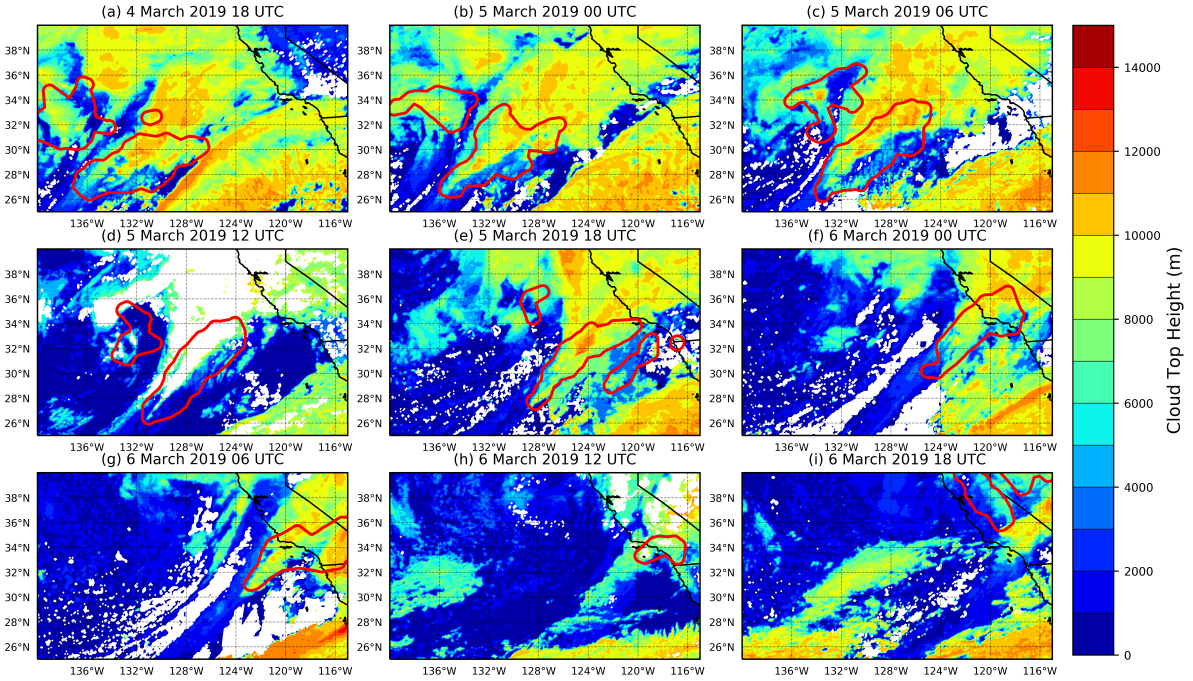

Figure A.7: GOES ABI L2 ACHC cloud top height (shaded; m) and the location of the majority of lightning flash points (red polygon) at each 6-hour time step between 4 March 2019 18 UTC and 6 March 2019 18 UTC.

References

Dettinger, M. D., Ralph, F., & Lavers, D. (2015). Setting the stage for a global science of atmospheric rivers. *Eos*, *97*(1), 7. https://doi.org/10.1029/2015eo038675

Guan, B., & Waliser, D. E. (2015). Detection of atmospheric rivers: Evaluation and application of an algorithm for global studies. *Journal of Geophysical Research: Atmospheres*, *120*(24), 12514–12535. https://doi.org/10.1002/2015jd024257

Ralph, F., Wilson, A. M., Shulgina, T., Kawzenuk, B., Sellars, S., Rutz, J. J., Lamjiri, M. A., Barnes, E. A., Gershunov, A., Guan, B., Nardi, K. M., Osborne, T., & Wick, G. A. (2019). ARTMIP-early start comparison of atmospheric river detection tools: how many atmospheric rivers hit northern California's Russian River watershed? *Climate Dynamics*, *52*, 4973–4994. https://doi.org/10.1007/s00382-018-4427-5

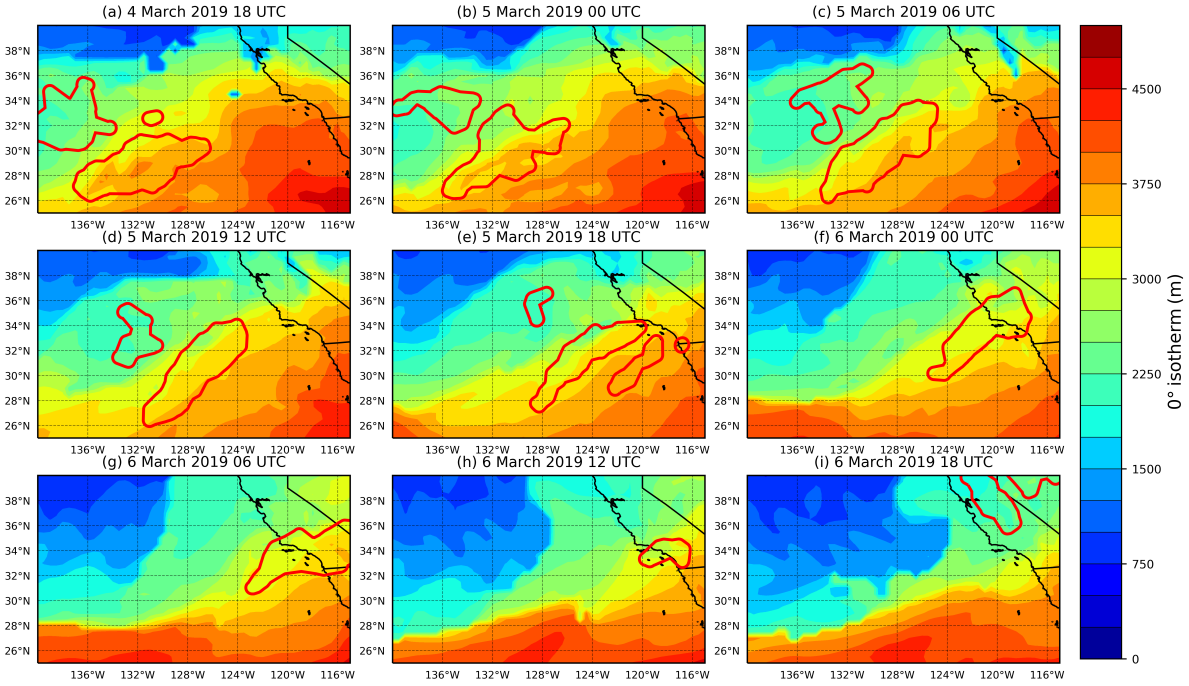

Figure A.8: CFSv2 height of 0°isotherm (shaded; m) and the location of the majority of lightning flash points (red polygon) at each 6-hour time step between 4 March 2019 18 UTC and 6 March 2019 18 UTC.

Appendix B

Chapter 3 Appendix

B.1 cEOF Analysis

For each of the ARs within DJFMAM, ERA5 meridional and zonal integrated water vapor transport (IVT) were subset to 20°E to 100°E and 10°N to 50°N. Next, the mean annual cycle (computed using the first two harmonics) of the atmospheric fields were subtracted, each grid cell was weighted by the square root of the cosine of the latitude, and the long-term mean was removed from the data. Variables were normalized by the standard deviation in space and time. This standardization transformed the 3-dimensional data into non-dimensional data with a standard deviation of one, which is necessary in cEOF for variables with different units. The data were then reshaped into a rectangular matrix Z, with dimensions of 3NM x n, where N and M are the numbers of grid points in the X and Y directions, m is the total number of grid points (i.e. $m = NxM$), and n is the number of separate AR cases. The covariance matrix (R) of Z was computed using the formula:

$$R = \frac{1}{NM - 1} Z_T Z \tag{B.1}$$

where R is the covariance matrix, N and M are the numbers of grid points in the X and Y directions, and Z is the nondimensional data with a standard deviation of 1. The covariance matrix for the spatial correlations between atmospheric fields was calculated from different snapshots in time (t-mode EOF), resulting in an mxm covariance matrix rather than temporal correlations between grid points (s-mode EOF), which results in an nxn covariance matrix (Compagnucci & Richman, 2008). The choice to use t-mode EOF versus s-mode EOF (spatial versus temporal correlations) was made to get objective comparisons between AR cases and differentiate between the different synoptic types of ARs in HMA. For more discussion on t-mode versus s-mode EOF, see Compagnucci and Richman (2008) and Mercer et al. (2012). Eigenvector decomposition (V) of the covariance matrix, R, was calculated giving the time coefficients for the data. Spatial loadings (cEOFs) were extracted by matrix multiplying the standardized,

non-dimensional data (Z) by the eigenvectors (V).

B.2 K-means cluster Analysis

K-means clustering is a form of iterative, unsupervised learning that classifies the data without having been previously trained (Wilks, 2019a). First, the number of clusters (k) is specified by the user and the algorithm randomly places cluster centers or centroids among the data points. Then each data point is assigned to the closest cluster by calculating its Euclidean distance with respect to each centroid. Once each data point is assigned to a cluster, then new centroids are calculated by computing the average of the data points assigned to that cluster. The data points are then reassigned to clusters based on the new centroid locations, and new centroid locations are determined. This process repeats until the data points are no longer assigned to a different cluster. The number of clusters is a subjective choice, so for this analysis, we tested k=2 through k=15 and chose the level of clustering that maximized covariance within clusters and minimized covariance between clusters. To determine the number of clusters that maximized covariance within clusters, we visually inspected the kernel density function of the first two cEOFs to identify potential maxima prior to k-means analysis. Silhouette scores were reiteratively calculated for clusters k=2 through k=15 to determine the optimal number of clusters that minimized covariance between clusters. The mean silhouette score describes how close each point in one cluster is to points in the other clusters, with a score of 1 indicating that the points in the cluster are far away from the other clusters (Wilks, 2019a). Last, we also visually inspected the resulting cluster synoptic composite maps to confirm that the choice in the number of clusters minimized covariance between clusters and maximized covariance within clusters.

B.3 Z-score Tests

To test the differences in the proportion of the different types of ARs between the positive, negative, and neutral conditions of climate modes, we test the difference in two population proportions using z-scores (Spiegel & Stephens, 2008). For example, we test the differences in the proportion of the frequency of Eastern HMA ARs that are El Niño and the frequency of Eastern HMA ARs that are La Niña). The null hypothesis is that the proportion of sample 1 (Eastern HMA ARs during El Niño) is equal to the proportion of sample 2 (Eastern HMA ARs during La Niña).

$$Z = \frac{(\hat{p}_1 - \hat{p}_2) - 0}{\sqrt{(\hat{p}(1-\hat{p})(\frac{1}{n_1} + \frac{1}{n_2})}} \tag{B.2}$$

and

$$\hat{p} = \frac{Y_1 + Y_2}{n_1 + n_2} \tag{B.3}$$

where n_1 and n_2 are the total number of observations in each sample (e.g., n_1 = total number of days that are considered El Niño during DJFMAM between 1979-2019), Y_1 is the number of the days considered Eastern HMA ARs and El Niño, Y_2 is the number of days considered Eastern HMA ARs and La Niña, $\hat{p}_1$ is the proportion of the sample 1 days to the number of days that are El Niño in DJFMAM between 1979-2019. $\hat{p}_2$ is the proportion of the sample 2 days to the number of days that are La Niña in DJFMAM between 1979-2019.

To test the difference of the means of the circulation and moisture variables, we used the z-score to test the null hypothesis that the sample means of sample 1 and sample 2 are equal (Spiegel & Stephens, 2008; Wilks, 2019b). For example, sample 1 are the days in which there is an Eastern HMA AR with El Niño conditions, and sample 2 are the days in which there is an Eastern HMA AR with La Niña conditions. We used the z-score given by the following equations to test the null hypothesis at 95% significance level:

$$z = \frac{\bar{X}_1 - \bar{X}_2}{\sigma_{\bar{X}1-\bar{X}2}} \tag{B.4}$$

and

$$\sigma_{\bar{X}1-\bar{X}2} = \sqrt{\frac{\sigma_1^2}{n_1} + \frac{\sigma_2^2}{n_2}} \tag{B.5}$$

where $\bar{X}_1$ and $\bar{X}_2$ are the sample means, σ_1 and σ_2 are the sample standard deviations, and n_1 and n_2 are the total number of observations in each sample.

B.4 Supplemental Material

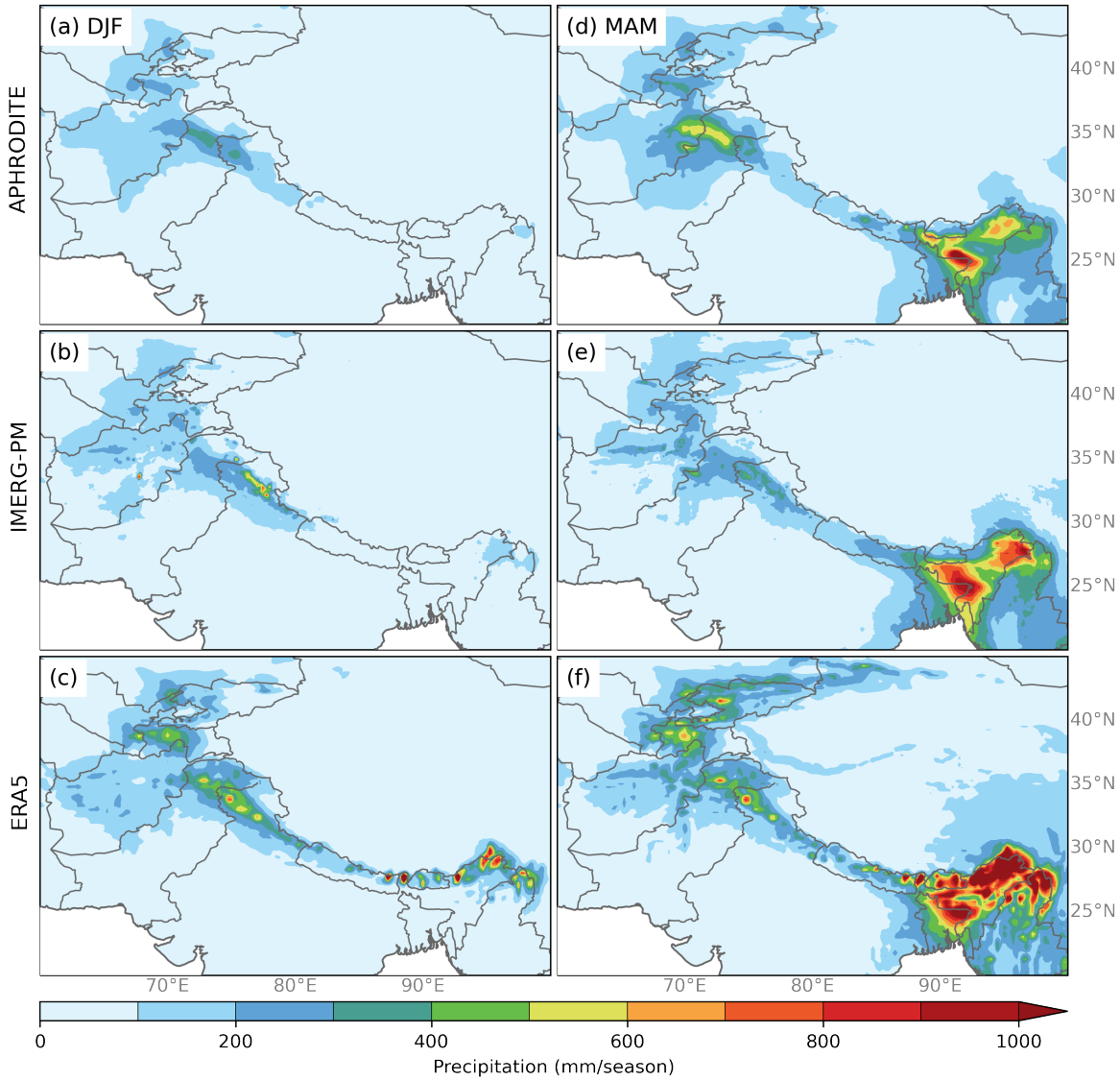

Figure B.1: The average seasonal (DJF - left and MAM - right) precipitation totals (shaded; mm season^{-1}) for APHRODITE (top row), IMERG-PM (middle row), and ERA5 (bottom row) data sources between December 2000 and March 2015.

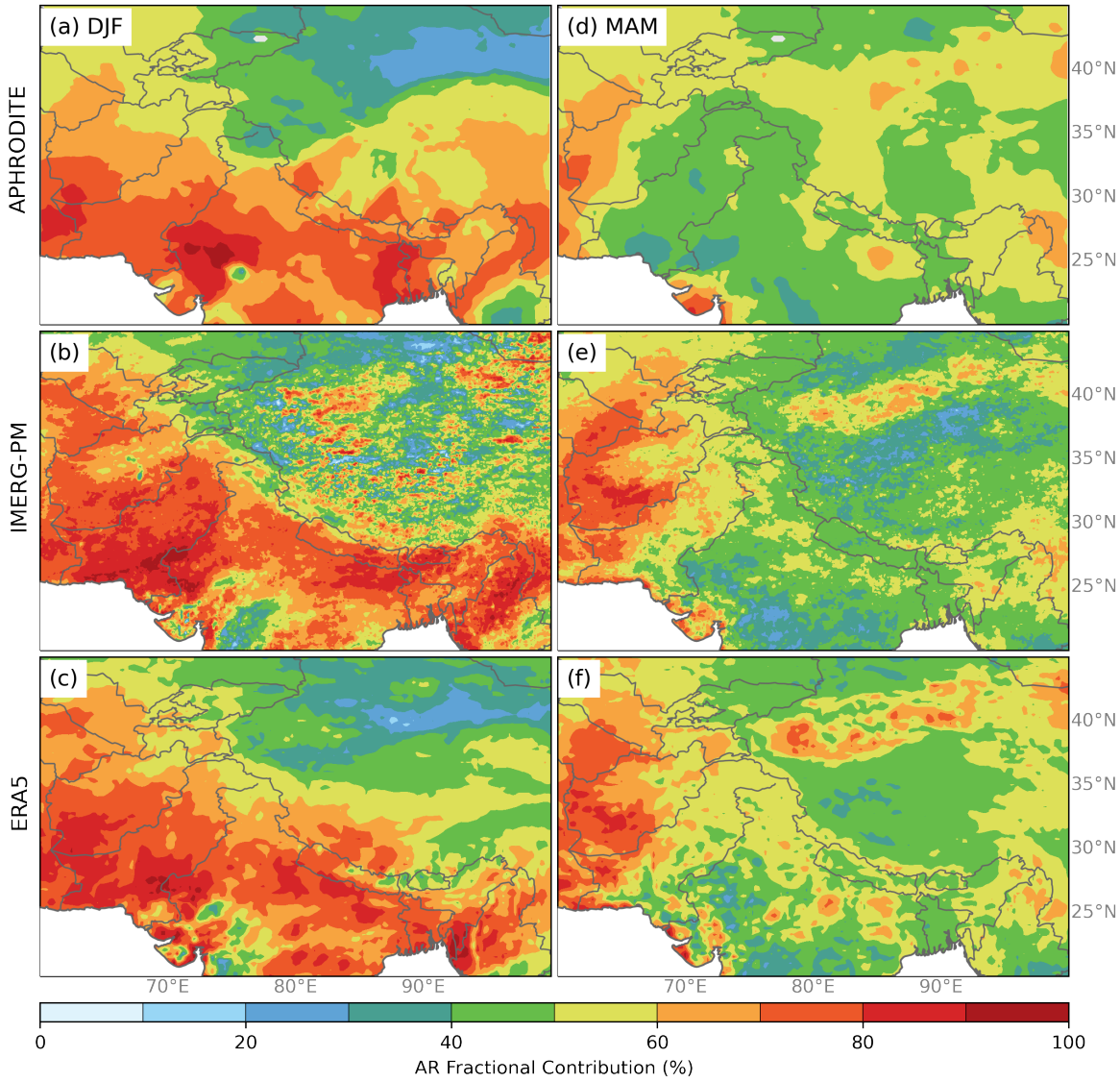

Figure B.2: The seasonal (DJF - left and MAM - right) AR precipitation fraction (shaded, %) for APHRODITE (top row), IMERG-PM (middle row), and ERA5 (bottom row) data sources between December 2000 and March 2015.

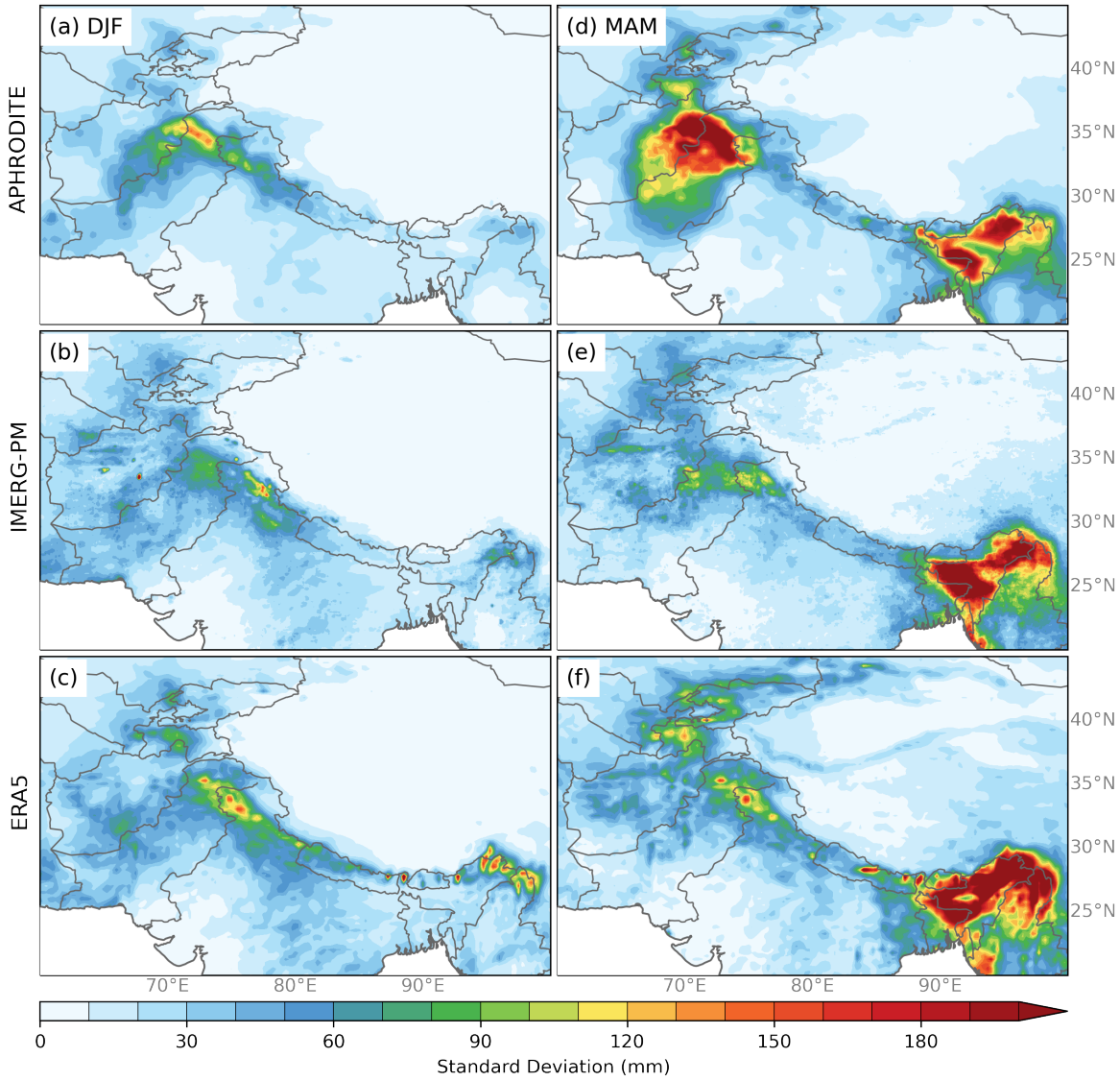

Figure B.3: The standard deviation (DJF - left and MAM - right) of precipitation during AR days (shaded; mm) for APHRODITE (top row), IMERG-PM (middle row), and ERA5 (bottom row) data sources between December 2000 and March 2015.

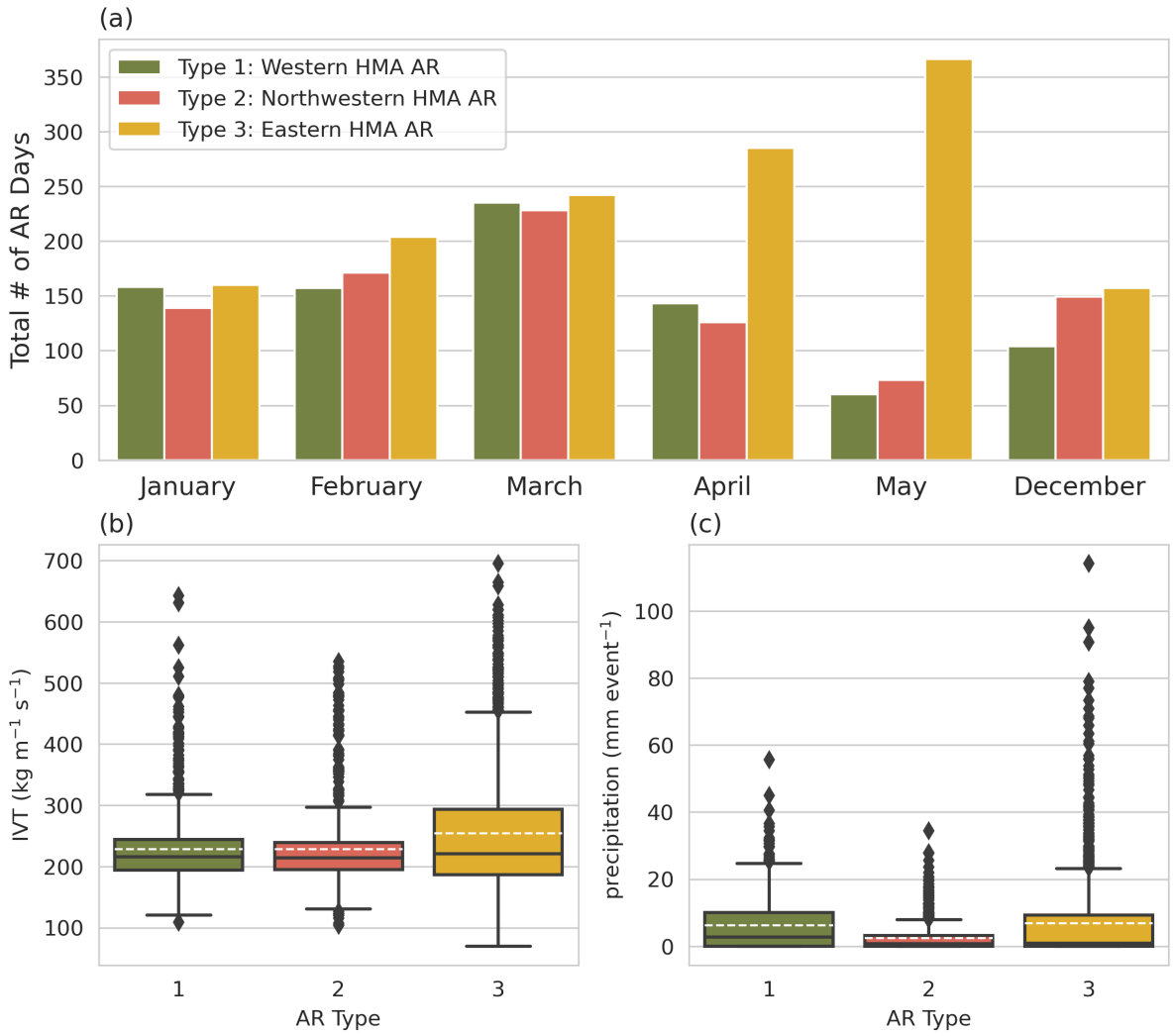

Figure B.4: (a) Frequency of the different AR Types during each month in DJFMAM. (b) Average IVT (kg m^{-1} s^{-1}) within ARs during Western HMA ARs (Type 1), Northwestern HMA ARs (Type 2), and Eastern HMA ARs (Type 3). The box extends from lower to upper quartiles of the data with a black line at the median and white dotted line at the mean. The whiskers show the range of the data and outliers are shown as points past the end of the whiskers. (c) The same as (b) but for weighted, area-averaged precipitation (mm $event^{-1}$) within a bounding box near where we see above-average precipitation for each AR Type (e.g. Type 1: Western HMA ARs (71-79°E, 32-37°N); Type 2: Northwestern HMA ARs (66-74°E, 37-40°N); Type 3: Eastern HMA ARs (90-100°E, 24-30°N).

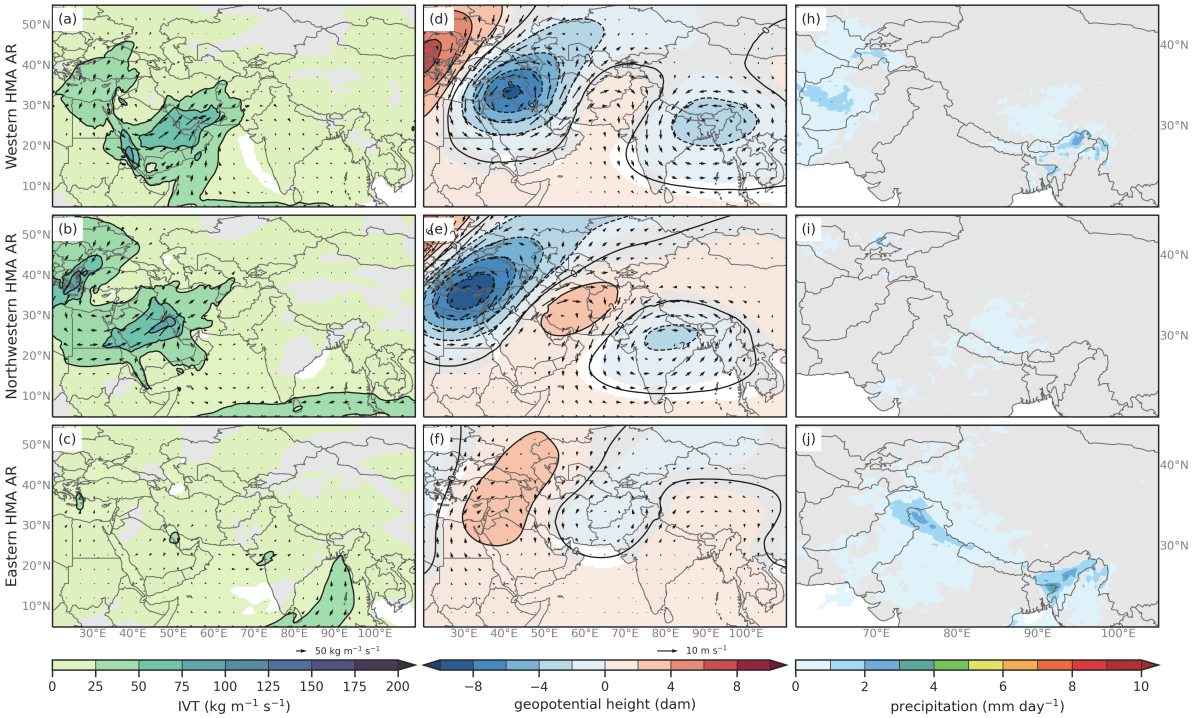

Figure B.5: Lead 2 DJFMAM average anomaly composites of (left column) IVT (shaded, contours, kg m^{-1} s^{-1}), (middle column) 250 hPa wind speeds (shaded and vectors; m s^{-1}) and 250 hPa geopotential height (contours; dam), and (right column) precipitation (shaded; mm day^{-1}) for Western HMA ARs (Type 1, first row), Northwestern HMA ARs (Type 2, second row), and Eastern HMA ARs (Type 3, third row). Only values that are considered statistically significant at the 95% confidence interval are shaded.

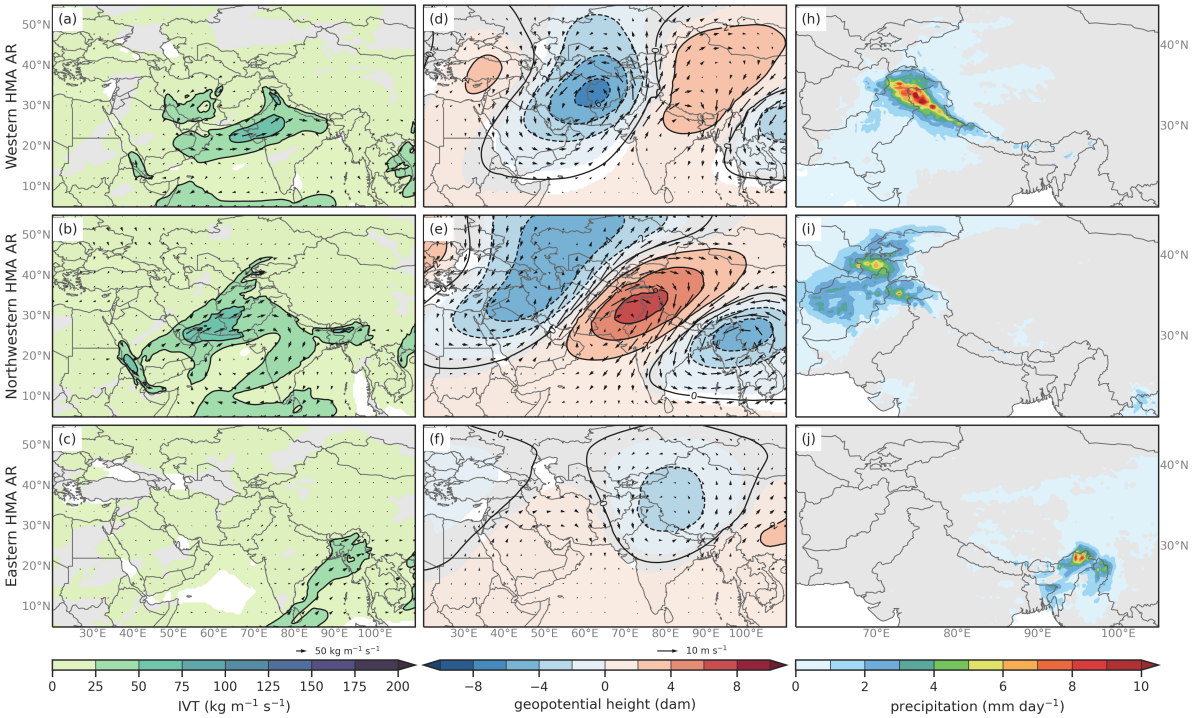

Figure B.6: Lag 2 DJFMAM average anomaly composites of (left column) IVT (shaded, contours, kg m^{-1} s^{-1}), (middle column) 250 hPa wind speeds (shaded and vectors; m s^{-1}) and 250 hPa geopotential height (contours; dam), and (right column) precipitation (shaded; mm day^{-1}) for Western HMA ARs (Type 1, first row), Northwestern HMA ARs (Type 2, second row), and Eastern HMA ARs (Type 3, third row). Only values that are considered statistically significant at the 95% confidence interval are shaded.

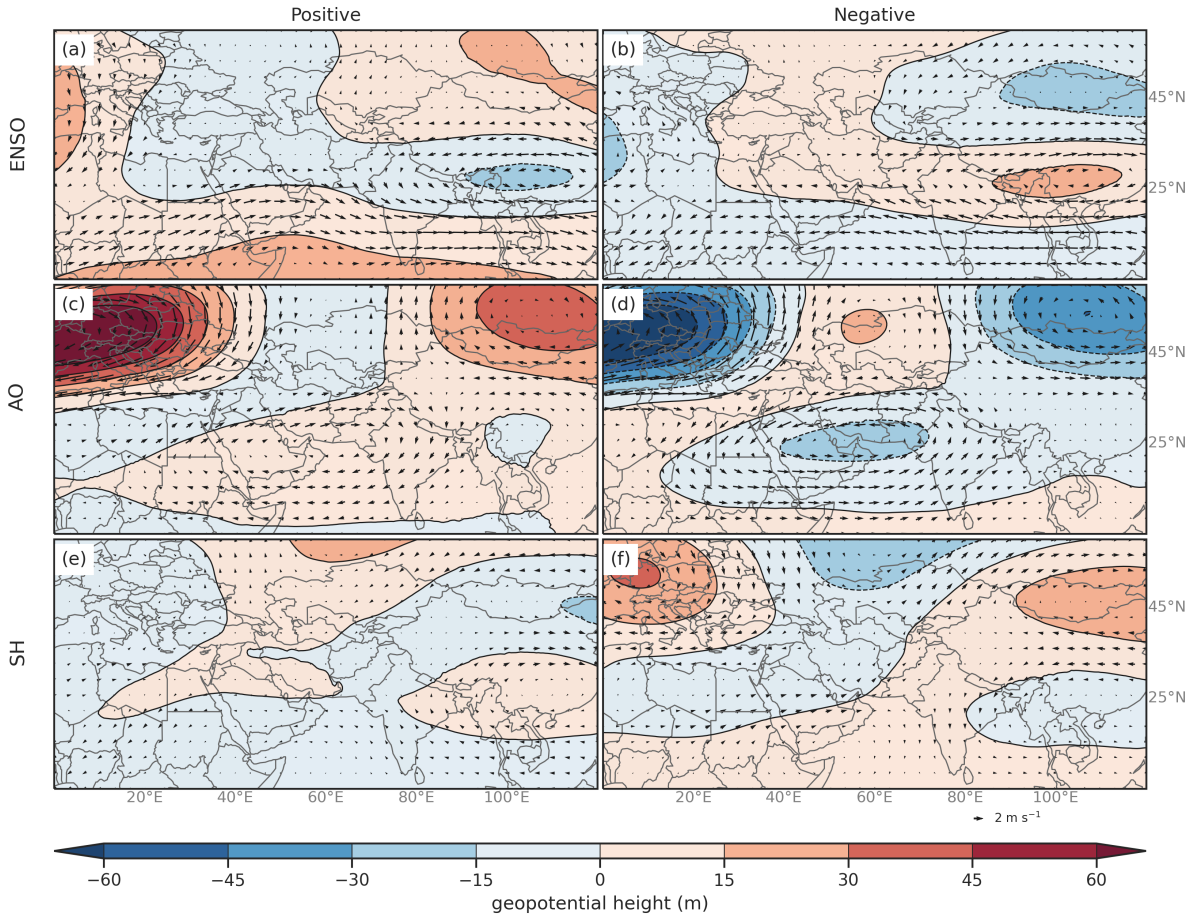

Figure B.7: Composites of 250 hPa geopotential height (shaded, contours, m) and winds (vectors, m s^{-1}) for all days in DJFMAM between 1979 and 2019 for (a) El Nino, (b) La Nina, (c) AO+, (d) AO-, (e) SH+, and (f) SH- conditions.

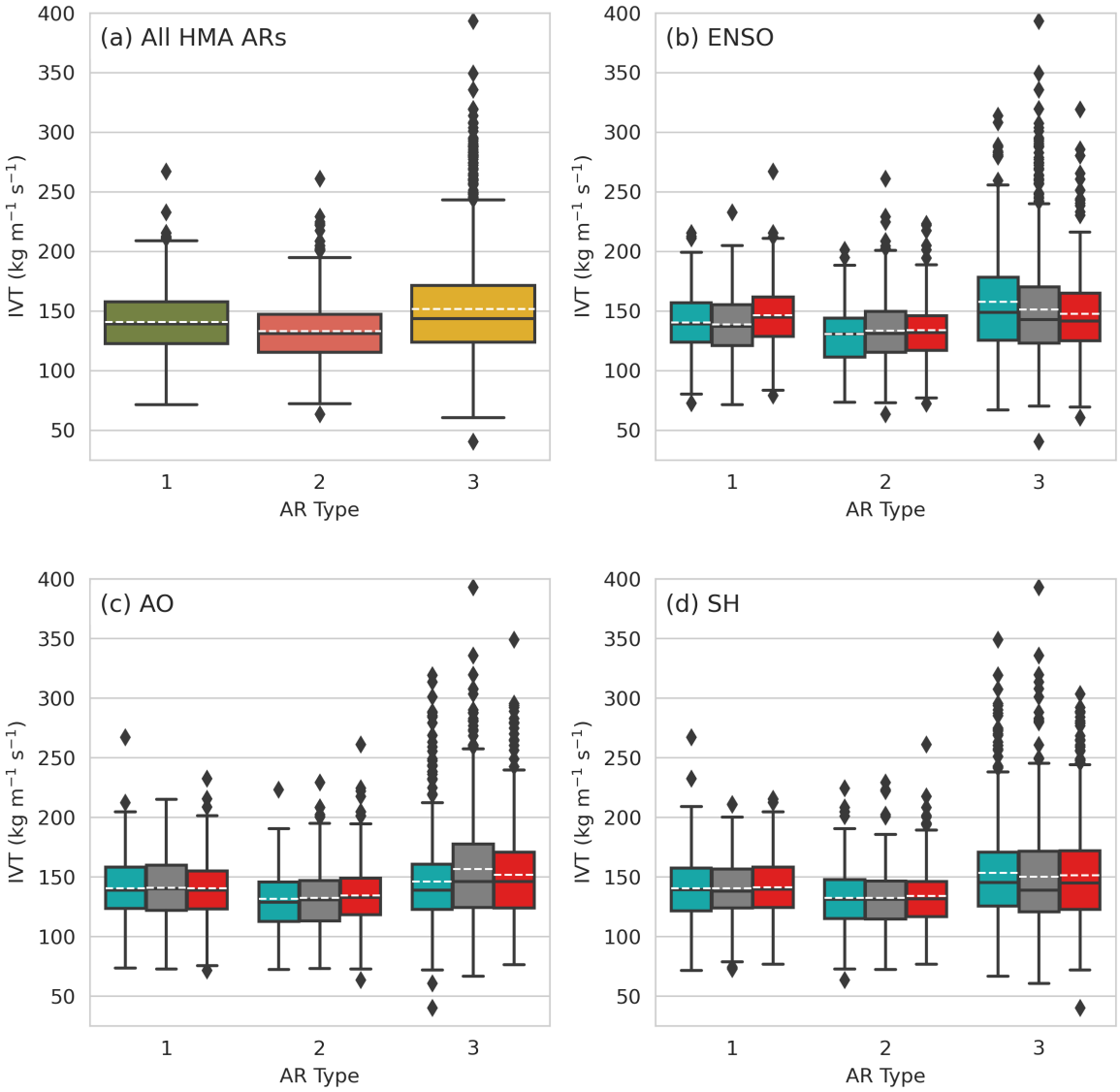

Figure B.8: (a) Average IVT anomalies within ARs during Western HMA ARs (Type 1), Northwestern HMA ARs (Type 2), and Eastern HMA ARs (Type 3). The box extends from lower to upper quartiles of the data with a black line at the median and white dotted line at the mean. The whiskers show the range of the data and outliers are shown as points past the end of the whiskers. (b) The same as (a) but broken down by ENSO negative (blue), neutral (grey), and positive (red) conditions. (c) The same as (b) but for AO. (d) The same as (b) but for SH.

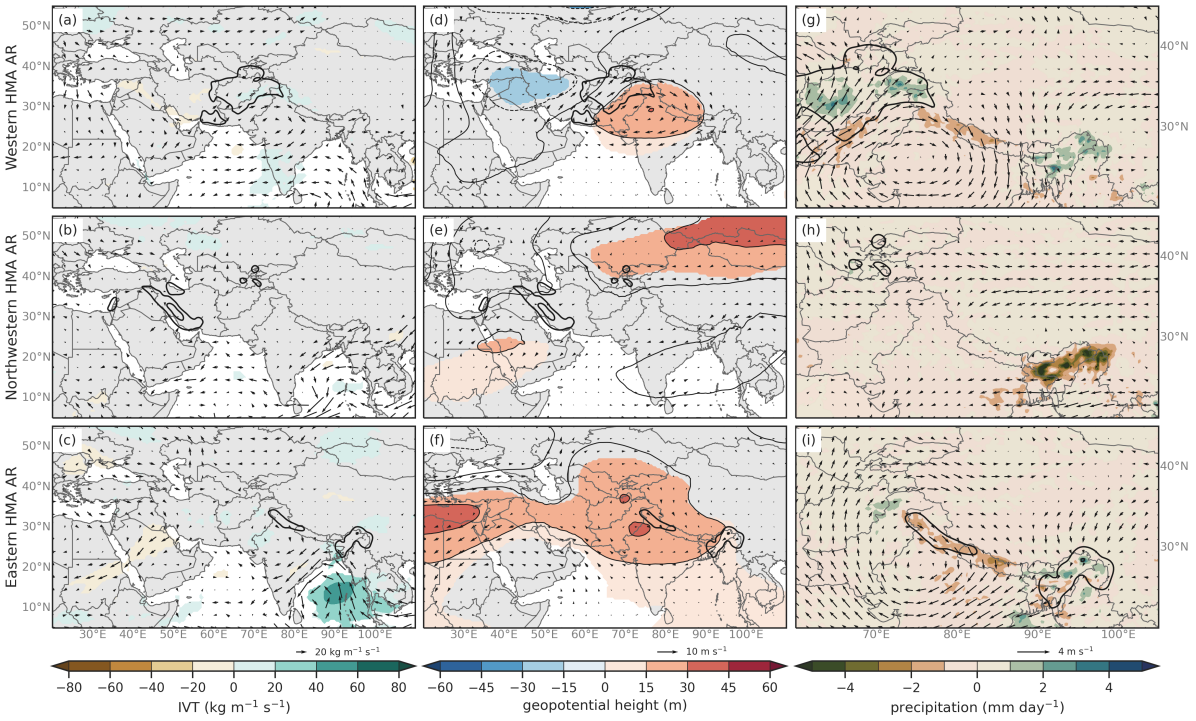

Figure B.9: (a) Composite differences of IVT (shaded and vectors, kg m^{-1} s^{-1}) for Western HMA ARs (Type 1) MJO and non-MJO conditions. Only differences in IVT that are considered at or above the 95% confidence level are shaded. (b) Same as (a) but for Northwestern ARs (Type 2). (c) Same as (a) but for Eastern HMA ARs (Type 3). (d) Composite differences of 250 hPa geopotential heights (shaded and contours, m) and winds (vectors, m s^{-1}) between HMA AR days for Western HMA ARs (Type 1) MJO and non-MJO conditions based on ERA5 for 1979-2019. Only differences in heights that are considered at or above the 95% confidence level are shaded. (e) Same as (d) but for Nortwestern HMA ARs (Type 2). (f) Same as (d) but for Eastern HMA ARs (Type 3). (g) Composite differences of precipitation (shaded, mm day^{-1}) and 500 hPa wind direction (vectors, m s^{-1}) for Western HMA ARs (Type 1) MJO and non-MJO conditions. (h) Same as (g) but for Northwestern HMA ARs (Type 2). (i) Same as (g) but for Eastern HMA ARs (Type 3). The thick black contours in all plots are showing the mean anomaly composite rainfall (mm day^{-1}) for their respective AR Type with intervals at 2 mm day^{-1}, 6 mm day^{-1}, and 10 mm day^{-1}.

References

Compagnucci, R. H., & Richman, M. B. (2008). Can principal component analysis provide atmospheric circulation or teleconnection patterns? *International Journal of Climatology*, *28*(6), 703–726. https://doi.org/10.1002/JOC.1574

Mercer, A. E., Shafer, C. M., Doswell, C. A., Leslie, L. M., & Richman, M. B. (2012). Synoptic composites of tornadic and nontornadic outbreaks. *Monthly Weather Review*, *140*(8), 2590–2608. https://doi.org/10.1175/MWR-D-12-00029.1

Spiegel, M. R., & Stephens, L. J. (2008). *Schaum's outline of probability and statistics* (4th ed). McGraw-Hill. https://doi.org/10.1036/0071485848

Wilks, D. S. (2019a). Chapter 16 - Cluster Analysis. In D. S. Wilks (Ed.), *Statistical methods in the atmospheric sciences (fourth edition)* (Fourth Edi, pp. 721–738). Elsevier. https://doi.org/https://doi.org/10.1016/B978-0-12-815823-4.00005-5

Wilks, D. S. (2019b). Chapter 5 - Frequentist Statistical Inference. In D. S. Wilks (Ed.), *Statistical methods in the atmospheric sciences (fourth edition)* (Fourth Edi, pp. 143–207). Elsevier. https://doi.org/https://doi.org/10.1016/B978-0-12-815823-4.00005-5

Appendix C

Chapter 4 Appendix

C.1 Calculation of IVT for WRF

Integrated water vapor transport (IVT), a variable widely used for the detection and identification of ARs (e.g. (Guan & Waliser, 2015; Ralph et al., 2019)) is derived from specific humidity and wind fields at 20 pressure levels between 1,000 and 250 hPa inclusive from the WRF 20 km and 6.7 km output. IVT is calculated in the zonal (x) and meridional (y) direction using the following equations:

$$IVT_x = -\frac{1}{g}\int_{1000}^{300} uqdp \tag{C.1}$$

$$IVT_y = -\frac{1}{g}\int_{1000}^{300} vqdp \tag{C.2}$$

where g is the gravitational acceleration (m s^{-2}), u is zonal wind (m s^{-1}), v is meridional wind (m s^{-1}), q is specific humidity (kg kg^{-1}), p is pressure (Pa = kg m^{-1} s^{-2}), and the column integration is between pressure levels 1000 and 250 hPa inclusive.

The magnitude of IVT is calculated using the following equation:

$$IVT = \sqrt{IVT_x^2 + IVT_y^2} \tag{C.3}$$

Specific humidity (kg kg^{-1}) is derived from water vapor mixing ratio (kg kg^{-1}) using the formula from Wallace and Hobbs (2006) where q is specific humidity and w is the water vapor mixing ratio.

$$q = \frac{w}{1+w} \tag{C.4}$$

References

Guan, B., & Waliser, D. E. (2015). Detection of atmospheric rivers: Evaluation and application of an algorithm for global studies. *Journal of Geophysical Research: Atmospheres*, *120*(24), 12514–12535. https://doi.org/10.1002/2015jd024257

Ralph, F., Rutz, J. J., Cordeira, J. M., Dettinger, M. D., Anderson, M., Reynolds, D., Schick, L. J., & Smallcomb, C. (2019). A scale to characterize the strength and impacts of atmospheric rivers. *Bulletin of the American Meteorological Society*, *100*(2), 269–289. https://doi.org/10.1175/BAMS-D-18-0023.1

Wallace, J. M., & Hobbs, P. V. (2006). *Atmospheric Science: An Introductory Survey*. Academic Press.